School of Electrical and Electronic Engineering

Newcastle University

Investigation of Frequency Domain Reflectometry as a Degradation Monitoring Technique for Lithium-Ion Batteries

A thesis submitted for the degree of

Doctor of Philosophy

by

Ama Baduba Asiedu-Asante

BSc., MSc.

September 2024

ABSTRACT

Frequency Domain Reflectometry (FDR) is an impedance-based diagnostic technique traditionally used in power systems to assess impedance changes in power cables. Recently, FDR has been applied to battery systems to measure high-frequency impedance, which is valuable for understanding battery performance in power line communication networks and assessing electromagnetic compatibility (EMC). Previous studies have highlighted FDR's ability to detect high-frequency processes like skin effect and ionic shunt effect, and its sensitivity to factors such as charging current, state of charge (SoC), and temperature. However, its potential for monitoring battery State of Health (SoH) has not been thoroughly explored.

This thesis investigates the use of FDR as a non-invasive, tool for monitoring SoH of lithium-ion batteries. The study involved two main stages of analysis. First, FDR was used to measure the impedance of 19 commercial coin cells (LIR 2032) across a frequency range of 300 kHz to 1 GHz. These cells were aged to varying SoH levels through controlled cyclic aging, and their SoH was benchmarked using Electrochemical Impedance Spectroscopy (EIS). The FDR impedance measurements were then compared to health indicators like battery capacity and internal resistance to evaluate FDR's sensitivity and accuracy in detecting aging-induced changes. The second stage involved a statistical evaluation of FDR's effectiveness in data-driven detection and prediction models, using techniques such as principal component analysis, multivariate statistical process control, and partial least squares regression.

The findings show that while FDR can detect changes in battery impedance related to aging, it has limitations in sensitivity to slower degradation processes and accuracy at lower impedance values. FDR demonstrated potential for single-cell SoH tracking but was less effective for multi-cell detection and capacity prediction compared to EIS. Despite these limitations, FDR could complement other health indicators in a multi-metric battery monitoring system, provided that careful setup design and calibration are employed.

Acknowledgements

First and foremost, I would like to thank God for the good health, strength and perseverance throughout this PhD journey.

I would like to express my deepest gratitude to my supervisory team Professor Volker Pickert, Professor Mohamed Mamlouk, and Professor Charalampos Tsimenidis, for their invaluable guidance, patience, and support. Your insightful feedback and continuous encouragement have been instrumental in navigating the complexities of this research, and for that, I am sincerely thankful.

I also extend my thanks to Dr. Jie Zhang for his guidance on the statistical evaluation aspect of this research. Your expertise has significantly enhanced the rigor of this work.

My appreciation also goes to the technical staff at the Electrical and Electronics Lab for their assistance and support throughout my studies. Your help in building prototype PCB boards for my experiments is greatly appreciated.

I am deeply grateful to IT Age Ghana Limited , the University of Mines and Technology (UMaT), the Engineering & Physical Sciences Research Council (EPSRC), and the Newcastle University DTP Partnership for providing the financial support that made this research possible.

Finally, I am forever indebted to my family for their emotional support, understanding, and encouragement. To my parents, Dr. and Mrs. Asiedu-Asante, thank you for looking after my son throughout my studies. To my husband and son, Nana Yaw Nti Snr and Nana Yaw Nti Jnr, your patience, love, and unwavering support have been my anchor during this journey. To my grandmother, sisters, and friends, thank you for the laughter, the distractions, and the much-needed breaks from my work.

This thesis is a culmination of the support, guidance, and inspiration of many people, and I am profoundly grateful to each and every one of you.

Table of Contents

List of Figures

LIST OF ABBREVIATIONS

AC	Alternating Current
AFD	Average Fréchet Distance
BC	Bidirectional Coupler
BH	Battery Holder
BMS	Battery Management System
C	Capacitor
CC-CV	Constant Current – Constant Voltage
CCM	Cross-Cell Monitoring
CE	Counter Electrode
CP	Connector PCB
CPE	Constant Phase Element
DUT	Device Under Test
DVA	Differential Voltage Analysis
ECMs	Equivalent Circuit Models
EIS	Electrochemical Impedance Spectroscopy
EM	Electromagnetic waves
EMC	Electromagnetic Compatibility
EMI	Electromagnetic Interference
ESL	Equivalent Series Inductance
ESR	Equivalent Series Resistance
EV	Electric Vehicles
FDR	Frequency Domain Reflectometry
GEIS	Galvanostatic Electrochemical Impedance Spectroscopy
ICA	Incremental Current Analysis
L	Inductor
LAM	Loss of Active Material
LLI	Loss of Lithium inventory
LV	Latent Variables
MSPC	Multivariate Statistical Process Control
MSPE	Mean Square Prediction Error
NR	Neutron Reflectometry
NZE	Net Zero Emissions

OCV	Open Circuit Voltage
OSLC	Open Short Load Compensation
OTDR	Optical Time Domain Reflectometry
PC	Principal Component
PCA	Principal Component Analysis
PCB	Printed Circuit Board
PEIS	Potentiostatic Electrochemical Impedance Spectroscopy
PLC	Power Line Communication
PLSR	Partial Least Square Regression
PN	Pseudo Noise
R	Resistor
RC	Resistor Capacitor
REF	Reference Electrode
RL	Resistor Inductor
RLS	Regression Least Square
RoC	Region of Confidence
SEI	Solid Electrolyte Interphase
SMA	Sub Miniature A
SoC	State of Charge
SoH	State of Health
SOL	Short Open Load
SOLT	Short Open Load Through
SPE	Squared Prediction Error
SSTDR	Spread Spectrum Time Domain Reflectometry
TDR	Time Domain Reflectometry
VNA	Vector Network Analyser
WE	Working Electrode
WS	Working Sense

Chapter 1 Introduction

1.1 Introduction

Battery technology, especially lithium-ion batteries, is integral in powering everything from portable electronics and medical devices to electric vehicles (EVs) and large-scale energy storage systems. According to the World Energy Outlook report, batteries are projected to account for 90% of the increase in storage capacity under the Net Zero Emissions (NZE) Scenario by 2050 [1]. Their deployment in EVs and energy storage systems is also expected to contribute to a 20% reduction in CO_2 emissions by 2030 [1]. This underscores the crucial role of batteries in achieving global commitments made at COP28, including the aim to triple renewable energy capacity by 2030.

However, battery performance degrades over time due to aging and exposure to environmental conditions, leading to capacity loss and increased internal impedance. Ensuring the reliability and longevity of batteries is therefore paramount, making State-of-Health (SoH) monitoring essential. SoH monitoring assesses a battery's ability to store and deliver energy relative to its original capacity using metrics such as capacity fade and internal impedance as health indicators [2]. Capacity fade reflects the progressive loss of charge storage capability, while impedance growth indicates increased resistance to current flow, both of which are crucial for determining a battery's remaining useful life [2, 3]. Accurately monitoring SoH requires reliable detection and characterization of these degradation metrics.

Several techniques exist for SoH estimation, employing a range of battery parameters as diagnostic metrics. Among these, impedance-based methods have proven particularly effective, as they provide insights into the underlying physical and chemical processes that drive battery aging. A well-established technique in this category is Electrochemical Impedance Spectroscopy (EIS), which probes battery behaviour across multiple time scales. However, EIS often requires complex instrumentation and is difficult to implement in real-time applications. This motivates the exploration of alternative impedance-based techniques for battery SoH monitoring.

Frequency Domain Reflectometry (FDR) is an impedance-based diagnostic technique widely used to detect impedance variations in cables and materials [4, 5]. This technique has been successfully applied in fault detection in power systems [6, 7] and aircraft wiring [6], as well as in the modelling and characterization of power semiconductor devices [8]. Additionally, FDR has been utilized to measure changes in the dielectric properties of soil and other materials [9, 10]. Given its proven effectiveness in diagnosing impedance-related changes across diverse applications, and its sensitivity to both impedance and dielectric variations, FDR presents an

interesting prospect for battery diagnostics, where impedance measurement plays a crucial role in SoH assessment.

In recent years, FDR has been explored for high-frequency battery impedance characterization, typically within the hundreds of kilohertz to several megahertz range [11, 12]. The technique operates by injecting high-frequency signals into a system and analysing the reflected signals to determine impedance characteristics over a wide frequency spectrum While lithium-ion batteries do not inherently operate at these frequency ranges, nor are they typically exposed to them, the high frequencies referenced in this context correspond primarily to the operational range of FDR. The intent is not to suggest that batteries function within these frequencies but rather to evaluate their response in this range as part of the FDR analysis. In [12], FDR was used in characterizing batteries as part of high-voltage (HV) power line communication (PLC) systems for battery management systems (BMS) [12]. Since PLC in battery communications operates in the megahertz range due to data rate, to ensure robustness and electromagnetic compatibility (EMC) requirements, understanding the high-frequency characteristics of Li-ion batteries, which form an integral part of PLC infrastructure, is essential.

Beyond PLC applications, FDR has also been employed in developing high-frequency battery models, investigating how battery geometry, state of charge (SoC), and temperature influence impedance measurements [12]. Additionally, FDR has been applied to study the electromagnetic interference (EMI) effects on batteries when placed near fast-switching power electronics, which operate in the megahertz region and can induce EMI that impacts battery performance [11]. These applications highlight the versatility of FDR in studying high-frequency battery behaviour.

This thesis is motivated by an exploratory investigation into whether FDR can be extended beyond its established applications to serve as a viable technique for SoH monitoring in lithium-ion batteries. While previous research has successfully employed FDR to detect cable faults, characterize power semiconductor devices, and study high-frequency battery impedance behaviour, its potential for tracking SoH remains largely unexplored. This research aims to evaluate FDR as a novel SoH monitoring tool by investigating its ability to detect impedance changes corresponding to decline in SoH and capacity loss. Since impedance growth and capacity fade are key indicators of battery degradation, using FDR's high-frequency sensitivity to impedance variations may provide a non-invasive, rapid, and real-time method for assessing SoH across a broad frequency range. By exploring the feasibility of FDR for battery SoH monitoring, this work seeks to contribute to the broader field of battery diagnostics and energy storage management. This approach has the potential to enhance battery health monitoring

methodologies by providing a non-invasive, real-time assessment of impedance changes within a wider range of frequencies. Its high-frequency sensitivity and rapid measurement capabilities could enable early detection of degradation.

1.2 Research Background and Motivation

The ongoing advancements in battery technology continue to drive the rapid growth of applications that employ batteries. This underscores the critical need for effective health monitoring of batteries to ensure the reliability and longevity of systems that depend on them.

1.2.1 Overview of State of Health Monitoring in Lithium-ion Batteries

State of Health (SoH) refers to the current condition of a battery relative to its ideal, full-capacity state. It is influenced by degradation mechanisms that negatively impact a battery's ability to store energy, meet power requirements, and ultimately shorten its lifespan. Thus, the detection and quantification of SoH, including degradation mechanisms, is essential for improving battery performance, predicting lifetime, and assessing a battery's suitability for second-life applications. Quantifying SoH is also vital for optimizing battery management systems (BMS) and ensuring safe, efficient operation across various applications.

The quantification of SoH is a complex task that involves evaluating key health indicators such as capacity and impedance. While extensive research has been conducted on characterizing degradation mechanisms, such as loss of lithium inventory (LLI), loss of active material (LAM), and classification-based approaches. This work focuses on SoH quantification rather than mechanistic characterization. The primary objective is to assess SoH based on observable parameters, such as increased impedance and capacity loss, which directly reflect the battery's ability to perform, rather than diagnosing specific degradation mechanisms.

SoH quantification remains a critical research area due to the numerous factors that influence battery health. These factors arise from the interplay of various physical and chemical processes, occurring both internally and externally, across spatial scales from the nanoscale to the macroscopic level, and over timescales ranging from seconds to years. Consequently, real-time monitoring and accurate quantification of SoH remain inherently complex challenges.

Several methods have been developed to quantify the SoH of lithium-ion batteries, with extensive literature exploring the strengths and limitations of these approaches [13, 14]. These methods typically focus on variations in key health indicators such as cell voltage, capacity, and internal impedance. Broadly, SoH quantification methods can be categorized into experimental methods, model-based methods, and data-driven methods [14, 15]. Model-based methods rely

on mathematical models that describe the processes and behaviours governing a battery's electrochemical and thermal dynamics [16]. There are also models in the form of equivalent circuit models (ECMs) that use electrical components to represent various battery processes. While these methods are highly accurate, they require extensive knowledge of the battery's internal processes and are computationally intensive [14, 17].

Data-driven methods employ statistical techniques or machine learning algorithms to predict SoH using large datasets of battery performance metrics [14]. These techniques are adept at handling complex, nonlinear relationships in data, making them powerful tools for SoH quantification [18]. However, data-driven methods are heavily reliant on high-quality, large-scale datasets, and their performance can be affected by variability across different battery chemistries and operating conditions [15, 17].

Experimental methods involve direct measurements of battery parameters such as voltage, current, impedance, or capacity, which provide valuable insights into overall battery health. These methods are straightforward, widely used, and reliable for monitoring battery performance, although they are prone to error accumulation over time. Electrochemical Impedance Spectroscopy (EIS), in particular, is a well-established experimental method that utilizes frequency analysis to probe dynamic battery characteristics across a wide range of timescales. While EIS is effective for characterizing degradation mechanisms, it is also highly valuable for quantifying SoH by evaluating changes in internal impedance [15, 19, 20]. In addition to measuring internal impedance, EIS has been applied to investigate mass transport processes [21], formation of the SEI layer [13, 22], and other degradation phenomena that influence SoH. Another widely used experimental approach is hybrid pulse power test (HPPT), which evaluates a battery's power capability and resistance by applying a series of charge and discharge pulses. HPPT is particularly useful for estimating internal resistance under dynamic operating conditions and can provide insights into both instantaneous power performance and long-term degradation [14].

While FDR shares similarities with these impedance-based techniques, particularly EIS, in its ability to track changes in battery characteristics over time, its underlying principles and measurement approach are distinct. Unlike EIS, which probes battery dynamics across multiple frequency ranges using sinusoidal perturbations, FDR analyses the reflection and transmission of high-frequency signals to infer impedance changes. This makes FDR inherently different in its sensitivity to various phenomena occurring in batteries. Whereas EIS provides well-established impedance spectra for mechanistic insights, FDR has the potential to serve as a fast, non-invasive alternative for detecting SoH trends which is yet to be proven and refined. FDR

is not yet known to match EIS in accuracy for SoH quantification and remains an evolving technique that requires further refinement to enhance its practical applicability

1.2.2 Frequency Domain Reflectometry (FDR) as an Impedance Measuring Method

Reflectometry is another impedance-based direct measurement method that is gaining attention in battery applications. It is a diagnostic technique that analyses the reflection and transmission of high-frequency waves within different media. The method functions by transmitting high-frequency electromagnetic waves at different frequencies through a system or material, where the impedance of the system determines the proportion of the incident signal that is reflected versus transmitted [6]. By analysing these reflected and transmitted signals, the impedance characteristics of the system can be determined.

Reflectometry has been widely applied in fault detection for power cables [6, 7], aging and failure diagnostics in power electronics [8], and characterization of material dielectrics [10, 23]. Various forms of reflectometry exist, distinguished by the type of incident signal employed [5]. Recent developments have extended reflectometry-based techniques to battery systems. Frequency-Domain Reflectometry, a specific type of reflectometry that utilizes sinusoidal waves at varying frequencies, has been explored in [24] and [25] to assess the feasibility of using batteries as transmission channels in power line communication in BMS. This approach aims to reduce cabling in BMS systems, particularly when advanced SoH monitoring is integrated. These studies employed the S_{11} reflection method to measure battery impedance in the frequency ranges from 300 kHz to 30 MHz and 1 MHz to 110 MHz, respectively, leading to the development of high-frequency models for battery characterization. However, a major limitation of the S_{11} reflection method is its insensitivity to impedance values below 1 Ω, making it unsuitable for SoH applications where aging-induced impedance variations can be significantly smaller.

Further studies, including [26] and [27] have employed FDR to characterize battery impedance while evaluating electromagnetic interference and compatibility (EMI/EMC) between 1 kHz and 300 MHz. Reference [26] utilized the S_{11} reflection method, while [27] employed a more precise shunt-through method introduced in [28]. Both studies extended the impedance measurement range to 300 MHz and developed models explaining the EMI behaviours of batteries. The shunt-through FDR method has also been used in [12] and [29] to study high-frequency processes in batteries between 1 kHz and 300 MHz. Reference [12] developed equivalent circuit models based on high-frequency impedance measurements, identifying key high-frequency phenomena such as ionic shunt effects and skin effects within

battery electrodes. This study also analysed the impact of physical design parameters such as geometry and electrode tab positioning on high-frequency impedance, showing that these factors significantly influence battery inductance. Additionally, state of charge (SoC) was found to affect high-frequency impedance, while temperature effects became more pronounced above 1 MHz.

These studies collectively demonstrate FDR's effectiveness in measuring battery impedance at high frequencies and its potential for characterizing battery systems. They also highlight the feasibility of using FDR-derived impedance models for various applications. However, despite these advancements, no study has yet explored the use of FDR-based impedance measurements for quantifying battery SoH, leaving a critical gap in research. This work is therefore motivated by the question of whether FDR, which has been successfully applied in EMI/EMC characterization and high-frequency battery impedance studies, can be extended beyond these applications to serve as a viable technique for SoH monitoring in lithium-ion batteries. Unlike conventional SoH estimation methods, which rely on time-domain voltage, current, and impedance measurements, FDR provides high-frequency impedance insights that may offer a novel pathway for tracking degradation-induced impedance changes. The challenge lies in determining whether these high-frequency impedance variations correlate meaningfully with battery aging and whether FDR can provide a more sensitive, scalable, or efficient alternative to existing SoH estimation techniques. Addressing this gap is essential to unlocking the full potential of FDR for battery health assessment.

1.3 Research Gap

Existing literature on the use of FDR for high-frequency impedance measurements in lithium-ion batteries remains limited. Among the few available studies, FDR has primarily been applied to characterize battery impedance for power line communication applications, electromagnetic compatibility evaluations, and to analyse the dependencies of high-frequency impedance on physical cell properties. These studies have contributed to advancing measurement setups, refining de-embedding protocols, developing impedance-based models, and examining the effects of temperature, SoC, and cell design on high-frequency impedance. However, they have not explicitly explored the potential of high-frequency impedance measurements for detecting or monitoring battery state of health.

Furthermore, FDR studies have typically been conducted on individual cells or small cell groups, raising questions about the scalability and broader applicability of the technique. Notably, [30] observed that the high-frequency signal reflected from a battery pack changed

when an aged cell was introduced, suggesting that FDR-based techniques could potentially be leveraged for SoH monitoring. Given its ability to provide non-invasive, rapid impedance measurements over a wide frequency range, FDR presents an opportunity for SoH assessment.

This work is therefore motivated by the question of whether FDR, which has been successfully applied in high-frequency battery impedance characterization, can be extended to serve as a viable technique for SoH monitoring in lithium-ion batteries. While impedance-based methods for battery health assessment are well-established, most studies have focused on lower frequency ranges and primarily relied on EIS [13, 17]. In contrast, FDR offers wider frequency coverage, faster measurements, and the ability to operate on live battery systems without requiring disconnection from external circuit, making it a promising alternative for SoH evaluation. The challenge lies in determining whether high-frequency impedance variations captured by FDR correlate meaningfully with battery aging and whether this approach can provide a more sensitive, scalable, or efficient alternative to existing SoH estimation methods. Addressing this gap is crucial to unlocking the full potential of FDR for battery health monitoring. It is important to note that this study investigates FDR for monitoring overall SoH rather than diagnosing specific degradation mechanism.

1.4 Research Objectives and Methodology

The primary objective of this study is to evaluate the effectiveness of FDR as a tool for detecting and diagnosing the SoH of lithium-ion batteries using battery capacity and internal resistance as health indicators. To achieve this objective, three key goals were outlined, each addressing a critical aspect of FDR's potential application in SoH monitoring:

1. To explore the potential of using FDR for battery SoH monitoring, it is first necessary to generate and characterize battery samples at different states of health. Thus, the initial goal of this thesis is to produce and evaluate samples at varying SoH levels. Commercial lithium-ion cells are used for this purpose, aged through a controlled constant current-constant voltage (CC-CV) cycling method for a predefined number of cycles. The aging process is intended to induce general degradation, rather than targeting specific mechanisms such as lithium plating, loss of active material (LAM), or loss of lithium inventory (LLI). This approach aligns with the study's focus on monitoring and quantifying overall SoH rather than identifying specific degradation pathways. To assess SoH, impedance and capacity are chosen as key indicators. Capacity directly reflects the battery's ability to store and deliver energy, making it a fundamental measure of performance and aging. Impedance, on the other hand, provides insight into the

internal resistance and electrochemical condition of the cell, which influences power capability and efficiency. Given that FDR is an impedance-based technique, impedance measurement is particularly relevant for evaluating its potential as a SoH monitoring tool. To validate the measured SoH and characterize the impedance of the samples EIS is used as a benchmark technique. EIS, like FDR, operates in the frequency domain and is a well-established method for impedance characterization, making it a suitable reference for comparison.

2. The second goal is to evaluate FDR performance in detecting aging amongst the sample cells as compared with health indicators. In this study, the health indicators used are battery capacity and impedance. Battery capacity was obtained during cyclic aging, and the impedance was obtained from EIS tests. This goal was achieved in two stages. Firstly, by evaluating FDR's performance in monitoring impedance changes of a single cell during cyclic aging and secondly by assessing FDR's accuracy in detecting aging amongst multiple cells.
3. The third goal of this study was to evaluate how FDR would work if it was used as input data in a data-driven model. This is achieved through the use of three statistical techniques. The first one was principal component analysis (PCA), which is used to reduce the data dimensionality and to observed how FDR differentiates cells of different SoH through clustering. Secondly, PCA-based multivariate statistical process control (MSPC) was used to test how FDR could perform in detection system where cells were sorted based on a pre-defined control limit. Thirdly, FDR's applicability in predictive models was tested using partial least squares regression (PLSR). These methods were selected because they handle large, correlated data sets well. Each of these techniques was also applied the EIS data for benchmark assessment.

1.5 Research Novelty and Contribution to Knowledge

The main outcome of this research is the comprehensive evaluation of FDR as a tool for battery SoH diagnosis. Consequently, this research has made the following contributions to knowledge;

- Evaluated the performance of FDR as a tool for SoH monitoring using capacity and EIS measured cell internal resistance as health metrics.
- Statistically evaluated FDR performance as SoH monitoring, diagnostic and predictive tool using PCA, MSPC and PLSR methods.
- Introduced a new definition of the region of confidence in FDR-based setups, optimizing it for the measurement of relative changes in impedance.

- Extended the application of resonance frequency analysis using FDR to batteries, demonstrating that FDR effectively detects resistance changes as the battery ages.
- Comparative analysis of EIS-measured impedance and FDR-measured impedance for battery SoH detection.

These contributions form the foundation for developing a novel SoH monitoring tool for lithium-ion batteries that has a potential for rapid non-invasive measurement over a wider range of frequencies. This would support the efficient use and longevity of batteries, thereby promoting the sustainable energy storage solutions necessary to achieve net zero emissions.

1.6 List of Publications

This research as resulted in publications in the MDPI batteries journal and three conference poster presentations:

- Asiedu-Asante, A.B., Pickert, V., Mamlouk, M., Tsimenidis, C. "Evaluating Frequency Domain Reflectometry as a Tool for Lithium-Ion Battery Health Prognosis", *Batteries* **2024**, [*10]*, 185, https://doi.org/10.3390/batteries10060185
- Asiedu-Asante, A.B., Pickert, V., Tsimenidis, C., and Mamlouk M., "Comparative study of Frequency Domain Reflectometry (FDR) and Electrochemical Impedance Spectroscopy (EIS) for Battery Health Detection: Implications for BMS Power Electronics Design", in 2024 *Centre For Power Electronics Annual Conference, 2024,* [Poster Presentation].
- Asiedu-Asante, A.B., Pickert, V., Tsimenidis, C., and Mamlouk M., "Battery State-of-Health Monitoring: Evaluating FDR Through Capacity Fade and Internal Resistance Metrics", in 2024 *Faraday Institution Conference, 2024,* [Poster Presentation].
- Asiedu-Asante, A.B., Pickert, V., Mamlouk, M., Tsimenidis, C., "Degradation Diagnostics for Lithium-ion Cells using Parameter Extraction from Impedance Spectra", in 2022*, Northeast Battery Alliance Conference 2022,* [Poster Presentation].

1.7 Structure of the Thesis

The remaining chapters of this thesis are structured as follows:
Chapter 2 presents detailed literature review on battery degradation mechanisms, SoH monitoring techniques and reflectometry. It discusses measurement principles and calibration methods employed in EIS and FDR measurements.

Chapter 3 discusses the characterisation of the sample cells used in this research. This chapter targets the first goal of this study. It gives details on the structure and chemistry of the sample cells. It also presents the details of how the benchmark tests were implemented and explains the study methodology.

Chapter 4 presents the evaluation of FDR performance as compared to the health indicators. This chapter achieves the second goal of this thesis. It presents the implementation of the FDR setup and the results and discussion on the FDR measurement performed on samples cells.

Chapter 5 gives the statistical evaluation of FDR data. It achieves the third research goal. Implementation and findings of PCA, MSPC and PLSR are presented in this chapter.

Chapter 6 contains the overall conclusions and future works recommendations.

Chapter 2 Literature Review

2.1 Introduction

This chapter lays the foundations for discussions on battery electrochemical processes, methodology design and results discussion in subsequent chapters. It delves into existing literature with the aim of providing an overview on the potential of FDR as a tool for battery SoH monitoring and how it compares to other monitoring techniques. Firstly, various degradation mechanisms that affect battery performance over time are discussed. This discussion lays the foundation for exploring the monitoring techniques used to characterize these mechanisms. Techniques discussions are limited to impedance based experimental techniques and equivalent circuit modelling methods (ECMs) relevant to this study. Secondly, principles and application of EIS in battery SoH assessment are presented in detail, as this method is used as the benchmark in this work. Following this, an overview of the FDR technique, is presented. This includes discussions on the principles and methods of measurement implementation. Also discussed are calibration and de-embedding methods necessary for accurate and reliable FDR measurement. Finally, the chapter concludes with applications of FDR in existing literature that have influence the aim to extend FDR applications to battery SoH monitoring.

2.2 Battery Degradation Mechanisms in Lithium-ion Batteries

Battery State of Health (SoH) reflects the overall condition and capacity of a battery relative to its original state and serves as a key indicator of its remaining useful life [2, 31]. SoH quantifies the extent of degradation a battery has undergone but is not a single, directly measurable parameter. Instead, it is assessed using multiple indicators, such as capacity and impedance, which evolve as the battery degrades [2]. As degradation progresses, these SoH metrics change significantly, directly impacting performance and longevity. Extensive studies on battery degradation have identified key degradation modes, including loss of lithium Inventory (LLI) and loss of active material (LAM) in both the positive and negative electrodes [2, 32]. LLI is primarily associated with side reactions that irreversibly consume lithium ions, reducing the amount of available charge carriers, while LAM results from the structural breakdown of electrode materials, diminishing the active area for lithium-ion intercalation [2, 17]. These degradation processes are influenced by a combination of electrochemical, mechanical, and thermal factors [33], as summarized in Figure 2.1. Also, internal and external conditions including battery design, cycling patterns, operating temperature, current load, depth of discharge (DoD), and storage conditions contribute to degradation [34]. During each charge-

discharge cycle, lithium-ion transport between the electrodes induces irreversible changes, leading to electrode stress, electrolyte decomposition, increased impedance, and eventual capacity loss [17, 35].

Since FDR measurements primarily probe impedance changes at the electrode-electrolyte boundary, this section highlights degradation mechanisms that significantly influence this region [11, 12]. The solid electrolyte interphase (SEI) layer forms during the early stages of a battery's life and plays a crucial role in stabilizing the electrode-electrolyte interface. However, with continued usage, electrochemical reactions at the electrode surface consume electrolyte components, contributing to SEI growth on the anode [31, 36]. While the SEI layer acts as a protective barrier, excessive growth can deplete electrolyte species, increase impedance, and lead to irreversible material loss and capacity fade [33]. Moreover, factors such as cycling patterns, elevated temperatures, and mechanical stress can accelerate SEI degradation, further impacting battery performance and long-term stability [37]. Additional details on SEI formation and related battery dynamics are presented in Appendix A. Another significant degradation process is lithium plating, which occurs when lithium ions are deposited as metallic lithium on the anode surface instead of intercalating into the anode structure. This phenomenon is most common during fast charging, low-temperature operation, or overcharging, when lithium intercalation rates are too slow to accommodate the incoming lithium ions [38, 39]. Several factors exacerbate lithium plating, including uneven potential distributions, local overpotentials, and high charge currents [40]. The formation of metallic lithium reduces the active lithium available for charge storage, causing capacity loss[40]. Additionally, lithium plating can trigger dendrite formation, which poses a safety risk as dendrites may grow and pierce the separator, leading to internal short circuits and potential thermal runaway [38, 39].

Another major degradation pathway is electrode cracking, a mechanical degradation process caused by repeated lithiation and de-lithiation cycles, which induce expansion and contraction of electrode materials. This issue is particularly severe in high-capacity anode materials, such as silicon, which experiences significant volume changes during cycling and may not as significant in the coin cell samples used [14]. As mechanical stress accumulates, microcracks form within the electrode, disrupting electronic and ionic conductivity pathways. The consequences include exposure of fresh electrode surfaces, leading to continuous SEI growth and electrolyte consumption, an increase in impedance due to loss of conductive pathways, and active material detachment from the current collector, reducing the effective electrochemical area and accelerating performance decline [40].

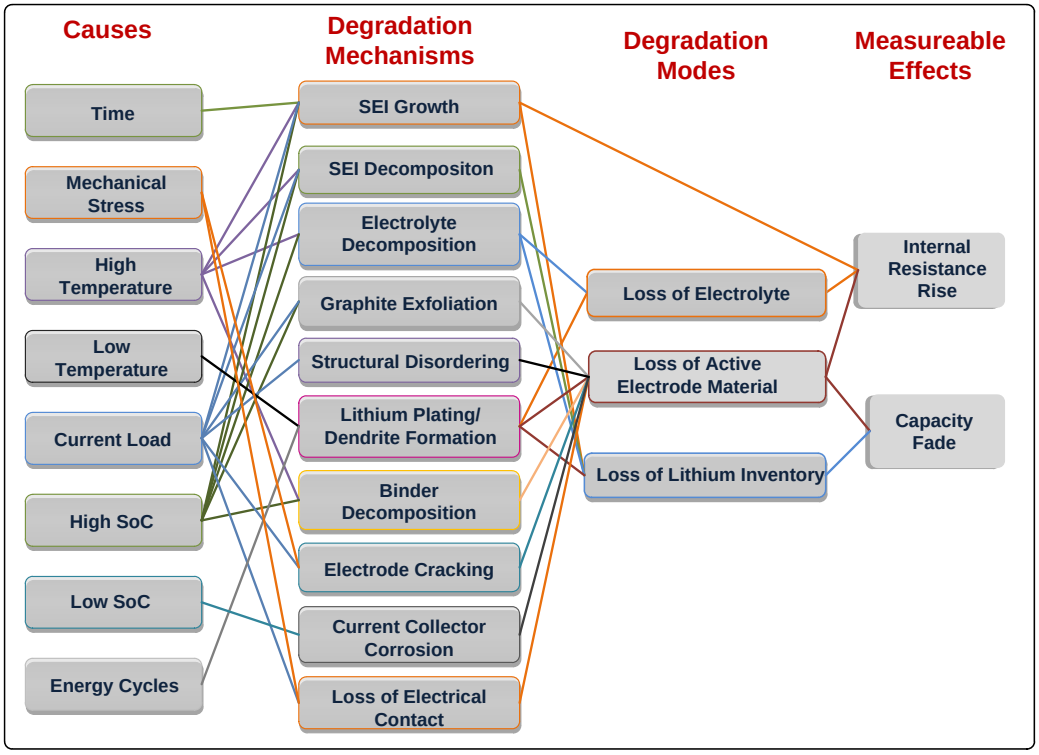

Figure 2.1 Causes of degradation mechanisms and their associated modes and measurable effects [2, 34, 41].

Crack propagation is influenced by cycling conditions, temperature fluctuations, and particle size distribution. In addition to mechanical and electrochemical degradation, electrolyte decomposition significantly impacts long-term battery performance. Electrolyte solvents and salts break down due to thermal, electrochemical, or oxidative stress, occurring under repeated use, high voltages, elevated temperatures [34, 41]. Electrolyte breakdown pathways include oxidation of electrolyte solvents at the cathode, forming gas bubbles and surface films that increase impedance, reduction of electrolyte components at the anode, contributing to SEI growth and lithium inventory loss, and salt decomposition, which corrodes electrodes and separators, further accelerating degradation. Electrolyte breakdown significantly affects capacity retention, impedance rise, and gas generation, impacting both battery performance and safety.

Numerous studies, such as [17, 32, 33], provide extensive reviews of degradation mechanisms in lithium-ion batteries and have explored the detailed mechanisms behind degradation. While these studies offer valuable insights into the underlying causes of battery aging, the primary focus of this research is not on identifying specific degradation pathways but on quantifying overall SoH via health indictors such capacity and impedance using FDR measured impedance. Regardless of the specific degradation mode, increased impedance and reduced capacity remain measurable indicators of SoH decline. Therefore, this study aims to

investigate impedance-based SoH monitoring using FDR as a potential monitoring tool. Since FDR measurements are particularly sensitive to changes at the electrode-electrolyte interface, understanding the key degradation processes affecting this region provides essential context for evaluating the feasibility of FDR for battery health assessment.

2.3 Overview of Monitoring Techniques for Battery State of Health

SoH monitoring focuses on tracking a battery's health status over time, however, it sometimes overlaps with degradation detection since SoH indicators reflect degradation effects. For instance, capacity fade and impedance growth, which are key SoH metrics, are direct consequences of degradation processes such as SEI growth, lithium plating, electrode cracking, and electrolyte decomposition. However, SoH monitoring techniques are primarily concerned with quantifying performance decline rather than identifying specific degradation mechanisms. In contrast, degradation detection methods, such as post-mortem analysis, X-ray diffraction (XRD), and scanning electron microscopy (SEM), aim to pinpoint the root causes of aging at a microscopic level [40, 42]. These however are invasive technologies and can be expensive.

SoH monitoring methods rely on various health indicators like capacity, impedance and internal resistance, where the actual charge-discharge characteristics and impedance are analysed over time [32]. Changes in capacity affects amount of charge a battery can hold, while changes internal resistance affects the efficiency of energy delivery and the available output power [2]. The impedance characterizes how a battery responds to alternating current and reflects the relationship between the applied alternating current and the resulting terminal voltage. The Open-circuit voltage (OCV), which is battery voltage at zero current, is also employed in SoH monitoring but is typically used in combination with other health indicators [2, 34]. Additionally, physical parameters such as temperature [16, 43], production of gases in batteries [44–46] and generation of sounds [47–49] are also utilised to diagnose aging processes occurring in batteries and to infer overall health.

Various techniques have been developed to assess SoH accurately, ranging from direct measurement methods, indirect measurement methods and advanced data-driven approaches. Direct measurement methods involve the direct measurement of health indicators. Indirect methods involve model-based approaches, such as Equivalent Circuit Models (ECM) and Machine Learning (ML) algorithms, which estimate SoH using data from measured health indicators. Additionally, data-driven approaches employ historical battery performance data and artificial intelligence to predict degradation trends. Table 2.1 summarises the main categories

of SoH monitoring while further discussion on each category is provided in sections 2.3.1 to 2.3.3.

Table 2.1 SoH Monitoring and Estimation Methods

	Key Benefits	Limitations
Experimental / Direct Methods Based on direct measurement/storage of battery operational and lifetime data.[13, 15]	• Easy to monitor and implement • Low computation cost • Can provide high accuracy	• Specialised equipment may be required. • Can be time consuming. • Prune to measurement inaccuracies. • Relatively difficult to modify during operation
Model-Based / Indirect Methods Uses models to simulate battery behaviour and estimate SoH measured parameters [14, 15, 17].	• Accurate SoH estimation • Provides information on underlying processes • A trade-off between computational complexity and estimation accuracy	• Estimation is sensitive to data quality • Algorithm development requires more experimentation and can be time-consuming • Model parameterization can be difficult. • Has tendency to be complex with more parameters are measured
Data-driven Methods Based on historical data on battery performance to train machine learning based algorithms for SoH prediction [17–19].	• Accurate for parameter estimation • Capable of self-learning • Suitable for non-linear systems • Suitable for different chemistries • Relatively easy implementation	• Require large amounts of training data for accurate estimation • High computational effort

2.3.1 Experimental/ Direct Methods Techniques

Experimental or direct SoH monitoring methods involve the direct measurement of battery parameters such as voltage, current, impedance, internal resistance, temperature, and gases to diagnose battery health. These methods provide precise, real-time data about battery health, making them critical for effective battery health determination. Popular direct SoH monitoring methods include capacity measurement [34], internal resistance and impedance measurement [17, 34], Coulomb counting [34], differential voltage analysis (DVA) [50], incremental capacity analysis (ICA) [50], electrochemical impedance spectroscopy (EIS) [17, 50], and hybrid power pulse testing (HPPT) [17].

Battery capacity reflects the amount of energy a fully charged battery can store and is widely used as a SoH indicator. When measured accurately, it provides a simple and precise way to infer SoH; however, accurately determining capacity in real-world operational conditions is challenging [34, 51]. Consequently, capacity measurement is mostly suitable in controlled environments such as laboratories [34].

Coulomb counting is another method that tracks the charge transferred during a full charge-discharge cycle [34, 50]. Achieving high accuracy with this method is difficult because it relies on precise current sensing to minimize accumulated errors. In laboratory conditions, capacity is typically measured by charging and discharging batteries at a constant current under controlled temperatures (20–25°C). While this approach is accurate, it is difficult to replicate in real-world applications such as electric vehicles (EVs) [34]. As a result, coulomb counting is often used in conjunction with other methods to verify capacity estimates [20]. Researchers in [20] explored incorporating depth of discharge (DoD) into SoH estimation, where DoD represents the amount of charge released relative to the battery's rated capacity, compensating for variations in charging and discharging efficiency [20].

The internal resistance of a battery directly influences the voltage drop across the battery when a current is applied, thereby affecting the available power output. Total internal resistance consists of both ohmic resistance and polarization resistance, with the former being the primary contributor to the voltage drop under normal operating conditions [17]. Hybrid power pulse testing (HPPT) is a common method used to measure this resistance, where resistance is calculated from the voltage change during current pulses [17, 34, 50]. The current and voltage variations are analysed, and the internal resistance is determined while considering SoC and temperature [52]. Several studies, such as [53, 54], have used HPPT to measure battery internal resistance and developed model-based SoH monitoring approaches that incorporate SoC and temperature effects. However, HPPT has some limitations. It is a time-consuming process, as each sample requires multiple charge-discharge cycles at different SoC levels to obtain reliable resistance values. Additionally, HPPT measures overall internal resistance but does not effectively separate different resistance components such as ohmic, polarization, and charge transfer resistance as techniques like EIS do. These limitations make HPPT less practical, particularly when analysing a large number of samples with limited testing resources.

Impedance measurement is another widely used approach for determining battery SoH, with EIS being one of the most established techniques. EIS evaluates battery health by measuring impedance over a wide frequency range, providing deeper insight into the electrochemical processes occurring within the battery. This is particularly useful because

capacity fade and impedance rise do not stem from a single cause but rather from multiple degradation mechanisms and their interactions. Since many of these processes occur on overlapping timescales, impedance spectroscopy across different frequencies offers a comprehensive characterization of battery health. EIS has been applied to study key degradation processes, including double-layer capacitance [32], charge transfer resistance [13, 32], SEI characteristics [39], mass transport [21], and internal resistance [13, 17]. Although EIS provides rich diagnostic information, its practical application is sometimes limited by long test durations and the need for stable testing conditions. To improve SoH estimation, ECMs are often employed, where EIS data is used to parameterize the models. Advanced techniques, such as particle swarm optimization (PSO), have been used to enhance ECM accuracy by refining these parameters. However, EIS results can be influenced by external factors such as temperature, SoC, and contact resistances that arise from connections used, which may impact measurement repeatability.

Other direct measurement methods include incremental capacity analysis (ICA) [55], differential voltage analysis (DVA) [56], temperature-based methods [16, 43], gas analysis methods [43, 46, 57], and acoustic-based methods [47, 58]. These approaches assess battery state by measuring capacity, internal resistance, temperature, gas emissions, or the time of flight of sound waves in batteries. However, a major drawback of these methods is that they do not effectively characterize the root causes of aging. Instead, they provide limited insight into the behavioural changes that lead to degradation. Additionally, techniques such as temperature and gas monitoring often serve as indicators of failure only after significant degradation has already occurred.

Compared to other direct measurement methods, EIS's ability to provide a detailed frequency response makes it an attractive choice for SoH diagnosis. It offers insights into specific degradation mechanisms that other methods fail to capture [17, 18, 59]. This advantage makes EIS a suitable benchmark when evaluating new impedance-based SoH monitoring techniques. In [59], EIS was used to monitor and characterize aging in battery cells as part of a real-time SoH diagnosis method. Similarly, [60] compared diffusion coefficient calculations obtained from EIS with those derived from conventional internal resistance monitoring methods, assessing their effectiveness in detecting early-stage short circuits. These studies used EIS's ability to correlate impedance measurements with electrochemical processes and quantify their impact on battery performance over time.

To further improve battery state diagnostics, EIS has been used alongside capacity fade to provide a holistic assessment of SoH. A study in [61] examined the role of SEI growth in

capacity fade and internal resistance rise in lithium-ion batteries. Using EIS-based models and cyclic capacity measurements, the authors quantified how lithium concentration levels in both the anode and cathode, along with changes in diffusion and ionic conductivity, contribute to battery performance degradation. Reference [62] also employed EIS alongside charge/discharge curves, ICA, and the average Fréchet distance (AFD) in a study identifying charge transfer resistance (R_{ct}), equivalent series resistance (ESR), and SEI resistance (R_{SEI}) as key contributors to increased resistance in aging batteries. Their findings showed that combining ESR and R_{SEI} improved offline SoH estimation accuracy.

While HPPT is commonly used to estimate internal resistance through current pulses, it has several limitations that make it less suitable as a benchmark technique for this study. HPPT provides an overall internal resistance measurement but does not effectively separate different resistance components (ohmic, polarization, and charge transfer resistance) as EIS does. Additionally, HPPT requires multiple charge-discharge cycles at different SoC levels, making it a time-consuming process given the number of samples and available testing resources. Instead, this study extracts the equivalent series resistance (ESR) directly from EIS data, as ESR serves the same purpose as the resistance measured via HPPT but is obtained more efficiently. Furthermore, EIS is used alongside an ECM to characterize battery samples before conducting FDR tests, streamlining the analysis process. Since EIS already provides both the impedance spectrum and ESR from a single experiment, incorporating HPPT would introduce unnecessary complexity without offering significant additional benefits. Moreover, both EIS and FDR are frequency-based techniques, making them more compatible for comparative analysis. By using EIS as the benchmark, this study aims to assess the feasibility of FDR as a SoH monitoring tool, focusing on capacity fade and resistance rise as key indicators of battery health. The use of frequency-domain methods enables a more comprehensive characterization of internal battery dynamics, reinforcing EIS as a more suitable reference technique than HPPT for this research.

2.3.2 Model-based/indirect Methods

Model-based methods employ mathematical models generated from experimental data to simulate battery behaviour while capturing various dependencies [17]. These models enable continuous SoH estimation by incorporating relevant battery parameters, such as temperature, electrochemical processes, physical construction, as well as some external factors that influence battery performance. The most common approaches include electrochemical models [18, 63], thermal models [64], and equivalent circuit models (ECMs) [18, 21, 65], as well as hybrid

approaches that combine multiple modelling techniques. Filters and observers such as Kalman filter [66, 67], extended Kalman [66] unscented Kalman filter [68] have also been used together with models to improve adaptability of the methods to new data. Table 2.2 summaries the commonly used SoH models.

Electrochemical models are based on the fundamental principles governing lithium-ion batteries, such as charge transport, SEI layer formation, and electrochemical reactions at the electrodes. These are originally developed in [69, 70], which describes lithium-ion diffusion through porous electrodes using partial differential equations. However, the solution difficulty and high computational pressure can hinder its use for online application and state estimation [34]. Improvements have been made in research leading to models such as the pseudo two dimensional (P2D) model and the single particle model which have been relatively simplified and require less computational power [34, 51]. Various observer-based approaches have been employed to estimate key battery parameters related to SoH. Methods such as the adaptive output-injection observer [71], proportional-integral (PI) observer [72], extended Kalman filter [73], multi-time-scale observer [74], and particle filter [73] have been used to determine internal resistance and capacity. Electrochemical models can also be enhanced by integrating chemical and mechanical degradation mechanisms, providing a more detailed representation of specific aging phenomena. For example, studies [75, 76] have refined the single particle model by incorporating the growth of the SEI layer, establishing a quantitative relationship between SEI formation and the number of charge-discharge cycles. While integrating electrochemical models with various aging mechanisms enables a more comprehensive understanding of degradation, achieving a unified model that accounts for all aging processes in different battery chemistries remains a significant challenge.

Thermal models help in understanding how temperature affects battery performance by providing insights into how heat generation and thermal characteristics change as the battery ages. In [77], a thermal model proposed that utilises internal temperature to estimate occurrence of temperature-dependent mechanisms such as double-layer resistance, SEI film growth and cathode cracking. References [15, 78] utilised temperature changes during cycling to estimate SoH. Differential temperature curves during constant charging were used in [78] while [15] used temperature rise during discharge. Reference [79] applied a three dimensional model that utilises particle swarm optimisation and neural networks to predict temperature at multiples points in a battery enhancing real-time monitoring. Also, [41] used thermal models to detect internal faults and inferred battery SoH under different thermal faults. Despite their wide

application and advantages, thermal models do not directly reflect electrochemical impedance characteristics, which are critical for frequency-domain analysis.

Table 2.2 Common Model-based SoH Estimation Methods

Method	Benefits	Limitations
Electrochemical models	▪ Accurate ▪ Suitable for non-linear systems ▪ Can be adjusted to different chemistries	▪ Becomes complex with large number of variables. ▪ Can require high computation effort
Equivalent circuit models	▪ Intuitive and easy to implement ▪ Accounts for physical law, electrochemical processes for characterisation	▪ Danger of overfitting ▪ Can be time-consuming
Thermal models	▪ Incorporates temperature dependencies	▪ Can require high computation effort ▪ Heavily dependent on model used ▪ Requires temperature sensors

ECMs replicate the electrochemical processes within a battery using electrical components such as resistors (R), capacitors (C), and sometimes inductors (L), making them intuitive and practical for various applications. They can also be relatively simple and computationally efficient, which makes them suitable for applications in diagnosis [65]. The selection of elements that constitute the ECM depends on the complexity of the impedance curve being modelled. A simplified R_{int} model, shown in Figure 2.2a, uses a resistor in series to represent the battery's inherent resistance, highlighting the basic drop in battery voltage when connected to load [80]. In Figure 2.2b and Figure 2.2c, the 1RC and 2RC models based on the Thevenin model are illustrated respectively. The 1RC model captures the battery’s ability to store charges and the resistances to charge migration, during charge and discharge cycles [81]. The dual polarization model (2RC) uses two RC branches to better capture more of the battery's dynamic processes. This is especially useful for applications requiring more accurate SoH monitoring [82, 83]. A 3RC branch model which adds an additional layer of accuracy capturing the non-linear processes using three parallel RC branches is sometimes used [80]. There is, however, the danger of overfitting, where RC branches are added to ECM, with little physical meaning. The model parameters are obtained by complex non-linear least squares fitting to the Nyquist plot of the impedance response curve [84].

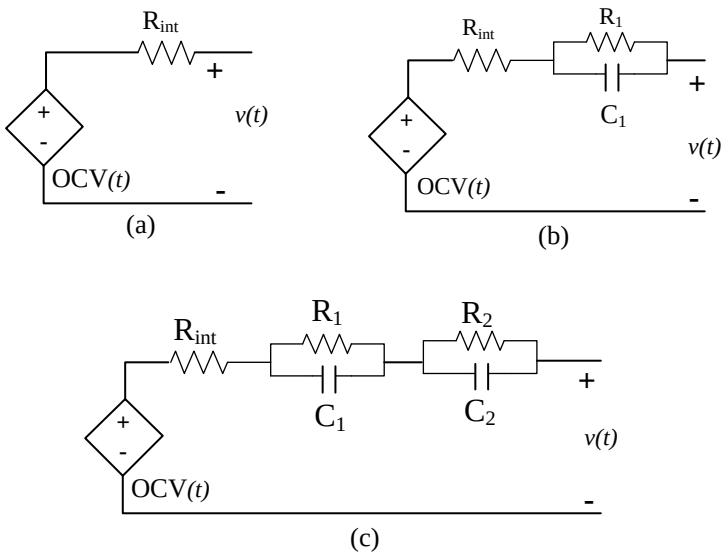

Figure 2.2 Equivalent circuit Models. (a) Simplified Rint Model. (b) 1RC model. (c) 2RC model [80, 85, 86].

The Randles circuit, in Figure 2.3 is a more complex RC model and it includes elements such as Warburg impedance (W) to represent diffusion limitations within the battery and a constant phase element (CPE) to account for non-ideal capacitances at the electrodes. This additional complexity allows the Randles circuit to capture processes like charge transfer at the electrode surfaces. It is preferred for applications where understanding the internal dynamics of the battery is important, such as analysing degradation mechanisms [13, 21]. References [87, 88] used this to estimate battery parameters like charge transfer resistance and double layer capacitance for SoH estimation. Reference [87] implemented this on microcontrollers to be used directly at the measurement site without needing a computer, highlighting how it can be computationally efficient. Also, ECMs have been integrated with filters [89, 90], statistical methods [91–93] and machine learning [18] for SoH studies. The above-mentioned studies showcase the effectiveness of ECM in providing simple, relatively accurate representation of battery dynamic processes. Based on these, Randles ECM was used to interpretate the EIS responses and characterise the state of the sample cells used in this work. Application of Randles circuit to characterise the cells is discussed in Chapter 3 and Appendix C.

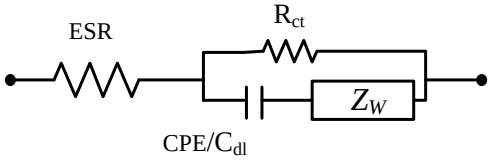

Figure 2.3 Randles circuit model [85, 86].

Given the trade-offs among different modelling techniques, ECMs were selected for this study due to their practicality, computational efficiency, and suitability for real-world applications. Unlike electrochemical models, which rely on complex partial differential equations to simulate lithium-ion transport, SEI layer growth, and electrode degradation, ECMs represent battery dynamics using simple electrical components such as resistors, capacitors, and inductors. Thermal models, on the other hand, focus on temperature-related effects and have been applied to estimate SoH based on temperature variations during cycling. Although useful for detecting internal faults and thermal anomalies, thermal models do not directly reflect electrochemical impedance characteristics, which are critical for frequency-domain analysis. ECMs offer a balance between simplicity and accuracy by effectively capturing key degradation indicators such as internal resistance increase, charge transfer resistance, and diffusion limitations. In this study, the Randles ECM was selected to interpret EIS responses and characterize the state of the sample cells before evaluating the feasibility of FDR for SoH monitoring, as it can be adapted to offer varying levels of complexity and accuracy. Unlike electrochemical and thermal models, FDR is not a model but an experimental impedance-based technique that shares similarities with EIS but operates in higher frequency regions. Previous studies, such as [12] and [11], have applied ECMs to characterize high-frequency impedance data, demonstrating their effectiveness in impedance analysis. Since this study represents an initial investigation into the suitability of FDR for SoH estimation, ECM provides a simple yet robust means of characterizing the samples using EIS impedance data. The application of the Randles circuit in this study is further discussed in Chapter 3 and Appendix C.

2.3.3 Data-driven Models

Data-driven models combine advanced algorithms and vast datasets to predict battery health and performance. Unlike traditional electrochemical models that rely on physical and chemical principles, data-driven approaches use historical and real-time data to develop predictive models. These methods encompass various forms, including machine learning algorithms [18, 94, 95], statistical models [96, 97]. Additionally, hybrid approaches integrate multiple modelling techniques such as combining machine learning with equivalent circuit models or fusing electrochemical models with data-driven estimations to improve accuracy [68, 80]. Hybrid approaches can also couple experimental data with models to refine predictions. For example, impedance spectroscopy data can be used to parameterize an ECM, ensuring that the model accurately reflects real-world battery behaviour [17]. Similarly, experimental aging studies can provide datasets for machine learning models, improving their ability to generalize

across different operating conditions [2]. In some cases, real-time sensor measurements such as voltage, temperature, or impedance are integrated into predictive models to continuously update SoH estimations [77]. Table 2.3 summarizes the most commonly used data-driven approaches.

Table 2.3 Most used methods for Data-driven SoH Models

Method	Advantages	Disadvantages
Fuzzy logic-based models [17, 94, 98, 99]	• Suitable complex, nonlinear systems • Self-learning capability • Relatively accurate • Can be applied to different chemistries	• Difficult to implement in situ • Complexity increases with larger variables and datasets • Requires large and diverse dataset
Statistical based models (PCA, Regression, least squares) [96, 97, 100–102]	• High flexibility • Easier Interpretability • Relatively simple implementation • Less data required as compared to machine learning methods	• High computational effort • Accuracy is dependent on model and choice of data features • Sensitive to outliers • Difficulty in capturing nonlinear relationships
Neural Networks [17, 41, 103–105]	• Suitable for parameter estimation • Requires lesser training data compared to fuzzy logic	• Heavily dependent on large training data • Model accuracy can affect precision • Complex to implement
Support Vector Machines [14, 106–108]	• Accurate • Nonparametric • Robust	• Accuracy is dependent on data diversity • High computational effort • Not ideal for nonlinear systems
Random Forest [109, 110]	• High accuracy • Less reliant on feature selection • Robustness to outliers	• Not easily interpretable • Higher data requirements • High computational cost
Hybrid models [94, 95, 98]	• Combines strengths of different methods • Flexible	• Increased complexity • Can be time-consuming

In battery SoH monitoring, estimation, and prediction, large datasets can arise from either extensive testing of a large number of samples or from advanced equipment that produces information-rich data**.** Statistical methods like PCA are particularly helpful in these cases because they can effectively handle large datasets and extract meaningful patterns from complex, high-dimensional data with moderate computational complexity [96, 111]. PCA reduces the dimensionality of dataset by transforming it into a set of orthogonal components that captures the most significant variance within the dataset [97, 103]. This transformation

simplifies the complexity of high-dimensional data for analysis, modelling or for use by other machine learning algorithms. Another commonly used statistical method is the PLSR, which, like PCA, can reduce dimensionality but also emphasizes the relationship between input variables and output responses [112].

References [96, 103] applied PCA to identify and extract variables in data that impact battery's SoH indicators, thus reducing redundancy and improving the efficiency of the models. Reference [96] focused on variables that influence deviations in temperature, voltage and state of charge while [103] identified variables significantly affecting the duration charging modes. Also, [110] developed a faster impedance-based SoH assessment by using PCA to simplify complex data obtained from time domain EIS impedance data. These works presented the key advantage of using PCA directly on high correlated data without the need for a pre-processing/feature selection stage typically required by other algorithms [55, 98, 108].

Regression-based algorithms, as used in [113] also simplify models by identifying key aging parameters that can be used to predict battery behaviour. Reference [113] demonstrates this by relating cell resistance and diffusion time to SoH using linear least squares regression. Another study in [114] employs Recursive Least Squares (RLS) regression to track battery parameters for an improved real-time SoH prediction. In [97] a modified approach to MSPC that combines PCA, and cross-cell monitoring (CCM) was used to develop a fault diagnosis tool for battery packs. PCA transformed measured operational data (cycle times, current voltage, temperature) into smaller dimensions while CCM compared voltages of single cell using statistical evaluations such as Hoteling's T-test and squared prediction error (SPE) analysis, to detect localised faults, making it sensitive and robust even under dynamic load profiles and sensor noise. The principles of multivariate statistical control and their adaptation of these method are further discussed Chapter 5.

2.4 Electrochemical Impedance Spectroscopy for Battery Impedance Measurement

The internal impedance of a battery represents its opposition to the flow of electrical current, encompassing both resistive and reactive (capacitive and inductive) components. Increased impedance during charging and discharging can result in voltage drops, reducing performance. As a battery ages, the resistive elements of impedance typically increase due to the degradation of electrode materials, electrolyte, and internal connections [13]. EIS is a widely applied non-invasive impedance measurement method for characterisation of batteries. The method involves the application of a low amplitude sinusoidal excitation signal and measurement of the battery response to this excitation over a frequency range. The applied excitation signal is typically a

sinusoidal current for galvanostatic EIS (GEIS) or a sinusoidal voltage for potentiostatic EIS (PEIS), and the measured response is composed of the amplitude and phase shift of the corresponding output voltage or current, respectively [13, 115]. The frequency dependent impedance $Z(j\omega)$, is defined by the relationship between voltage and current expressed as (2.1) [14, 116].

$$Z(j\omega) = \frac{V(j\omega)}{I(j\omega)} = |Z(j\omega)|e^{j\varphi(\omega)} = \mathbb{R}\{Z(j\omega)\} + j.\Im\{Z(j\omega)\} \tag{2.1}$$

where $\mathbb{R}$ and $\Im$ are the real and imaginary part operators, respectively. Z is the complex impedance, $j = \sqrt{-1}$, ω is the angular frequency, φ is the phase angle, $V(j\omega)$ and $I(j\omega)$ are complex frequency dependent sinusoidal voltage and current signals respectively. At an instance of angular frequency (ω_0), (2.1) can be expressed as (2.2) [13, 116]. Where $\hat{V}$ and $\hat{I}$ are the instantaneous voltage and current respectively and with their respective phase angles φ_V and φ_I.

$$Z(j\omega_0) = \frac{\hat{V}e^{j\omega t+\varphi_v}}{\hat{I}e^{j\omega t+\varphi_I}} = |Z(j\omega_0)|e^{j\omega_0[\varphi_v-\varphi_i]} \tag{2.2}$$

The most common EIS measurement configurations are the 2-electrode and 4-electrode configurations shown in Figure 2.4 [13, 117]. Four electrodes are typically involved in EIS measurement setup namely the working electrode (WE), counter electrode (CE), working sense electrode (WS) and the reference electrode (REF) [117]. The WE injects the excitation signal into the battery electrode and the CE completes the electrical circuit within the battery allowing the AC perturbation current to flow [117]. WS together with the REF measures the voltage response of the battery to the AC perturbation [118]. The WS is typically positioned close to the working electrode to accurately capture the voltage changes occurring during the measurement [117]. In the 2-electrode configuration a single lead connects both the WE and WS to the battery, while another lead connects the REF and CE, shown in Figure 2.4a. This creates a shared current path for both the excitation current and the actual battery current, while the REF and WS measure the combined voltage drop across the battery and the connecting wires [117]. This 2-electrode setup is quick to implement but it incorporates the impedance of the connecting wires into the overall measurement which can potentially mask the low impedance of the battery [13, 117].

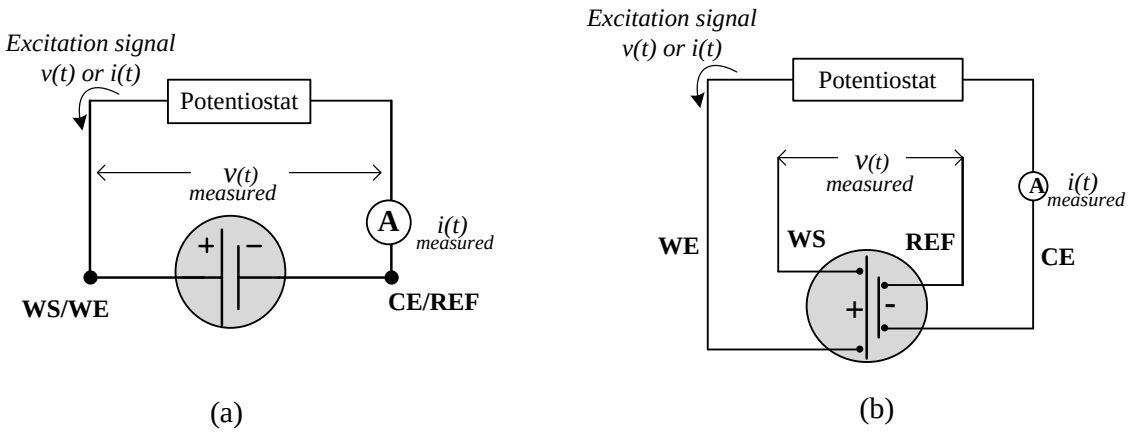

Figure 2.4 Schematic for EIS measurement setup. (a) 2-electrode measurement configuration. (b) 4-electrode measurement configuration [13, 117].

The 4-terminal configuration, (also known as the Kelvin connection) handles this limitation by physically separating the signal-carrying leads (WE and CE) from the sense leads (REF and WS) illustrated in Figure 2.4b and thus provide a more accurate and reliable impedance measurement. Based on its accurate and reliability in measuring small impedance changes, various forms of the Kelvin method is applied in several impedance measurement technique including conductivity tests and FDR S_{21} shunt-through method [28, 119].

The Nyquist plot, which plots the real part of the complex impedance (Z') against the imaginary part (Z'') provides a graphical representation of the impedance spectrum. It reveals distinct semicircular arcs and linear regions corresponding to various electrochemical processes as shown in Figure 2.5. A resistor is included to represent the ESR, this represents the combined resistance of the electrolyte, electrodes, and current collectors. An inductor or a parallel circuit of inductor and resistor is added when an inductive tail is present at the high frequency end of the spectrum [63]. This inductance is primarily due to cable inductance and the inductance of the current collectors. Parallel circuits of a resistor and a capacitor are also used to describe interface loss processes, such as the charge transfer process between the electrode and electrolyte. In this case, the resistor represents the limited exchange rate and the capacitor accounts for the capacitance of the double-layer and the SEI [40, 120]. These interfacial capacitances are not ideal, and their relaxation time constant is not a single value but distributed around a mean value [116, 121]. In the impedance locus, this effect causes a deviation in the semicircular arcs as shown by the broken lines in Figure 2.6 [32, 121]. As explain in Section 2.3, the CPE is a component used to describe the deviations resulting from frequency dispersion effects. The CPE accounts for this deviation by introducing an exponential parameter (n), where $n \in [0,1]$.

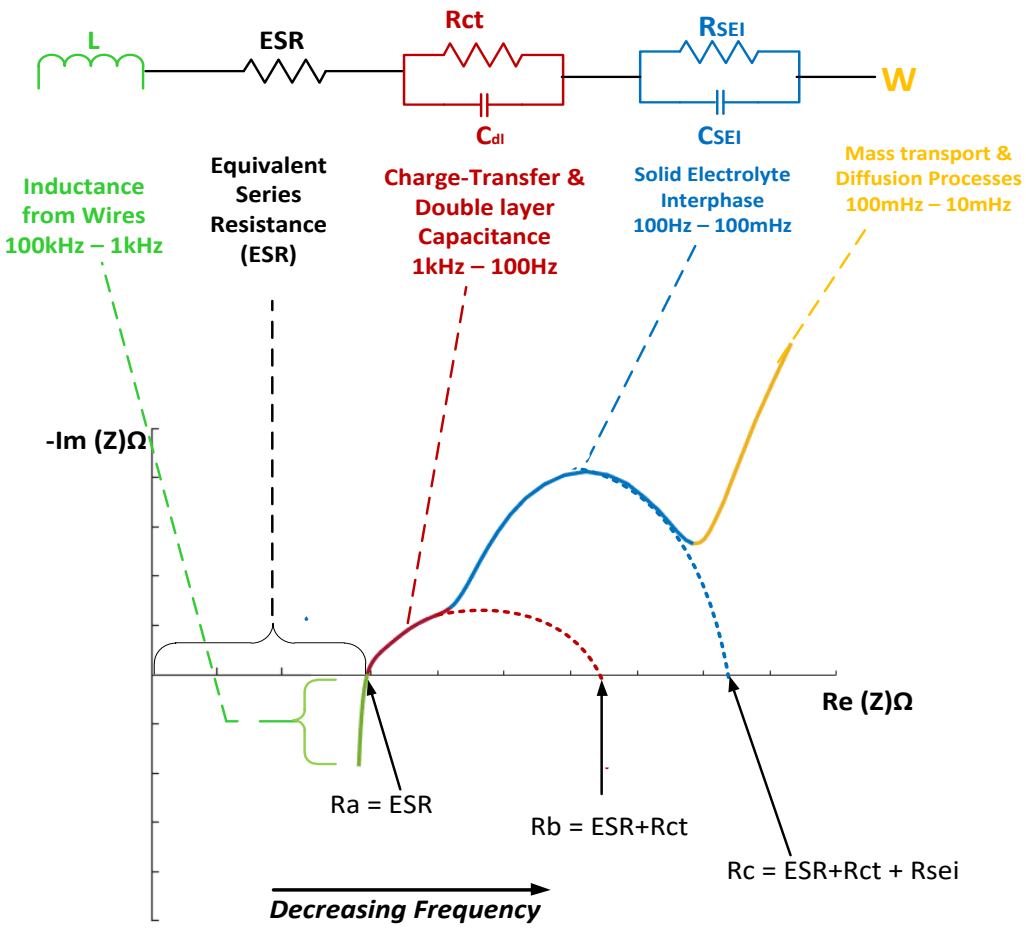

Figure 2.5 EIS impedance response of a typical Li-ion battery with an ECM showing various electrochemical processes and their associated frequency range of occurrence [13, 21, 40, 122].

The impedance of the CPE element (Z_{CPE}) is defined by (2.3) where Yo is the capacitance of the CPE and n is the exponent which controls the frequency dependence of the CPE impedance. When n = 1 the impedance is the same as that of an ideal capacitor, when n = 0, the CPE becomes frequency independent and behaves like a resistor [121, 123]. Between one and zero, n represents a non-ideal capacitor.

The Warburg element presents diffusion and mass transport processes. Further description of diffusion and mass transport processes are discussed in Appendix A. These are incorporated into ECMs such as the Randles circuits for interpretation of impedance response. EIS measurements are susceptible to systematic and random errors that can originate from various sources, affecting measurement accuracy and reproducibility. Systematic errors may arise from imperfections within the EIS instrument itself, such as component aging, thermal drift, or internal noise, which can accumulate over time and affect impedance readings [13].

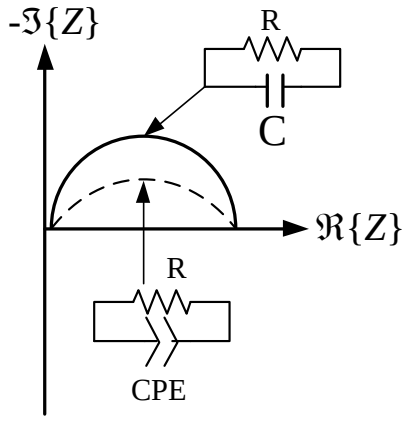

Figure 2.6 Parallel RC and RCPE models for impedance loci of different frequency dispersion [116, 124].

$$Z_{CPE} = \frac{1}{Y_0(j\omega)^n} \tag{2.3}$$

Additionally, variations in the experimental setup including inconsistent test fixtures, differences in cable lengths, and contact resistances can introduce deviations. These errors are particularly pronounced over repeated use, as small inconsistencies compound over multiple tests.

Beyond the instrument itself, variations in the experimental setup can introduce further errors. Factors such as inconsistent test fixtures, differences in cable lengths, and variations in contact resistance at the electrode terminals can all affect the measured impedance. These variations become more pronounced when testing multiple cells or performing repeated measurements over time. Even minor inconsistencies in how test leads are connected or how pressure is applied at contact points can alter the impedance response, particularly at higher frequencies. Such discrepancies can compromise the comparability of results across different experiments and battery samples, making it difficult to establish reliable SoH trends. Random errors, on the other hand, arise from external influences such as environmental noise, temperature fluctuations, and electromagnetic interference from surrounding equipment. These unpredictable factors can introduce variability between successive measurements, reducing the precision of impedance readings. The presence of random noise can obscure subtle impedance changes associated with early-stage degradation, potentially delaying the detection of battery aging. Moreover, at very low or very high frequencies, signal-to-noise ratio limitations can introduce further uncertainty, particularly in cases where the measured impedance approaches the instrument's sensitivity threshold. The combined impact of these errors can lead to inaccurate estimations of battery SoH, misclassification of degradation severity, and

inconsistencies in long-term monitoring. If not properly accounted for, EIS measurements may overestimate or fail to detect early-stage degradation, leading to unexpected failures or suboptimal battery management decisions. To mitigate these issues, careful attention must be given to instrument calibration, experimental setup standardization, and environmental control.

In the context of this work, where a variety of equipment are employed, for EIS and FDR tests, and a number of battery samples are tested, calibration ensures uniformity and consistency across all measurements. Commercially, equipment manufacturers provide standard calibration kits consisting of Faraday shield cage and custom-built setup, for periodic equipment calibration [125]. Also, the widely used Open Short Load Compensation (OSLC) is at times applied to bespoke fixtures to ensure test accuracy and repeatability [13]. In [13, 126] and [127], this method was applied to four-terminal impedance meters to reduce the measurement error associated with test fixture and connection leads. The OSLC method involves measuring an open, short and load impedance using the intended test setup, where the Device Under Test (DUT) is replaced by high impedance, zero impedance and known reference impedance standards respectively. The effective impedance of the DUT (Z_{DUT}) is then obtained from (2.4) [13, 126, 127].

$$Z_{DUT} = Z_{REF}\frac{(1 - Z_{mREF}Y_0)(Z_{DUT} - Z_s)}{(1 - Z_{DUT}Y_0)(Z_{DUT} - Z_s)} \tag{2.4}$$

Where $Y_0 = {}^{1}/_{Z_0}$ is the open admittance obtained from open impedance (Z_o) measurement, Zs is the short-circuit impedance, Z_{mREF} is the measured value of the known reference impedance. Modified versions OSLC compensation technique has also been applied to FDR measurement in [128]. This would be further discussed in section 2.5.

2.5 Frequency Domain Reflectometry (FDR) for Impedance Measurement

Reflectometry is a non-invasive diagnostic technique used to analyse the characteristics of various materials and systems by measuring the reflection and transmission of signals through them. The fundamental principle involves injecting a low-voltage, high-frequency signal into a system or material. Any change in the system's physical characteristics such as breaks, corrosion, or variations in material properties alters the impedance profile, leading to reflections of the incident signal which is analysed to characterise the anomaly. Frequency Domain Reflectometry (FDR) is a specific type of reflectometry that operates by sweeping the input signal across a range of frequencies and analysing the response. In FDR, the input consists of

stepped-frequency sine waves that travel through the material or cable under test. Any anomalies within the structure cause reflections, allowing for precise identification of impedance variations [6].

FDR has been widely used as a diagnostic tool, particularly for detecting faults in cables and transmission lines [6, 7, 129]. Its immunity to system noise makes it particularly effective for use in live or energized systems, as test frequencies can be selected to avoid interference with existing signals or background noise [5, 7]. Initially, FDR was primarily applied in power and communication networks, helping to pinpoint faults in underground cables [7, 129, 130], aircraft wiring [6], and industrial power lines [7] without requiring physical disassembly. It has been instrumental in identifying insulation degradation [131], loose connections [Aircraft], and impedance mismatches [130, 132], thereby preventing catastrophic failures and reducing maintenance costs.

Beyond cable diagnostics, FDR has also been applied in material science, where it has been used to assess the dielectric properties of materials. By analysing high-frequency responses, valuable insights have been gained into how different structures interact with electromagnetic signals [9, 10, 133]. In the aerospace industry, where long, intertwined wiring systems are often located in confined spaces, [6] proposed an FDR-based system for non-destructive wire integrity testing. This system can determine wire length and terminating impedance from single-ended measurements, providing an efficient means of diagnosing faults without physical access to the entire wiring network. Similarly, in semiconductor applications, FDR has been used to monitor bond wires and signal traces in printed circuit boards [132, 134]. Even minute impedance fluctuations in these components can indicate material fatigue, corrosion, or thermal stress, allowing for early fault detection and improved reliability.

More recently, FDR has been explored for its potential in battery impedance measurement. Studies have demonstrated its ability to measure the high-frequency impedance of cells between 300 kHz to 300 MHz, offering insights into their electrical characteristics at these frequencies [12]. These are further discussed in Section 2.6. Given FDR's success in detecting structural and material-related impedance shifts, and its initial application to battery impedance analysis, it is scientifically intriguing to investigate whether FDR could also serve as a tool for SoH monitoring based on impedance monitoring.

Batteries undergo significant internal changes over their lifetime, including electrode degradation, electrolyte breakdown, and SEI layer growth, all of which influence their impedance characteristics. Since FDR is sensitive to impedance variations, it presents a promising non-invasive method to monitor these internal changes and potentially correlate them

with battery SoH. If FDR can reliably track impedance evolution in batteries, it could offer a novel approach for real-time SoH estimation, extending the frequency range beyond traditional EIS methods.

2.5.1 Reflectometry Theory

Reflectometry utilizes the interaction of electromagnetic (EM) waves with boundaries within a medium to gain insights into its properties and structure. The fundamental principles of reflectometry involve wave propagation, reflection, and transmission within different media [135]. When an incident wave encounters a boundary between two materials with differing properties (such as refractive index or conductivity or impedance), a portion of the wave is reflected back into the original medium, while another portion is transmitted through the second medium [7, 136]. The amount of reflection and transmission depends on the characteristics of both materials and the properties of the wave itself. This behaviour of EM waves in both forward and backward propagation is governed by Maxwell's equations [135]. In conductors, the Telegrapher's equations and transmission line theory apply the concepts of Maxwell's equations to the propagation of voltage and current signals on transmission lines while considering the distributed resistance, inductance, capacitance, and conductance [136]. By this concept, electrical conductors (coaxial cables, copper rods and PCB copper traces) are modelled as a series of impedances representing resistances, capacitances and inductances encountered along the conductors as shown in [135, 136].

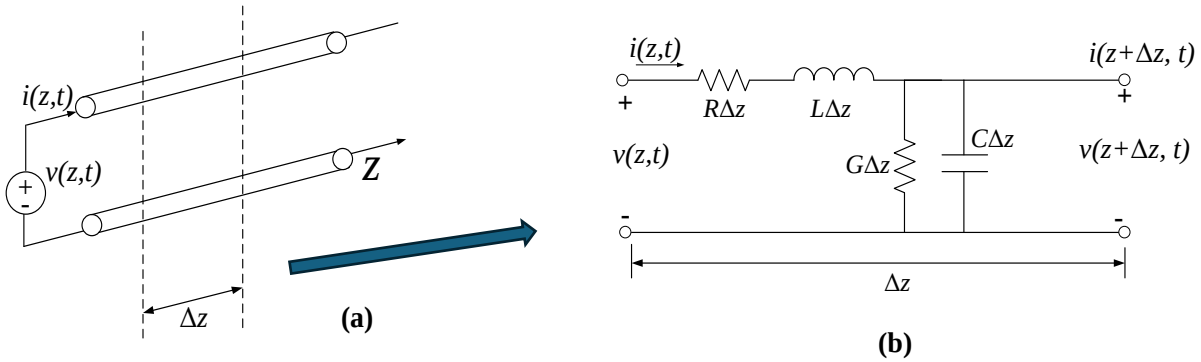

Figure 2.7 Voltage and current definitions for a segment of transmission line. (a) A segment of transmission line. (b) Equivalent lumped-element model [135, 136].

Figure 2.7a shows a generic representation of a two-wire transmission line with uniform cross section along its length where $v(z,t)$ represents the voltage, and $i(z,t)$ represents the current at position x and time t along the transmission line.

Figure 2.7b illustrates a lumped-element model of an infinitesimal length, Δz, of Figure 2.7a, where R (in $\frac{\Omega}{m}$) is series resistance per unit length representing finite conductivity of the conductors. L (in $\frac{\mathrm{H}}{m}$) represents the series inductance of the wires, and capacitance formed by the close proximity of the conductors is represented by the shunt capacitor C (in $\frac{\mathrm{F}}{m}$). Also included is the shunt conductance per unit length, G (in $\mathrm{S}\frac{1}{m}$), that arises due to the dielectric loss of the material between the conductors. Further details of the transmission line and wave equations that govern wave propagation along conductors are presented in Appendix A.

A critical parameter in transmission line theory is the characteristic impedance (Z_o) of the line, which is defined in (2.5) [2, 135].

$$Z_o = \frac{V_0^+}{I_0^+} = \frac{-V_0^-}{I_0^-} = \frac{R + j\omega L}{\gamma} = \sqrt{\frac{R + j\omega L}{G + j\omega C}} \tag{2.5}$$

Where, V_0^+ and I_0^+ are voltage and current phasors travelling in the forward $+z$ direction and V_0^- and I_0^- represents the voltage and current waves traveling backwards in the $-z$ direction [136]. γ is the frequency-dependent propagation constant expressed in (A.7) in Appendix A [135]. The characteristic impedance determines how signals are transmitted and reflected on the line. When a signal travels along a transmission line and encounters a load with an impedance different from the characteristic impedance, part of the signal is reflected back towards the source [4]. The reflection coefficient (Γ) quantifies the ratio of the reflected wave to the incident wave and is given by (2.6) [135, 137].

$$\Gamma = \frac{V_0^-}{V_0^+} = \frac{Z_L - Z_o}{Z_L + Z_o} \tag{2.6}$$

Where Z_L is the impedance of a load or a second medium connected to the transmission line. When $Z_L = Z_o$, $\Gamma = 0$, implying no reflection and transmission of maximum power. However, when $\Gamma = 1$, ($Z_L \gg Z_o$ or $Z_L \ll Z_o$), maximum reflection occurs, and no power is transmitted [135]. This loss is termed as the return loss (RL) and is given in dB as (2.7).

$$RL\ (dB) = -20log|\Gamma| \tag{2.7}$$

When partial reflection occurs, the transmitted part of an incident wave continues to propagate through the load, while the reflected wave travels back towards the source. The relationship between the reflected, and transmitted waves can be described using the reflection coefficient and the transmission coefficient (*T*) in (2.8) [135].

$$T = 1 + \Gamma = 1 + \frac{Z_L - Z_o}{Z_L + Z_o} = \frac{2Z_L}{Z_L + Z_o} \tag{2.8}$$

2.5.2 FDR Measurement Implementation

Vector Network Analysers (VNA) are used in FDR measurements. VNAs are multiport instruments capable of determining the magnitude and phase of both waves that are transmitted through and reflected from the system under study [138]. The incident wave is typically a low-voltage sinusoidal incident wave (0.20 mV_{rms} to 900 mV_{rms}, equipment dependent), which is stepped over a given bandwidth [139]. In Figure 2.8 is the schematic of a generic 2-port VNA that is setup to measure a 2-port network (equivalent to a four-terminal network) [139]. In the forward path, depicted by the orange line, a part of the incident wave is sent to the reference receiver at port 1 (Ref 1). The remaining incident wave is fed to the DUT through a bidirectional coupler (BC 1). The directional output of the bidirectional coupler only detects the signals reflected from port 1 of the DUT, shown in blue, which is then sent to the port 1 receiver.

The remainder of the signal that is not reflected passes through the DUT and is detected by the port 2 receiver as the transmitted signal, as shown as a green path [5, 139]. The measurements performed by ports 1 and 2 receivers are compared to measurements performed by reference receiver 1 (Ref 1) for phase shift calculation and also helps to eliminate source variations [139]. The input reflection at port 1 based on the wave incident on port 1 is represented by S_{11} and the transmission output of port 2 based on the port 1 incident wave is given as S_{21} [139, 140].

The entire process is repeated automatically but in reverse. In the reverse case, the Ref 2 receives the emitted incident signals and port 2 senses the reflected signals, whereas the port 1 receiver detects the transmitted signals. In this mode, the S_{22} parameter represents the input reflection at port 2 and S_{12} parameter represents the detected transmitted signals at port 1. These ratios are summarised in (2.9) to (2.12).

The VNA outputs *S*-parameters which are ratios that reflect a measure of how much of the incident signal is reflected and transmitted at each port and are expressed as (2.9) to (2.12) [138, 139]. In (2.9) to (2.12), the voltage signals are complex values, and the calculated *S*-parameters are complex values, typically given in dB. Equations (2.9) and (2.10) are the

reflection coefficients at ports 1 and 2, respectively, and these are equivalent to (2.6) such that $V_{o\,(port\,1)}^{-}$ is the reflected wave travelling backwards from port 1 and $V_{o\,(port\,1)}^{+}$ is the forward travelling incident wave on port 1 [141]. In (2.9) to (2.12), the port numbers are included to indicate the port of measurement. Z_L is the complex impedance of the load under study (DUT) and Zo is the system characteristic impedance established by VNA manufacturer. The typical value of Zo is 50 Ω [28, 139].

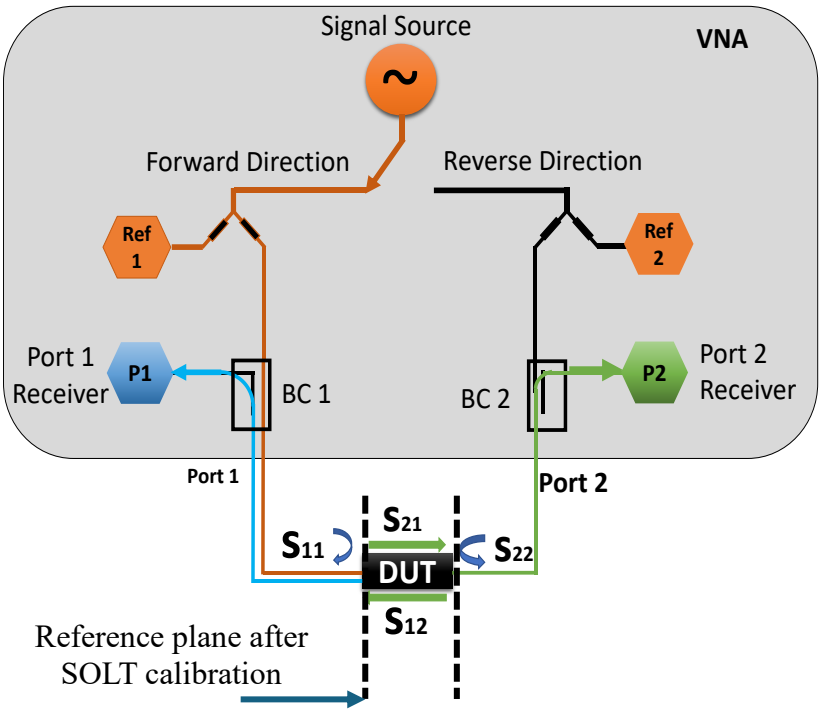

Figure 2.8 Schematic of 2-port VNA [138, 139]

$$S_{11}(\mathrm{dB}) = \frac{Voltage\ signal\ reflected\ from\ port\ 1 (V_{o\,(port\,1)}^{-})}{Voltage\ signal\ incident\ on\ port\ 1\ (V_{o\,(port\,1)}^{+})} \tag{2.9}$$

$$S_{22}(\mathrm{dB}) = \frac{Voltage\ signal\ reflected\ from\ port\ 2\ (V_{o\,(port\,2)}^{-})}{Voltage\ signal\ incident\ on\ port\ 2\ (V_{o\,(port\,2)}^{+})} \tag{2.10}$$

$$S_{21}(\mathrm{dB}) = \frac{Voltage\ signal\ transmitted\ out\ of\ port\ 2 (V_{o\,(port\,2)}^{-})}{Voltage\ signal\ incident\ on\ port\ 1 (V_{o\,(port\,1)}^{+})} \tag{2.11}$$

$$S_{12}(\mathrm{dB}) = \frac{Voltage\ signal\ transmitted\ out\ of\ port\ 1\ (V_{o\,(port\,1)}^{-})}{Voltage\ signal\ incident\ on\ port\ 2\ (V_{o\,(port\,2)}^{+})} \tag{2.12}$$

Several types of networks with varying number of ports have been used in FDR measurements [28]. Most common network configuration used in battery applications include the one-port network (reflection method), shunt-through network, and series-through network. These are illustrated in Table 2.4 [138, 142]. Applications of these setups and their advantages and limitations are discussed in section 2.6. Equations (2.13) – (2.17) show the variations of S_{11} and S_{21} equations for each network configuration. These equations have modifications that account for the position of the DUT with respect to the reflected and incident waves [25, 28, 29].

Table 2.4 Schematics and S-parameter equations for FDR networks used in battery applications.

One-port Network	
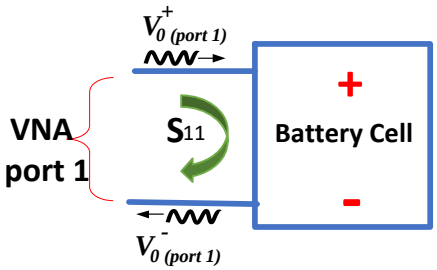	$S_{11} = \frac{Z_L - Z_o}{Z_L + Z_O}$ (2.13)
Shunt-through Network	
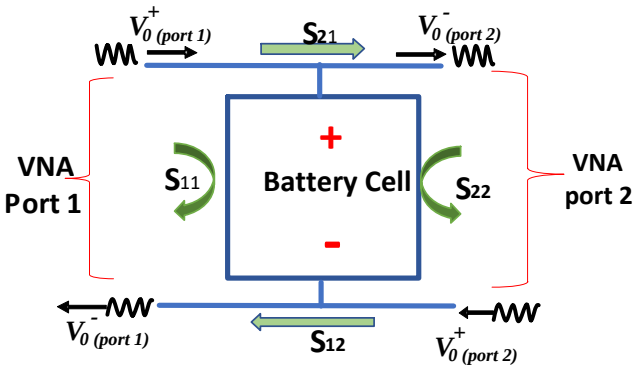	$S_{11} = \frac{-Z_o}{2Z_L + Z_O}$ (2.14) $S_{21} = \frac{2Z_L}{2Z_L + Z_O}$ (2.15)
Series-Through Network	
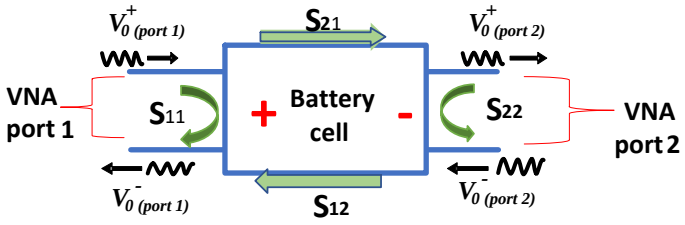	$S_{11} = \frac{Z_L}{Z_L + 2Z_O}$ (2.16) $S_{21} = \frac{2Z_p}{Z_L + 2Z_O}$ (2.17)

References [143] and [24] used the reflection method (the one-port network from Table 2.4) to assess the impedance of cells between 100 kHz – 200 MHz and 300 kHz – 30 MHz,

respectively. However, this method is a two-terminal setup and is known to be less sensitive to impedance values below 1 Ω [28]. This reduced sensitivity can limit the detection of subtle impedance variations associated with battery aging, potentially leading to lower accuracy in SoH monitoring using FDR. Since degradation mechanisms such as SEI layer growth and lithium plating can manifest as small impedance changes in the milliohm range, a method that struggles to resolve values below 1 Ω may fail to capture early-stage degradation, reducing diagnostic detail and increasing the risk of misinterpreting battery health. The more sensitive shunt-through method, outlined in [28] was used in [27, 28] to measure and characterise high frequency impedance of LiBs from 1 kHz to 300 MHz. Reference [144] used the series-through method, which is not recommended by VNA manufacturers due to low ohmic nature of batteries [27, 28]. Therefore, for this work the shunt-through was a more promising choice for monitoring of impedance changes associated with aging.

2.5.3 Setup Calibration Methods for Frequency Domain Reflectometry

Irrespective of the network configuration, pre-measurement VNA calibration is essential to correct the effects of errors within the VNA and the test cables. Calibration of the VNA helps to mitigate systematic errors by creating a reference measurement plane at ends of the test cables as shown in Figure 2.8 [139]. The one-port and two-port calibration methods are the common types of calibration used [139]. It is noteworthy that these are not the same as the one-port and two-port networks shown in Table 2.4 but rather these (one-port and two-port calibration methods) are calibration methods used on these networks (one-port and two-port networks) types. For easier clarification, the one-port calibration method is herein referred to as single-ended method and the two-port calibration method as double-ended method. The single-ended method is illustrated in Figure 2.9a. The method uses short, open and load (SOL) standards for VNA calibration [138, 139]. This is a basic calibration used on one-port networks whereas the double-ended method is a more comprehensive calibration that adds an additional through standard to the SOL calibration to produce a SOLT calibration, shown in Figure 2.9b [139]. In both calibration methods, open standard represents an ideal open circuit, where there is no connection between ports 1 and 2 of the VNA hence an infinite impedance between the ports [138]. The short standard defines direct connection between the ports of the VNA and represents zero impedance while the load standard is a precise 50 Ω standard for a VNA with 50 Ω characteristic impedance [139, 140]. The through standard represents a calibration scenario where a high-quality cable with a known impedance, typically 50 Ω, is connected between the VNA ports. Its purpose is to establish a reference for the transmission

characteristics of such cable, enabling accurate measurement of the device under test (DUT) that is either similar or different to a cable of 50 Ω [139]. With the calibration standards connected, the error correction is done via the software supplied by the manufacturer.

In Figure 2.9a, the VNA is setup for a single-ended calibration and in Figure 2.9b, the VNA is setup for double-ended calibration. In each calibration method, the calibration standards are connected to the ends of the coaxial cables in turns and the connection sequence is dictated by manufacturer software.

2.5.4 De-embedding Methods in Frequency Domain Reflectometry setups

After a SOLT or SOL VNA calibration, the measurement reference plane is at the end of the test leads as indicated by the red lines in Figure 2.10. However, there are cases where the DUT needs to be mounted on an intermediary connector such as extra cable lengths, PCBs or bespoke connector ports.

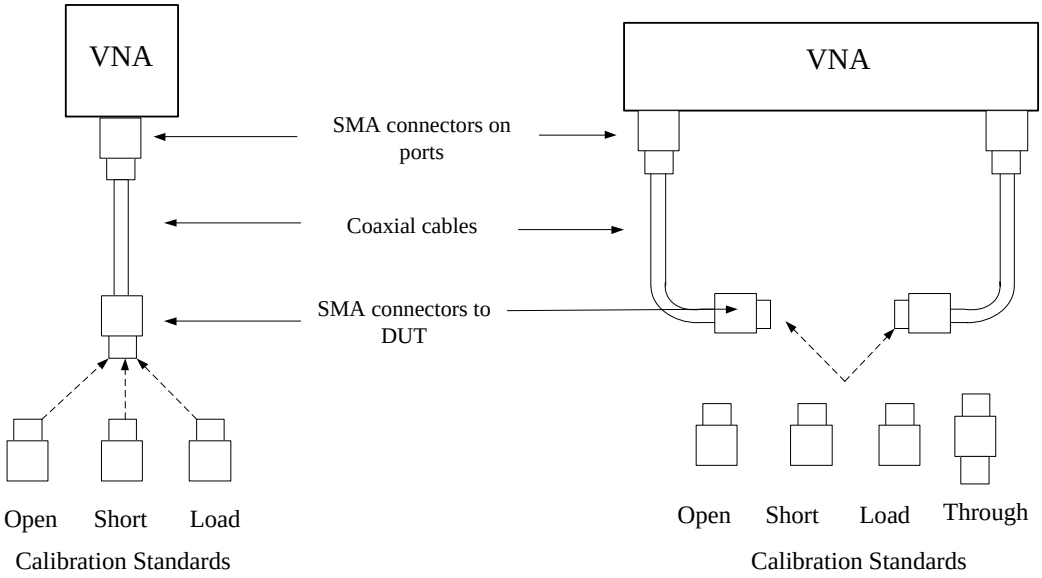

Figure 2.9 VNA calibration Methods. (a) Single-ended method. (b) Double-ended.

This is usually the case where the DUT such as a battery, is not typically fitted with an SMA connected therefore intermediary connectors are required to interface between the DUT and the VNA. In these circumstances, an additional de-embedding step after the SOLT or SOL calibration process is required to obtain the impedance of the DUT without the effects of the intermediary connector. Thus, moving the measurement reference plane to the point indicated by the green line in Figure 2.10 becomes essential.

Several de-embedding methods have been proposed in applications where batteries were connected to VNAs. Reference [24] connected the protruding terminals of a battery directly to a VNA using an additional length of coaxial cables. For each battery terminal, the one end of the cable was soldered onto the terminal while the other end of the cable was fitted with an SMA connector for direct connection to the VNA. This formed a one-port reflection network. By doing this the SOLT calibration was performed with the extra cables connected to the VNA, and hence the reference plane was positioned at the end of the extra cable leads, instead of the end of the VNA cables. This method removed the need for de-embedding since test cables were compensated for during calibration and no additional connection is used. Although simple, this method is only suitable for batteries with extended terminals such as pouched cells or cells with bolt terminals but would be challenging with cylindrical or coin cells. The method also required soldering of the battery terminals to the VNA cables, which pose further limitations for in-situ applications. Reference [27] improved this setup and developed a PCB fixture instead for mounting a cylindrical cell to a VNA in shunt-through network configuration.

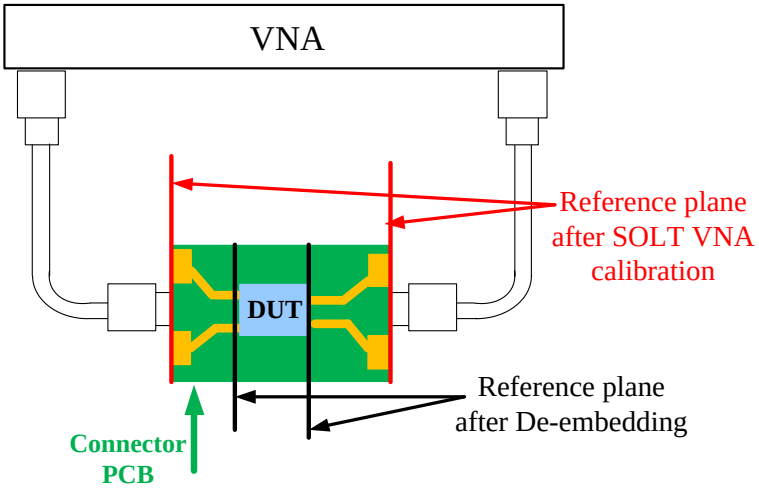

Figure 2.10 Shifting of measurement reference plane to the ends of the DUT using de-embedding.

The PCB fixture was designed to have traces that terminated with SMA connectors. This allowed for de-embedding to be done using the VNA's built-in port extension feature. The port extension feature is a feature available in some VNAs that compensates for phase delay errors introduced by cables or fixtures between the VNA ports and the DUT. It virtually moves the measurement reference plane to the DUT based on the known dimensions of the intermediary connectors. Despite the improved use of a PCB as compared to the use of cables, the major drawback of this method is the required soldering of the cells to the fixture. Particularly, this

makes the method not ideal for in-situ testing where batteries to be tested are still in use. Using this method will also be challenging when several batteries need to be connected and disconnected for intermittent testing. Reference [143] also designed a cylindrical test fixture for connecting an 18650 cylindrical cell to a VNA that did not involve soldering the cells to the connector fixture. However, their method was based on the less sensitive reflection method which is not ideal for SoH detection purposes. In their study, authors in [143] developed an ECM model for the connector fixture and the cell being tested. These models were then applied mathematically to de-embed the effects of connector fixture from the measurement. This proposed de-embedding method, though does not involve soldering, is computationally complex and only suitable for the less sensitivity one-port reflection method.

In [128], the authors of [27] further improved their setup and developed a generalised de-embedding technique for shunt-through configurations. This improved setup employed a battery holder mounted on a PCB to form the intermediary PCB, and hence eliminated the need for soldering as was the case in [27]. The proposed generalised de-embedding technique is based on OSLC compensation for EIS discussed in section 2.4. The generalised technique included the following workflow:

i. Calibrate VNA using double-ended SOLT method to establish the reference plane indicated by red line in Figure 2.10.
ii. Connect the intermediary PCB and measure the S-parameters for high impedance, low impedance and a matched load. When measuring the S-parameters for high and low impedances, the terminals of the battery holder in the intermediary PCB are open-circuited and short-circuited respectively. A 50 Ω resistor with 0.1% tolerance and short leads is connected across the battery holder terminals to measure the S-parameters of the matched load.
iii. The measured S-parameters are converted to impedance using (2.14) and (2.15) since the shunt-through method was being used.
iv. Equation (2.4) is then applied using the calculated impedances to determine the impedance of the DUT when measured at reference plane indicated by the green in Figure 2.10.
v. Further in this process, the inductive and capacitive coupling established between the cell's outer casing and PCB at high frequency were also compensated for. This was done by;
    a. First machining a copper cylinder to the same dimensions as the battery. This is then measured in the same manner as the battery would be measured.

b. Measured S-parameters are converted to impedance using (2.14) and (2.15). Equation (2.18) is then applied to obtain the impedance of DUT only.

$$Z_{DUT} = Z_{DUT,OSLC} - Z_{Cu} \tag{2.18}$$

Where Z_{DUT} is the impedance of the DUT with the effects of intermediary fixture and the inductive and capacitive couplings removed. $Z_{DUT,OSLC}$ is the DUT impedance after the OSLC compensation but before the removal of the coupling inductance and capacitance. Z_{Cu} is calculated impedance of a copper cylinder. This was done such that the size of copper cylinder would effectively generate similar coupling inductance and capacitance as the battery would with the PCB. This method is relatively easy to implement, accounts bespoke test fixtures and the cell type being used. Also, its successful application in EIS suggests promising application in impedance measurements. Further, this technique does not require soldering of cells and is most suitable of testing large number of samples. Therefore, this method was adopted in this research and its application in this work will be further discussed in Chapter 4.

2.6 Review of Reflectometry Techniques in Battery Applications

The application of reflectometry in battery impedance measurement has been relatively underexplored in the existing literature. In recent years, different forms of reflectometry have been applied in battery systems. Amongst these, FDR has been used to determine and characterise battery impedance for high frequency applications such as EMC evaluations [26, 29], spread spectrum time domain reflectometry (SSTDR) has also been applied in identifying aged cells within a battery pack [30] and neutron reflectometry (NR) has been employed in studying SEI formation [145, 146]. Also, optical time domain reflectometry (OTDR) has been employed alongside machine learning algorithms to monitor and detect changes in capacity and occurrence of potential faults in a pool of repurposed batteries [147]. These successful applications of reflectometry suggest advantageous potential in battery SoH monitoring. However, methods such as NR and OTDR require complex systems and specialised equipment such as titanium adhesion layer for neutron reflection and fibre optic cables for optical transmission [145–147]. They also tend to be computationally complex and are easily susceptible to external interference [143]. These hinder their adoption into online applications.

SSTDR, as used in [30], is traditionally favoured for live systems due to its ability to operate without interfering with existing signals. It achieves this by using a pseudo-random binary sequence (PRBS) as the incident signal, which allows for easy identification amidst

system noise [30]. However, when applied to battery impedance measurements, particularly in single-cell configurations, SSTDR encounters a challenge known as the "blind spot effect". The blind spot effect occurs when the incident and reflected signals overlap in time, making it difficult to distinguish between the original transmitted signal and the reflections caused by impedance discontinuities within the system [30, 148]. This issue arises because SSTDR operates in the time domain, meaning reflections from internal battery components with different impedances can interfere with the detection of meaningful impedance variations. In large-scale systems like power grids or long cables, the propagation delay between the incident and reflected signals is sufficient to separate them. However, in batteries, where internal distances are relatively short this overlap is more pronounced, reducing the ability to resolve impedance changes accurately. To mitigate this, additional cabling is often required to artificially extend the propagation distance, effectively separating the incident and reflected signals. While this workaround improves signal analysis, it introduces additional complexity and potential measurement inaccuracies. Furthermore, in applications where batteries are not arranged in series strings (e.g., single-cell configurations), the limited propagation distance further restricts the effectiveness of SSTDR. Without sufficient separation between reflections from different internal structures, the interpretation of impedance data becomes significantly more complex. This limitation makes SSTDR less ideal for standalone battery impedance measurements, though it remains viable for larger battery packs or series-connected cells where greater signal travel distances help mitigate the blind spot effect. Table 2.5 summarizes the most common forms of reflectometry techniques used in battery applications. For this work, focus would be placed on the use of FDR and how these have influenced the aim of this study.

In [12, 25], to assess the use of batteries as part of power line communication network in BMS, FDR was used to characterize battery impedance at high frequencies between 300kHz – 300 MHz collectively. Similarly, [149] also used FDR to determine high frequency impedance of batteries while assessing their electromagnetic interference and compatibility (EMI/C). These studies developed high frequency ECMs, that were used to characterise the impedance spectrum. Their responses revealed the occurrence of high frequency processes such as ionic shunt effect and skin effect in addition to known processes from EIS. This makes the FDR technique attractive as it does not just detect changes in impedance but can provide information used to characterise battery high frequency impedance. In [11, 12, 150], FDR-based impedance analysis was used to investigate the effects of cell design, state of charge (SoC), and operating temperature on high-frequency impedance.

Table 2.5 Reflectometry methods in battery applications

Technique	Benefits	Limitations	Application in Battery Systems
Time Domain Reflectometry (TDR) Uses a short rise time voltage step or pulse as the incident signal	• Simple and easy to implement. • Accurate fault location.	• Limited in use on energised systems. • Cannot measure complex-value impedance. • Extended test lead may be required to avoid overlapping of incident and reflected signals.	• Identification of aged cell in a series connected battery pack.
Sequence Time Domain Reflectometry (STDR) Uses a pseudo noise (PN) code as the test signal	• Can be used on energized systems. can be utilised below system noise floor due to low amplitude incident signal • can measure real and complex impedance. • Resistant to interference, • high resolution. • Can detect intermittent faults/changes in impedance.	• Complex processing • Specialised equipment. • Extended test lead may be required to avoid overlapping of incident and reflected signals. • Limited sensitivity for short distances between faults. • Can measure reflection coefficient only.	• Identification of aged cell in a series connected battery pack.
Spread Spectrum Time Domain Reflectometry (SSTDR) uses a PN code modulated by a sine or square wave.			
Frequency Domain Reflectometry (FDR) Measures reflected signals at different frequencies	• Provides more details on faults • Good for complex impedance/load measurement. • Resistant to interference • Improved resolution. • Can measure both reflection and transmission coefficients.	• Data processing can be complex. • Accuracy depends on setup calibration • Relatively costly equipment as compared to TDR	• Impedance measurement • Determination of effects of SoC, cell design and temperature on battery high frequency impedance

Reference [12] demonstrated that above 1 MHz, impedance responses vary significantly with temperature due to increased ionic current flow within the electrolyte. In contrast, variations in

SoC show only minor impedance changes below 1 MHz. At high frequencies, ionic currents primarily flow radially across the electrode layers, bypassing most of the electrode bulk, a phenomenon influenced by both frequency-dependent shunting effects and the skin effect [12, 151].

Cell design, particularly the location of current-collecting tabs, plays a critical role in shaping the high-frequency impedance response. As highlighted in [12, 150] and further explored in [151], the positioning of the tabs affects the distribution of current pathways within the cell, which in turn influences the inductive and resistive components of impedance. Cells with centrally located tabs exhibit more symmetric current distribution, leading to lower overall impedance, while asymmetric tab placement can introduce uneven current flow, increasing localized inductance. At higher frequencies, this inductance contributes significantly to the total impedance, as the induced magnetic fields create additional opposition to current flow.

Furthermore, the study in [151] shows that in large-format pouch and prismatic cells, where tabs are positioned at the edges, the current must travel a longer lateral path before reaching the electrode bulk. This results in a higher effective impedance compared to cells with centrally positioned tabs, where current paths are shorter and more uniform. The interaction between the tabs and the high-frequency current distribution also leads to variations in inductance, making tab placement a key factor in high-frequency impedance measurements. These effects become particularly pronounced above 100 kHz, where the skin effect and non-uniform current pathways further modify the impedance characteristics of the cell. In this work, where coin cells with tabs placed at the ends are used, the current is expected to traverse the entire electrode surface before reaching the tab connections. This configuration results in longer current pathways compared to centrally tabbed designs, leading to increased resistive and inductive impedance components at high frequencies. Furthermore, as frequency increases above 100 kHz, the skin effect and radial current flow across the electrode layers further modify the impedance response, similar to the effects observed in larger cells. However, due to the smaller size of coin cells, these impedance variations may be even more pronounced, as the limited electrode area restricts current redistribution.

These studies have applied FDR to measure and characterise battery impedance at high frequency and have advanced knowledge by developing and improving measurement setups, modelling, and exploring battery high frequency impedance dependencies on temperature, SoC, and cell design.

However, these studies do not explicitly investigate the application of high-frequency impedance measurements for battery SoH estimation, nor do they evaluate the impact of SoH

on the measured high-frequency impedance. In addition, these works have been carried out on either a single cell or less than a handful of cells, which raises the question of the universality of the method. Battery aging can cause various physical changes in the battery, which can influence the measured impedance, particularly at high frequencies [30]. Therefore, as cell design, SoC, and temperature have been explored, there is the need to investigate to what extent aging influences the high frequency impedance of cells. Building on the existing knowledge of how FDR has been used to characterise high frequency impedance, and its adaptation for use in an online BMS integration in [40], suggests its prospect as a non-invasive, wide-band technique for SoH monitoring.

2.7 Summary

Battery SoH serves as an indicator of its overall health, representing the degree of degradation it has experienced relative to its original condition. SoH is evaluated through a combination of metrics such as capacity and internal resistance, both of which deteriorate as the battery undergoes various degradation mechanisms.

This chapter first presented an overview of the factors and measurable effects of these degradation mechanisms, and the methods used in monitoring and estimating their effects on batteries. Several SoH monitoring and estimation methods exist that either monitor battery aging, characterise the extent of aging or predict the aging patterns in batteries. These are either experimental based, model-based or data-driven techniques. Experimental techniques offer simple direct measurement of battery parameters. Particularly, EIS has been used for characterizing battery SoH due to its ability to detect and characterise complex electrochemical processes into distinct impedance contributions, particularly at low frequencies. In addition, EIS can detect subtle changes in internal resistance, making it sensitive to early signs of degradation before significant decrease in capacity occurs. Model-based methods, often add interpretation to experimental data. Based on identified relationships in measured variables, models are developed to characterise battery behaviours under various operating conditions. Notably, ECM have typically been used to interpretate EIS response of batteries. By representing electrochemical processes with electrical circuit elements, the use of ECMs in conjunction with EIS offers a simple and intuitive method for characterising battery impedance.

Data-driven methods, particularly PCA, and PLSR, use statistical techniques to reduce datasets with large number of variables to smaller sizes that can be easily analysed. These methods also identify correlations between measured battery parameters and battery health indicators to predict battery SoH.

Also discussed in this chapter is the FDR technique. FDR is an impedance-based diagnostic tool that uses high frequency to characterise systems. It has been applied to characterize battery behaviour in frequency regions typically outside the EIS range and has been employed in dielectric measurements of novel materials. In battery applications, FDR has been used to measure and characterise the impedance of batteries at high frequencies. It has been used to identify high frequencies mechanisms such as ionic shunt effect and skin effect that influence battery high frequency impedance. However, current studies have not extensively explored the influence of battery SoH on high-frequency impedance measurements or the potential application of FDR for SoH monitoring or diagnosis. Exploiting FDR's capabilities in determining changes in impedance offers a promising prospect for online wide-band impedance measurement.

Therefore, this study aims to evaluate the potential of applying FDR to battery SoH monitoring using capacity and internal resistance as health metrics. This study also employs the well-established EIS method as benchmark method. Statistically, PCA, PLSR and MSPC, are also used to evaluate FDR’s applicability in monitoring, detection and predictive models.

Chapter 3 Cyclic Aging and Characterisation of Sample Lithium-ion Batteries

3.1 Introduction

This chapter provides information on the sample cells tested in this study and presents details on their cell chemistry, internal structure, aging process, and EIS tests. As this work involves the evaluation of the dependency of high-frequency impedance measurements on the cell SoH, it is essential to generate samples at different SoH. However, as outlined in [31], aging and degradation mechanisms in cells can arise from diverse causes and occur on different timescales, both at the micro and macroscopic levels. These factors pose a challenge when collecting data as they require cycling several cells under diverse conditions that mimic real-world situations. In this regard, nineteen sample cells in this study were cycled to different ages between 102 and 442 cycles through controlled cycling with varying charge and discharge currents. It must be noted that the samples cells were exposed to generic cyclic aging to mimic general use, but not to induce a specific degradation mechanism. During this process, the internal impedance changes were monitored using intermittent EIS testing. In addition to internal impedance, the cell capacity was also monitored, and both were used as metrics to characterise the SoH of the sample cells. This approach produced samples with varying capacities, internal impedances, and electrochemical states, providing a range of samples for testing. This chapter further outlines the workflow used for cyclic aging and EIS testing processes. Considering that EIS tests are conducted at a different frequency range from the FDR tests, the results of the EIS were mainly used to validate that the cells were indeed aged and to what extent the aging had occurred.

3.2 Cell Chemistry and Structure

The nineteen cells used were commercial LIR2032 coin cells with rated voltage 4.2 V and capacity 40mAh (±5 mAh). The cells were composed of a Lithium Cobalt Oxide ($LiCoO_2$) cathode and a graphite (C) anode, both of which were coated onto their respective current collectors [152]. $LiCoO_2$ is a widely used cathode material because of its stability and high energy density, whereas graphite is used as the anode to provide a reversible host for lithium ions during charge and discharge cycles [153]. The cell separator is made of polyethylene (PE) which physically separates the cathode and anode, thereby preventing short circuits. It is soaked in an electrolyte composed of a blend of ethylene carbonate ($C_3H_4O_3$) and lithium hexafluorophosphate ($LiPF_6$) which serves as a conductive medium for ion transport [152].

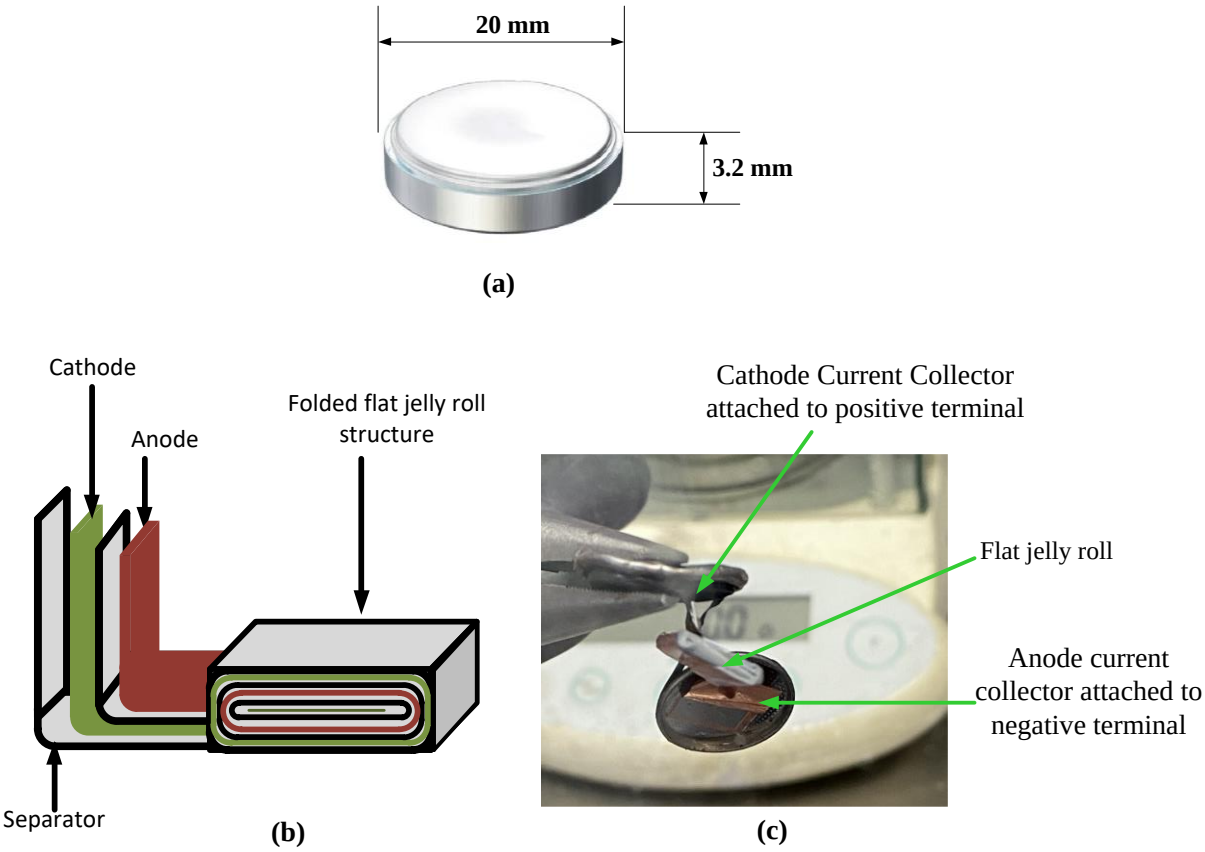

Figure 3.1 Cell structure. (a) Dimensions of cell. (b) Arrangement of cell electrodes and separator into flat jelly roll [29]. (c) Image of internal arrangement of cell taken.

With the separator placed between the coated cathode and the anode current collector foils, all three were rolled into a flat jelly roll, as shown in Figure 3.1. In Figure 3.1, (a) shows the dimensions of the cell, (b) adopted from [153], illustrates the flat jelly roll arrangement of the electrodes and separator in the cell, and (c) shows an image of the internal structure of the LIR2032 cell. Figure 3.1(c) was obtained by opening the cell in a Braun UNILAB glovebox. The image shows that the coin cells have wound electrodes similar to those in the cylindrical cells presented in [12]. At high frequencies, the impedance of wound electrodes becomes more pronounced due to the combined effects of inductive behaviour and the redistribution of ionic currents, known as the ionic shunt effect [12]. In wound electrode configurations, the tightly coiled structure introduces additional inductive impedance, as the spiral geometry forms closed-loop current paths that inherently resist changes in current flow [116]. As frequency increases, the inductive contribution becomes more significant, leading to a measurable rise in impedance. Additionally, the ionic shunt effect occurs because ionic currents tend to follow paths of least resistance, diverting away from the bulk electrode material and instead traveling through the

surface of the electrode. This non-uniform current distribution alters the impedance response, making it more pronounced at high frequencies. Consequently, the interaction between the inductive nature of the wound structure and the shifting ionic pathways leads to an overall increase in impedance, a phenomenon that can influence the high-frequency impedance characteristics in these cell formats.

Also found within the cells are electrode terminals, known as tabs, that serve as connection points for external circuits. In the coin cells tested, these were located at the ends of the electrodes when the rolled jelly expanded. This arrangement is similar to cells in [12], in which such positioning of the tabs increase the inductance of the cell measured at high frequency as compared to mid positioned tabs. The electrical properties of the cells are summarised in Table 3.1 [154].

Table 3.1 Electrical properties of cells

Cell Property	Value
Capacity	40±5mAh
Charging Voltage	4.2V
Standard Charging method	CC: 8mA, CV:4.2 V
Discharge Cut-off Voltage	2.75V
Cycle Life	>500 cycles at 0.2C mA discharge
Standard Charge/Discharge Temperature	Charge: 0ºC -45ºC, Discharge: -20ºC -60ºC
Charge State Internal Impedance	≤600mΩ with AC 1kHz

It is acknowledged that coin cells can introduce their own impedance contributions, potentially affecting measured values. Additionally, coin cells tend to exhibit greater measurement errors compared to cell larger formats such as 18650 or prismatic cells. Another challenge is the risk of manufacturing inconsistencies that can manifest as variations in charge transfer impedance, a known issue in coin cells, albeit to a lesser extent in larger cells [155].

Despite these limitations, the use of coin cells in this study serves as a proof of concept for applying FDR to battery SoH monitoring. Developing new diagnostic tools such as the FDR method assessed here, requires an initial validation phase, and coin cells provide a practical and controlled platform for this purpose. Their smaller size allows for precise control over temperature and other environmental factors, facilitating a more systematic investigation of impedance changes over time. This also enables us to assess whether FDR is sensitive to cell-to-cell variations, similar to EIS. Furthermore, previous studies employing similar aging methods (e.g., cyclic aging, different C-rates) have successfully utilized coin cells to investigate battery health degradation mechanisms [18, 156], demonstrating their viability for fundamental

research. To mitigate the impact of cell-to-cell variation, consistent cell selection and standardized measurement procedures were implemented to ensure repeatability and uniformity. It is noted that while coin cells serve as an effective proof of concept, future research should extend this investigation to larger cell formats, such as 18650 or prismatic cells as discussed in Section 6.1.

3.3 Cell Cycling: Experimental Setup and Data Analysis

Cycling was performed using the standard constant current–constant voltage (CC-CV) method with the test parameters outlined in Figure 3.2. The protocol was implemented to simulate the aging that naturally occurs during typical use. This approach was not designed to target a specific degradation mechanism but rather to replicate general cyclic aging reflects real-world operating conditions, providing insights into how the cells degrade over time. The charge and discharge current values were based on cell parameters outlined in Table 3.1. The CC-CV method is a well-known battery cycling protocol and it has been used in this study because it is easy to implement and has the added benefit of stabilising the cell voltage prior to EIS and FDR tests [157].

The C-rate employed in the CC-CV process was changed depending on the cycling stage of the cells, as outlined in Figure 3.2. To assess the initial state of the cells, EIS and FDR tests were conducted in their out-of-box condition. Not all cells were initially at 4.2V; therefore, some were slowly charged to 4.2V at a 0.05C rate before testing. This was followed by two conditioning cycles at a low C-rate of 0.05C (2mA) for all samples. These cycles were implemented to facilitate the proper formation of the solid electrolyte interphase (SEI) layer, which acts as a protective barrier between the electrode and electrolyte, preventing unwanted side reactions that consume lithium ions in the early stages of battery life [31, 116]. The cells used were commercially available; however, the manufacturer did not confirm whether they had been pre-conditioned. Therefore, the low C-rate cycles were included as a precautionary measure to ensure consistency across all samples. Since the out-of-box voltages varied, a shared baseline was established after the two slow cycles. The choice of C-rate value within this stage was based on the manufacturer's recommendation, as it allowed for controlled and gradual charging and discharging of batteries [154].

After the initial slow cycles, the cells were divided into two batches. The first batch, herein referred to as Batch A, consisted of four cells, namely cells 16 to 19. These underwent the next sixty cycles at a 1C-rate (40mA), followed by the continuation of cycling at a 2C-rate (80mA).

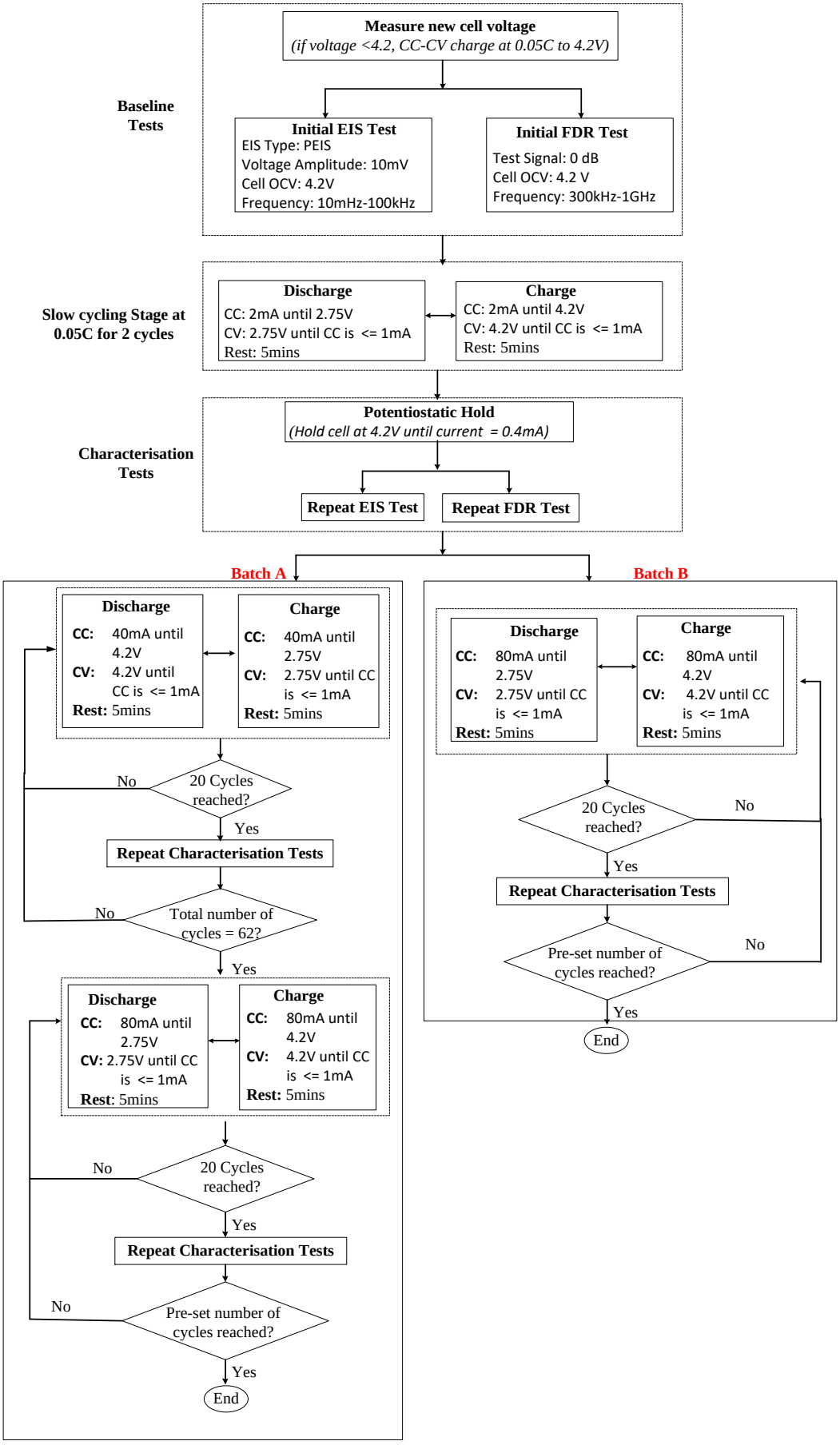

Figure 3.2 Cyclic aging and intermittent testing process for cell samples.

Concurrently, the remaining 15 cells within the alternate cohort, designated as Batch B, were cycled at a 2C-rate after the initial two slow cycles. This was performed to generate data from the cells exposed to both slow and fast charging current regimes such that they can be used to evaluate FDR's sensitivity to varying C-rates.

Batch A was limited to four cells because this represented approximately a quarter of the test sample population. Also, cycling tests on these cells were anticipated to be time-consuming due to slower cycling rates, therefore utilizing a smaller sample size (4 cells) allowed for a more efficient use of available equipment and ensured completion of the tests within the designated timeframe. This allowed for parallel testing of other samples in Batch B. Charging rates of 1C and 2C were chosen because, 1C represented ideal battery conditions, whereas 2C represented sustained high current charge/discharge while staying within the safety limits of the test equipment.

Both batches underwent intermittent EIS and FDR tests every 20 cycles during the aging process to monitor changes in cell characteristics. To ensure consistency, the tests were conducted at a fixed SoC of 4.2 V. Prior to each EIS and FDR measurement, a potentiostatic hold was applied to allow the cell voltage to stabilize, minimizing transient effects. During the potentiostatic hold, cells were held at 4.2 V, until the charging current reduced to 0.4mA [154].

Cycling was performed using a Maccor 4200 cycler, with the cells placed in a Binder FD 115 environment chamber for temperature control, at room temperature of 25 ºC. Figure 3.3 shows the capacity fading of cells over cycling. In Figure 3.3a, cells 16, 17, and 19 from Batch A initially retained a higher capacity for the first 60 cycles which were performed at 1C, as shown in the insert. This is a consequence of slow cycling that allows cells to operate at close to optimal conditions that reduce stress on electrodes and, in turn, reduce the rate of degradation mechanisms, such as electrolyte decomposition and excessive growth of the SEI layer [158]. As the C-rate is increased, so does the occurrence of electrochemical processes occur which facilitate further reduction in capacity after the first 60 cycles. This effect was also seen in the majority of cells from Batch B when the C-rate was increased after the initial slow cycles. A malfunction of cycler occurred during cycles 14 to 22 for cell 18 and cycles 270 to 300 for cell 19, resulting in unintentional short-circuiting of these cells during these respective intervals. Shown in Figure 3.3b, cells 18 and 19 were inadvertently exposed to short-circuit conditions due to the malfunction in the cycler channels to which they were connected. This produced a 23% and 28% decrease in the capacity of cells 18 and 19, respectively. Again, additional electrochemical processes appeared to have been triggered which caused further loss of capacity

in cells 18 and 19 beyond cycles 22 and 300, respectively. This is further discussed in Section 3.4.

Overall, based on the remaining capacity at the last cycle, two cells were above 60 %, eight cells were between 60 % and 30 %, and nine were below 30 %. Table 3.2 in section 3.4 summarises the individual cell states as characterised by EIS test results and remaining capacity.

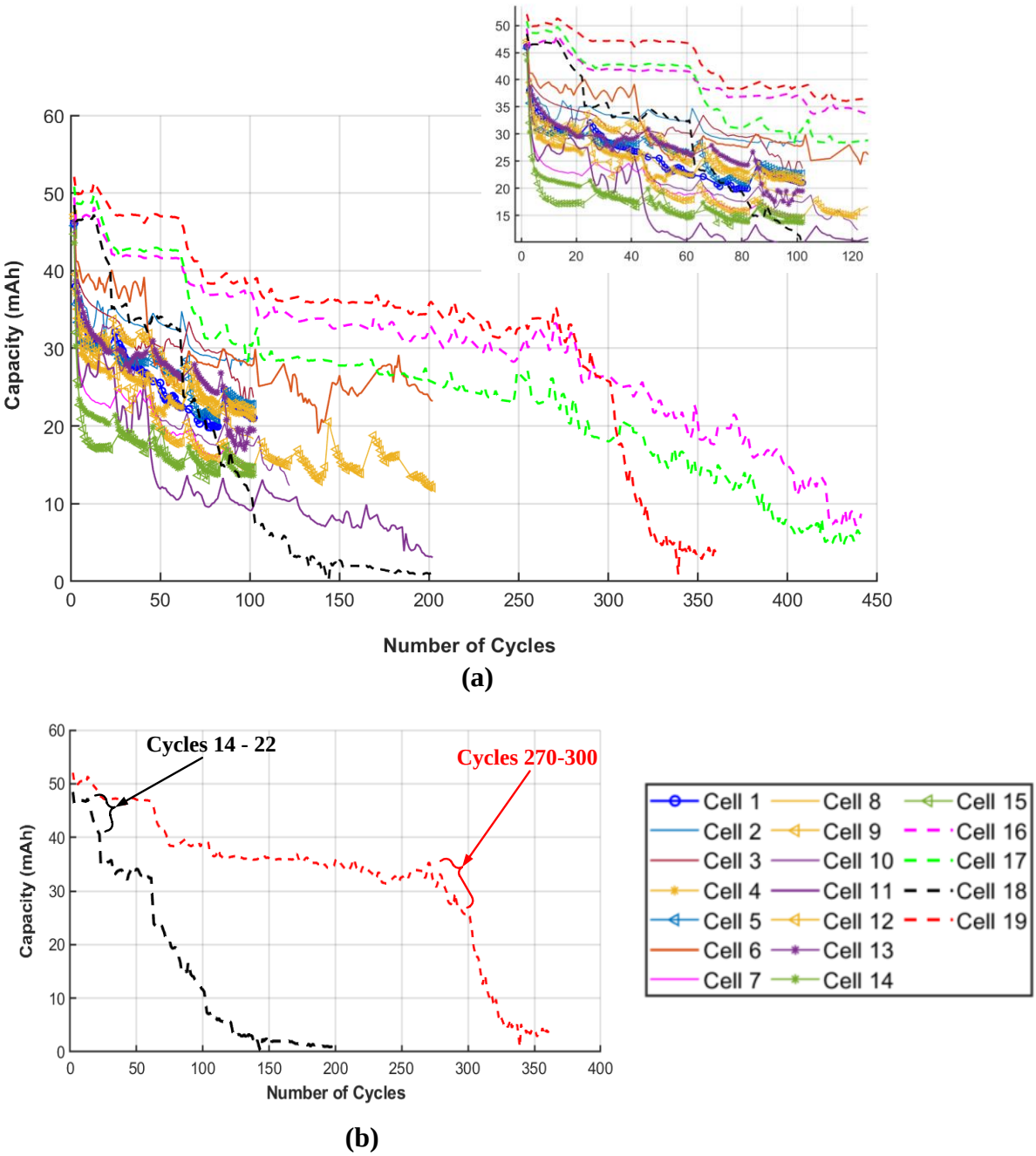

Figure 3.3 Cell capacity over cycling. (a) Cell capacity over entire cycling range with insert showing zoomed capacities from cycles 0-100. (b) Capacity of cells 18 and 19 showing regions of high discharge current.

3.4 Electrochemical Impedance Spectroscopy (EIS)

The potentiostatic EIS (PEIS) is used in this study as it ensures control over the cell voltage during measurement. Additionally, identifying the correct perturbation amplitude to ensure linearity in cell response can be challenging with GEIS whereas in PEIS tests, a standard of 5-10mV is well established [159, 160]. Initially, EIS tests were performed on the cells in their out-of-box state and then after the first two cycles. Subsequent tests were conducted after every 20^{th} charge-discharge cycle. As indicated in Figure 3.2, the test frequency range was 10 mHz to 100 kHz with a signal amplitude of 10mV that was chosen to ensure response linearity. The cells were tested at 25 ºC and 4.2 V using an Autolab 302N Potentiostat and the Gamry Interface 5000E potentiostat. It is noted that while SoH variations can be observed across different SoC levels, the sample cells were tested at 4.2 V (100% SoC) as this provided a stable reference point where impedance-based changes were more clearly detected. Although EIS is capable of capturing trends across various SoCs, initial FDR tests at lower SoCs yielded less conclusive results, likely due to increased signal variability and SoC-dependent influences [12]. In contrast, at 100% SoC, the FDR response exhibited more distinct and interpretable trends, making this SoC a more suitable condition for assessing battery health using both EIS and FDR. Figure 3.4 shows the EIS test setups. In Figure 3.4a is the initial setup using the two terminal setup with extended test lead and Figure 3.4b shows the setup with an improved cell holder from Autolab for a four-terminal configuration. Figure 3.5 shows the EIS impedance response of tests performed on the cells after the first two cycles and their respective last cycles. For easier description, the cell state after their first two cycles would be referred to as “new state” and the cell state at their last cycle would be referred to as “aged state”. The responses of the sample cells were compared with the typical EIS impedance response shown in Figure 2.5.

The Nyquist plots of the cells in their new state are shown in Figure 3.5a. The vertical line below the x-axis represents the inductive reactance. This mainly arises from the inductive contributions of the connecting wires, wound battery electrodes, and porous battery structure [12]. In cells 16-19, the inductance was relatively larger than that of the other cells. This is due to the long test leads initially used to connect the cells to the potentiostat shown in Figure 3.4a. In subsequent tests, an improved battery holder shown in Figure 3.4b was employed which led to reduced inductive reactance, as was also observed in Figure 3.5b. After the inductance tail, most of the cells were observed to have either one large semicircle or two merged semicircles. These represent the presence of reaction processes related to charge transfer, double-layer capacitance, and SEI formation as discussed in Chapter 2.

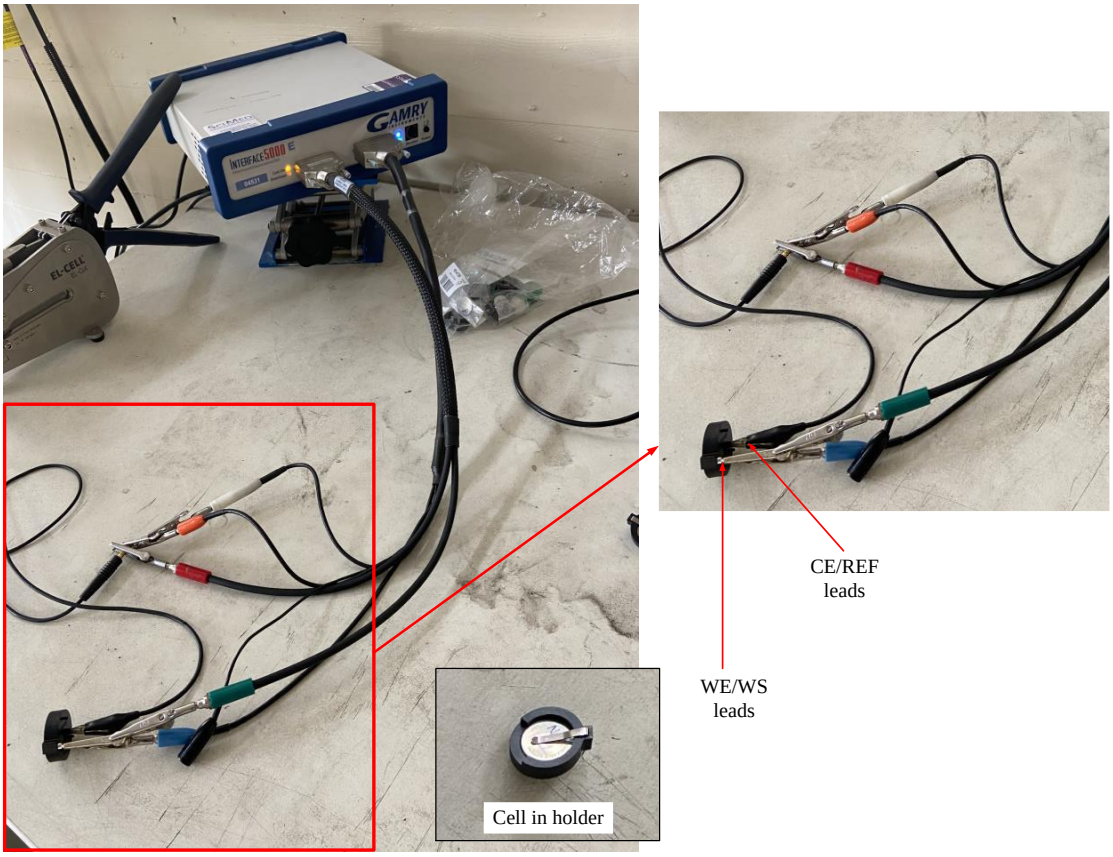

(a)

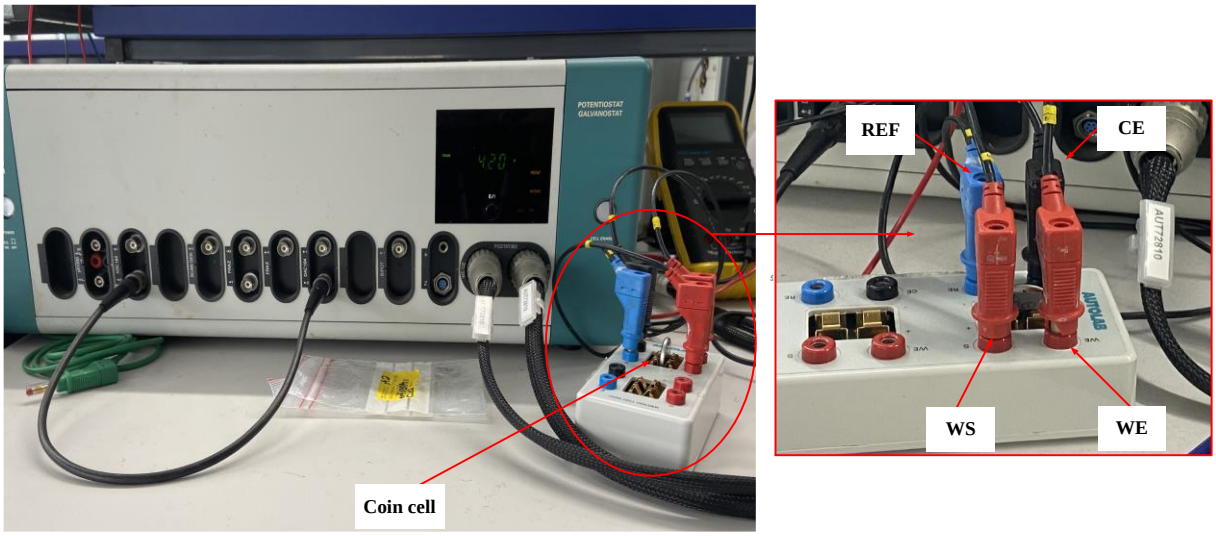

(b)

Figure 3.4 EIS test setup. (a) Two-terminal connection to battery via a coin cell holder used in initial stages of experiment. (b) Upgraded setup using the four-terminal setup using Autolab coin cell holder.

Combining the physical observations in the impedance response and literature on electrochemical processes presented in Chapter 2, an ECM was developed based on variations of the Randles model and fitted to the impedance response of the cells to quantify the electrochemical processes. This allowed for a more accurate comparison between the

impedance responses of the new and aged states responses of the cells. The values extracted from the models, cell capacities, and number of cycles are summarised in Table 3.2. In Table 3.2, these are sorted by increasing value of aged-state ESR values. Fitting of the ECM circuit was performed using local search and genetic algorithms using the EISyfit Software. The fitting algorithms used ensured a fair combination of speed and accuracy. Details of the model circuits, parameters, and fitted responses for each of the 19 cells in their new and aged states are shown in Appendix C.

In Figure 3.5b, it is observed that most cells in their aged state exhibit an enlarged second semicircle, leading to an increase in the impedance between the Ra and Rc points (highlighted in Figure 2.5). Within this range, the maximum values for the real part of the impedance (Z') increased from between 1.2 Ω- 2.5 Ω to 1.7Ω - 9 Ω, while the imaginary part (-Z'') increased from between 0.3Ω - 0.64 Ω to 0.5Ω – 4.9 Ω, excluding the unique case of Cell 18. The enlargement of the second semicircle is a significant contributor to the increased impedance. From the fitted models, this increment is attributed to phenomena such as electrolyte decomposition and the formation and growth of the SEI layer, which influences the impedance characteristics within this frequency range of the second semicircles as discussed in Appendix A. Cell 18 in its aged state (Figure 3.5b) exhibited a significantly larger second semicircle and was devoid of the 45 °diffusion process line. This is because in this case, the effects of electrolyte decomposition and growth of the SEI layer are more pronounced which impedes the diffusion of lithium ions, such that the diffusion rate is slowed to a timescale that falls out of the test frequency range. This can be attributed to the combination of the initial high discharge stress and prolonged cycling. A similar case is observed in Cells 6 and 19. Another parameter used to indicate aging in cells is the equivalent series resistance (ESR). According to [122, 161], the ESR reflects the bulk resistance of the electrolyte solution, and the resistance associated with the migration of ions through the electrolyte. In the context of aging in batteries, it has been employed as an indicator owing to its sensitivity to changes in the internal cell resistance. In this light, ESR values were extracted from EIS impedance responses over the cyclic aging period for each cell. This is shown in Figure 3.6. These values are taken as the high-frequency intercept point (Ra in Figure 2.5), which was found to be at 7.9 kHz.

Initially, ESR values ranges from 0.17- 0.24 Ω in the in the first few cycles. This range is consistent with the manufacturer's value of < 600mΩ in the new state. At their aged states, resistances of cells 1-15 showed a slight and gradual increase to a range between 0.22 Ω - 0.27

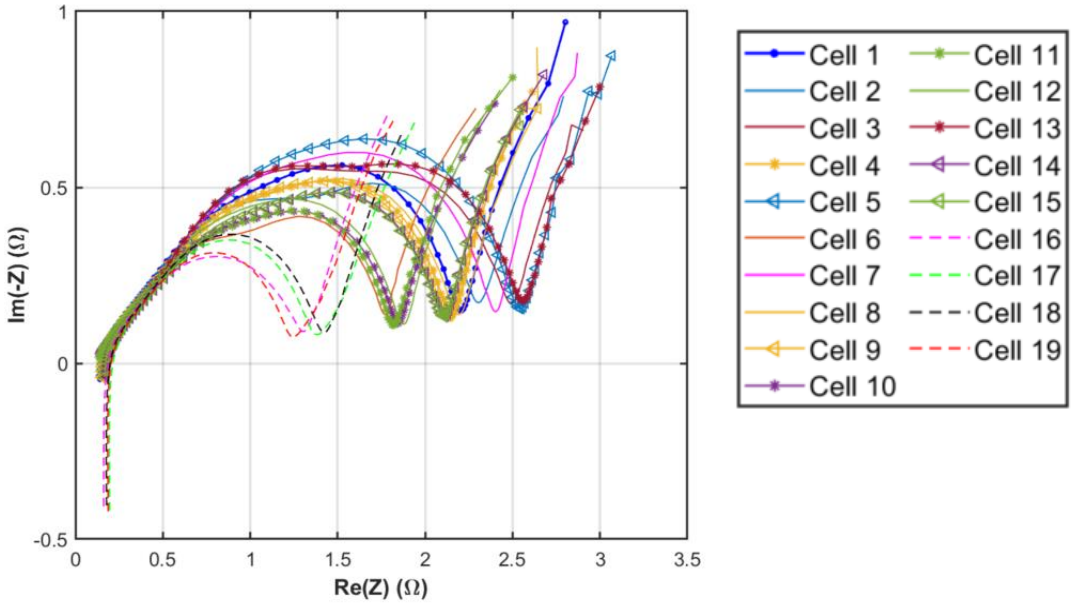

(a)

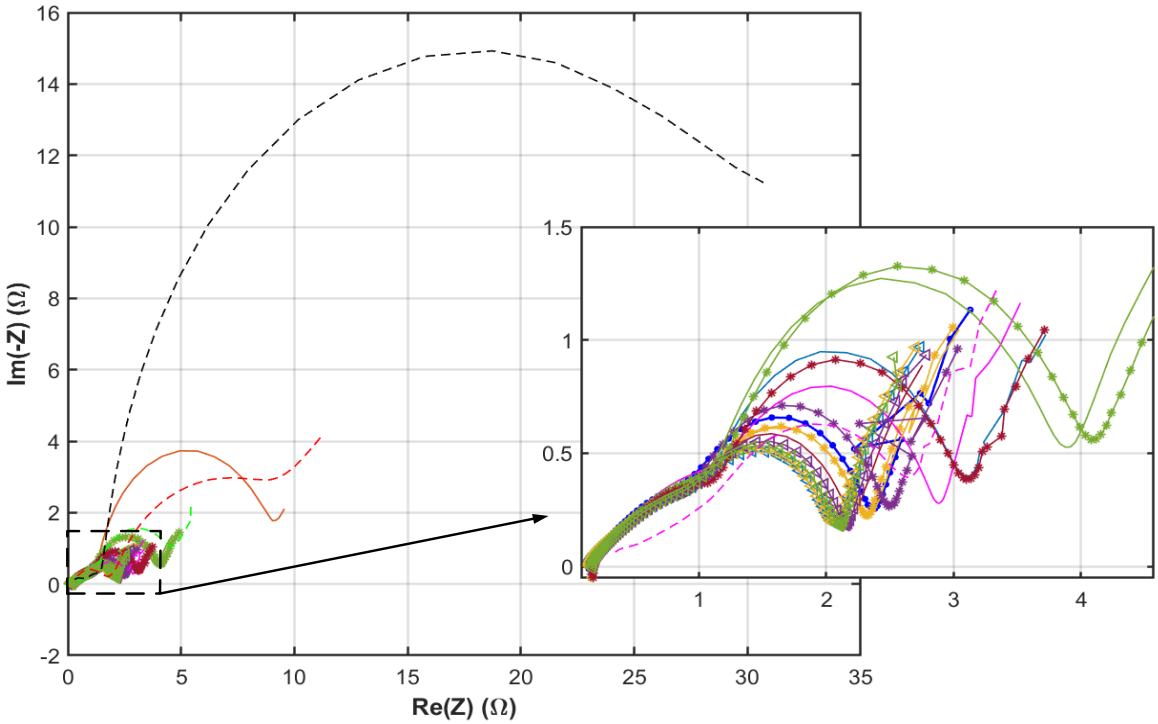

(b)

Figure 3.5 EIS Impedance response of sample cells. (a) Impedance response of cells in the new state. (b) Impedance response of cell in the aged state.

Ω. This gradual increase over cycling confirms the increase in ionic conduction resistance at the electrode-electrolyte interface and within the electrolyte. For Cells 16 -19 over 80% increase in ESR is observed.

Table 3.2 Summarised parameters of sample cells

Cell ID	No. of Cycle	Capacity Values (mAh)		EIS-based ESR Values (Ω)		Charge transfer Resistance Values (Ω)		Double layer capacitance (F)		Resistance SEI layer (Ω)	
		New state	Aged state	New state	Aged state	New state	Aged state	New state	Aged state	New state	Aged state
1	102	46.1	21	0.19	0.204	0.735	1.434	0.024	0.055	1.209	1.241
2	102	46	28.8	0.20	0.217	0.396	1.397	0.085	0.104	1.980	1.398
3	102	46.1	23.7	0.20	0.220	0.557	0.740	0.013	0.101	1.960	1.236
4	102	46.2	20.8	0.21	0.223	0.584	0.857	0.023	0.052	1.373	1.158
5	102	45.8	22.8	0.21	0.224	0.790	0.621	0.015	0.051	1.575	1.259
6	202	47.5	23.2	0.17	0.228	0.391	6.650	0.063	0.100	1.214	1.310
7	102	45.6	14.7	0.21	0.230	0.879	0.776	0.016	0.096	1.222	1.168
8	102	43.9	18.3	0.22	0.240	0.532	2.284	0.019	0.062	1.089	1.355
9	102	46.8	21.7	0.21	0.241	0.532	2.284	0.019	0.062	1.089	1.355
10	122	46.7	12.3	0.20	0.242	0.496	0.776	0.051	0.096	1.828	1.168
11	202	45.3	3.1	0.21	0.244	0.674	0.729	0.024	0.046	1.135	1.155
12	202	47.2	12.1	0.20	0.252	0.622	1.884	0.008	0.064	1.118	1.342
13	102	46.2	19.5	0.23	0.266	0.540	3.258	0.011	0.065	1.116	1.268
14	102	43.6	13.7	0.24	0.272	0.389	5.388	0.016	0.056	0.804	1.087
15	102	44.7	14.6	0.23	0.272	0.562	6.454	0.010	0.057	1.158	1.426
16	442	49.4	8.7	0.20	0.487	0.336	0.791	0.017	0.121	0.759	1.992
17	442	50.8	6	0.18	0.521	0.451	2.148	0.012	0.158	0.699	4.565
18	202	48.4	1.1	0.23	0.576	0.093	30.30	0.001	0.108	1.099	2.342
19	362	52.1	3.8	0.22	1.028	0.400	3.861	0.012	0.114	0.626	2.059

In cells 18 and 19, which were exposed to short-circuit faults, capacity declined from 33 mAh to 25 mAh, while ESR increased significantly from 0.23 Ω to 1.028 Ω. This suggests that the short-circuit accelerated certain degradation mechanisms, leading to a rapid decline in battery performance. One consequence of short-circuiting is the intensified lithium plating and dendrite growth, which occurs due to the sudden and uncontrolled current surge . The increased current density at localized sites promotes excessive lithium deposition on the anode surface, leading to uneven lithium distribution and permanent loss of active lithium, both of which contribute to capacity fade [127]. Additionally, short-circuit events can contribute to localized heating, causing thermal decomposition of the electrolyte which can result in higher charge transfer resistance, further restricting ion transport and exacerbating the rise in ESR. The thermal stress from the short circuit can also induce mechanical degradation, leading to structural collapse or cracking of the electrode materials, which in turn reduces the effective surface area available for lithium-ion intercalation. Since these degradation mechanisms primarily occur at the electrode-electrolyte interface, they are likely to influence high-frequency FDR measurements, which are particularly sensitive to interfacial impedance changes [12, 162]. For cells 16 and 17, the increase was gradual, as seen in cells 1 to 15. This suggests that the aging can be from the

cumulative effect of repeated cycling, change in C-rates, and stress on the electrodes and electrolyte, as the cells reach approximately 442 of the intended 500 life cycles, ultimately leading to electrolyte decomposition and electrode material degradation.

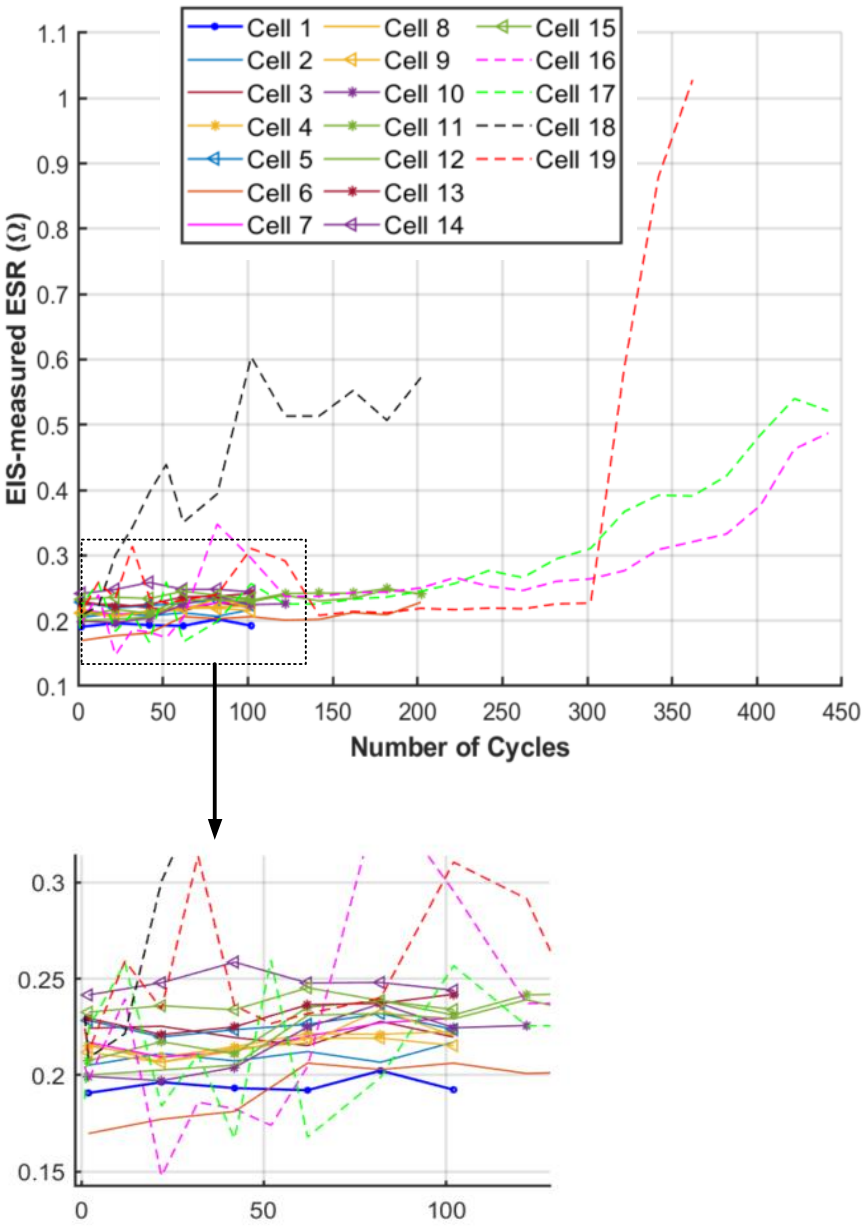

Figure 3.6 EIS-measured equivalent series resistance (ESR) of cells measured over cyclic aging.

3.5 Summary

This chapter describes the characterization and aging process of the sample cells used in this research. Nineteen commercial LIR2032 coin cells (4.2V, 40mAh) were cycled under controlled

conditions to study their electrochemical behaviour and impedance changes with aging. Internally, these cells featured electrodes and separators wound into a flat jelly roll with electrode tabs at either end, an arrangement known to increase impedance at higher frequencies due to ionic shunt resistance.

The aging process was not designed to induce specific degradation mechanisms but rather to mimic generic cyclic aging likely to occur during normal usage. The cells were divided into two batches, A and B, for cycling under distinct protocols to capture the effects of different C-rates on aging. Batch A (4 cells) underwent slower initial cycling at 1C for the first 60 cycles before transitioning to 2C, whereas Batch B (15 cells) cycled continuously at 2C after initial conditioning. This division aimed to observe the impact of slower and faster cycling on the cells' electrochemical and physical degradation. Batch A exhibited greater variance in results, as slower cycling reduced stress on the electrodes, leading to lower capacity fade in the early stages compared to Batch B. However, the transition to 2C increased the occurrence of degradation mechanisms, narrowing the performance gap between the batches over time. These observations highlight the sensitivity of the cells' aging process to variations in cycling protocols, even within the same experimental framework.

Additionally, significant anomalies were observed in Batch A, specifically in cells 18 and 19, due to short-circuit incidents caused by cycler malfunctions. These short circuits occurred during cycles 14–22 for cell 18 and cycles 270–300 for cell 19, resulting in rapid capacity losses of 23% and 28%, respectively. The short-circuiting triggered additional electrochemical degradation, including accelerated electrolyte decomposition and SEI growth, further amplifying the resistance and capacity fading beyond these cycles. The short-circuits observed in Batch A were not repeated in Batch B because these incidents were due to equipment malfunctions specific to the channels used for cells 18 and 19 in Batch A. In Batch B, these issues were mitigated by improved monitoring and the use of fully functional cycler channels, ensuring a consistent and reliable experimental setup.

Across all samples, intermittent EIS tests conducted every 20 cycles revealed clear aging trends. ESR values increased from an initial range of 0.17–0.24 Ω to between 0.27–1 Ω by the sample end state, with the highest increases observed in the short-circuited cells of Batch A. ECM modelling attributed the observed impedance growth to processes like charge transfer resistance, double-layer capacitance, and SEI formation, which were further exacerbated in cells exposed to high stress or short circuits. In total, two cells retained capacities above 60%, eight fell between 60% and 30%, and nine dropped below 30%.

These finding of the end-stage ESR values and capacity confirm the occurrence of aging-induced degradation in all sample cells while emphasizing the role of cycling conditions and unexpected anomalies in driving variance. While the results validate the expected trends of capacity fade and resistance increase with aging, the narrow resistance range across most samples suggests potential challenges in utilizing FDR sensitivity for precise differentiation of aging states.

Chapter 4

Evaluating Frequency Domain Reflectometry for Battery Health Diagnostics

4.1 Introduction

This chapter evaluates FDR as a tool for detecting and diagnosing battery SoH. It covers the design, calibration, and de-embedding of the setup used in FDR measurements, as well as the characterization of the setup and the definition of the confidence region for the measurements. With the FDR setup calibrated and characterized, the chapter then evaluates the application of FDR to lithium-ion batteries. This evaluation is conducted in two stages. The first stage involves a single-cell analysis, studying the impedance changes in a sample cell during its aging process. This stage simulates a continuous monitoring scenario and assesses FDR's applicability. The second stage involves analysing all samples at their end-of-life state, comparing different cells at various states of health, and assessing FDR's ability to diagnose different states of batteries.

4.2 Frequency Domain Reflectometry Measurement Setup

From Figure 3.6, the ESR of the majority of the sample cells changed by an average of 0.1Ω during the aging process. Considering these low ohmic values, research suggests that using a 4-point impedance measurement method is required to eliminate the resistance from the measurement equipment and improve accuracy [27, 163]. The FDR setup was therefore designed based on the shunt-through network. This enabled the measurement of the S_{21} parameter that is equivalent to a 4-point measurement method [12, 28]. Figure 4.1 shows an image of the overall FDR experimental setup, highlighting the VNA, connector PCB and the sample cells used in the tests. The setup consists of the PicoVNA 106 and a connector PCB, that is used as an intermediary connector between the batteries and the VNA. The connector PCB is required to interface the battery terminals to the SMA ports of the VNA. Although the setup measured all four S-parameters, focus was placed on the S_{21} parameter as this offers most accuracy within the range of impedance values under consideration. The principles of S_{21} measurements and details on the design of the connector PCB are illustrated in Figure 4.2. Figure 4.2a illustrates the S_{21} measurement circuit within a VNA. *Vs* is the VNA signal source whose current is limited by the series-connected 50 Ω resistor. Part of the source current is measured using the parallel-connected voltage sensor *Vin* and a 50 Ω resistor (this is equivalent to Ref 1 in Figure 2.11).

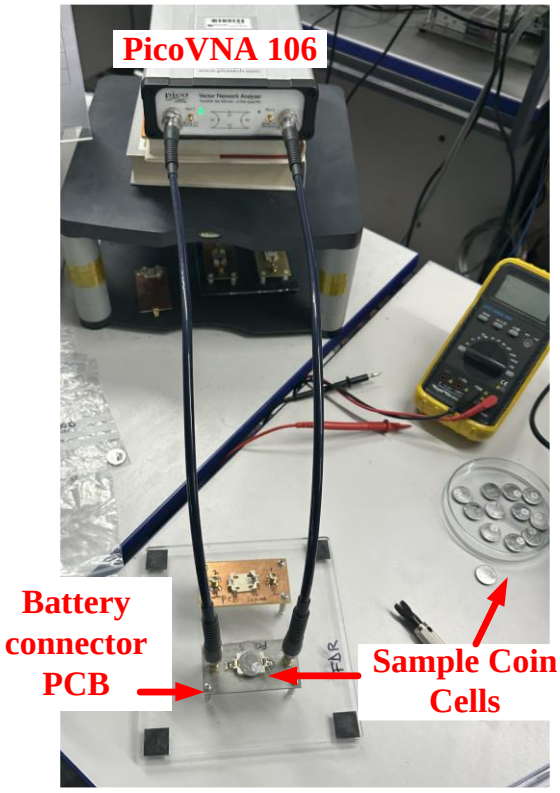

Figure 4.1 Experimental setup for FDR measurement.

The value is compared with the transmitted signal for magnitude and phase calculations. As the current propagates through the circuit, a voltage drop occurs across the cell. This voltage drop is picked up by the port 2 voltage sensor V_T, which includes the effects of both the cell and the connector PCB. The voltage sensor V_T is equivalent to the P2 receiver in Figure 2.11.

Figure 4.2c illustrates how the battery shunts the two VNA SMA ports using the PCB connector and Figure 4.2b shows the up-close image of the connector PCB with the SMA ports and a sample cell inserted. Figures 4.2d and 4.2e shows the 3d model of the PCB. The PCB gerber file showing the design layout of the PCB is shown in Figure F.24 in Appendix F.5 In Figure 4.2b, a battery holder is placed on a PCB to form a connector PCB. For clarity, the entire entity that consists of battery holder and PCB would be referred to as Connector PCB (CP) and the coin cell holder only would be referred to as Battery Holder (BH). The CP design uses two SMA connectors and a BH mounted on the PCB. These are connected such that the positive terminal of the BH connects to the inner pin of the SMA via the top plane of the PCB and the negative terminal connects the outer pins of the SMA through the bottom plane of the PCB. The BH negative terminal is electrically isolated from the PCB top layer, this is indicated in Figure 4.2c by the white rectangle around the negative sign.

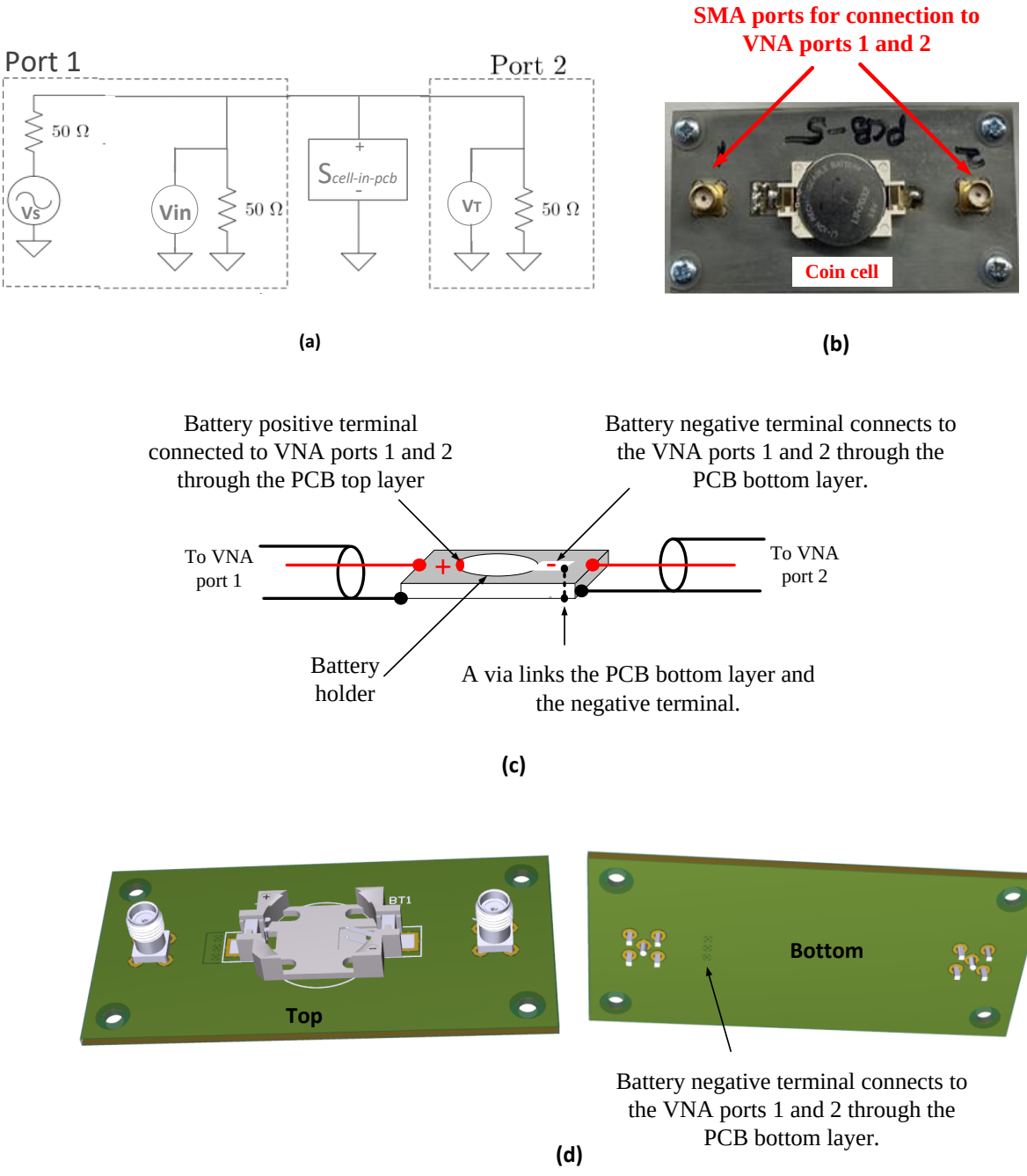

Figure 4.2 S_{21} measurement setup based on FDR Shunt-through network. (a) Equivalent circuit for S21 measurement. (b) Image of designed PCB connector used for FDR testing [18, 29]. (c) Illustration of Shunt-through network implementation on a PCB. (d) 3D Image of PCB showing top and bottom layouts.

A through-hole via is used to electrically connect the BH negative terminal to the bottom layer. A double-layer PCB was used to limit high frequency interferences that occur when multiple conductive tracks are placed side by side on a PCB [164]. This separation also helps to minimise capacitive coupling between tracks [164]. Also, the negative terminal at the bottom provides grounding.

4.3 Definition of FDR Measurement Parameters

The FDR tests were conducted between 300 kHz to 1 GHz, with a source voltage of 0 dBm (1mV). The frequency was chosen to extend the 1 kHz – 300 MHz range covered by previous research [25, 27]. The lower limit was dictated by the PicoVNA 106, which operates at a minimum frequency of 300 kHz. The upper limit of 1 GHz was selected to investigate potential impedance characteristics above 300 MHz. However, preliminary findings indicated no significant findings in the higher frequency range, leading to the decision not to pursue further exploration beyond this frequency.

The source voltage was chosen to obtain maximum VNA sensitivity while ensuring batteries linear response during the test. With 0 dBm in the 300 kHz to 1 GHz frequency range, the dynamic range of the VNA is 90 dB. This implies that the VNA is set up to measure a wider range of signal levels, enhancing its ability to detect signals ranging from the VNA average noise floor level of −118 dB to signals of 90 dB or higher [139].

To ensure the linear response of batteries, impedance tests such as EIS apply small perturbation amplitudes in milli volts region [122]. At such small amplitudes, battery responses are assumed to be linear. This implies that the relationship between input voltage and output current, or vice-versa is linear, which simplifies analysis [13]. Therefore, in this study, 1 mV (0 dBm) source amplitude was chosen as it offers both maximum sensitivity with the measurement frequency range and is small enough to ensure cell linear response.

4.4 FDR Setup Calibration and De-Embedding

Prior to testing, the VNA was calibrated using the SOLT calibration method outlined in section 2.5. This calibration method was chosen because it is the most suitable for a two-port network and provides a comprehensive calibration of a two-port network [139]. The calibration standards used were supplied by the VNA manufacturer. The SOLT calibration only compensated for the effects of VNA and the coaxial cables. However, since the batteries had to be placed in the CP, further de-embedding was required to remove the effects of the CP on the measured impedance. The OSLC de-embedding technique outlined in section 2.5 was adopted because it is relatively simple and allowed for adaptation to the specific setup. This de-embedding technique could also be used on several samples without the need to solder the sample batteries. Using this method required the application of (2.4) and (2.18) to the FDR measurements. Equations (2.4) and (2.18) are adopted to FDR measurement as expressed in (4.1(4.1) and (4.2) based on [128].

$$Z_{cell,OSLC} = Z_{REF} \frac{(Z_{open} - Z_{load})(Z_{cell-in-pcb} - Z_{short})}{(Z_{load} - Z_{short})(Z_{open} - Z_{cell-in-pcb})} \quad (4.1)$$

$$Z_{cell} = Z_{cell,OSLC} - Z_{Cu} \quad (4.2)$$

Z_{open}, Z_{short}, Z_{load} and Z_{cu} are calculated impedances from S-parameters S_{open}, S_{short}, S_{load} and S_{Cu} respectively using (2.14) and (2.15). S_{open}, S_{short}, S_{load} are the S-parameters measured when the BH terminals were open-circuited, short-circuited and connected to 50 Ω matched load as shown in Figure 4.3a and 4.3c respectively. For S_{open} measurement the BH terminals were left open whereas for S_{short} the BH terminals were short-circuited using a piece of conductor. The 50 Ω matched load was chosen to match the 50Ω characteristic impedance of the PicoVNA 106. This simulates a scenario where an ideal DUT of same impedance as the VNA is connected [128, 139].

S_{Cu} represents the S-parameters of a copper coin that has been machined to the same dimensions as the battery coin cells, shown in Figure 4.3d. The S-parameters of the copper coin are used to remove the effect of inductive and capacitive coupling between the outer casing of the cells and the CP using (4.2) [128]. As presented in [128], a copper coin with the same dimensions as the battery can be assumed to have similar external inductance and capacitance to the battery. Z_{REF} is the ideal load value of 50 Ω, $Z_{cell-in-pcb}$, is the FDR impedance of each sample cell, including the effects of CP and is calculated from the S-parameters ($S_{cell-in-pcb}$) using (2.14) and (2.15). $Z_{cell,OSLC}$ is the impedance of the cell after the OSLC de-embedding but before the external inductance and capacitance are removed. Z_{cell} is the impedance of the cell with the external inductance and capacitance removed.

It must be noted that S_{open}, S_{short}, S_{load} and S_{Cu} are measured and converted to impedances once, however, (2.14), (2.15), (4.1) and (4.2) are repeatedly applied to each FDR measurement of each sample cell during the aging process to obtain the high frequency impedance of the samples at various stages in the aging process. Also, though (2.14) is used to determine the impedance based on the S_{11} parameter, only the S_{21} parameter (therefore Z_{21} impedance) are considered in this stage of the study. This is because of the proven sensitivity of S_{21} to low impedance values. Also, the SOLT calibration was performed within the VNA's software, ensuring accurate and repeatable measurements by compensating for systematic errors in the instrument and coaxial cables. Since the calibration process is managed internally, standalone calibration data is not explicitly generated. However, the responses of the open, short, and load test cases (illustrated in Figure 4.3), along with a sample cell used in the de-embedding stage, are provided in Appendix G.

However, all *S*-parameters, including S_{11} were also calculated in this study to be used in the statistical analysis in Chapter 5. Methods such as PCA and Multivariate statistical process control, have the ability to detect both magnitude changes and changes in relationships between measured variables, therefore all S-parameters were initially used in the statistical analysis to explore if changes in the overall relationship between all *S*-parameters of a cell correlated with either capacity fade or increase in internal resistance before focusing on S_{21}.

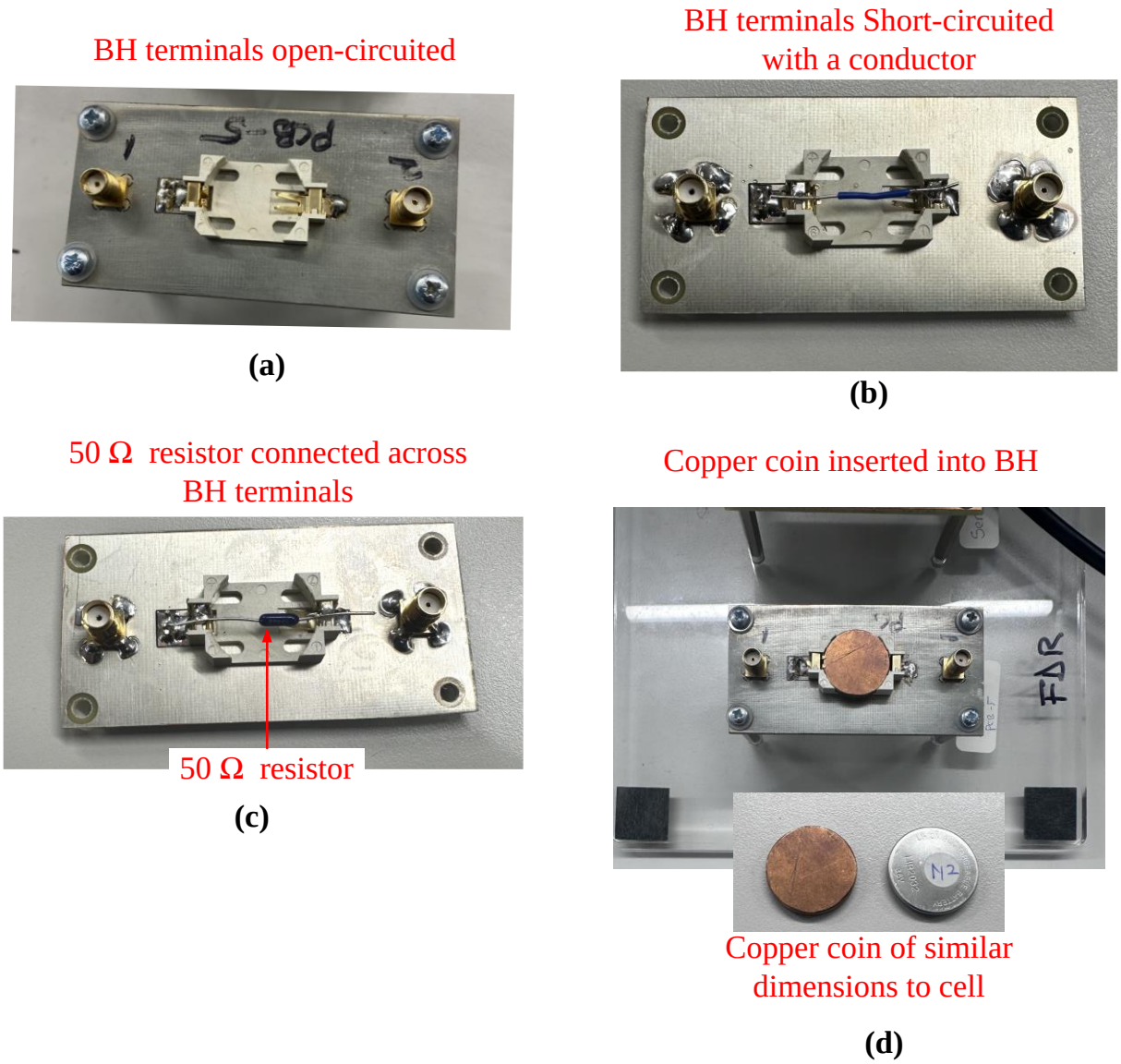

Figure 4.3 Test standards used in OSLC de-embedding method. (a) Open-circuit setup configuration. (b) Short-circuit setup configuration. (c) 50Ω load setup configuration. (d) Copper coin used in the de-embedding stage.

4.5 Region of Confidence Definition for FDR Measurement

After calibrating the FDR setup and measuring the OSLC de-embedding parameters, the setup was characterised to assess it performance and also to establish a Region of Confidence (RoC) before testing of the sample batteries. This step helps to quantify the trustworthiness of the measurement results and identify any potential limitations. Reference [128] defined the RoC as the region within the spectrum where the Z_{open} and Z_{short} responses were the highest and lowest impedance values respectively, and the Z_{load} response was relatively closer to the open circuit than the short circuit. Also in this region, a cell with a relatively low impedance is expected to be closer to the short-circuit response than the open-circuit response. The region within the spectrum where all these conditions are true is therefore considered as region of confidence within which measurement results are optimal. This definition holds when single impedance measurement being considered but maybe insufficient when considering relative changes in impedance. This falls short in providing information of the sensitivity of the setup and its calibration to small changes in impedance. Therefore, in this study the definition of RoC was expanded by identifying sections of the spectrum where changes in passive element responses were related to the changes in values of the respective element being measured. This addition required the testing of passive elements to establish the performance of the setup. The set of passive elements used are listed in Table 4.1. Figure 4.4 shows a portion of the passive elements and how they were mounted on the FDR setup.

In the Figure 4.4, a plastic coin having the same dimensions as the battery cell was fabricated such that it can be inserted into the BH. Copper strips were used to connect either leads of each element to the BH terminals. The plastic material was used so it would not contribute electrically to the impedance measured. Values of the test resistors (R) listed in Table 4.1 were selected initially based on manufacturer datasheet. From the datasheet in [154], cell resistance values were estimated to be less than 0.6 Ω, however, after initial EIS measurements, the ESR values ranged mostly within 0.1 Ω to 0.2 Ω. Assuming majority of the sample cells will experience an approximately 5 mΩ (2%) minimum increment in impedance, the resistors were selected to be around values of 5mΩ - 1Ω. The 10 Ω and 100 Ω resistors were also included to characterise instances of higher impedance changes. Capacitor (C) and inductor (L) values were chosen to span a wider range since preliminary incremental values was not known prior. The components listed in Table 4.1 were high-frequency components selected for their stability and accuracy within the frequency range of interest. Although single instances of the components were used in the tests, their tight tolerances (±0.1% for resistors, ±5% for

capacitors, and ±0.3 nH for inductors) ensured minimal deviation from nominal values during the measurements.

(a)

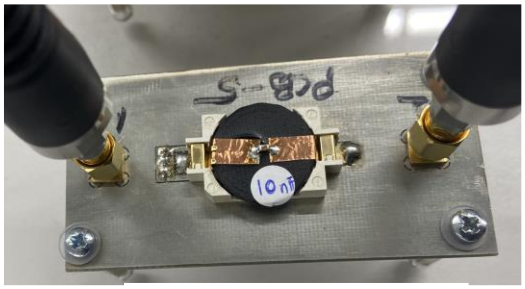

(b)

Figure 4.4 Portion of passive elements used in setup characterisation. (a) Passive elements mounted on plastic coins. (b) Connection of a test capacitor in the FDR setup.

Using the selected passive elements, the RoC was defined for both the pre- and post-OSLC compensation stages. This was to fully appreciate the performance of the setup before and after the OSLC compensation. The impedance obtained before OSLC compensation will herein be referred to as pre-OSLC impedance and that obtained after OSLC compensation will be referred to as post-OSLC compensation. Figures 4.5 and 4.6 show the pre- and post- OSLC compensation responses for passive elements respectively.

In Figure 4.5, are the magnitudes and phase angles of the pre-OSLC impedance of tested RLC elements. The inserts in Figure 4.5b, d and f, show the zoomed in plot of phase angles at 300 kHz to 200 MHz. Variations amongst all the tested elements, that are consistent with the varying values of each element, are observed between 300 kHz and 200 MHz.

Table 4.1 Values of Passive Elements used in RoC Definition.

Resistors	Inductors	Capacitors
5 mΩ	0.1 nH	10 pF
10 mΩ	1 nH	91 pF
0.2 Ω	47 nH	200 pF
1 Ω	100 nH	470 pF
10 Ω	220 nH	560 pF
100 Ω	400 nH	680 pF
	820 nH	750 pF
	2.2 uH	820 pF
	11 uH	1 nF
	33 uH	10 nF
	47 uH	22 nF
	2.2 uH	47 nF
	11 uH	57 nF
		100 nF

Above 200 MHz, no significant variations are observed. This is likely due to the interference of the PCB at high frequencies as this is observed in all elements but absent in the post-OSLC impedance in Figure 4.6. Also, all elements are observed to exhibit resonance-like behaviours between the 300 kHz -200 MHz range where the observed peak coincides with a zero-crossing of the phase angles. The occurrence of the resonances suggests interactions between inserted elements and the PCB's inherent RLCs. This is confirmed by the absence of resonance in the post-OSLC impedance.

In Figure 4.5a and 4.5b, the resonance frequency of the resistors does not shift with changes in resistance. The peak values, however, are observed to decrease with increasing resistance. This is due to the damping effect of resistance on resonance peak. The phase angles of the resistors, shown in Figure 4.5b, start at approximately 0º and increase to 90º because as the frequency increases the inductance of the copper strip used to connect the elements to the BH begin to increase and influence the impedance measured. For capacitors and inductors in Figure 4.5c-f, the frequency of resonances decreases with increasing values of capacitance and inductance. The capacitor responses in Figure 4.5e and 4.5f, show two resonance effects. The first set of resonances occurs between 4 MHz and 130 MHz has the behaviour of a series resonance circuit while the second set of resonances occurs between 130 MHz – 185 MHz and has the behaviour of a parallel resonance circuit. The occurrence of both resonances is similar to the antiresonance effect observed in [165]. This phenomenon is typically observed when two capacitors with dissimilar self-resonant frequencies are connected in parallel [165]. This is further explained in Appendix E.

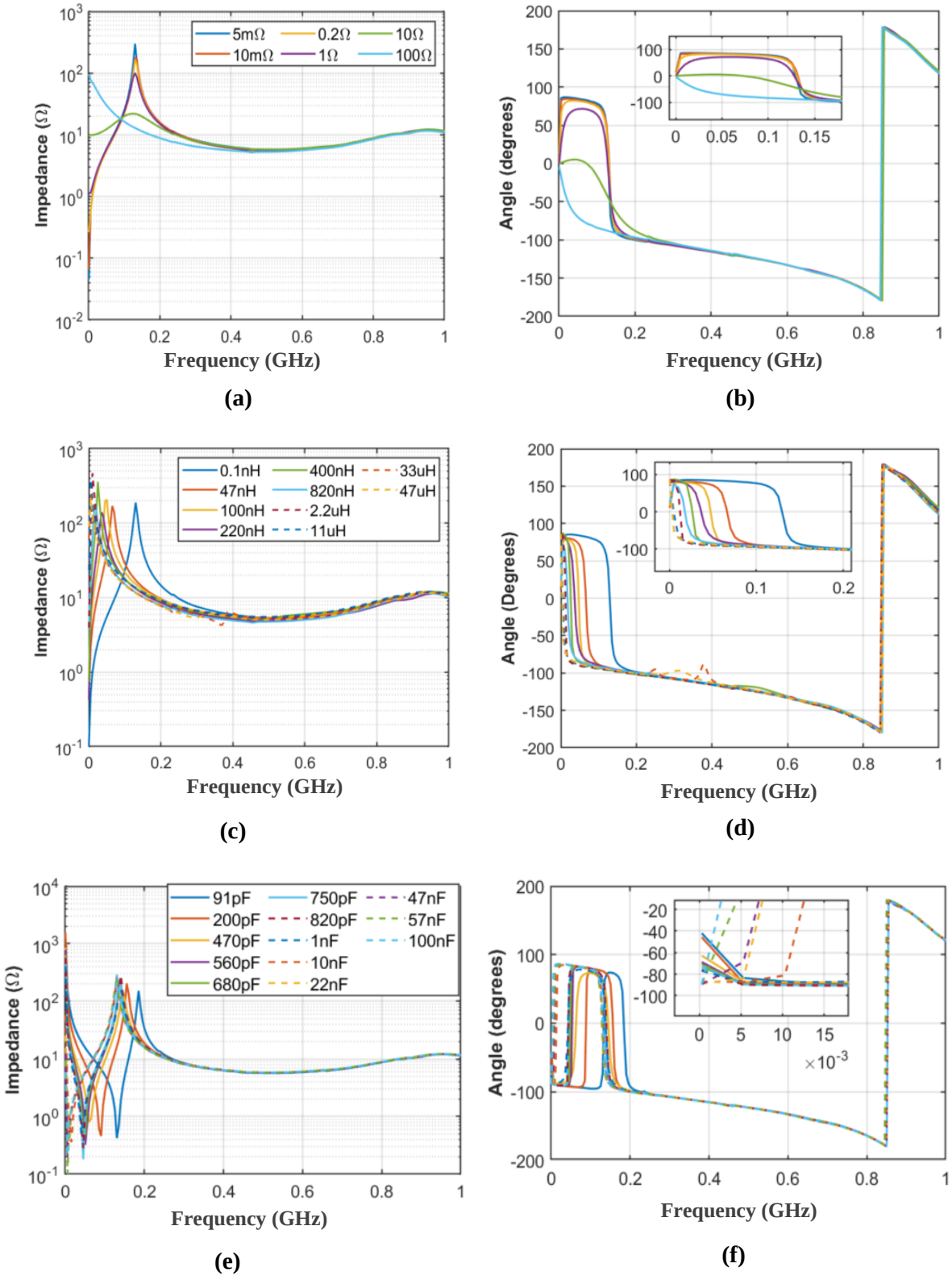

Figure 4.5 Pre-OSLC impedance of tested passive elements with PCB parasitics. (a)-(b) Magnitude and phase of resistors interacting with PCB parasitics. (c)-(d) Magnitude and phase of inductors interacting with PCB parasitics. (e)-(f) Magnitude and phase of capacitors interacting with PCB parasitics.

In the case of the FDR setup, the occurrence of the antiresonance is likely due to the parallel connection between the PCB inherent capacitance and inductance and the inserted capacitors under test. The series resonance occurs when the inserted capacitors whose capacitance are relatively larger than the PCB capacitance resonates first. After the initial resonance, the equivalent series inductance (ESL) of the inserted test element dominates the element's response, observed as the increase in impedance with increasing frequency. This forms a parallel circuit with the PCB capacitance and resonates between 130 MHz and 185 MHz.

Figure 4.6 shows the post-OSLC impedances of the passive elements. With the effects of the PCB removed, the resonances observed between 300 kHz and 200 MHz are also eliminated. An improved sensitivity across the entire spectrum is also observed, particularly with resistors and capacitor responses in Figure 4.6a, b and Figure 4.6 e, f respectively. Despite the improved sensitivity, accuracy is still limited to the 300 kHz to 200 MHz region for capacitors and inductors while resistor accuracy region is reduced to between 300 kHz and 100 MHz. These regions of accuracy were taken as the regions where the variation in responses were consistent with the values being measured.

Considering both pre-OSLC and post-OSLC impedance responses, the region of confidence for this setup was taken to be between 300 kHz and 100 MHz as it is relevant for both pre – and post -OSLC compensation. This is therefore the region where the FDR setup is assumed to be most sensitive. To establish the accuracy within this region, the measured impedance values were compared with known values of the passive elements. To do this, the values of the capacitors and inductors were estimated at selected frequencies within the RoC. These frequencies were selected at a 10 MHz interval between 300 kHz and 100 MHz . Since the VNA, recorded 21 frequency points between 300 kHz and 100 MHz at 5 MHz intervals. Using a 10 MHz interval, aside the boundary frequencies (300 kHz and 1 MHz), helped to select half of the total frequency points within the RoC, for easier calculation. Following the frequency selection, values of capacitors and inductors were calculated at each of these selected frequencies and compared with the FDR-measured impedance (both pre- and post OSLC compensation) at each respective frequency. These are summarised in Appendix E. The most accurate values were recorded at 300 kHz and are summarised in Figure 4.7.

Figure 4.7 presents the measured values of passive elements within the RoC, specifically at 300 kHz, where the highest sensitivity and accuracy were observed in both pre-OSLC and post-OSLC cases. Figure 4.7a compares the measured resistor values at pre- and post-OSLC stages with their expected values at 300 kHz.

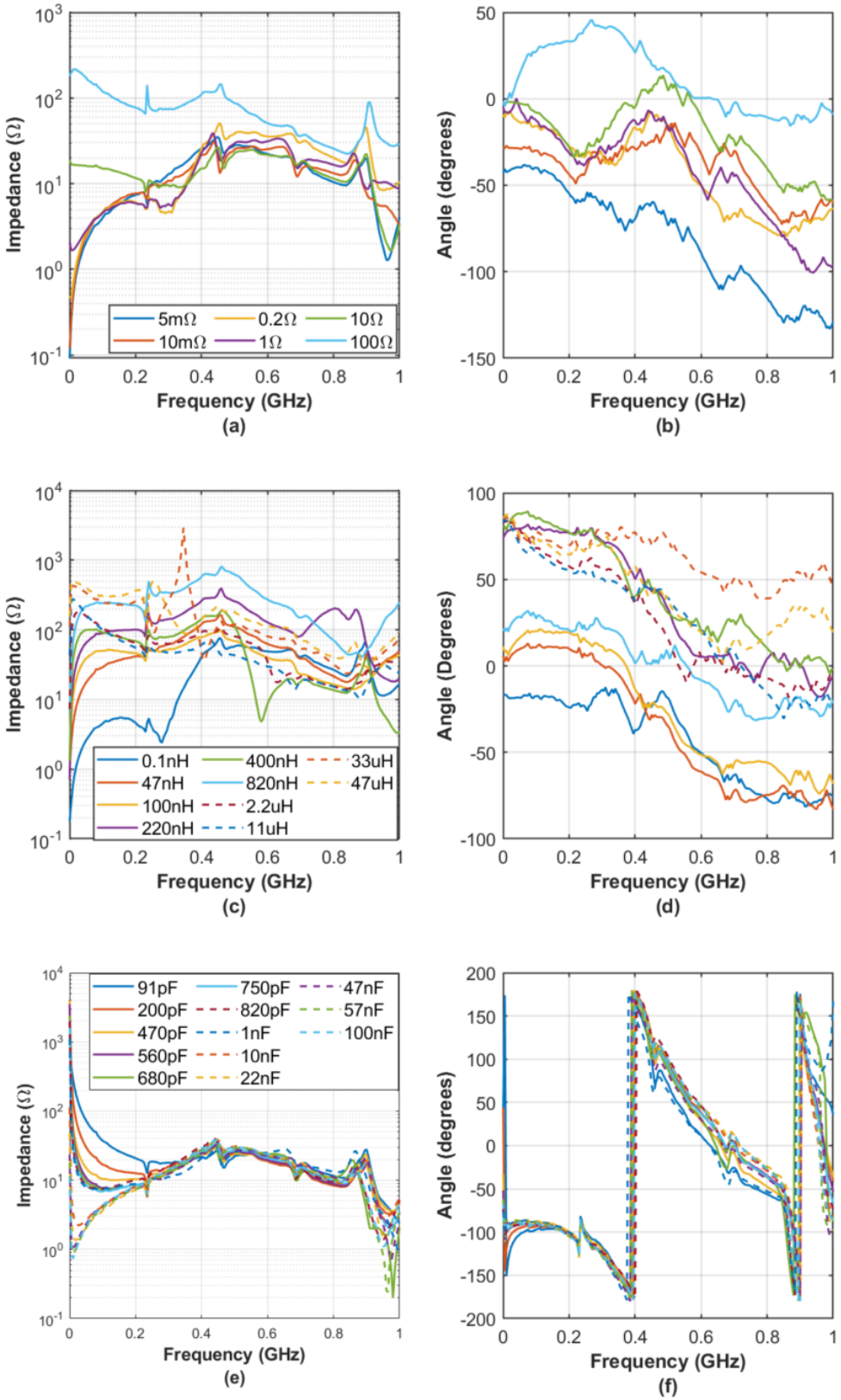

Figure 4.6 Post-OSLC impedance of tested passive elements. (a)-(b) Magnitude and phase of Resistors. (c)-(d) Magnitude and phase of Inductors. (e)-(f) Magnitude and phase of Capacitors.

Similarly, Figure 4.7b and Figure 4.7c illustrate the results for inductors and capacitors, respectively. Additionally, each plot includes the shift in resonance frequency as component values change, highlighting how the FDR setup captures variations in resistors, capacitors, and inductors.

From Figure 4.7, it is observed that the setup is less accurate when measuring values within the range of 5–10 mΩ, 0.1–1 nH, and 10–200 pF in both pre- and post-OSLC phases. The accuracy improves with increasing values, particularly in pre-OSLC measurements. While the reduced accuracy in the capacitance (10–200 pF) and inductance (0.1–1 nH) ranges is unlikely to significantly impact the overall analysis, as these parameters are less critical for assessing state of health (SoH), the limited accuracy in the 5–10 mΩ resistance range is more concerning. This is particularly important because the expected resistance values of the sample cells fall within this range, making precise measurements within this range crucial for tracking SoH. Since small resistance changes are key indicators of SoH variations, the inaccuracy in this range directly affects the reliability of the shunt-through method for detecting subtle resistance shifts.

Additionally, the reduction in accuracy after de-embedding is attributed to parasitic inductances and capacitances introduced during the measurement of S-parameters for the short and load conditions in OSLC compensation. The inserted wire for the short-circuit condition (Figure 4.3b) and the 50 Ω resistor for the load condition (Figure 4.3c) create capacitive and inductive coupling with the PCB, which are not fully accounted for by the de-embedding equations (4.1) and (4.2). These unaccounted parasitics contribute to deviations in measurement, with their impact being particularly significant in the low-resistance region—precisely where accurate detection is most critical. These further challenges the effectiveness of the shunt-through method for assessing small resistance variations necessary for reliable SoH evaluation.

4.6 FDR Test on Lithium-ion Batteries

The calibrated, de-embedded, and characterised setup was then applied to test the sample cells. The primary goal was to identify changes in the impedance responses of the sample cells that corresponded to their known state of health, as characterized by EIS. The analysis on the sample cells were done in two stages. Firstly, a single-cell analysis was performed where impedance changes for each sample cell was studied during it aging process. The second stage involved analysis of all samples at the end-of-life, thus comparing different cells at different states of health.

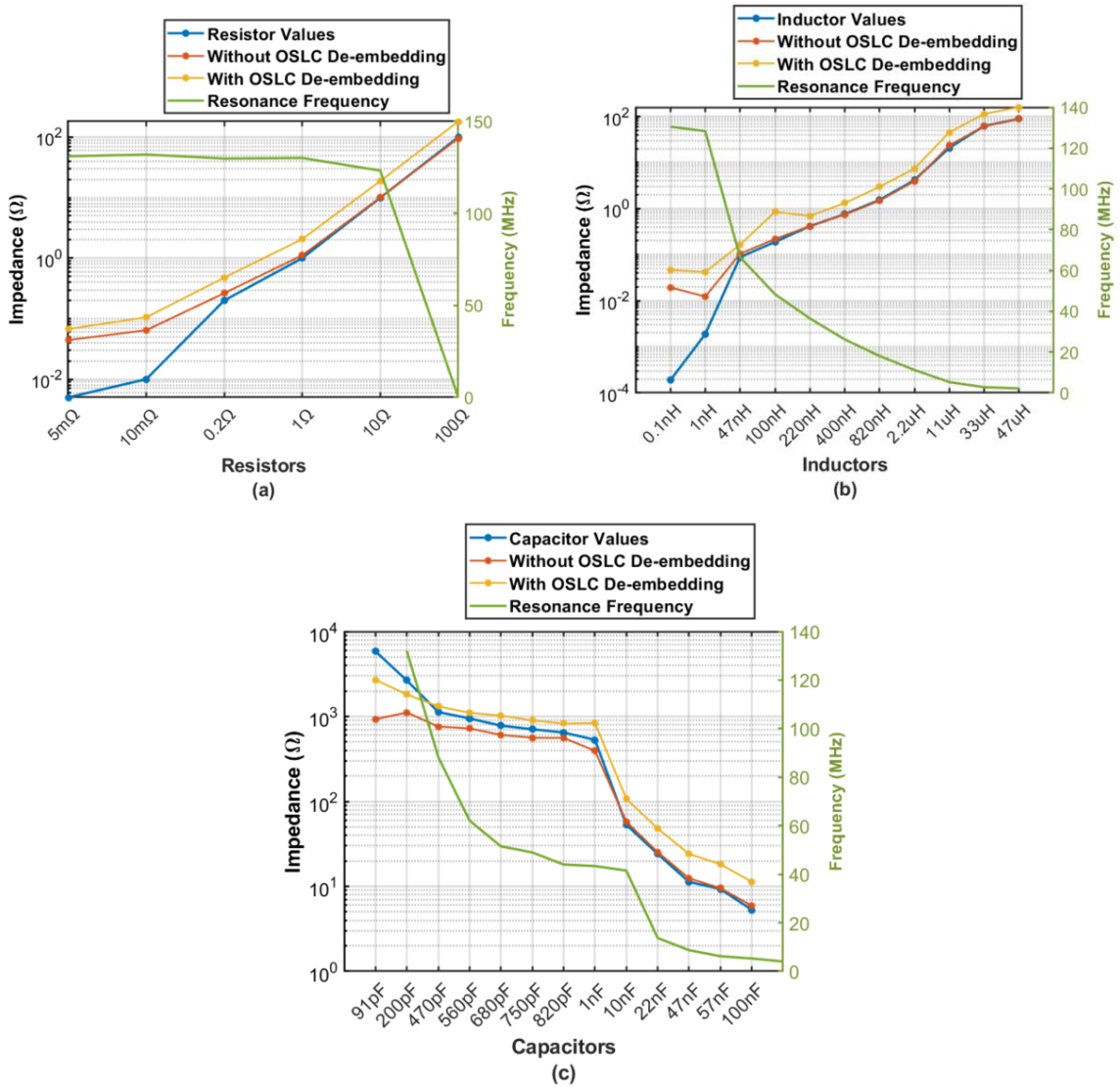

Figure 4.7 RLC impedance values from pre-compensation and post-compensation responses at 300 kHz within the region of confidence. (a) Resistor responses, (b) inductor responses, (c) capacitor responses.

The first stage of single-cell analysis assesses FDR's capabilities in being used a continuous monitoring or tracking tool while the second multi-cell analysis stage, assess it prospects in being used as a detecting and diagnostic tool when assessing large number of cells.

4.6.1 FDR as a Tool for Continuous Aging Monitoring for Cells

As illustrated in Figure 3.2, FDR tests were performed intermittently after each 20th cycle during the aging process of the sample cells. Figures 4.8 and 4.9 show the full spectrum pre-OSCL impedance of cells 1 and 19 respectively, taken at different cycles. These cells are samples of batch A and B to illustrate the full spectrum FDR response. The responses for all the other cells are shown in Appendix F.

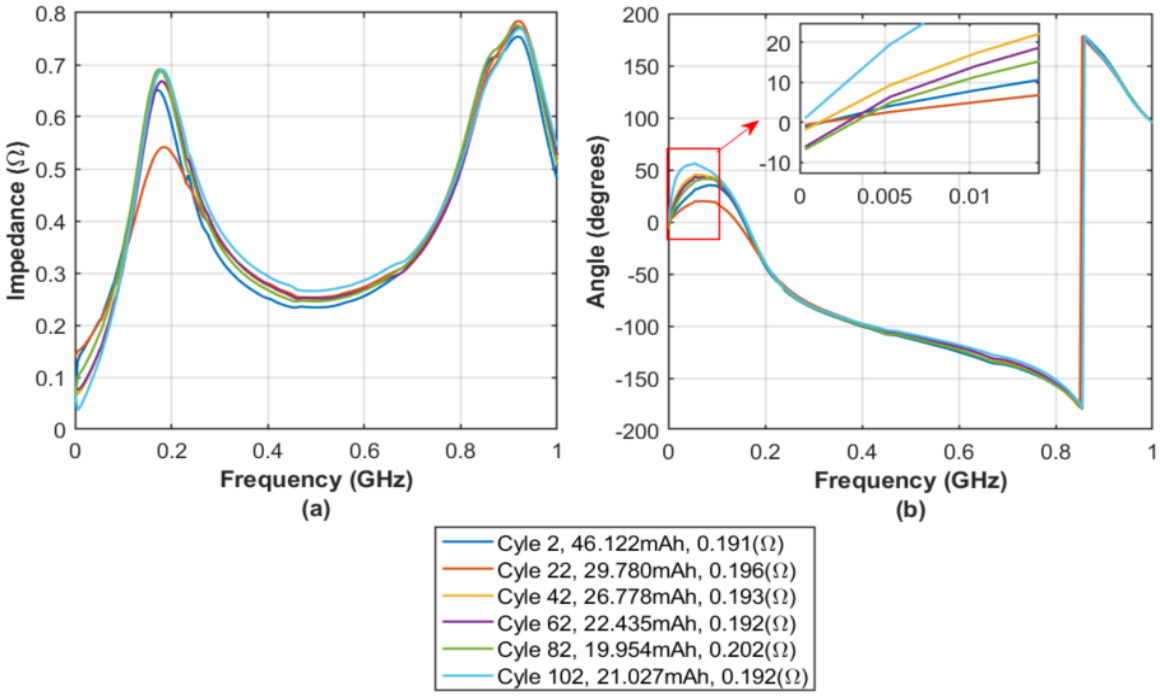

Figure 4.8 Full spectrum pre-OSLC impedance of Cell 1. (a) Magnitude and phase of pre-OSLC impedance of Cell 1. (b) Phase angles of pre-OSLC impedance of Cell 1.

Figure 4.8a and 4.8b show the magnitude and phase of pre-OSLC impedance of cell 1 and Figure 4.9a and 4.9b show the same for cell 19. In both responses, two resonances are observed at 180 MHz and 855 MHz (± 5MHz), similar to the behaviour exhibited by the passive elements in Figure 4.5. Another similarity observed between the cells and the passive elements is the reduced variations at the 855 MHz resonance. Based on this, it can be assumed that the resonance at 855 MHz is primarily influenced by PCB effects rather than the cell or the connected element. However, the resonance amplitude is higher in cells than passive elements, due to the increase in the interaction between the inductance of the cell outer casing and the PCB at high frequency. Also noticed is the responses of cycles 302-362 of cell 19 in Figure 4.9, at this resonance frequency occurs at ~ 900 MHz, instead of 855 MHz. The shift in frequency occurred when the BH holder was replaced due to wear and tear on the previous one that posed the risk of loose connection during measurement. The observed shift in response, happening only at the high frequency resonance further confirms significant effect of PCB at that frequency.

At the lower frequency resonance (180 MHz), the amplitudes of the resonances are observed to change with the cyclic responses of the cells. However, no significant change in the resonance frequencies is observed. This pattern is similar to the behaviour seen in the

resistor responses in Figure 4.5a and b. The phase of the cells also starts from ~0º and increases until the resonance frequency. These suggests that the FDR is detecting changes in cell that can be related to variation in the resistive properties of the cells. However, in contrast to the resistors, these changes are not consistent with either of the health indicators used in this study. For each cell shown in Figures 4.8 and 4.9, the legend shows the cycle number and health indicators (thus the capacity and measured ESR value at each cycle), determined from cyclic aging and EIS tests. The lack of correlation between the resonance amplitude and the health indicators could be due to the combined effects of PCB and cell interaction and the reduced sensitivity and accuracy outside of the RoC. Therefore, changes in resonance amplitude cannot be used reliably as predictors of capacity fade or increase in ESR of cells.

Although the resonance amplitudes did not correlate with the health indicators, these provided information on the overall behaviour of the FDR measured responses. Based on the similarities between the cell responses and the passive elements, particularly, the responses of resistors, the definition of RoC in section 4.5 is assumed to be relevant to cells. Therefore, focus is placed on impedance measured at 300 kHz within the RoC, where the most accurate values were measured. To assess FDR's capabilities in monitoring/tracking a cell's state of health, the measured FDR impedance of cell 19, over its lifetime, was compared with measured cell capacity and ESR. This is illustrated in Figures 4.10 and 4.11. Figures 4.10a and 4.10b show how the FDR-measured resistance (real part of the FDR impedance) changes during the aging process as compared to the cell capacity and ESR respectively. In the same way, Figures 4.11a and 4.11b illustrate how the FDR-measured reactance (imaginary part of the impedance), also change during aging in comparison to cell capacity and ESR. The responses were separated because the FDR response is being compared to ESR values, which represent resistance. Plotting in both real and imaginary formats also helps visualize how each component of the FDR impedance correlates with key health indicators, such as capacity and ESR.

Cell 19 was selected amongst the samples because it had experienced, all the different cycling regimes (0.02C, 1C and 2C), been exposed to short-circuit during it aging process, and had been cycled for 362 cycles. The other samples either had smaller number of cycles or had not gone through these different scenarios within their lifetime. Samples from batch B reached a maximum of 202 cycles and considering that EIS and FDR tests were done after each 20th cycle, these had limited number of data points to establish a significant trend. This is illustrated in Appendix F. Therefore cell 19 was chosen to illustrate FDR's capability to tracking cell aging. Figures 4.10a and 4.11a illustrate how FDR-measured resistance and reactance evolve over cycling in comparison to cell capacity.

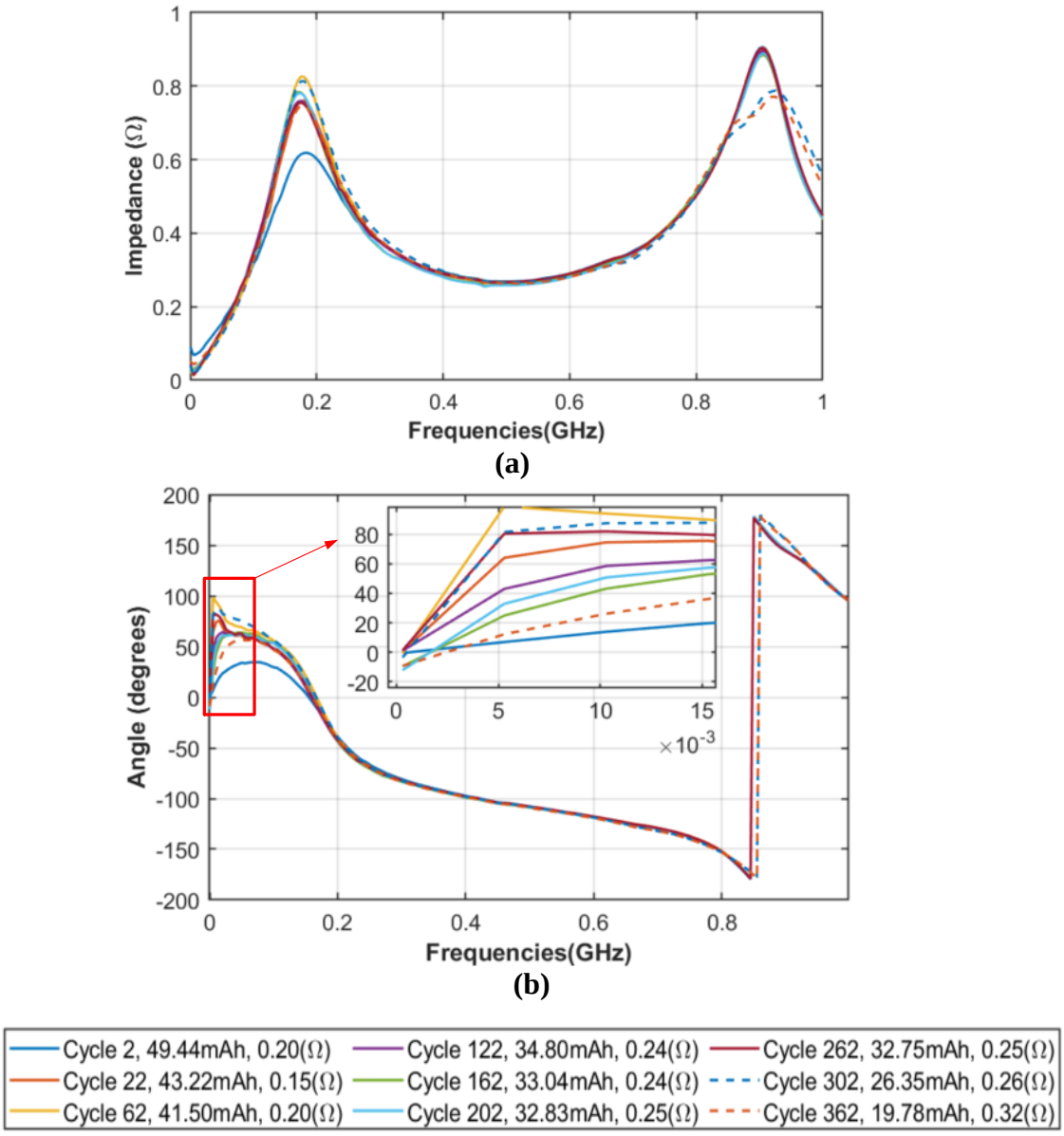

Figure 4.9 Full spectrum pre-OSLC impedance of Cell 19. (a) Magnitude and phase of pre-OSLC impedance of Cell 19. (b) Phase angles of pre-OSLC impedance of Cell 19.

Since capacity and impedance datasets differ in both units and magnitudes, separate scales are used for left and right y-axes. In contrast, Figures 4.10b and 4.11b present both dataset of ESR and FDR resistance and reactance in ohms, albeit with differing magnitudes. To enhance comparability, normalized values are used in these plots. However, it is important to note that FDR-measured resistance is consistently higher than EIS-measured ESR, as evident by the right y-axis in Figure 4.10a. Figures F.22 and F.23 in Appendix F.4 display the raw values of FDR-measured resistance and reactance, respectively, each compared with the raw values of EIS-measured ESR. The high resistance observed in FDR measurements may be influenced by the PCB used in the setup. Parasitic effects from the PCB, including plane resistance, contact

resistance, and additional impedance contributions, were not de-embedded from the Pre-OSLC measurements. Consequently, these PCB-related artifacts likely contributed to the elevated resistance values observed in FDR measurements compared to EIS.

Initially, in Figures 4.10a and 4.11a, the cell capacity falls from 50 mAh to 47 mAh within the first 22 cycles (from phases P1 to early part of P2), where the C-rate is changed from 0.02 to 1C. With the increase from 0.02C to 1C, there is a 0.05Ω increment in the ESR values. The FDR resistance (Figure 4.10a and Figure 4.11a) initially showed a spike in resistance before point P1 at cycle 2. However, this spike is not consistently present across all samples and may be due to measurement noise, contact resistance, or a faulty cycler channel.

Following these phases, the capacity declines more gradually, until cycle 62, (end of P2) where the C-rate is then increased to 2C. Between 1C and 2C increment, (start of P2 to start of P3), ESR showed a spiked at cycle 27 but remained relatively constant otherwise. During P2, when the cell was being cycled at 1C, FDR resistance initially falls to 0.51Ω and then shows a steady rise in FDR resistance to 0.64 Ω. At point start of P3, when the C-rate is again changed from 1C to 2C, a sharp rise in FDR resistance is observed. This continues up until cycle 100 when the responses begin to fluctuate. The FDR reactance (Figure 4.11b), on the other hand, shows a gradual increase in throughout these phases with a dip at cycle 82.

The degradation phases marked observed between P1 and P2 in Figures 4.10 and 4.11 can be attributed to the increased C-rates. Higher C-rates accelerate the intercalation and de-intercalation of lithium ions, leading to further lithium plating and further growth of the SEI layer [2, 144]. These phenomena contribute to a rise in internal resistance and a decline in capacity [13, 14]. Lithium plating, which occurs more readily at higher charge rates, results in the deposition of metallic lithium on the anode surface instead of intercalating into the graphite structure. This not only reduces the amount of active lithium available for charge storage but also leads to the growth of dendrites [17, 120]. Also, the SEI layer becomes thicker and more resistive at higher C-rates.

Between cycles 63 and 270 (region P3), a gradual change in both capacity and ESR is observed, indicative of normal cyclic aging [14]. During this period, the capacity declines at a slower rate, and the ESR changes by approximately 0.02 Ω. This can be attributed to typical aging mechanisms such as a slower growth of the SEI layer, loss of active lithium, and the gradual increase in internal impedance due to minor structural changes in the electrode materials [13]. FDR resistance fluctuates significantly within this region while the FDR reactance continues to rise steadily. The fluctuations in the FDR resistance can be due to the reduced accuracy in detecting values less than 0.1 Ω [28, 128].

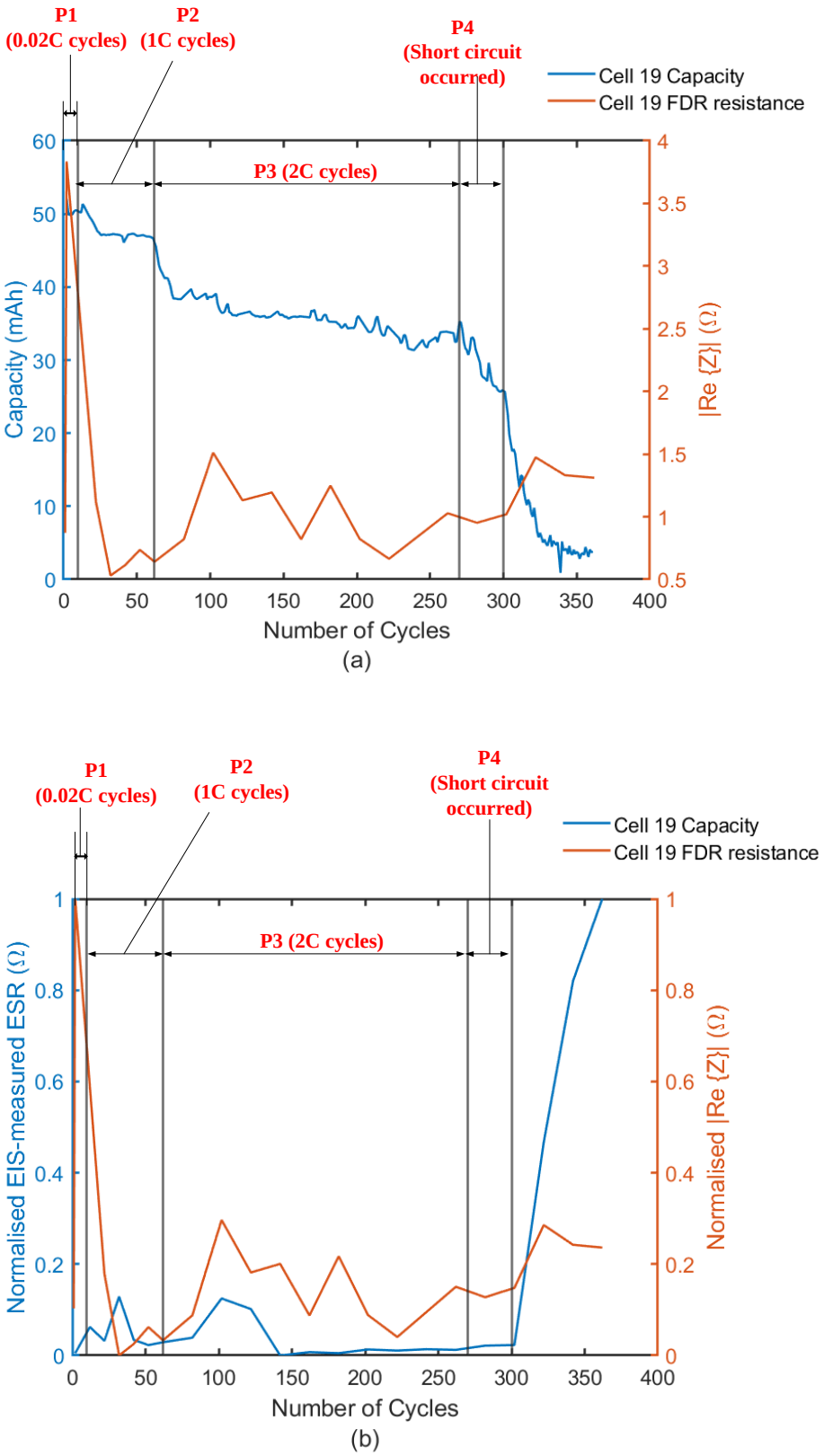

Figure 4.10 Variations in FDR measured resistance of Cell 19 at 300 kHz compared with variations in health indicators. (a) Comparison of FDR measured resistance and cell capacity. (b) Comparison of FDR measured resistance and cell ESR.

Between cycles 270-300, the short-circuit fault occurs (region P4), after which a sharp drop in capacity is observed with a corresponding rise in ESR. The short-circuit causes more significant lithium plating and dendrite formation which can lead to reduced amount of lithium available for intercalation and increasing the impedance due to the damaged electrode structure and thicker SEI layer [2]. Short-circuit faults can also lead to increased cell internal temperature which can cause breakdown of the electrode materials, further increasing the internal resistance [31] and facilitating the decomposition of the electrolyte [41]. The short-circuit effect is more pronounced in the FDR reactance than the resistance.

These processes occur on the surface of the electrodes and at the electrode-electrolyte boundary where high frequency FDR measurements are most sensitive [11, 12]. At high frequencies, lithium ions in the electrolyte struggle to respond quickly to the rapidly alternating electric field, leading to charge accumulation at the electrode-electrolyte interface [12]. Unlike at lower frequencies, where ions have sufficient time to migrate and participate in charge transfer reactions, high-frequency signals change direction so rapidly that ions cannot fully reach the electrode before the field reverses. As a result, an excess of ions builds up within the electrode-electrolyte interface, increasing the impedance measured at these frequencies [166, 167]. In [166], the authors observed that when a high-frequency sine wave current (specifically at 10 kHz and above) is applied, the Faraday current in the electrode is relatively small. This suggests that ions are not able to respond effectively to the rapid changes in the electric field, limiting ionic movement and reaction. Additionally, in [12], the study revealed that at high frequencies, ions concentrate at the surface of the electrode due to a phenomenon known as the skin effect. This skin effect occurs because at high frequencies, the alternating electric field tends to drive current flow near the surface of the conductor, preventing the ions from penetrating deeper into the material. The skin effect is a result of the rapid reversal of the electric field, causing a buildup of charge at the electrode surface rather than allowing the ions to diffuse throughout the bulk of the electrode. A combination of these factors helps explain the correlation between increased ESR and FDR-measured impedance (resistance and reactance). Changes in phenomena such as SEI growth and lithium plating, which influence ESR, also affect the electrode-electrolyte interface and, consequently, FDR measurements.

Also, when lithium plating occurs, the electrode surface changes, leading to a further increase in impedance due to the altered electrochemical dynamics. In [162], a novel, non-destructive detection method for internal lithium plating in lithium-ion batteries was introduced, utilizing high-frequency electromagnetic signals to monitor impedance changes.

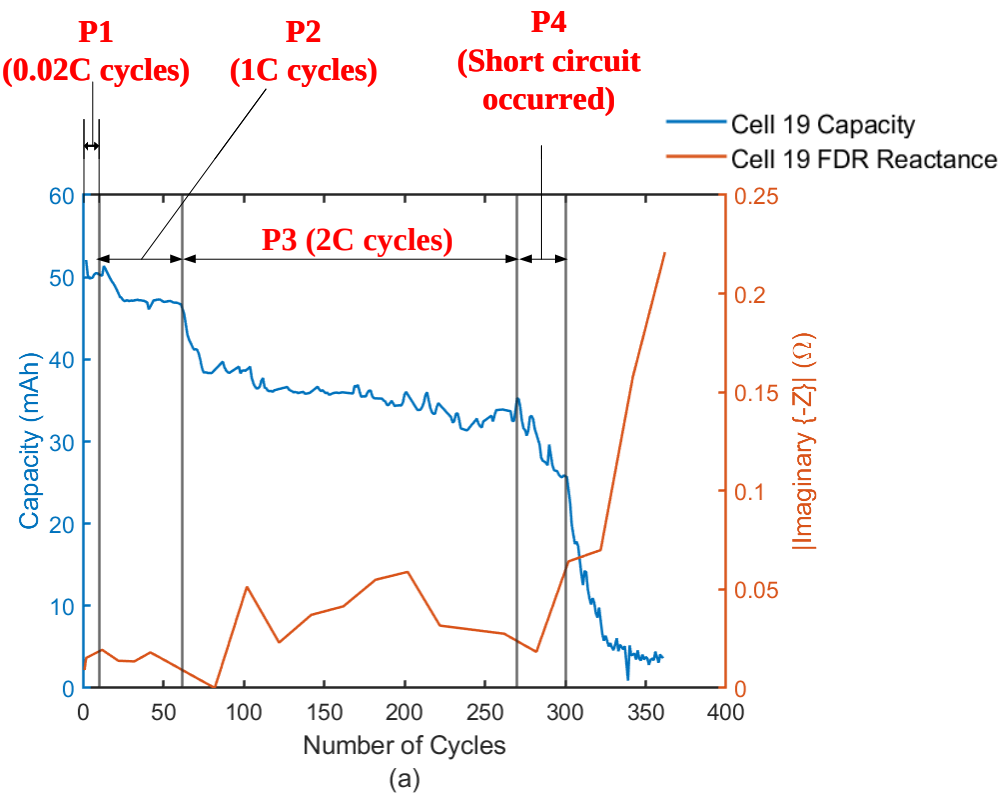

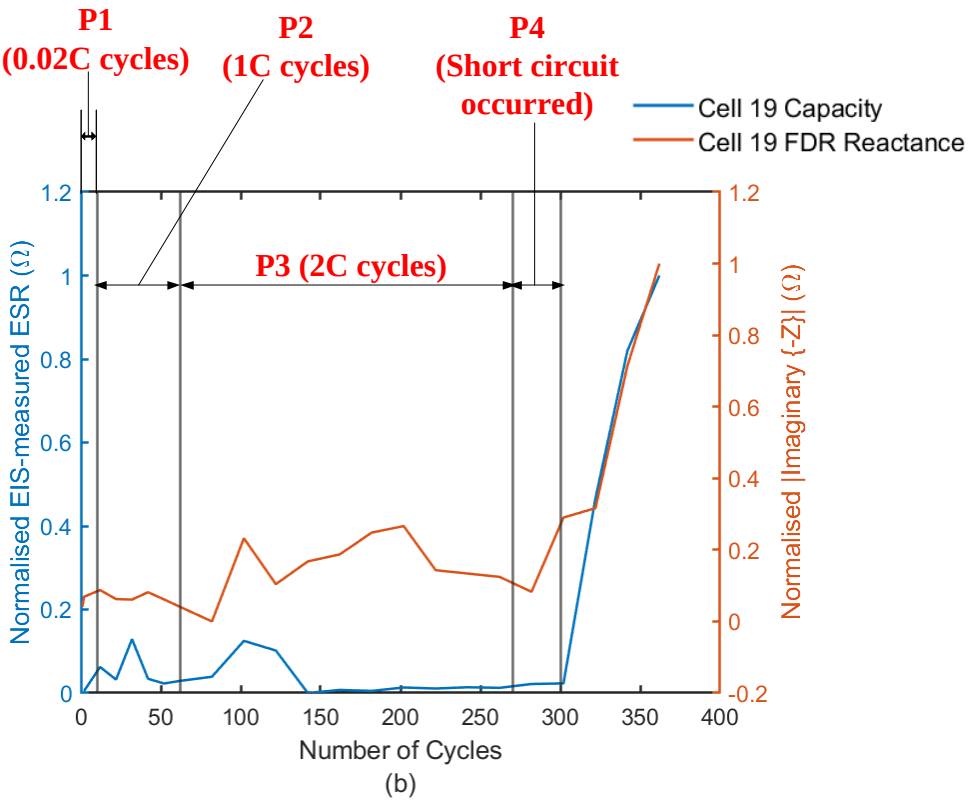

Figure 4.11 Variations in FDR measured reactance of Cell 19 at 300 kHz compared with variations in health indicators. (a) Comparison of FDR measured reactance and cell capacity. (b) Comparison of FDR measured reactance and cell ESR.

Tested under fast-changing conditions, the method was effective in commercial lithium-ion batteries and led to the development of a sensor capable of monitoring cycle-by-cycle growth of Li-metal plating. This further explains why changes in processes affecting the electrode-electrolyte boundary also influence FDR measurements.

During the external short-circuit phase, the battery experiences high discharge currents, which can lead to increased internal temperature and localized heating [17]. This heating can cause electrolyte decomposition and damage to the electrode-electrolyte interface, which may be reflected in FDR measurements [9, 166]. The effect of the short-circuit is more pronounced in FDR reactance than in resistance. This can be attributed to the thermal degradation of the cell components, including potential changes in the dielectric properties of the electrolyte and the damage to the electrode surface. The increased temperature and breakdown of the electrolyte lead to both capacitive and inductive effects, which influence the cell's reactive response and increase the FDR reactance.

So far, the similar behaviour observed amongst the responses of cells from Batch A and B (in Figures 4.8 and 4.9) is evident that the different cyclic regimes do not manifest in significant changes in the shape of FDR responses as that observed in EIS (Figure 3.5). However, within the RoC, at 300 kHz, the FDR impedance appears to have a correlation with the health indicators. Particularly, the FDR reactance is observed to change in a similar way to the ESR. This suggests that reactance is more sensitive to interfacial changes in the battery, such as variations in electrolyte composition and SEI layer growth. In contrast, FDR resistance does not exhibit as strong an alignment with the health indicators. This could be due to the reduced accuracy of resistance measurements in the 5–10 mΩ range, where the expected cell impedance falls, as well as the fact that resistance is influenced by multiple degradation mechanisms, some of which may not directly impact ESR. Additionally, the frequency dependence of impedance may contribute to this difference, as ESR is typically measured at lower frequencies, while FDR operates at much higher frequencies where different physical processes may dominate. While these findings indicate that FDR has promising prospects as a monitoring tool, its application in practical systems may be limited by the range of values and frequencies over which measurement can be achieved accurately and reliably.

4.6.2 FDR as a Tool for Aging Detection Amongst Multiple Cells

To assess FDR's potential in diagnosis aging amongst multiple cells, FDR impedance of the samples at their respective last cycles were compared. The cells SoH at this stage of analysis

are same as that summarised in Table 3.2. The goal was to distinguish between cells at different SoH using FDR-measured impedance. To achieve this, first, the resonance frequencies and the amplitudes of all the sample cells are analysed to confirm the patterns observed in the single-cell analysis are same amongst different cells. Which will provide information and confirmation to assume the same definition of RoC for this stage. Figure 4.12 summarises resonance frequencies and amplitudes of the different cells. The full spectrum impedance plot of the different cells are illustrated in Appendix F.

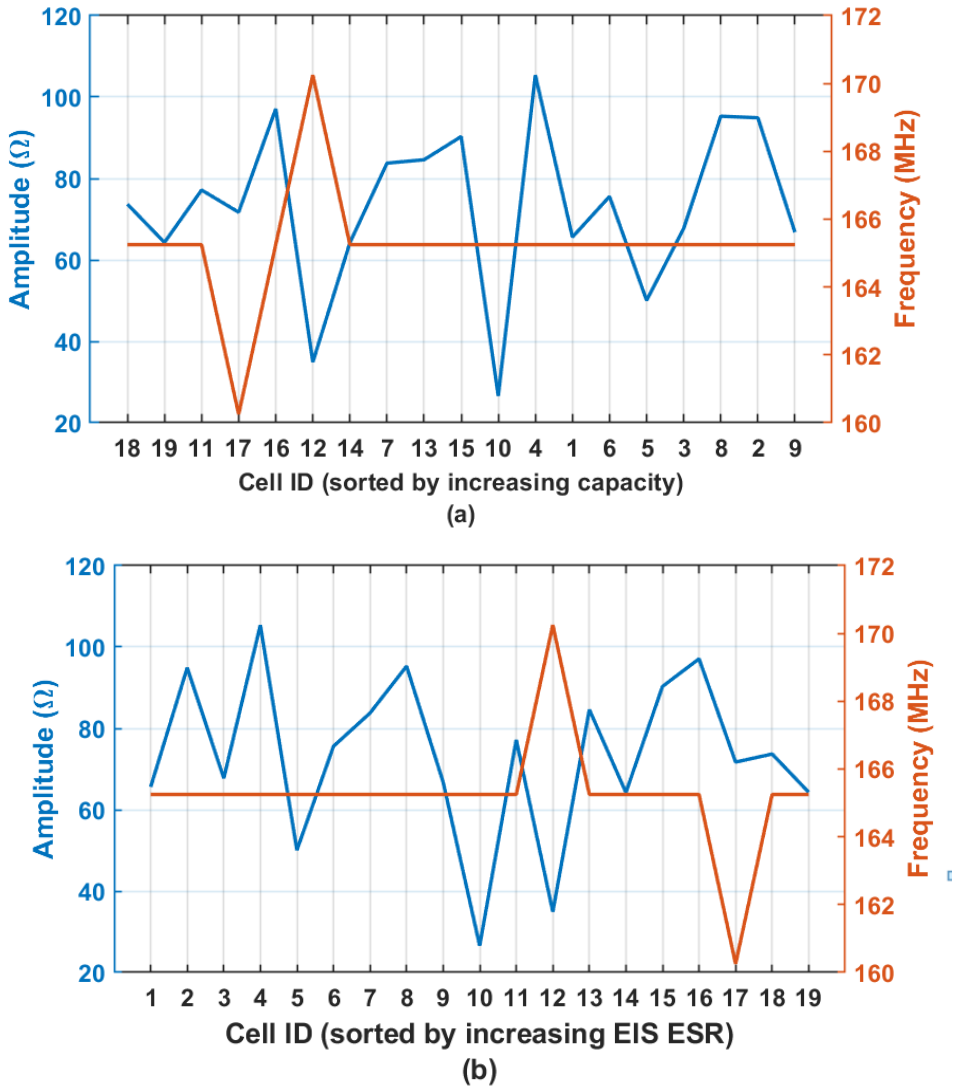

Figure 4.12 FDR impedance resonance frequencies and amplitudes of sample cells at different SoH. (a) FDR impedance resonance amplitude and frequency of different cells of increasing cell capacity. (b) FDR impedance resonance amplitude and frequency of different cell of increasing cell ESR.

In Figure 4.12a, the variations in resonance amplitude and resonance frequency for the sample cells are presented. The cells are arranged in increasing order of capacity, indicated by the cell ID on the x-axis. The amplitude is seen to fluctuate significantly between 27 and 105 Ω. The resonance frequency, however, remains relatively stable around 166 MHz, with cells 12 and 17 being outliers. A similar occurrence is observed in Figure 4.12b, in which the sample cells are sorted in increasing order of ESR values. In both cases, this pattern is similar to the behaviour observed in the resistor responses, seen in Figure 4.7a, which confirms that changes are influenced by the alteration of cell resistive properties. However, these changes are inconsistent with the changes in cell SoH as characterised by the health indicators used this study. This could be due to either a more complex structural changes or occurrence of electrochemical processes outside the range of the FDR frequency that lead to the variations in resonance amplitude. Therefore, resonance amplitude from FDR cannot reliably detect changes in cell impedance that correlates with either capacity or ESR when working with multiple cells.

Having confirmed that the overall impedances responses of the cells at different SoH are similar to passive elements and the single cell profiles, the RoC definition is also applied in this stage. Within the RoC region, Figure 4.13 illustrates the relationship between FDR resistance, cell capacity, and ESR. Figure 4.13a shows how the FDR resistance changes for the cells of different capacities. The cells are sorted in increasing order of capacity. Figure 4.13b shows the variations of the FDR resistance with the increasing order of ESR. In both scenarios, Figures 4.13a and 4.13b demonstrate that FDR resistance doesn't exhibit a clear correlation with cell capacity and ESR respectively. While some cells with higher capacities show lower FDR resistance, the overall trend is scattered, suggesting amongst different cells, FDR resistance is not a strong indicator of capacity.

Capacity fade in lithium-ion cells can result from various factors such as slowed mass transport, increased internal cell temperature, and electrolyte decomposition. However, not all of these factors necessarily cause a resistance change detectable by FDR. In electrochemical impedance spectroscopy (EIS), equivalent series resistance (ESR) is measured at relatively lower frequencies and accounts for the total resistance encountered by ions as they move through the entire cell. FDR, on the other hand, primarily detects resistance changes at the electrode-electrolyte interface.

At the high frequencies used in FDR, ions do not have sufficient time to fully respond to the alternating electric fields. Additionally, the skin effect forces charge carriers to concentrate near the electrode surfaces rather than penetrating deep into the bulk material [151]. As a result, the resistance measured by FDR is dominated by surface and interfacial effects

rather than total bulk resistance. Consequently, resistance changes caused by bulk material degradation or lithium inventory loss which contribute to ESR in EIS may not be as dominant in FDR measurements. Furthermore, as shown in Figure 4.13b, the variations in ESR among different cells are less than 0.1Ω, a range that falls within the least accurate region for FDR resistance measurement. This reduced accuracy, combined with variability among different cells, limits the reliability of FDR resistance as an indicator of state of health (SoH) in heterogeneous samples.

However, FDR reactance exhibits an improved correlation with capacity and ESR, as illustrated in Figures 4.14a and 4.14b. One possible explanation for this correlation is the influence of electrode-electrolyte interfacial processes on FDR measurements. Since FDR operates at high frequencies, ionic movement within the electrode is concentrated within the thin interfacial region due to the skin effect [12]. The limited ability of ions to adjust to the rapidly oscillating electric field further restricts their mobility within the electrolyte, making FDR impedance measurements more sensitive to interfacial phenomena [12].

Aging-related degradation processes such as solid-electrolyte interphase (SEI) growth, electrolyte decomposition, and reaction by-product accumulation significantly impact the electrode-electrolyte interface, influencing both ESR and FDR reactance [14, 17]. SEI growth leads to the formation of an insulating layer on the electrode surface, impeding lithium-ion transport and increasing ESR by introducing additional resistance to charge transfer [2]. This also reduces the effective double-layer capacitance, as SEI limits charge accumulation at the interface[13]. Electrolyte decomposition further degrades the electrode-electrolyte interface by producing by-products that alter the dielectric properties of the electrolyte [21].

$$X_c = \frac{1}{2\pi f C}$$

Where X_c is the capacitive reactance, f is the frequency and C is the capacitance. Since FDR measurements are particularly sensitive to interfacial dielectric variations, these degradation processes significantly impact the measured reactance. As electrolyte decomposition progresses, the dielectric permittivity of the electrolyte decreases [153], leading to a reduction in capacitance which manifests as reduced capacitive reactance at a given frequency based on (4.3). Additionally, electrolyte decomposition contributes to the increase in ESR measured in EIS, further reinforcing the observed correlation between FDR reactance and ESR. The relationship likely arises from both the reduced dielectric permittivity affecting FDR capacitive reactance and the increased resistive losses in the electrolyte contributing to ESR in EIS. contributing to ESR in EIS.

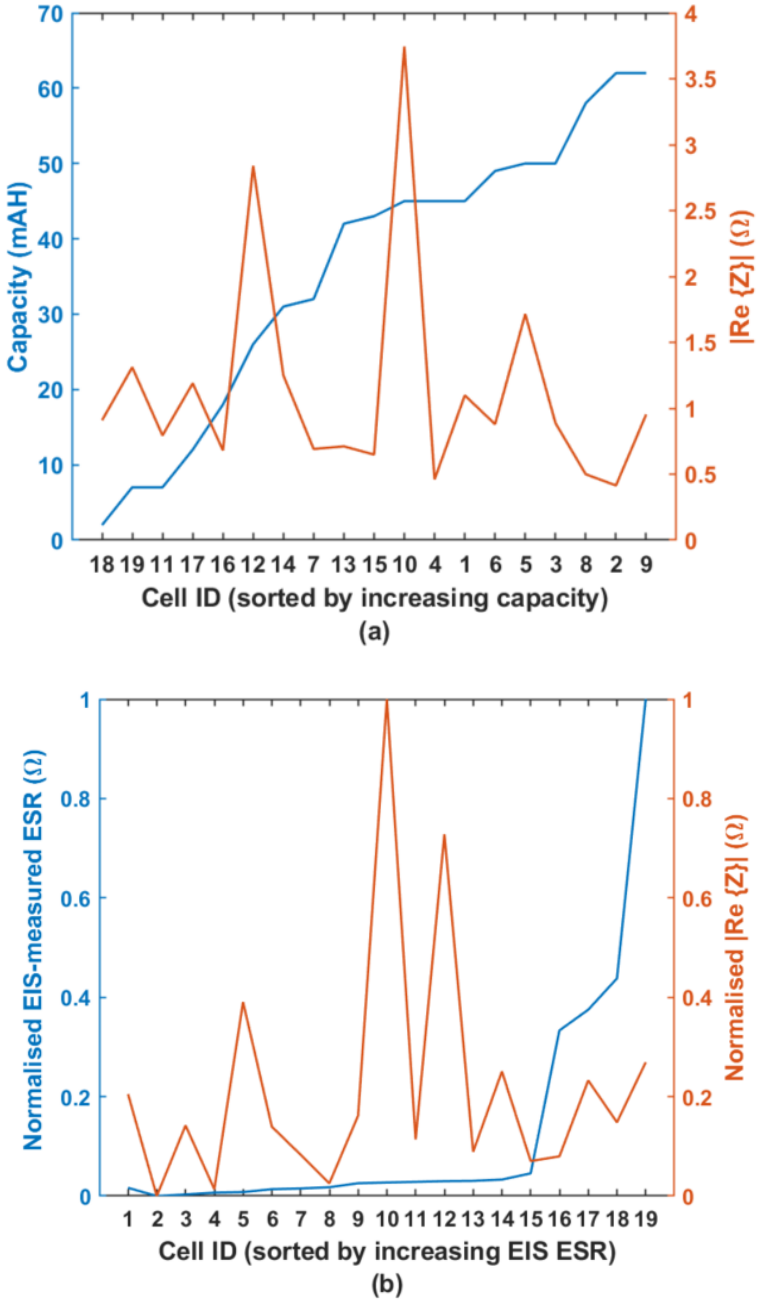

Figure 4.13 FDR resistance of sample cells at different SoH. (a) FDR resistance of different cells with increasing cell capacity. (b) FDR resistance of different cells with increasing cell ESR.

It is acknowledged that FDR reactance values are significantly lower than EIS ESR values, and in practical applications, distinguishing these changes from systematic noise can be challenging. However, while ESR in EIS represents a combination of resistive losses from multiple sources including charge transfer resistance, electrolyte resistance, and SEI resistance FDR reactance is primarily influenced by interfacial dielectric property changes. Studies such as [133] and [9] have applied FDR techniques to capture electrolyte dielectric variations in different media, supporting the idea that FDR is highly sensitive to dielectric changes.

Additionally, [162, 167] demonstrated that high-frequency methods can effectively detect lithium plating and other interfacial phenomena, further supporting the notion that high-frequency impedance measurements are influenced by electrode-electrolyte interfacial properties.

These findings explain the observed correlation between FDR reactance with cell ESR in both homogeneous (single-cell) and heterogeneous (multiple-cell) samples. However, careful attention must still be given to the FDR measurement setup, as limitations in accuracy and range can affect reliability in practical applications.

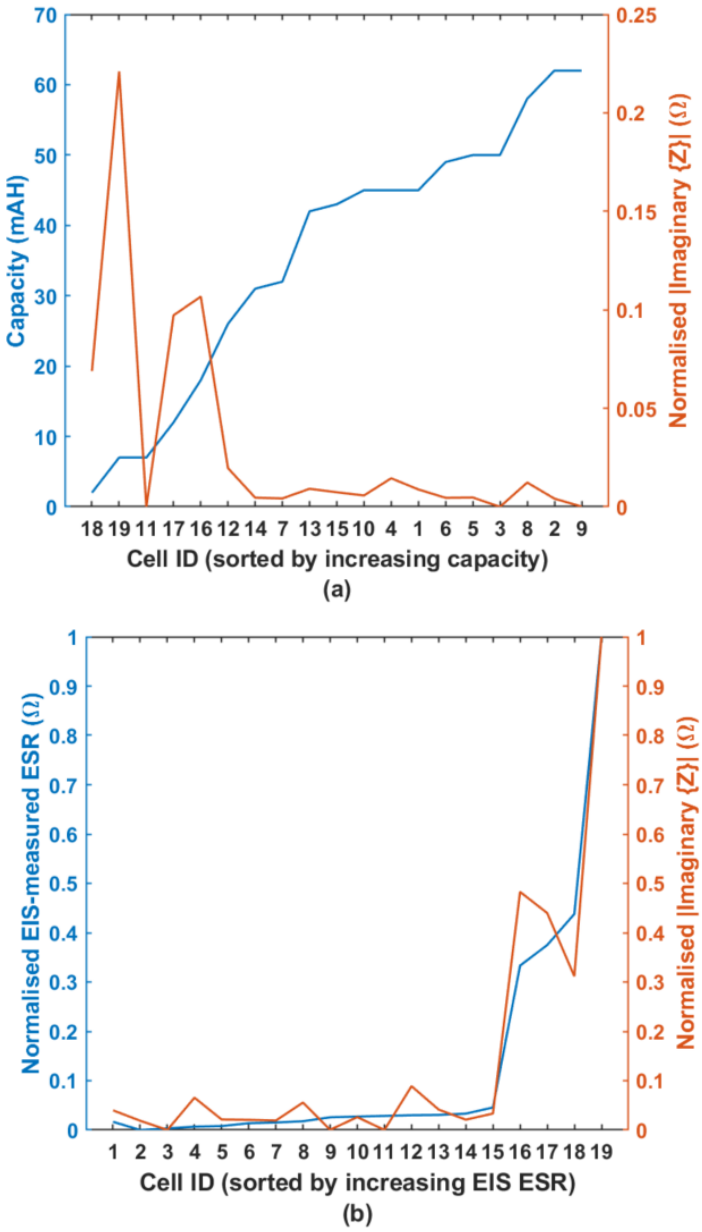

Figure 4.14 FDR reactance of sample cells at different SoH. (a) FDR reactance of different cells with increasing cell capacity. (b) FDR reactance of different cells with increasing cell ESR.

4.7 Summary

This chapter presented an evaluation of FDR as tool for aging diagnosis and detection in li-ion batteries. The setup used was based on the two-port shunt-through network as this made it possible to measure S_{21} parameter, which offers the most accuracy in measuring impedances values less than 1Ω. A connector PCB was designed to interface between the VNA and the batteries. The VNA used was the PicoVNA 106 and the measurements were done with a test signal of 0 dBm between 300 kHz and 1 GHz. The setup was calibrated and de-embedded using the SOLT calibration and OSLC de-embedding methods respectively.

Prior to testing batteries, the setup performance was characterised by tests on different values of resistors, capacitors and inductors. These revealed that based on the element connected, the setup resonated between 170 MHz and 185 MHz. The resonance frequencies within this range changed with the value to the capacitors and inductors whereas the resistors exhibited more changes in resonance amplitude. Also, the tests on these elements, was used to determine a region of confidence where FDR had maximum sensitivity and accuracy. Maximum sensitivity was between 300 kHz and 100 MHz, while maximum accuracy was at 300 kHz. Within this region, FDR pre-OSLC compensation responses had better accuracy than post-OSLC compensation. This was due to the introduction of parasitic inductance and capacitance by elements used in the OSLC compensation stage.

With the setup calibrated and characterised, test on batteries were done in two stages. The first stage was based on single-cell analysis where FDR's applicability to continuous monitoring was evaluated. In this stage, initial test on batteries revealed that the responses of the cells were similar to that of the resistors. Although the changes in resonance amplitude did not correlate with the health indicators, it revealed that the changes detected by FDR was related to changes in cell resistive properties. However, at 300 kHz, both FDR resistance and reactance showed correlation with cell capacity and ESR. Notably, the FDR reactance exhibits similar trend to the ESR.

With C-rates increased from 0.02C to 1C, sample capacity fell from 50 mAh to 47 mAh, ESR increased by 0.05Ω. From 1C to 2C, capacity fell from 47 mAh to 45 mAh, however, ESR remain relatively constant with a few spikes. During these phases, FDR resistance also rose by 0.03 Ω when c-rate was increased from 0.02C to 1C with spike at cycle 22 but remained relatively constant from 1C to 2C. These could be attributed to mechanisms such as lithium plating and SEI layer growth [162, 167]. [162] demonstrated that high-frequency impedance measurements can be used to detect lithium plating and other interfacial phenomena. In this study, changes in FDR resistance were observed with increasing C-rates, which may indicate

interfacial modifications such as lithium plating or SEI growth. However, post-mortem analysis would be required to confirm the presence of lithium plating.

FDR reactance stayed constant during both changes in C-rates. The FDR response to the changes in C-rate is explained by accumulation of ions at the electrode-electrolyte boundary at high frequencies. This influences the FDR measurement. The FDR resistance experience the more instantaneous changes associated with reduced ionic current movement whereas the FDR reactance experiences the more gradual change in the capacitive and inductive changes within the cells. Between cycles 62 to 270, cells' capacity fell gradually by 12 mAh. ESR showed fluctuations between 0.2 Ω and 0.3 Ω. The normal cyclic aging cells is attributed to the gradual change in the parameters. FDR resistance within this phase showed significant fluctuations but increased by 0.6 Ω and the FDR reactance also rose from 0.009 to 0.02 ohms. The increment in FDR reactance points to the increased deterioration of cell capacitive and inductive components such as electrode structure and electrolyte composition that has begun to reflect in the FDR reactance. The short-circuit introduced between cycles 270 and 300 led to 8 mAh drop in capacity. ESR initially remained constant but increased by 0.8Ω in subsequent cycles. FDR resistance increased from 1.03 Ω to 1.4 Ω. FDR reactance increase sharply with the ESR from 0.06 Ω to 0.2 Ω. The short-circuit caused more significant lithium plating and dendrite formation which led to reduced amount of lithium available for intercalation and also led to increased cell internal temperature and localized currents. These mechanisms occur at the electrode-electrolyte boundary which can influence the FDR resistance. Further, short-circuit can result in localized heating within the cell, that facilitates the decomposition of the electrolyte and accelerate the growth of the SEI layer, significantly influencing the capacitive properties of the cell and hence the FDR reactance.

These suggests both FDR resistance and reactance are necessary for accurate characterisation of the cell state. The correlation observed shows promising prospect for FDR's application in continuous SoH monitoring. However, fluctuations and lack of sensitivity to slow occurring mechanisms suggests that FDR needs to be used with other health indicators

The second stage involved, a multi-cell analysis where FDR measurement from different cells with different SoH was evaluated. This was to assess FDR's ability to diagnose cells with different SoH. This revealed FDR's resistance is not a strong predictor of cell capacities in heterogenous samples. This lack of correlation is in contrast to the relatively better correlation observed between FDR resistance and the capacity and ESR of the single cell. This is because in a single-cell, aging-induced resistance changes are consistent over the cell's lifetime. The structural changes, electrolyte decomposition, SEI layer growth all happen

consistently at different cycles/stages within the cells life but ultimately contribute to the overall resistance. However, some of these degradation mechanisms might not manifest in changes in ESR. This is observed in Figure 4.10a, between cycles 182 and 222, when a decrease in capacity did not correspond with an increase in FDR resistance. Hence in the case of multiple cell tests, when a cell's capacity fade is caused by factors that are not detectable by FDR, the method fails to diagnosis it states appropriately.

FDR reactance demonstrates a stronger correlation with ESR and capacity, suggesting that both parameters are influenced by similar interfacial processes. This relationship can be linked to the fundamental aging mechanisms in lithium-ion batteries, where electrolyte decomposition and SEI layer formation progressively alter the electrode–electrolyte interface, impacting both resistive and capacitive characteristics. While ESR in EIS is measured at lower frequencies and reflects a combination of bulk resistance components, FDR operates at significantly higher frequencies, where charge carriers struggle to keep up with rapid field oscillations. This limitation results in charge accumulation at the electrode surface, enhancing interfacial polarization and making FDR reactance particularly sensitive to dielectric and impedance changes at the boundary. As electrolyte breakdown occurs over time, the dielectric constant of the electrolyte decreases, leading to a reduction in capacitance at the interface. Since capacitive reactance is inversely related to capacitance, this reduction causes an increase in reactance at a given frequency. Given that electrolyte degradation is also a key factor in the increase of ESR in EIS, this explains why FDR reactance aligns well with ESR trends.

On the other hand, FDR resistance does not follow the same pattern as ESR, largely because it is also constrained by the limited ion mobility at high frequencies. Unlike ESR in EIS, which accounts for the total bulk resistance encountered by ions across the entire cell, FDR resistance is dominated by localized conduction effects near the interface, making it less representative of overall ionic transport.

The above findings suggest that FDR has promising prospects in battery health diagnosis, particularly in non-invasive probing of interfacial phenomena such as changes in electrolyte dielectrics. However, careful practical designs of FDR must be done to ensure improved sensitivity and accuracy.

Chapter 5

Multivariate Statistical Analysis of Frequency Domain Reflectometry for Battery SoH Monitoring

5.1 Introduction

This chapter presents a statistical analysis of FDR to evaluate its effectiveness in diagnosing battery health, addressing the third research objective of this thesis. The motivation for this analysis arises from the complexity and high dimensionality of the FDR dataset, which consists of impedance measurements across multiple frequency points, requiring statistical techniques to extract further meaningful insights. By systematically applying multivariate statistical methods, this work aims to determine the extent to which FDR can differentiate between healthy and aged cells, track battery degradation, and serve as a predictive tool for SoH estimation.

To achieve this, Principal Component Analysis (PCA), PCA-based Multivariate Statistical Process Control (MSPC), and Partial Least Squares Regression (PLSR) are employed. Each statistical technique was applied to answer a specific question: PCA was used to determine whether FDR impedance data reflects aging patterns; MSPC was tested for its ability to classify aged vs. healthy cells; and PLSR was used to evaluate if FDR can predict battery capacity.

For comparative validation, these statistical techniques are also applied to EIS data from the same set of cells. Since EIS is an established technique in battery diagnostics, this provides a benchmark for evaluating the relative performance of FDR. The use of these statistical methods is justified given the structure of the dataset, where the number of variables (frequency-dependent impedance measurements) significantly exceeds the number of samples. In such cases, traditional analytical methods may not be sufficient, making dimensionality reduction and multivariate modelling essential for extracting useful trends.

By conducting this analysis, this chapter contributes to the broader research by determining whether FDR can provide meaningful diagnostic insights comparable to EIS. The findings will help establish whether FDR is a viable alternative or complementary tool for SoH monitoring.

The PCA was employed to evaluate how FDR responses of the different sample cells vary from each other. Thus, the complex FDR responses (comprising of all four s-parameters) from the sample cells are initially transformed into principal components by the PCA algorithm, that capture the most significant variations in the dataset [111]. When plotted, these components create clusters of points representing a sample cell [111]. When samples with different SoH

form distinct clusters, it indicates that the FDR responses vary with aging and therefore indicate capability to differentiate the samples.

The PCA-based MSPC, was also employed to test FDR's applicability in a binary detection scenario where cells are sorted based on a pre-defined threshold. This is the case where a limit is set, above which a cell is deemed unhealthy for a specific application. In this study, the threshold was set such that cells with 70% capacity were considered healthy and otherwise aged. The threshold limit was statistically determined using the Hoteling's T^2 test and squared prediction error (SPE) based on data from samples in their healthy states (capacity > 70%). The Hoteling's T^2 test compared deviations in the magnitude between responses of cells of different SoH to that of the healthy cells whereas SPE, compared the changes in relationship between healthy and aged cells [111]. Together, these determined if a cell was above or below the set threshold based on both changes in response values and the relationship between response variables.

The PLSR, evaluated FDR's applicability in SoH prediction, by identifying correlations between FDR responses and cell capacity [112]. The regression algorithm is first trained with FDR responses from part of the sample cells and then responses of remaining cells are employed in algorithm validation.

All three statistical methods were also applied to EIS data from the cells. This was to provide a benchmark for comparison. The evaluation metrics included accuracy in associating changes in the impedance responses with changes in capacity or cycling regimes, the ability to differentiate between healthy and aged cells, and the capability of applying FDR data to develop predictive models. These methods were chosen because they are suitable for handling large datasets where the number of variables significantly exceeds the number of samples, which is a characteristic of the dataset used in this study [168]. Additionally, these techniques are well suited for highly correlated datasets; they are relatively easy to implement and offer a good balance of efficiency and simplicity. All statistical evaluations were done in MATLAB, as it offers an RF Toolbox that provides functions to read and analyse the touchstone files from the VNA.

5.2 Implementation of Principal Component Analysis (PCA)

PCA is a technique applied to reduce the dimensionality of measured data while retaining as much data variance as possible [168]. It is particularly suitable for correlated multivariate data such as impedance spectroscopy data [169]. Dimension reduction is achieved by the creation

of new uncorrelated variables known as principal components (PCs) which are a linear combination of the original data variables.

5.2.1 Data Matrix Formation and Standardisation

The first step in PCA implementation is the formation and standardisation of data to be used. In this study, PCA was implemented on both EIS-based impedance and FDR-impedance datasets. In both cases, the dataset used was obtained from the 19 sample cells at different cycles, within their lifetimes. The capacities and ESR values of the sample at various cycles are shown in Figure 5.1a and 5.1b, respectively. Further details of the samples are shown in Appendix D. The aim of using PCA is to first reduce the dimensionality of the FDR-measured impedance and secondly, visualise how the variation in the impedance correlates with aging indicators and, in both instances, how FDR compares with EIS.

A 130 × 142 data matrix was used for the EIS-based PCA. This is the raw EIS data matrix and was made up of 130 impedance measurements from the 19 cells recorded at various stages within their cyclic aging. The 142 variables (columns) were the frequencies at which the EIS-impedance were measured. The potentiostats used, collected 10 points per decade within the 10 mHz to 100kHz frequency range. This produced 71 frequency points for each cell at which the impedance was measured. At each frequency point, the impedance measured is a complex impedance reading; hence, the real and imaginary components are considered as separate variables (columns) to produce 142 variables in the matrix. This is illustrated in Figure 5.2a. The separation of the real and imaginary parts of the impedance helps improve the interpretability of the results because they each represent different attributes of processes occurring at each frequency within the battery. By separating them, the contributions from each component can be better evaluated. In addition, separating the impedance data ensures that PCA treats each column as a separate variable which allows it to better handle the interdependencies and effectively reduce dimensionality.

Figure 5.2 illustrates how the real and imaginary parts of the EIS impedance (Figure 5.2a) and the real and imaginary parts of the FDR impedance converted from S-parameters (Figure 5.2b) are combined to form the raw matrices for their respective datasets. The labels above the plots indicate the regions corresponding to different parts of the impedance spectrum, helping to clarify what each column of the raw matrices represents. The dataset includes impedance measurements from all 19 cells, covering a range of states of health (SoH). Rather than selecting EIS data randomly, this approach ensures that the full range of SoH is captured, allowing PCA to assess whether FDR data reveals consistent patterns linked to health indicators.

The SoH of the samples, characterized by capacity and ESR over their lifespan, is illustrated in Figures 3.3 and 3.6, respectively.

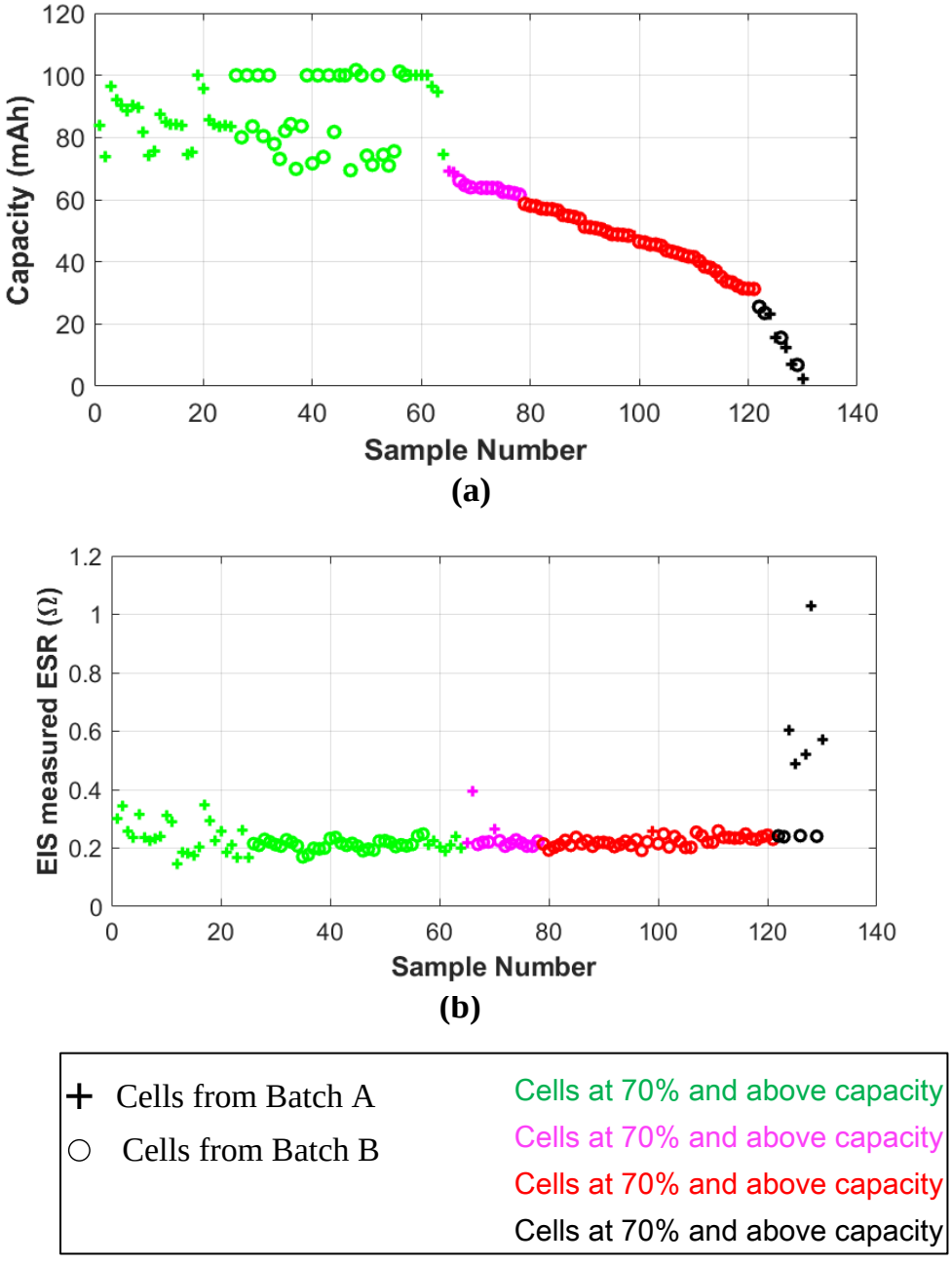

Figure 5.1 Capacity and ESR of samples used in PCA. (a) Sample capacities. (b) Samples ESR values

The FDR-based data matrix used was a 106 ×1608 matrix. This is the raw FDR data matrix and is formed from the FDR-based impedance calculated from measured S-parameters. The VNA measured 57 points per decade and generated 201 frequency points at which S-parameters were measured. At each frequency point, four complex S-parameters were measured (S_{11}, S_{21}, S_{12},

S_{22}) which are the converted using (2.14) and (2.15). Separating each into real and imaginary parts produced 1608 variables. This is illustrated in Figure 5.2b.

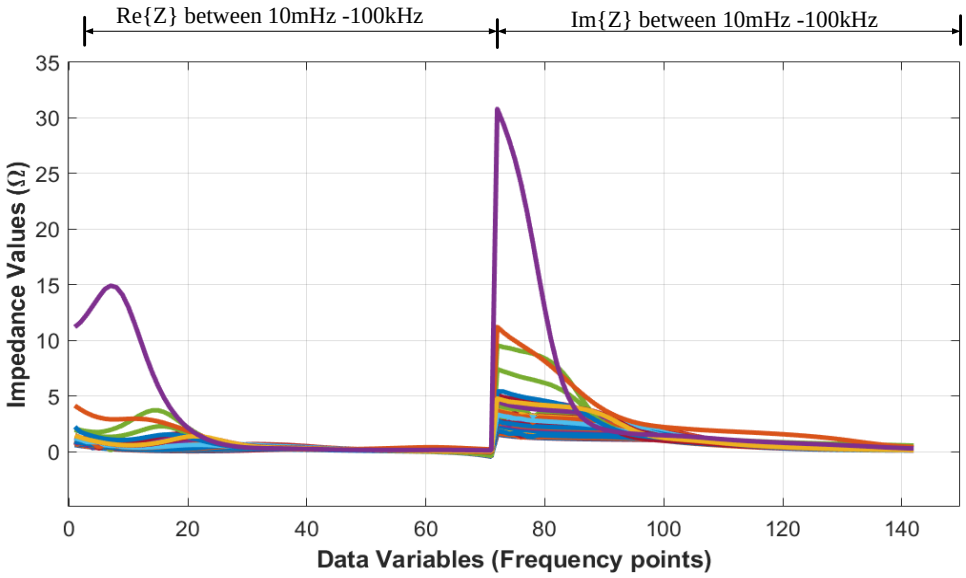

(a)

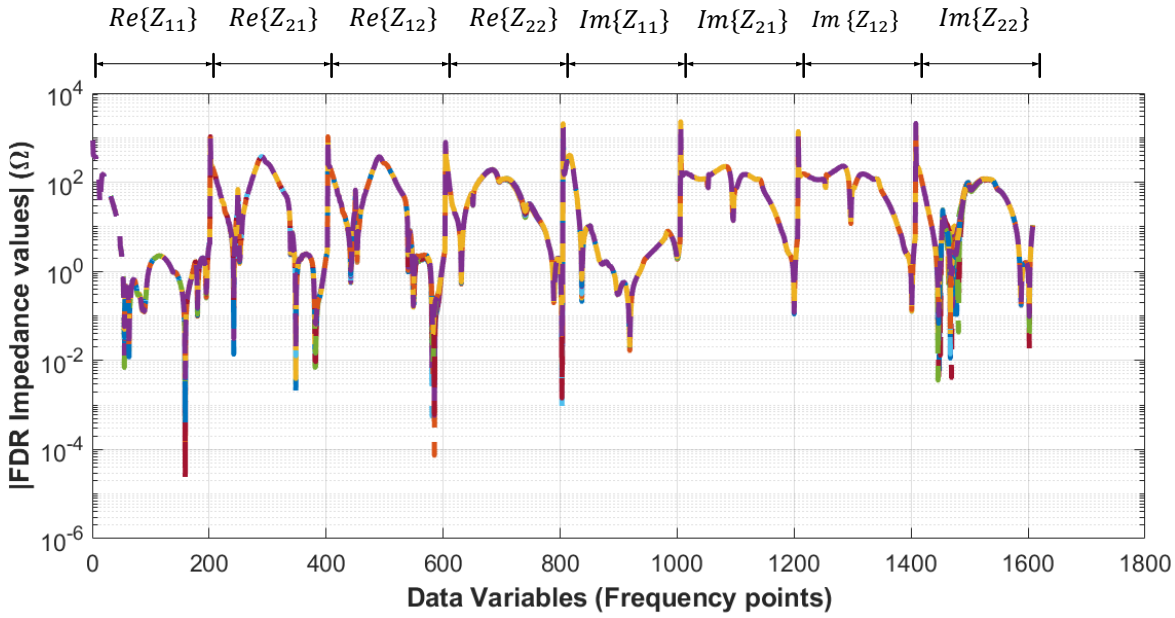

(b)

Figure 5.2 PCA matrix variables from the EIS and FDR datasets. (a) EIS matrix variables. (b) Real and imaginary parts of the FDR-measured impedance that forms the data matrix used in PCA. Each of the indicated impedance subgroups contained 201 measured impedance data points.

It is acknowledged that, the experimental methodology was designed to reflect real-world usage conditions of the cells, including charge-discharge scenarios that induce generic aging, rather

than strictly adhering to a Design of Experiments (DoE) framework for statistical analysis. The primary objective was to evaluate FDR as a diagnostic tool under practical aging conditions, with statistical analysis serving as a complementary assessment alongside analytical evaluations. While the dataset was not structured using a formal DoE approach, it was designed to capture data under representative cyclic aging conditions, allowing for an initial statistical evaluation of FDR. Future studies could incorporate a structured DoE framework to further optimize data collection for statistical modelling while maintaining real-world relevance.

For each test data (i.e. EIS and FDR), having obtained the raw data matrix, X, such that $X \in \mathbb{R}^{m \times n}$ where m is the number of samples or observations (e.g. batteries at different SoH) and n is the data variables (e.g. impedance measured at different frequency points), the matrix is first standardised using (5.1).

$$x_{stand} = \frac{(x - \bar{X})}{S} \tag{5.1}$$

Where x represent each sample, $\bar{X}$ is the data mean, S is the standard deviation and x_{stand} represents the standardised version of the raw data matrix [169]. The raw matrix required standardisation to ensure that each variable has equal weight. Since PCA relies on variances in data, this step ensures that influences of different scales are mitigated to enable PCA identify actual underlying patterns within the dataset [168].

5.2.2 Construction of Principal Components

Secondly, after data standardisation, (5.2) is used to obtain the covariance matrix, X_{cov}. The covariance matrix quantifies the covariance between the variables and is relevant to explore the relationship between the measured impedance responses at different frequencies [168].

$$X_{cov} = \frac{1}{m-1} X^T X \tag{5.2}$$

where X_{cov} is the covariance matrix of standardised matrix, X_{stand}. It is a symmetric $n \times n$ matrix. X^T is the transpose of X. Eigenvector decomposition was then applied to X_{cov}, such that X_{cov} can be expressed as (5.3) [169].

$$X_{cov} = V \Lambda V^T \tag{5.3}$$

where $V \in \mathbb{R}^{n \times n}$ is a unitary matrix, whose columns are the eigenvectors of X_{cov}. $\Lambda \in \mathbb{R}^{n \times n}$ is a diagonal matrix containing the corresponding eigenvalues of X_{cov}. These eigenvalues are sorted in decreasing order such that $(\lambda_1 \geq \lambda_2 \geq \ ... \ \geq \lambda_n \geq 0)$. The eigenvalues are a measure of the

variance in original data captured by their corresponding eigenvectors [168]. The columns of V also represent the newly formed PCs and are sorted in the same order as the eigenvalues in Λ. In each column in V, the elements in the column represent the loadings the PC, which are the coefficients of the linear relation formed between the original data variables.

A transformation matrix or loading matrix $P_{pc} \in \mathbb{R}^{n \times \gamma}$, is obtained by selecting the first γ columns of the V matrix (i.e. the first γ eigenvectors) corresponding to the γ highest eigenvalues in matrix Λ. The transformation matrix P_{pc} is employed to transform the measured data into a reduced dimension space such that the original matrix, $X \in \mathbb{R}^{m \times n}$ becomes $T \in \mathbb{R}^{m \times \gamma}, \gamma < n$ [168]. Equation (5.4) is used to achieve this [112].

$$T = X_{stand} P_{pc} \tag{5.4}$$

where T is known as score matrix which represents the projection of the original standardised data values into the new principal components. The columns of T are the known as PC scores and the elements in the columns correspond to the how much each observation deviates from the mean along the new PCs formed [170]. An observation with higher PC score is more strongly characterised by the pattern captured by that principal component and also indicates that the observation deviates more from the mean along that principal component's direction of maximum variance [170]. The score matrix T, in the reduced space can be transformed back to the original data space by (5.5)

$$\hat{X} = T P_{pc}^T + E = X P_{pc} P_{pc}^T + E \tag{5.5}$$

where $\hat{X}$ is the reconstructed data matrix from the PC subspace. E represents the residual matrix formed by the remaining $n - \gamma$ eigenvalues and eigenvectors and can be expressed as (5.6) [97].

$$E = X - \hat{X} = X(I - P_{pc} P_{pc}^T) \tag{5.6}$$

The chosen PCs explain most of the data variability and $T P_{pc}^T$ contains most of the sources of this variability, whereas the residuals are the unexplained variability mainly associated with process noise. Therefore, the number of chosen PCs (γ), is an important parameter and must be chosen carefully. Methods such as cross-validation, the scree plot method, feature selection, and the cumulative percent variance procedure have been applied [97].

5.2.3 Results and Discussion on EIS-based PCA and FDR-based PCA

Based on (5.1) to (5.6), the code in Appendix D, was developed to implement PCA in MATLAB. Equations (5.2) and (5.3) were then applied to obtain the PCs (i.e. eigenvectors of the standardised matrices). Figure 5.3a and 5.3b show the scree plots for PCA formed on the EIS and FDR datasets, respectively, and the percentage of variances (i.e. eigenvalues) in each dataset captured by each PC. Only the first 20 PCs (out of 130) obtained from each dataset are shown because beyond the 8th PC, the amount of variance captured is relatively negligible. The cumulative variance explained by the PCs is also shown. In both plots, the first PC explained less than 50% of the data variability; therefore, more components were required to capture more variance. Using the scree plot method, the first three PCs were selected for the EIS dataset. This accounted for 88% of the variance in the original dataset. For the FDR dataset, five PCs were selected, accounting for 88% of the data variance. The scree plot method offers a simple and visually intuitive method to identify the "elbow " point where PCs transition from components that explain substantial variance in the dataset to those that contribute minimally [171].

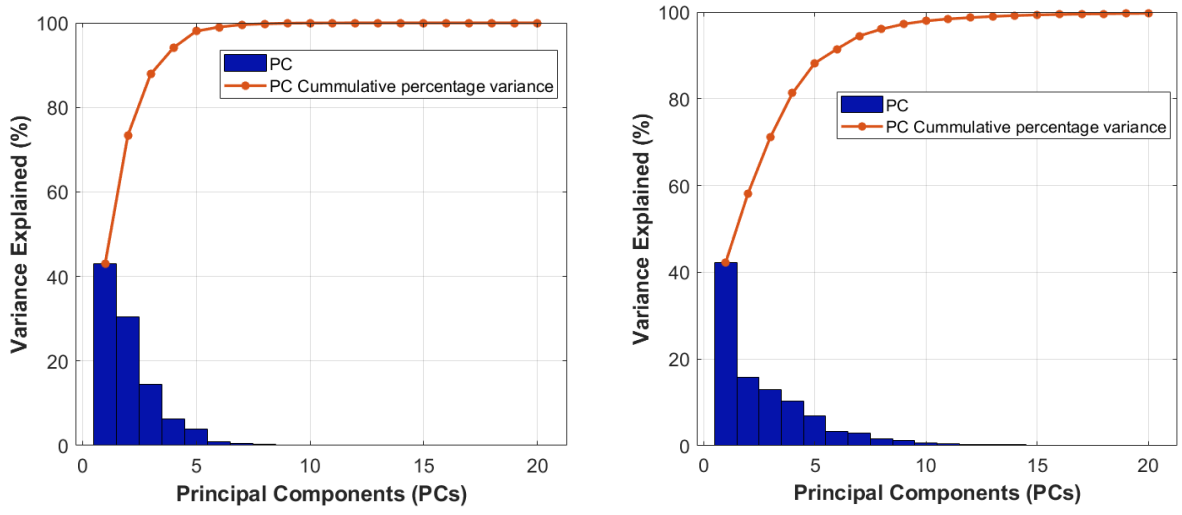

Figure 5.3 PCA Scree plots. (a) Principal components of the EIS data. (b) Principal components of FDR Data.

Therefore, from (5.3), choosing five PCs implies $\gamma = 5$ for the FDR data and choosing three PCs implies $\gamma = 3$ for the EIS data. The need for five PCs to explain 88% of the variability in FDR impedance, while only three PCs explain the same in EIS impedance data, could be due to the high dimensionality of the FDR data (1608 variables) as compared with 142 variables of EIS data. This also suggests that the FDR impedance is more complex and has more correlated relationships than the simpler, lower-dimensional EIS impedance data. This implies that EIS

impedance data would be easier to model and analyse, whereas FDR impedance may require more sophisticated techniques owing to their higher complexity and dimensionality.

The score plots shown in Figure 5.4, is achieved using (5.4). It shows the projections of the scaled and mean-centred impedance values onto the first two PCs. Only the first two PCs are plotted, because it is difficult to show more than a 2D plot. In the EIS score plot shown in Figure 5.4a, the EIS scores were divided into two clusters: E1 and E2. Samples in cluster E1 were from Batch A cells, and those in cluster E2 were from Batch B cells. This highlights the sensitivity of EIS to varying cycling regimes and its impact on cell impedance. Samples in batch A gained stability when initially cycled at 1C [6]. This reduced the electrode stress, slowed the electrolyte decomposition, and improved the SEI layer growth [120]. When high stress was introduced by transitioning to 2C, these samples appear to have retained the foundational stability and therefore have different impedance trajectories from the samples in batch B, which have been consistently exposed to 2C rates. The samples in batch B, which were cycled at a faster rate, experienced rapid degradation processes, such as lithium plating, SEI layer growth, and electrolyte decomposition.

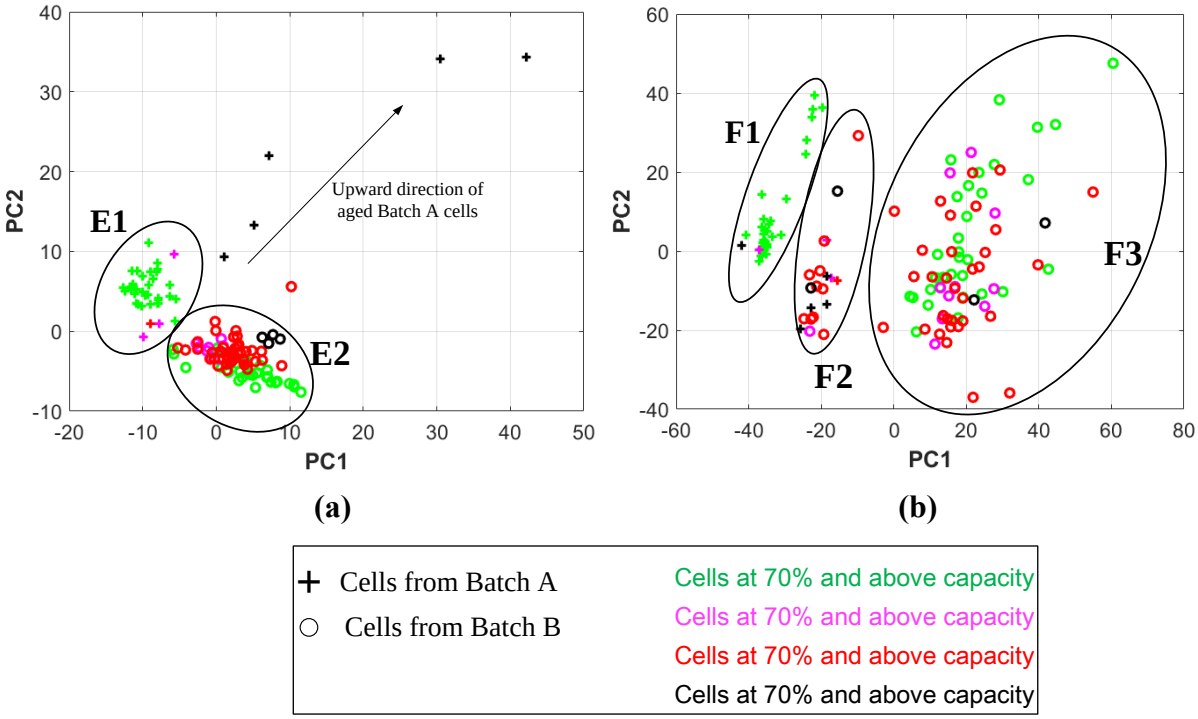

Figure 5.4 Projection of PCA sample scores onto PCs 1 and 2. (a) Projection of EIS sample scores. (b) Projection of FDR sample scores.

In addition, samples in the cluster E2 showed an upward drift with aging. This further shows how the EIS based impedance captures the changes related to the cell SoH. In Figure 5.4b, three

main clusters can be observed. Cluster F1 is mostly composed of batch A samples with capacities equal or greater than 70%. The samples in cluster F2 are from the last cycles of the cells; thus, at the stages listed in Table 3.2, cluster F3 is composed of samples from cells in batch B. The separation of samples into clusters F1 and F3 shows FDR-measured impedance is affected by the different cycling regimes, similar to those observed in the EIS data. The clustering of cells in their last cycles into cluster F2, irrespective of their initial cycling conditions, suggests a common dominant factor, such as the growth of the SEI layer, which influences the accumulated effect of aging at this stage [80]. As high-frequency impedance is influenced by the electrode-electrolyte interface impedance, the increased thickness of the SEI over time is likely to impact the impedance measured regardless of the initial cycling rate [2]. As observed in Table 3.2, at the late stage, the resistance of the SEI layer of all cells increased to values above 1 Ω, while other model parameters showed varying ranges above and below 1 Ω for different cells. This could potentially influence the formation of cluster F2.

The selected PC for each dataset (3 PCs for EIS and 5 PCs for FDR) are not individual variables from the original data matrix but rather linear combinations of all variables. Each PC is a weighted sum of the original variables, where the weight (coefficient) indicates the contribution of each variable to that component [97, 112, 130]. For the EIS dataset, the first three PCs capture most of the variance. Figure 5.5(a) shows that the variables with the highest coefficients in the first PC are primarily within indices 50-70, corresponding to the real part of impedance in the high-frequency range (1kHz - 79kHz). These variables in this frequency range are closely linked to key electrochemical processes, such as ESR and charge transfer resistance [13, 21]. This suggests that the grouping of EIS scores (e.g., separation by C-rates into E1 and E2) is predominantly influenced by variations in these high-frequency impedance values.

For the FDR dataset, the first five PCs are needed to explain the same level of variance, likely due to the dataset's higher dimensionality. Figure 5.5(b) illustrates that the most influential variables in the first PC include the real parts of Z21 and Z12 parameters up to 400MHz and the imaginary part up to 600MHz. Unlike the EIS dataset, the contributing variables in the FDR dataset are more evenly distributed, meaning additional analytical techniques may be required to pinpoint the most dominant contributors. It is also noted that some variables have negative coefficients, meaning they contribute to the observed patterns in the opposite direction compared to those with positive coefficients [112]. However, the variables with the largest coefficients have the strongest influence on grouping and variance explanation [97]. Notably, FDR using 1608 variables can be complex and computationally inefficient, especially with larger sample sizes or when considering a wider frequency range

with more points per decade. To address this issue, different S-parameters can be selected based on the intended application.

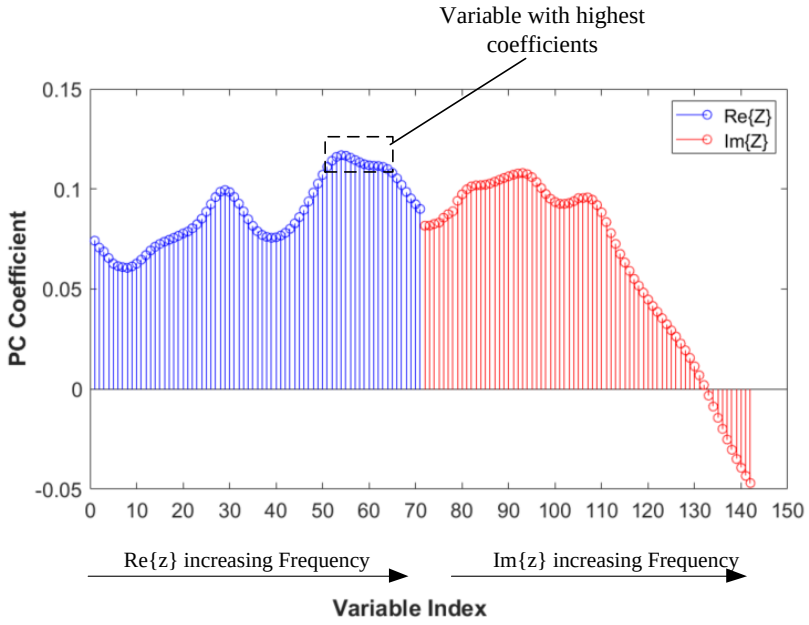

(a)

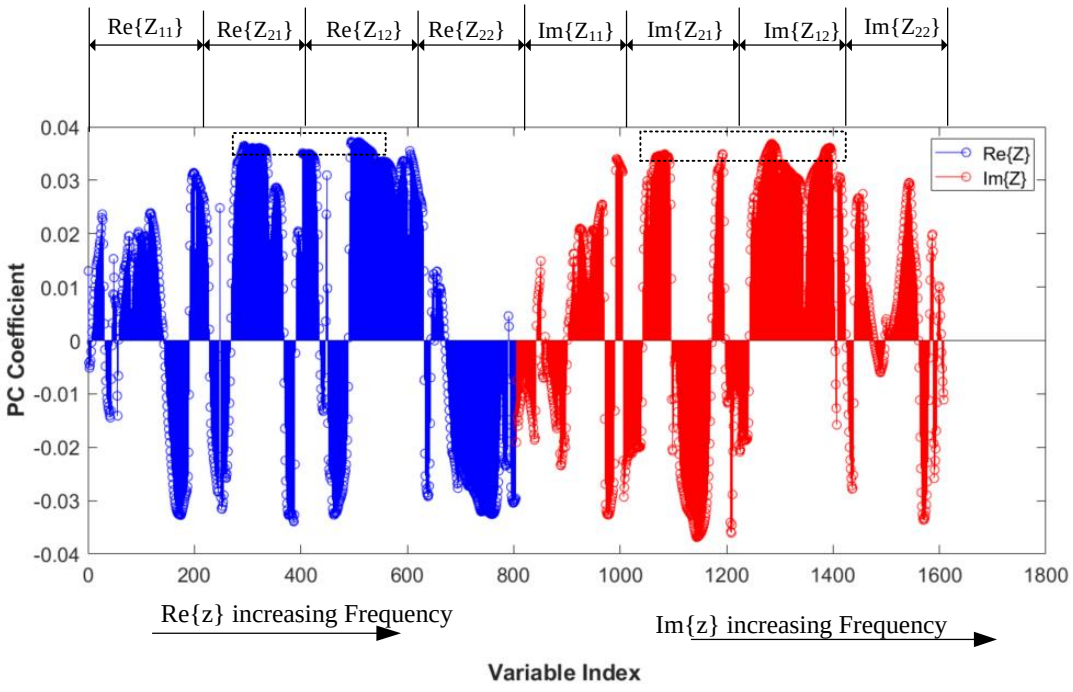

(b)

Figure 5.5 Coefficients of variables in the first PC. (a) Coefficients of variables in the first PC for EIS dataset. (b) Coefficients of variables in the first PC for EIS dataset.

In this study, knowing that the impedance values were mostly less than 1Ω, the FDR variables were limited to include only the S_{21} parameter (therefore Z_{21} variable), which is known to provide better accuracy within this range. Using the real and imaginary components of Z_{21}, the FDR data matrix was reduced to a 130×402 matrix, enhancing computational efficiency without compromising the accuracy of the analysis. Figure 5.6a and 5.6b shows the scree and score plots for the reduced FDR matrix, respectively.

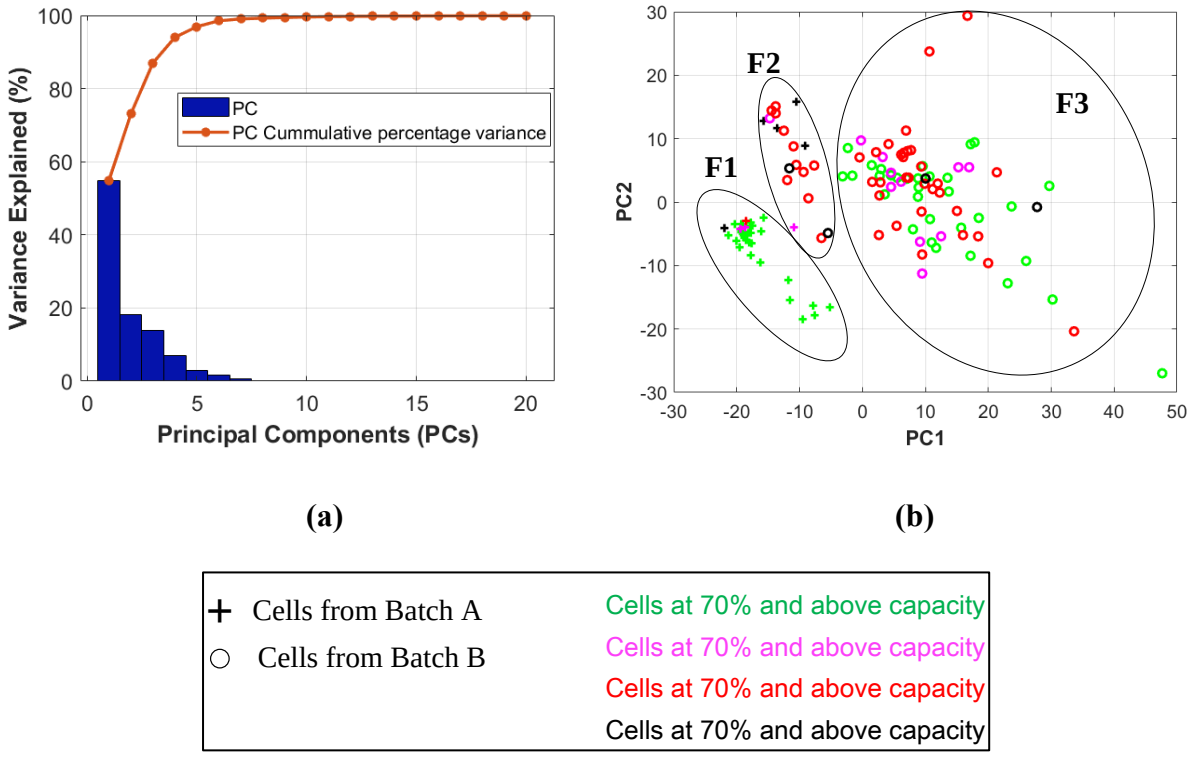

Figure 5.6 PC scree plot and PC scores for data based on FDR Z_{21} variables.

The first three PCs explained 86% of the data variance, whereas the score plot presented clustering similar to that shown in Figure 5.4b. The clustering of samples into cluster F1, F2 and F3 are similar to that obtained with the full set of S-parameters in Figure 5.4b. The similarity of clusters in the score plots suggest that the primary variability in the data is captured effectively by fewer components in the reduced matrix. This indicates that Z_{21}, contains much of the information that influences the clustering observed in Figure 5.4b. This is likely because S_{21} is most sensitive to low ohmic impedance changes.

In terms of pattern recognition, both the FDR and EIS impedances are sensitive to different cycling rates. The EIS data also showed a gradual variation with aging, leading to outwards drift of the aged samples. In contrast, FDR had limited sensitivity to gradual aging, but detected variations in samples at relatively late-stage cycles with at least a 40% loss in capacity and a

5% increase in ESR values. Considering the large and complex nature of the initial FDR matrix, focusing on S_{21} simplifies and streamlines data collection, processing, and model development without sacrificing the accuracy. This reduction in variables can have potential benefits in real-time monitoring and cost reduction, but the sensitivity of FDR as a method requires optimisation.

5.3 Implementation of multivariate statistical process control (MSPC)

Having explored the correlation between changes in FDR-measured impedance and sample SoH, the goal of applying MSPC with FDR data was not to predict the SoH, but to evaluate the performance of the FDR-measured impedance in binary detection applications. Specifically, the aim was to assess whether FDR data could be used to distinguish between cells that are aged or require further analysis and those that do not. In situations where preliminary detection or early-stage diagnostics are necessary to determine whether in-depth analysis is required, threshold-based sorting is typically performed [113]. A predefined limit is set, above which the cell is considered aged or requires further analysis. To assess whether FDR-measured impedance can be applied in these methods and how it performs, PCA-based MSPC with Hotelling's T^2 and SPE statistics is used on both FDR and EIS data. The same set of data used in section 5.2 for PCA implementation is also used here. However, in this method, the datasets are first split into training and validation sets. The training set is considered as a fault-free dataset and consists of cell samples with capacities equal to or greater than 70%, as shown in Figure 5.7. The 70% threshold was chosen because lithium-ion batteries experience a noticeable decline in performance when they degrade to 70-80% of their original capacity [67]. The validation set consists of cell samples with different capacities, shown in Figure 5.7.

5.3.1 Definition of Terms

Monitoring statistics and multivariate control charts are often used in multivariate statistical process control to monitor variations between new measured data and historical fault-free data [172]. Hoteling's T^2 statistic and the squared prediction error (SPE/Q-statistic) are the two popular monitoring statistics used [168, 169]. Hoteling's T^2 statistic represents changes in the PC subspace, indicating the distance between the new sample projected to the PC space and the centre of the nominal PC space. Therefore, a deviation from its control limit implies a systematic shift in the measured cell data [111].

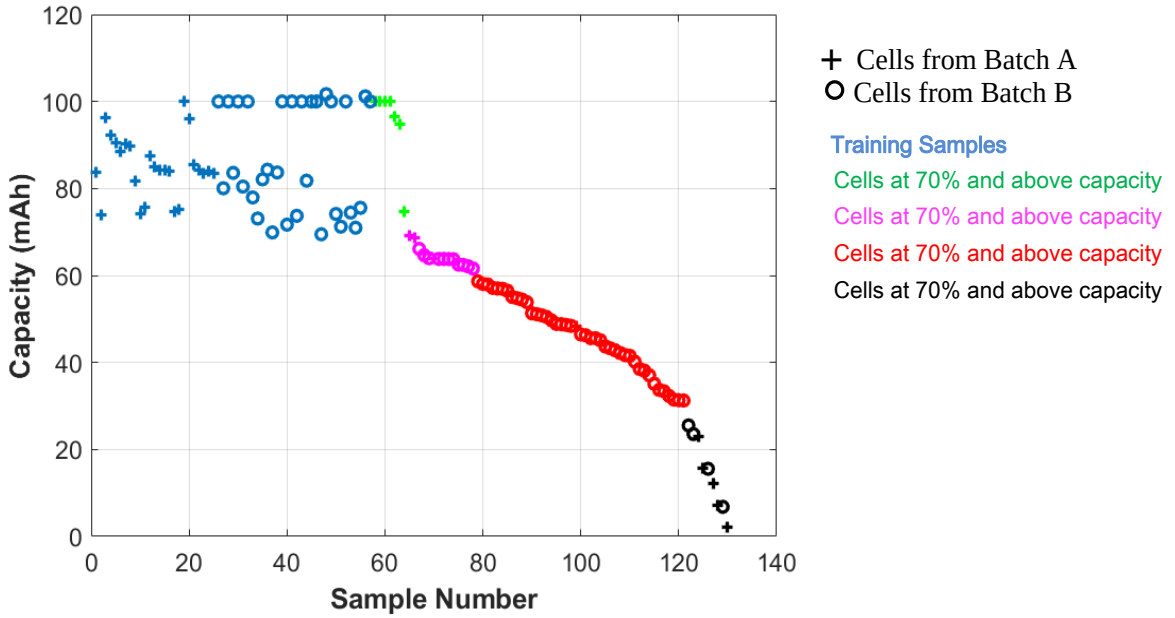

Figure 5.7 Capacity of Training and Validation samples for MSPC implementation

The SPE indicates changes in the residual subspace due to changes in the variable correlation structure and is therefore more indicative of random variations in the measurements [168]. In addition, SPE is a measure of the lack-of-fit of a new sample (cell measurement) to the PCA model. This indicates changes in the correlation relationship between the variables [129]. For a new measured data sample, $z \in \mathbb{R}^{1\times n}$, that is mean-centred and scaled to unit variance using mean and variance from the original dataset, the T^2 statistic is calculated using (5.7) [112].

$$T^2 = zP_{pc}\lambda_{pc}^{-1}P_{pc}^{T}z^{T}. \tag{5.7}$$

This is also known as the Mahalanobis distance of z from the centre of the normal data in the reduced PCA space, where λ_{PC} is the diagonal matrix formed by the first γ largest eigenvalues of X_{cov}. Using the assumption of normality, the T^2 upper control limit is calculated using (5.8) [112, 129] on the basis of its relation to an F-distribution. For a given significance level, α, the new measured data, z, is considered fault-free (normal) if

$$T_{(z)}^2 \leq T_{th}^2 = \frac{\gamma(m^2-1)}{m(m-\gamma)}F_\alpha(\gamma, m-\gamma) \tag{5.8}$$

where $T_{(z)}^2$ is the T^2 statistic for the new measurement, T_{th}^2 is the upper control limit or threshold calculated based on the fault-free data and $F_\alpha(\gamma, m-\gamma)$ is the critical value of the F-distribution with γ and $m-\gamma$ degrees of freedom and a significant level of α. In practice, 99% (α =0.01) or

95% (α =0.05) control limits are usually used [97]. The SPE statistic for the new sample, z, is the residual and is obtained using (5.9) [168].

$$SPE(z) = z(I - P_{pc}P_{pc}^{T})z^{T}. \tag{5.9}$$

This can be written as a decomposition of variable contributions using (5.10) [97].

$$SPE_{(z)} = \sum_{i=1}^{n}(x_i - \hat{x}_i)^2 \tag{5.10}$$

The upper control limit for SPE, for α significance level, is calculated using (5.11) such that a new measured data z is normal if $SPE_{(Z)} \leq SPE_{\text{th}}$, with SPE_{th} given by

$$SPE_{th} = \theta_1 \left[\frac{c_\alpha \sqrt{2\theta_2 h_0^2}}{\theta_1} + \frac{\theta_2 h_0 (h_0 - 1)}{\theta_1^2} + 1 \right]^{\frac{1}{h_0}} \tag{5.11}$$

where SPE_{th} is the SPE control limit and c_α is the normal variate with the same sign as h_0. The remaining quantities are defined as follows.

$$\theta_i = \sum_{j=\gamma+1}^{m} \lambda_j^i \tag{5.12}$$

$$h_0 = 1 - \frac{2\theta_1\theta_3}{3\theta_2^2}. \tag{5.13}$$

When a change in the data is caused by a significant deviation of one or more values of the variables while maintaining the underlying relationship between all variables, a corresponding translation in the scores plane will result. This produces an increase in T^2 values while the SPE values remain below the threshold. Conversely, the SPE will increase if the change is due to a new event not handled in the reference data, which alters the relationship between measured variables, thus changing the covariance matrix. By analysing the contribution of each variable to T^2 and SPE statistics, the variables most affected by the fault can be identified. In (5.10), $(x_i - \hat{x}_i)^2$ determines the contribution of the *i*-th variable to the SPE.

5.3.2 Results and Discussion on EIS-based MSPC and FDR-based MSPC

The threshold limits were set using Hotelling's T^2 and SPE (Q-test) statistics, and their respective control charts were used to visualise the performance of FDR and EIS with the validation set. These methods were selected because they are simple and efficient for handling datasets with a large number of variables. While the T^2-test detects shifts in the mean vector by identifying the variation within the principal components, the Q-test (SPE) measures the

variation in the residuals [128]. The Q-test identifies deviations in the data structure that are not explained by principal components. This dual test allows for the assessment of both the magnitude and structure of data, making their combined use effective for monitoring complex datasets. Appendix D contains the MATLAB algorithm based on (5.7) - (5.13) used to implement MSPC.

The EIS training data matrix was 57 × 142 and the FDR was 57 × 402. The validation datasets used were 73 × 142 and 73 × 402 for the EIS and FDR datasets, respectively. The FDR dataset was limited to Z_{21} variable based on the findings of the PCA method. Appendix D shows the similar results obtained with the entire 1608 variables which confirms using the Z_{21}, is computationally efficient. PCA is firstly applied to the standardised training matrix of both tests, to reduce dimensionality using (5.1) to (5.3). Figure 5.8a and 5.8b show the PCs and how much variance in training data each captures for EIS and FDR data respectively. Using the scree plot method, the first three PCs are chosen for the EIS datasets ($\gamma = 2$) and the first two PCs are chosen for the FDR data ($\gamma = 3$). These captured 90% and 91% of the variance in the EIS and FDR training sets respectively. T^2 values for the reduced PC space are determined using (5.7) where z is the training matrix, P_{pc} is the PCA transformational matrix and λ_{PC} is the diagonal matrix formed by the chosen γ. SPE values are determined for the residual subspace using (5.9). Equations (5.8) and (5.11-5.13) are used to calculate the T^2 and SPE limits respectively.

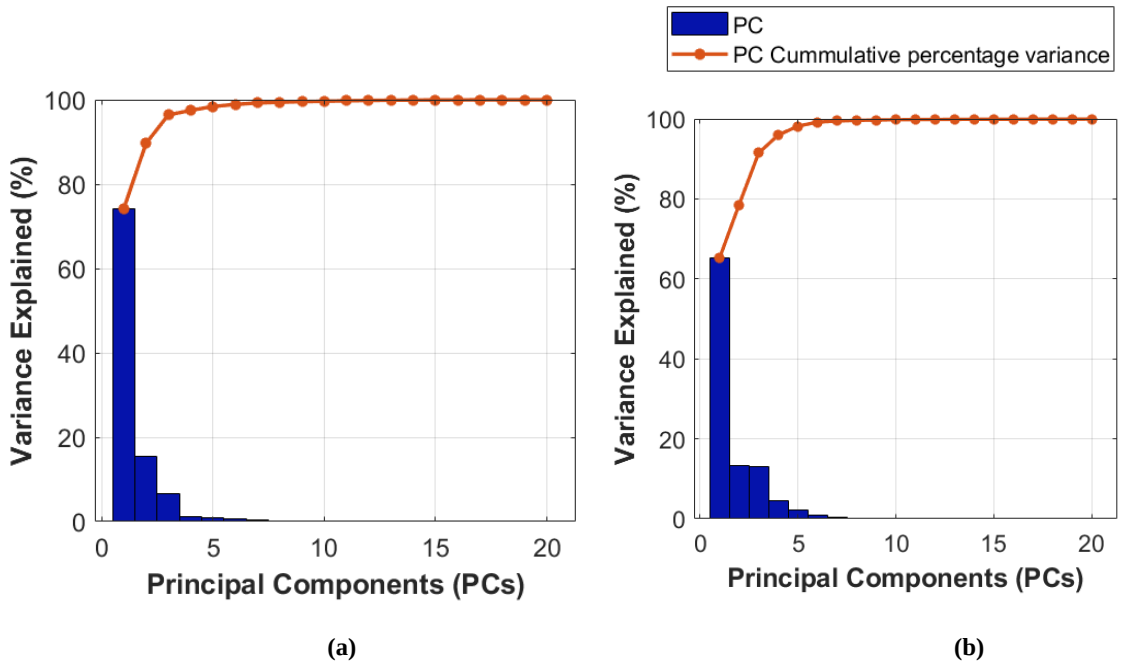

Figure 5.8 Principal Components of Training data. (a) PCs of EIS training data. (b) PCs of FDR training data.

These are the statistical control limit above which impedance data from a sample has deviated from both PC and residual subspaces and is deemed faulty. A significance level of α=0.05 was used, assuming a 5% chance of false detection. This level strikes a practical balance between being overly lenient and excessively stringent [173]. The T^2 limit was determined using critical value, $F_\alpha(\gamma, m-\gamma) = 2.54$ which is obtained from F-distribution with $\gamma = 3$ and $m - \gamma = 54$ degrees of freedom, where m is the number of samples. Figure 5.9 shows the score projection onto the first 2 PCs for each data set. Both EIS and FDR cluster scores according to the cycling regimes similar to Figure 5.4. This suggests that the different degradation processes caused in each cycling regime is reflected in the variations in the impedance measured by both EIS and FDR. Compared to Figure 5.4, FDR performed better (i.e. required three PCs instead of five), when the sample types are streamlined confirming it sensitivity to C-rate.

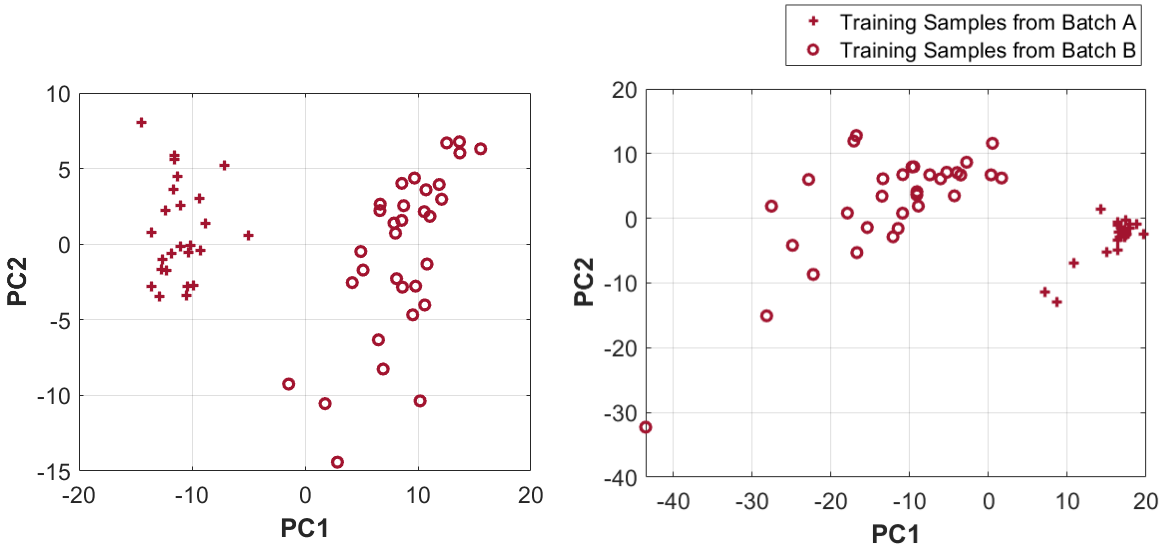

Figure 5.9 Score projections on the first two PCs. (a) EIS score projections. (b) FDR score projections.

The SPE control limits for FDR and EIS are calculated using (5.11) – (5.13). For FDR, h_0 = 0.1523 and the normal variate, $c_\alpha = 1.645$. This value was obtained from normal distribution table with a mean of zero and standard deviation of one, $N(0,1)$, as the standardised data was achieved using these criteria. θ_1, θ_2 and θ_3 were calculated to be 34.26, 425.15 and 6.7×10^3 respectively. For EIS, h_0 = 0.0734 and the normal variate, $c_\alpha = 1.645$. θ_1, θ_2 and θ_3 were 14.67, 96.78 and 887.15 respectively.

The validation samples are transformed using the transformation matrices, P_{pc}. The T^2 and SPE values for each sample were calculated and compared with the threshold limit. This is

illustrated in Figures 5.9 and 5.10. In Figure 5.10, the T^2 control charts for EIS and FDR show that both methods exhibit similar overall performance, with majority of samples falling below the T^2 limit. This suggests that the impedance of these samples has minimal deviation from the mean vector of healthy cells. However, EIS demonstrated relatively better detection capability by accurately identifying 15 out of 73 sample cells with deviations, compared to only 4 detected by FDR. This disparity in performance could be attributed to the higher sensitivity particularly at lower frequencies where slow electrochemical changes and variations in impedance spectra are typically measured. In Figure 5.11, the SPE control charts indicate that both EIS and FDR accurately identified all samples with capacity above 70%, similar performance to T^2 test. Table 5.1 summarises the performance of both FDR and EIS. This reduction in diagnostic accuracy in the mid-range capacity levels suggests that in both EIS and FDR, moderate levels of battery degradation do not manifest as significantly different from the fault-free samples, in the PC subspace. EIS however, showed improved performance for samples with capacities below 30%. Comparing results from T^2 and SPE control charts, it is observed that binary detection based solely on impedance using FDR might not be ideal due to limited sensitivity and complexity of aging across different cells.

Table 5.1 EIS and FDR accuracy in detecting cells at different capacities using T^2 and SPE test statistics.

	Hotelling T^2 test		**SPE Test**	
Sample Capacity	**EIS**	**FDR**	**EIS**	**FDR**
Above 70%	100%	100%	100%	100%
69%-60%	21.4%	0%	42.8%	14.3%
59%-30%	25%	14%	46.5%	32.5%
Below 30%	89.9%	11%	100%	77.8%

5.4 Implementation of Partial Least Squares Regression

The third statistical evaluation was done to assess how FDR data performs as a predictive model. Partial least squares regression was used to build a predictive model by finding the relationship between FDR measured impedance and cell capacity. It was chosen because of its ability to handle large, correlated datasets, particularly, when the number of variables significantly exceeds the number of samples [172]. While traditional multiple linear regression risk over-fitting of models when applied to datasets with large number of variables, the PLSR avoids this by extracting the relevant latent factors that explain the variance of the response variable [168].

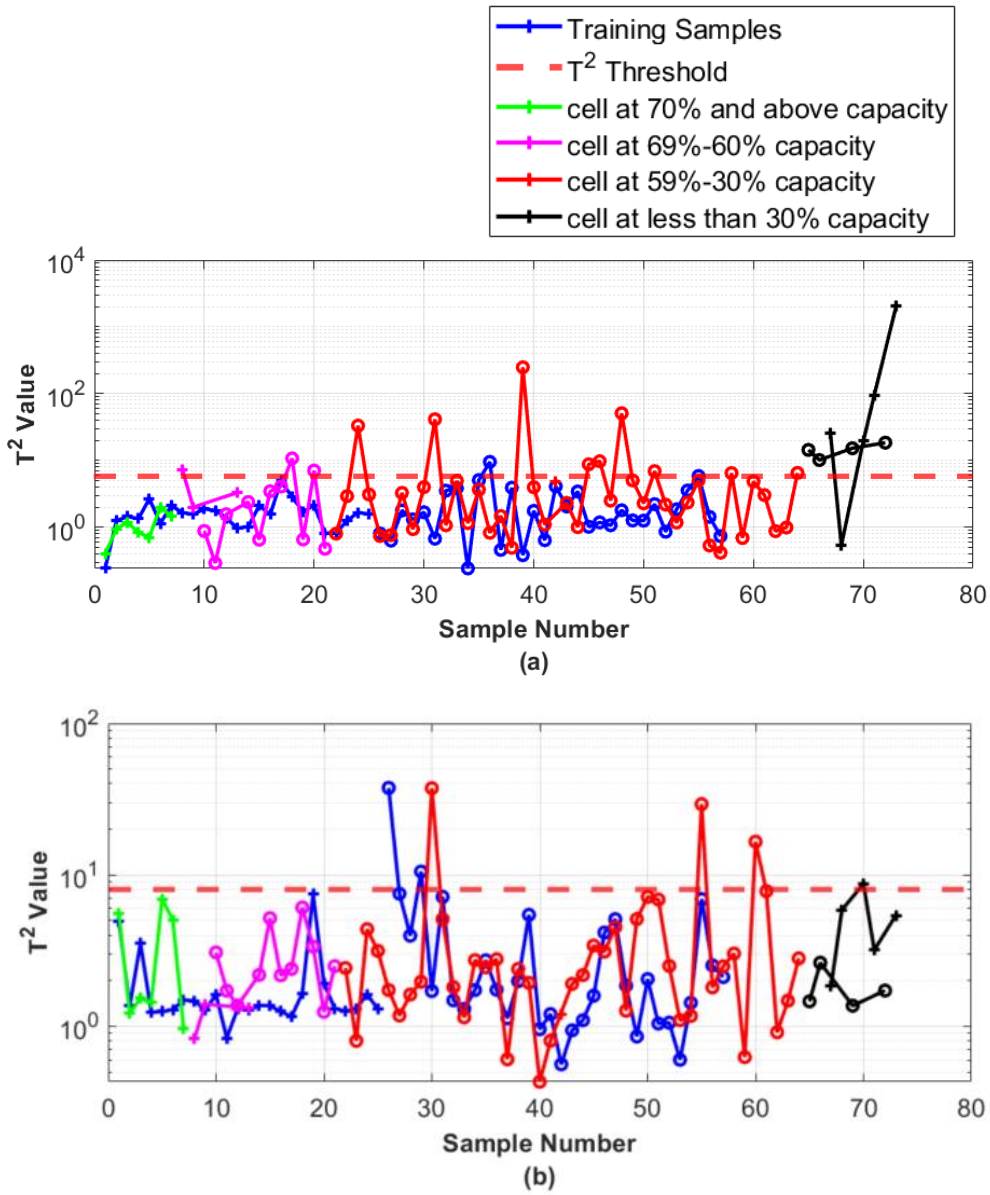

Figure 5.10 T^2 control chart. (a) EIS T^2 control chart. (b) FDR T^2 control chart.

5.4.1 Definition of Terms

To implement PLSR, the available data is typically split into the training set for model construction and the validation set for model testing. Given a training dataset with a predictor (input) matrix $X \in \mathbb{R}^{m \times n}$, and response (output) matrix $Y \in \mathbb{R}^{m \times p}$, both are standardised to obtain $Xstandard,$ and $Ystandard$ respectively, using (5.1), where m is the number of observations, n is the number of features/variables in the predictor matrix and p is the number of response variables. The predictor and response matrices are decomposed into scores and loadings by (5.14) and (5.15) [112, 168];

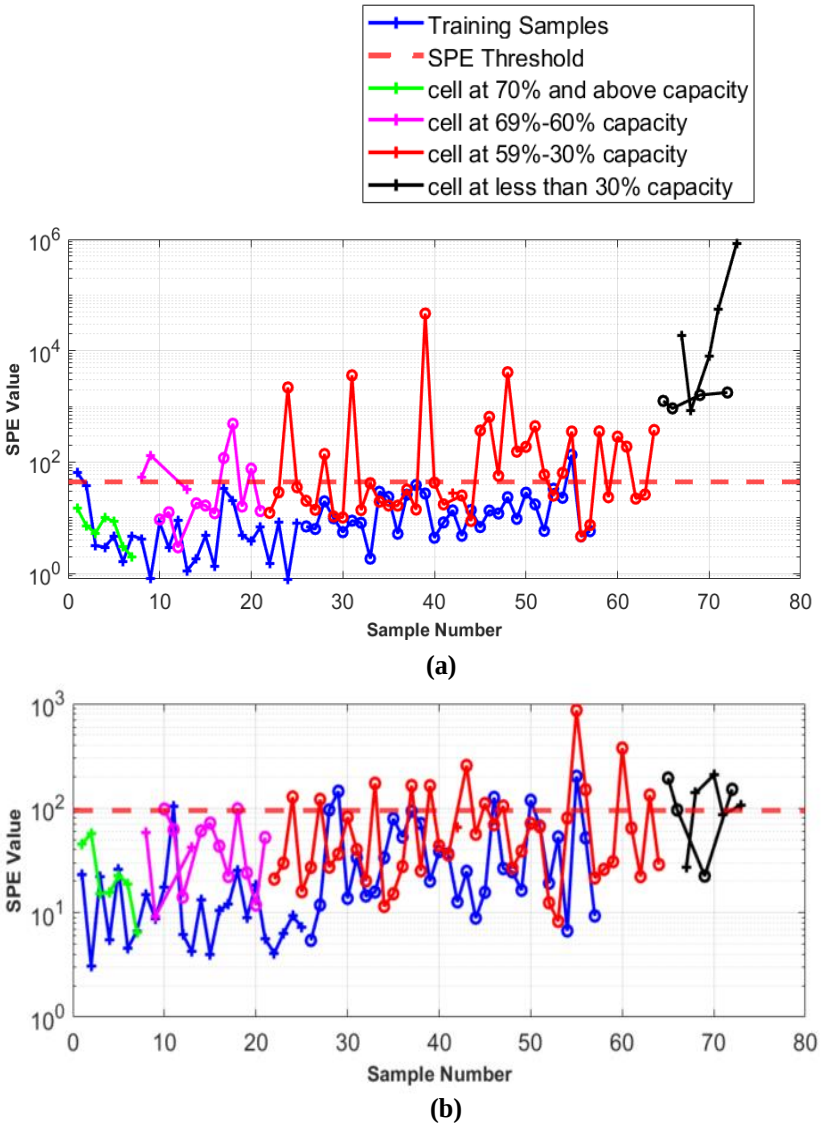

Figure 5.11 SPE control charts. (a) SPE control chart for EIS data. (b) SPE control chart with FDR data.

$$Xstandardised = TP^T + E \tag{5.14}$$

$$Ystandardised = UQ^T + F \tag{5.15}$$

Where T, P and E are the scores, loadings and residuals of the predictor matrix respectively, and U, Q and F are the same for the response matrix. The columns in T and U are known as the latent variables (LV) and are a linear combination of the variables in X and Y respectively [112]. Unlike in PCA where the PCs are found by single calculation of eigen decomposition, the LVs in PLSR are determined by performing algorithms such singular value decomposition (SVD) or eigen decomposition iteratively to ensure maximum covariance between X and Y variables [112]. These are outlined in Appendix B.

5.4.2 Results and Discussion on EIS-based PLSR and FDR-based PLSR

Similar to MSPC, the data was split into training half and validation half. However, in this case, the training and validation portions comprised of data from entire lifetime of selected cells. To ensure accurate capacity prediction based on measured impedance (both EIS and FDR), the model is trained using impedance data spanning the lifespan range (new state to aged state). This approach captures the full degradation trend, as the relationship between impedance and capacity evolves at different stages of battery aging. Training on the complete SoH range allows the model to generalize across various degradation phases, ensuring it remains effective even at lower SoH levels. Limiting the training data to only the 100%-70% SoH range may improve short-term accuracy for practical applications but risks biasing the model toward early-stage degradation patterns and failing to generalize at later stages.

This therefore implies, training was performed on impedance response from selected cells using the impedance data from new state to aged state of these cells. The obtained model was tested on the remaining cells. This is different from the healthy and unhealthy sets used in MSPC stage. Data from cells 5, 8, 12,14 and 17 were used for validation and the remaining cells were used in training. These were chosen arbitrary to represent a quarter of the samples at different capacities. As done in the MSPC test, only Z_{21} was used as FDR predictor variables.

The training predictor matrix for FDR was 134×402 and that of EIS was 134×142. Details of 134 samples are summarised in Appendix D. The response matrix is the same for EIS and FDR and is made up of the capacities of the samples measured at the corresponding cycles at which the FDR and EIS impedances were measured. It is a 134 ×1 matrix.

Figure 5.12a shows the scree plot of the PLSR performed on the EIS data. This illustrates the amount of variance in the response matrix (variance in cell capacities), captured by the predictors (measured impedances at different frequencies). Unlike the PCA, the LVs in PLSR are sorted according to the predictive power and not by the percentage variance captured [171]. Therefore cross-validation method is used to determine the optimal number of components to use for the model. This method estimates the model's mean squared prediction error (MSPE) based on the number of LVs and helps to avoid model overfitting [171]. It is also simple and can be easily implement in MATLAB. The EIS cross-validation MSPE for each number of components selected is illustrated in Figure 5.12b.

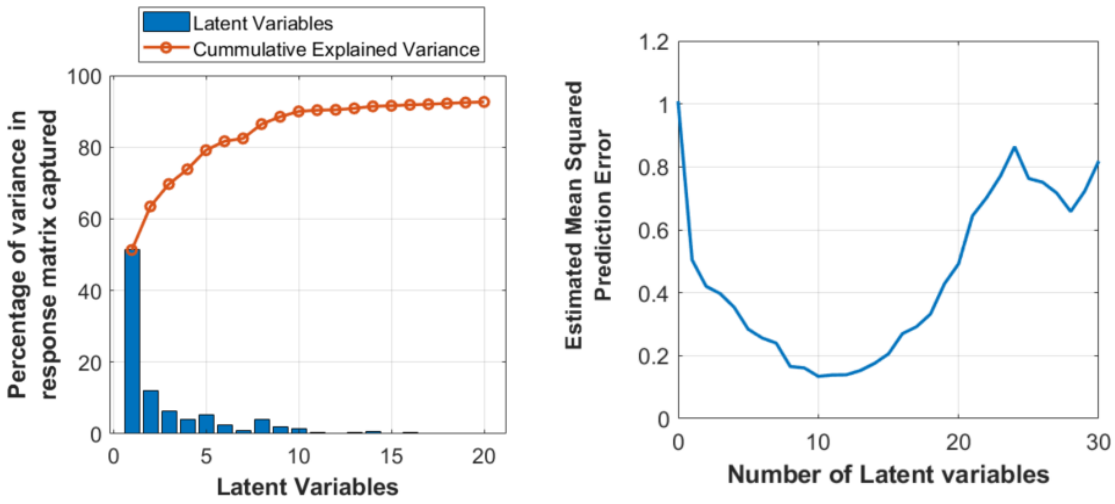

Figure 5.12 Latent variables of PLSR on EIS data. (a) Scree plot of EIS latent variables. (b) Cross-validation estimated mean square prediction error on EIS data.

For both EIS and FDR datasets, a 30-fold cross-validation was undertaken. During this, the training data was divided into 30 subsets and the cross-validation was performed 30 times, with each subset, used as validation and the remaining 29 subsets used to train. Considering the large number of variables, a 30-fold cross-validation was used to ensure robustness as this allows for more training and testing cycles of the data, as compared to 5-fold or 10-fold. From Figure 5.12b, using 10 LVs would produce a model with minimal prediction error, implying that this model would perform well on new unseen data. The model is tested first on the training data to assess the model performance. Equation (5.16) based on standard PLSR form was applied to the validation data to predict capacity of samples [112]. Similarly, for the FDR model, (5.17) was used.

$$\widehat{Y_{EIS}} = X_{EIS} \times B_{EIS} \tag{5.16}$$

$$\widehat{Y_{FDR}} = X_{FDR} \times B_{FDR} \tag{5.17}$$

Where $\widehat{Y_{EIS}}$, $\widehat{Y_{FDR}}$ are the predicted capacity based on EIS data and FDR data respectivley, X_{EIS} and X_{FDR} are the matrices of predictor variables which in this scenario are the EIS and FDR impedance data across different frequencies. B_{EIS} and B_{FDR} are the matrices of regression coefficients learned from the PLSR model. A table of coefficients for both EIS model and FDR model is shown in Appendix D.7.

An R^2value of 0.899 was obtained when the model was tested on the training data. This indicates that the model explains approximately 89.9% of the variance in the capacity values

using the EIS impedance. This high R^2 suggests a high predictive power of the training data variables, implying that the model can reliably explain and predict the cell capacities based on the available impedance variables. This is illustrated in Figure 5.13, in which PLSR model response is compared with the original training response matrix. The sharp peaks observed are the staring points of data for different cells. The model response to the validation data set is also shown in Figure 5.14. The R^2 value for the validation data is 0.7781.

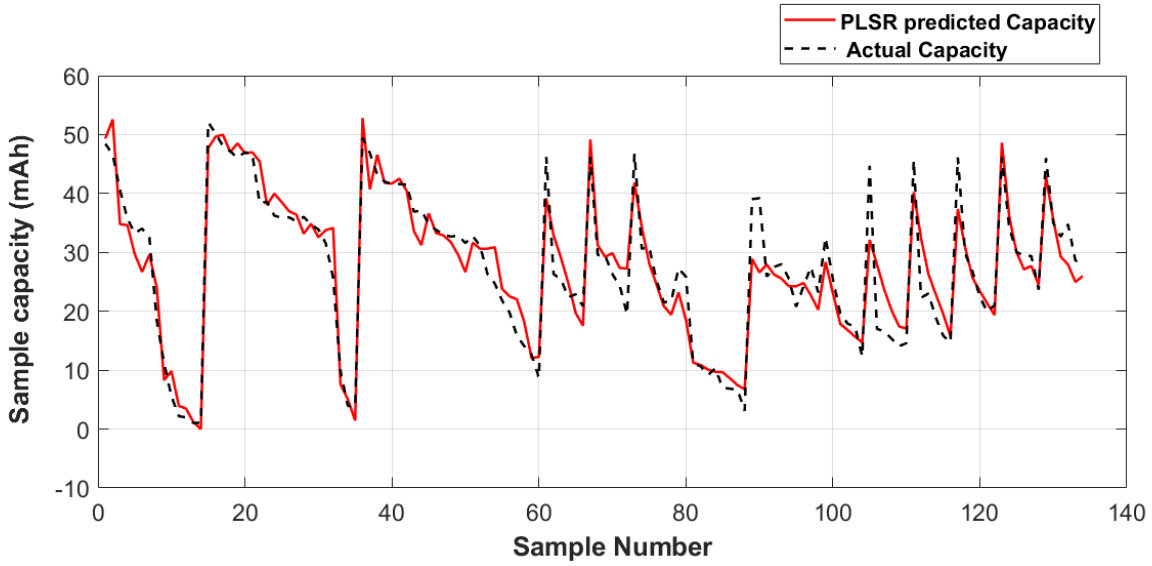

Figure 5.13 EIS-based PLSR model response compared with actual sample capacity.

With the fitting of the validation data producing R^2 of 0.7781 suggest the model captures 77.8% of the variance in capacities of validation sample cells. The slight drop in R^2 value is expected within reasonable range and it suggest, the risk of overfitting to the training data is minimal.

For the FDR datasets, Figure 5.15a and 5.15b show the scree plot and the cross-validation MSPE for the training dataset. In this case, although the cross-validation results show that using eight LVs would ensure minimal prediction error, 10 LVs were used. This was done to ensure a significant percentage of the variability in the response (cell capacities) is captured by selected LVs. For the EIS data, a combination of the first 10 LV captured 90% of the response variability and hence coincided with the number of LVs required to ensure minimal MSPE.

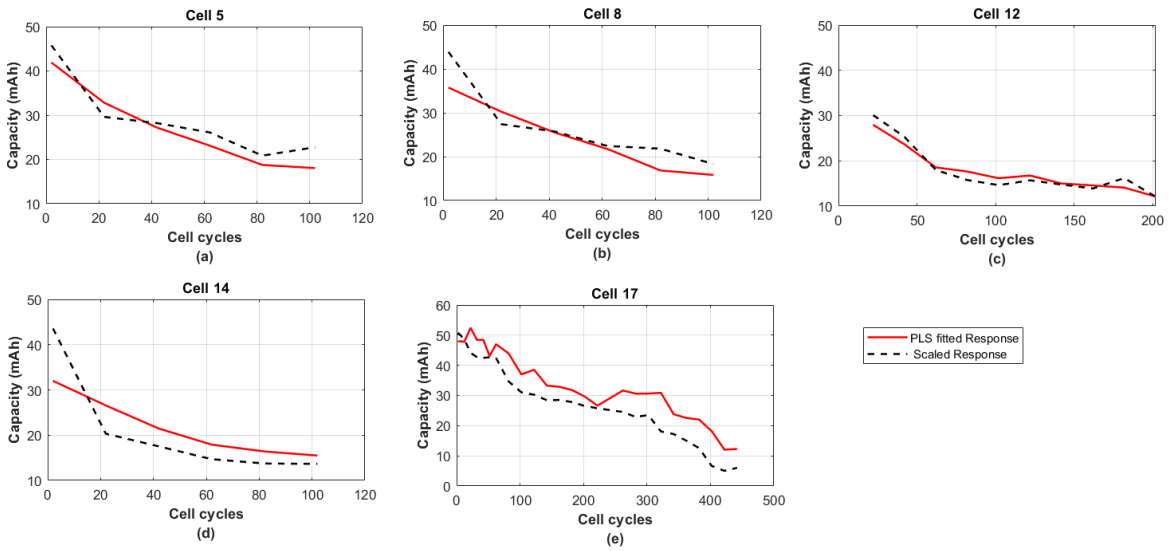

Figure 5.14 EIS-based PLSR model test on validation sample cells.

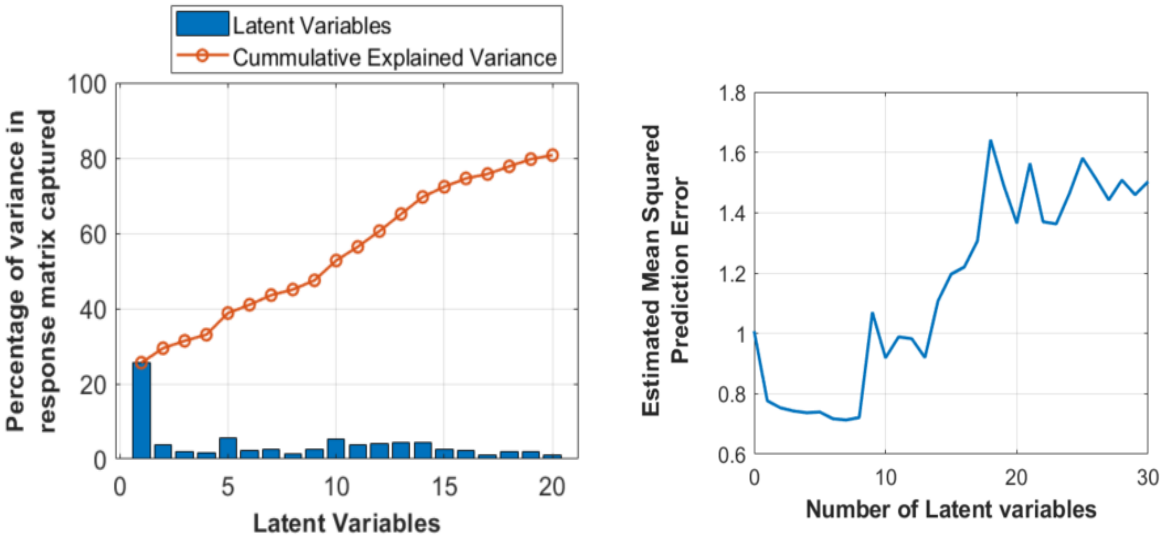

Figure 5.15 Latent variables for FDR-based PLSR. (a) Scree plot for FDR-based PLSR. (b) Cross-validation for MSPE using FDR dataset.

In contrast, apart from the first LV, the FDR LVs closely capture similar amount of variance. This is due to the existing correlation relationship between the variables (measured impedance with the frequency range). Therefore using 10 LVs captures 53% variability while providing a moderate MSPE value of 0.9. The response of the FDR-based model when fitted to the training data is shown in Figure 5.16. The R^2 value for the training data is 0.527, which is comparable to the expected 53%.

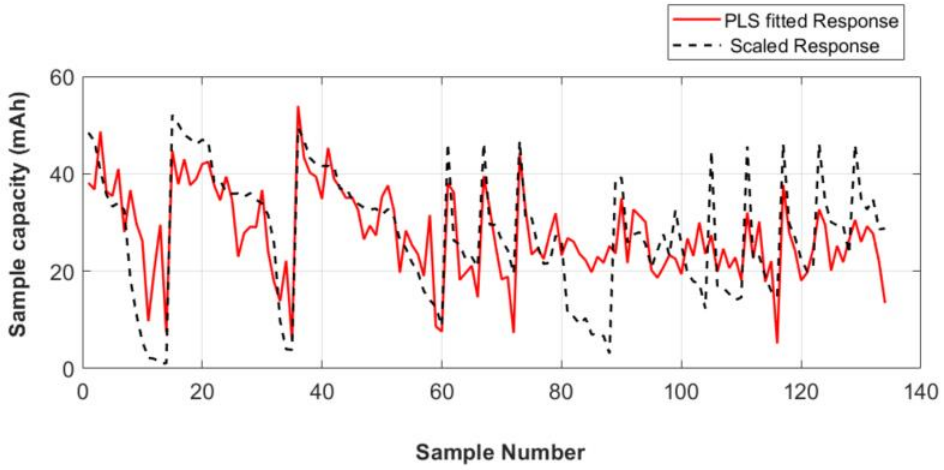

Figure 5.16 FDR-based PLSR model response compared with actual sample capacity

Test on the validation data produced an R^2value of 0.42. Similar to the EIS results, the slight drop suggests a low risk of overfitting and the model explains 42% of the variability in the validation data. Figure 5.17 shows the model fitting to the validation sample cells.

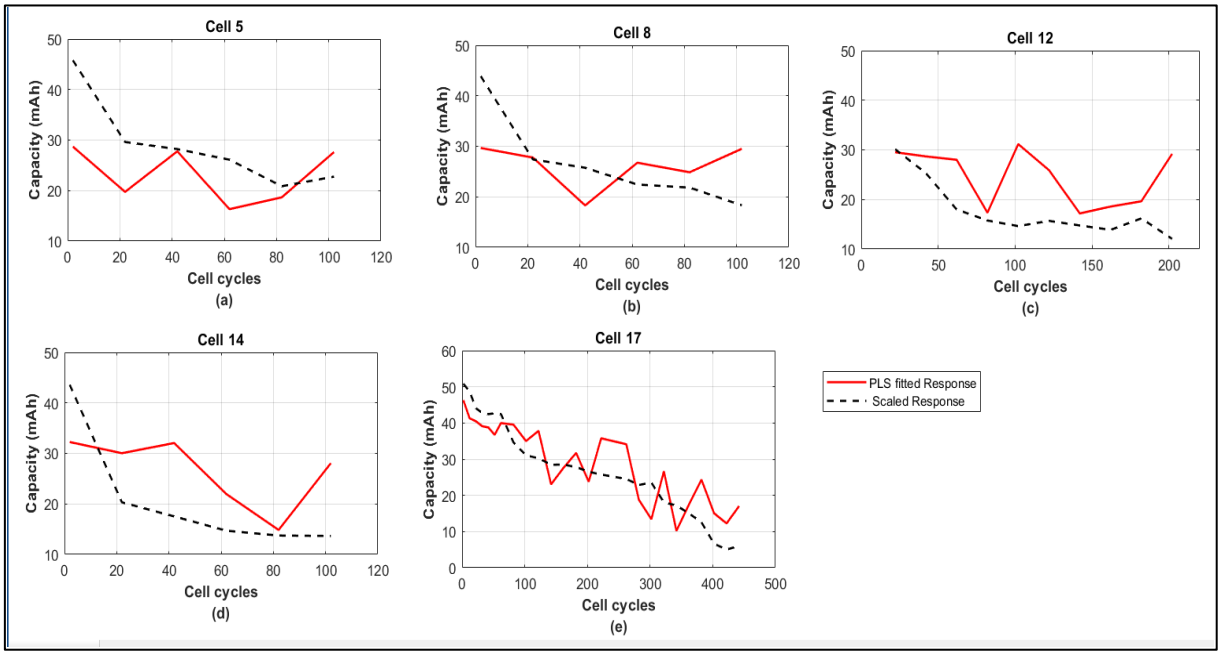

Figure 5.17 FDR-based PLSR model test on validation sample cells.

The high R^2 values for both EIS training (0.89) and validation (0.78) stages confirm that the EIS impedance data is highly predictive of the battery's capacity. The low MSPE (0.18) further indicates its reliability in making accurate predictions on future data. This makes EIS

impedance a robust tool for developing models that need to provide reliable and accurate battery health diagnostics in real-world applications. On the other hand, the lower R^2 values for FDR training (0.53) and validation (0.42) datasets suggest that FDR measured impedance are less effective at capturing the relationships necessary for accurate capacity predictions. This indicates that models based on FDR data may struggle to generalize well to new data. This limits their practical use for real-time monitoring. Further higher R^2 and lower MSPE of the EIS data indicate that resulting models based on EIS data are more robust and are more likely to capture different states of health. This is likely due EIS ability to capture more information on electrochemical processes whereas the high frequency nature of the FDR impedance is incapable of detecting such slow processes.

The R^2 values of 0.42 and 0.53 for the FDR-based model are lower than the corresponding values for EIS (0.89 and 0.78 for training and validation, respectively). These lower R^2 values for FDR are expected due to the nature of the impedance data and the limitations of the FDR method in capturing the full complexity of battery health. The FDR method, which uses high-frequency impedance measurements, is less sensitive to slower electrochemical processes compared to EIS. This results in FDR being less effective at capturing all the relevant information needed for accurate capacity predictions, leading to lower predictive power (i.e., lower R^2). As a result, while FDR data can still provide valuable insights, it is less robust than EIS for predicting battery capacity and might not generalize as well to new data.

5.5 Summary

This chapter presented a statistical evaluation of Frequency Domain Reflectometry (FDR) for State of Health (SoH) monitoring, using capacity and Equivalent Series Resistance (ESR) as health indicators. Given the complexity of FDR impedance data, three multivariate statistical techniques were employed to extract meaningful insights: Principal Component Analysis (PCA), Multivariate Statistical Process Control (MSPC), and Partial Least Squares Regression (PLSR).

PCA was first applied to identify key patterns in FDR impedance data and assess whether it could differentiate between healthy and aged cells. The results showed that while FDR exhibited sensitivity to C-rate effects and grouped late-stage aged cells into distinct clusters, it was less effective than EIS in tracking gradual aging trends. MSPC was then used to evaluate FDR's ability to classify cells based on a predefined threshold, distinguishing healthy cells (≥70% capacity) from aged cells (<70%). Using Hotelling's T^2 and Squared Prediction Error (SPE) statistics, EIS demonstrated higher detection accuracy, correctly identifying 29% (T^2)

and 57.5% (SPE) of aged cells, compared to 19% and 41% for FDR, respectively. These findings suggest that aging effects in FDR data are more apparent in changes in variable relationships rather than in their absolute values, although its classification performance remains inferior to EIS.

Finally, PLSR was employed to assess FDR's predictive capability for battery capacity estimation. The EIS-based model achieved strong predictive accuracy, with R^2 values of 0.89 for training and 0.78 for validation, and a low Mean Squared Prediction Error (MSPE) of 0.18. In contrast, the FDR-based model demonstrated significantly weaker performance, with R^2 values of 0.53 for training and 0.42 for validation, and a higher MSPE of 0.9, indicating that FDR lacks the robustness required for accurate capacity estimation when applied to new datasets.

These results demonstrate that while FDR can capture certain aging effects, particularly at high frequencies, it is less effective than EIS for tracking gradual degradation. FDR was found to be more effective in detecting late-stage aging but struggled to differentiate between cells in early or moderate stages of degradation. The lower predictive accuracy of FDR-based models suggests that it is not yet suitable as a standalone health diagnostic tool. However, FDR may still hold value as a supplementary technique, particularly for high-frequency diagnostics, where additional insights could complement established methods. These findings highlight the need for further optimization of FDR data processing to enhance its sensitivity to early-stage degradation and improve its overall reliability in battery health monitoring.

Chapter 6 Conclusion

This thesis investigated the feasibility of using FDR for lithium-ion battery SoH, using capacity and ESR as health indicators. To achieve this Nineteen commercial LIR2032 coin cells, rated at 4.2 V and 40 ±5 mAh, were used as samples. The cells underwent controlled cyclic aging using the CC-CV method, with a cutoff charging voltage of 4.2V and a discharge cutoff of 3V, all conducted at 25°C. The cycling was done to induce generic aging and not a specific degradation mechanism. Initially, when the cycling rate increased from 0.02C to 1C (over 2 cycles), capacity decreased from 50 mAh to 47 mAh at an average rate of 1.5 mAh per cycle, while ESR increased from 0.2 Ω to 0.24 Ω at a rate of 0.02 Ω. With a further C-rate increment from 1C to 2C, capacity of cells in Batch A declined from 47 mAh to 45 mAh, at a reduced rate of 0.03 mAh per cycles (over 60 cycles), while ESR remained relatively stable with intermittent spikes. These capacity and resistance changes were attributed to increased lithium plating and SEI layer growth, which are known to occur at higher C-rates and contribute to capacity fade and increased resistance. Within these phases, FDR resistance increased from 0.8 Ω to 1.12 Ω when the C-rate was raised from 0.02C to 1C, corresponding to an average increase of 0.16 Ω per cycle, with a notable spike observed at cycle 22. However, FDR resistance remained relatively stable when the C-rate increased from 1C to 2C, suggesting that the initial rise was primarily driven by early-stage impedance changes rather than continued degradation at higher discharge rates. Overall, this study sort to address three research questions through experimental characterization, statistical evaluation, and performance comparison of FDR with EIS using these sample cells.

The first research question was to assess the impedance measured using FDR correlate with battery health indicators such as capacity and ESR. The results demonstrated that FDR impedance exhibits a measurable correlation with battery SoH, particularly the reactive impedance at 300KHz. The FDR measured resistance showed correlation with capacity and ESR from homogenous sample while the FDR reactance showed a more consistent correlation with ESR and capacity for both homogenous and heterogenous samples. However, the measured FDR reactance values were so low, that in practical purposes, these would be difficult to differentiate between system noise. Also, while FDR captured changes in cell impedance associated with aging, its response did not consistently align with capacity fade in the same manner as EIS. ESR extracted from EIS provided a more reliable metric for tracking degradation. FDR was found to be more sensitive to rapid degradation events such as high C-rate cycling and short-circuit conditions but was less effective at detecting gradual aging trends.

This suggests that FDR, in its current form, is not a direct replacement for EIS but may serve as a complementary diagnostic tool.

The second research question was to assess if FDR be used to classify battery cells into healthy and aged states. Multivariate Statistical Process Control (MSPC) was applied to determine the effectiveness of FDR in binary classification of healthy (capacity ≥70%) and aged (capacity <70%) cells. While FDR-based MSPC was able to classify cells with some success, EIS outperformed FDR in detection accuracy, correctly identifying 29% (Hotelling's T^2) and 57.5% (SPE) of aged cells compared to 19% and 41% for FDR, respectively. The higher SPE indicate that aging effects in FDR data are more apparent in the relationships between measured variables rather than in absolute impedance values. However, FDR exhibited better sensitivity in the SPE test, suggesting its potential for capturing subtle system-wide changes rather than individual parameter shifts.

The third research question was to find out if FDR be used as a predictive tool for estimating battery capacity. Partial Least Squares Regression (PLSR) was used to evaluate the predictive capability of FDR for estimating battery capacity. The EIS-based model achieved high predictive accuracy with R^2 values of 0.89 (training) and 0.78 (validation), along with a low Mean Squared Prediction Error (MSPE) of 0.18. In contrast, the FDR-based model performed significantly less good, with R^2 values of 0.53 (training) and 0.42 (validation), and an MSPE of 0.9. These results indicate that FDR lacks the robustness required for accurate capacity prediction and is not suitable as a standalone SoH estimation tool.

Overall, this research highlights that while FDR demonstrates some sensitivity to aging effects, it is less effective than EIS for comprehensive SoH monitoring. FDR showed potential in high-frequency diagnostics, particularly in detecting late-stage aging, but struggled to differentiate early to moderate degradation. Future improvements in data processing and refinement of FDR measurement techniques are necessary to enhance its utility in real-world applications.

6.1 Future works

Several areas require further investigation to improve the effectiveness and applicability of FDR for battery SoH monitoring:

- **Cell Format and Chemistry:** This study focused on coin cells, but the impact of cell geometry and chemistry on FDR measurements needs to be explored. Future work should extend the analysis to prismatic and cylindrical cells to evaluate FDR's performance across different battery designs.

- **Robust Design of Experiments (DoE):** A more extensive and structured DoE is required to generate a richer dataset that captures a broader range of aging mechanisms. This would enhance the statistical robustness of FDR-based models and improve generalization to real-world conditions.
- **Controlled and Variable Ambient Conditions:** The impact of temperature and environmental factors on FDR impedance measurements should be systematically examined. Investigating FDR responses under varying ambient conditions can provide insights into its reliability for field applications.
- **State of Charge (SoC) Dependency:** The SoC level at which EIS and FDR measurements are taken can influence impedance characteristics. Future work should assess the effect of different SoC levels on FDR responses to optimize measurement protocols.
- **System-Level Integration:** Evaluating FDR in battery packs with parallel and series connections will provide insights into its effectiveness in large-scale applications. Investigating whether FDR can detect aging effects in multi-cell configurations is crucial for its practical implementation in battery management systems (BMS).

This study has provided a comprehensive evaluation of FDR as a SoH monitoring tool for lithium-ion batteries. The findings suggest that FDR has potential for single-cell SoH tracking and as a non-invasive probe to study electrode-electrolyte capacitive mechanisms. However, proper setup design and de-embedding are required to improve accuracy and reliability. Future research should focus on refining FDR methodologies to enhance sensitivity, reliability, and applicability in practical battery monitoring systems.

Appendix A-Battery Dynamics and Transmission Line Theory

A.1 Fundamentals of Impedance-based Battery Dynamics

Battery dynamics encompass a range of electrical and electrochemical processes that dictate the behaviour and performance of lithium-ion batteries (LiBs). This section focuses on the impedance-based description of battery processes and provides support information on discussions in Chapters 4 and 5, particularly in identifying relationships between the state of sample cells and measured impedance from EIS and FDR. Figure A.1 summarises electrochemical processes and their respective frequency ranges within which they typically occur.

A.1.1 Solid Electrolyte Interphase Layer

The Solid Electrolyte Interphase (SEI) layer is formed initially but not exclusively, during the initial cycles on the anode surface [144, 174]. This is a thin passivating layer formed by accumulation of organic and inorganic components from the electrolyte as its decomposed through electrochemical processes [174]. Lithium, the electrolyte solvent, and additives such as vinylene carbonate, react with the shell of the graphite on the anode to create a protective film on the graphite anode [35, 175]. This is illustrated in A.2. The formation of this layer uses up 5-10% of the lithium in the battery cell on the first cycle [176]. SEI is known to primarily form on the anode. This is attributed to the lower potential of the anode as compared to the cathode, that makes its surface more susceptible to reduction reactions with the electrolyte [144].

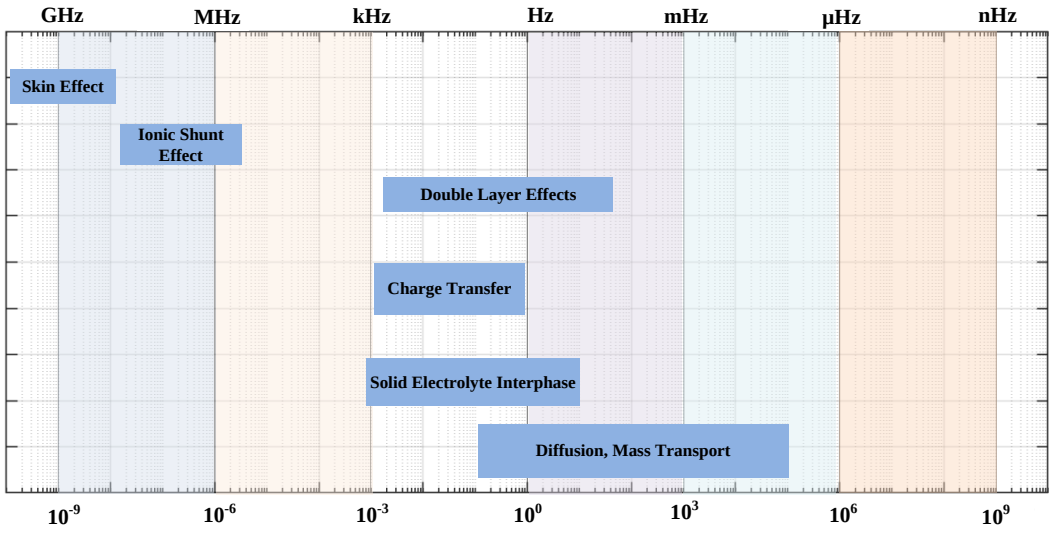

Figure A.1 Dynamic processes in Li-ion battery and their relaxation times and frequencies [41, 116, 144].

On the cathode, the Cathode Electrolyte Interphase (CEI) is thought to occur. The effect of this mechanism on cell degradation is less well-understood compared to SEI formation, but it's believed to involve the oxidation of the electrolyte at the cathode surface [175, 177]. While a stable SEI enhances cycle life and safety by mitigating electrode degradation and electrolyte depletion, an unstable or porous SEI can exacerbate capacity fading and increase charge transfer resistance [144].

The effects of SEI mechanism has been modelled as a parallel resistor (R)-capacitor (C) circuit in impedance based analysis [13, 175]. While not a perfect conductor, it allows for the movement of ions (Li^+) through it. However, this movement is not instantaneous and experiences some resistance. This resistance to ion transport arises from several factors, including the inherent chemical nature of the SEI components, their porosity, and the size and charge of the migrating Li^+ ions [122]. The resistance to ion transport is represented by the **resistor** element in the parallel RC circuit. The capacitive behaviour is attributed to the creating of a temporary separation of charge between SEI and the electrolyte or electrode [171, 178].

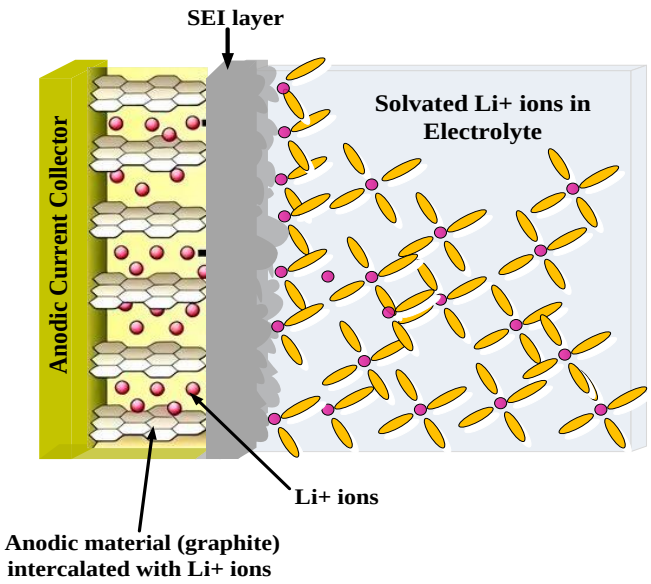

Figure A.2 SEI formation from solvated lithium ions decomposed on the anode material surface during initial cycling [116, 161, 179].

A.1.2 Electric Double Layer

The Electric Double Layer (EDL) refers to the interfacial layer formed between the electrodes and the electrolyte boundary due to electrostatic interactions. While the SEI is a permanent, passivating layer formed through chemical phenomenon involving decomposition products on the anode, the EDL is formed through a physical phenomenon arising from the accumulation

of ions due to electrostatic attraction and occurs on both electrodes [36, 122, 173]. With a potential applied to the battery, the positively charged ions in the electrolyte accumulate near the negatively charged electrode surface (anode) and vice-versa for the cathode. This occurs in two layers as illustrated in Figure A.3. The first layer known as the Inner Helmholtz plane (IHP), is the closest to the electrode surface. It is composed of ions strongly bonded to the electrode surface forming a semi-permanent layer forming a region of high charge density. The second layer is a more diffused layer known as Outer Helmholtz Plane (OHP), is made up of ions less attracted to the electrode surface area. This layer is made up of ions of opposite charge to those in the IHP and it extends into the bulk of the electrolyte solution. The electric double layer capacitance (EDLC) refers to the capacitance associated with the EDL. It represents the ability of the electric double layer to store electrical charge in response to an applied voltage.

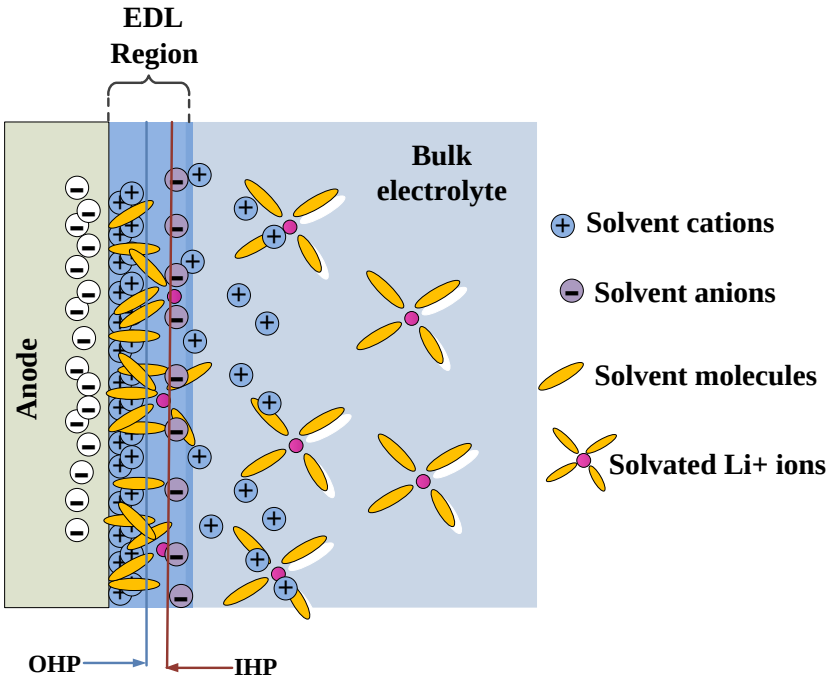

Figure A.3 Formation of inner and outer Helmholtz layers and the electric double layer region on anode electrode due to electrostatic attraction between electrolyte ions and anode [173, 180].

The EDLC is typically characterized by its capacitance value and is influenced by factors such as the electrode material, electrolyte composition, and surface area of the electrode [173, 181]. A larger surface area allows for more ions to accumulate at the electrode/electrolyte interphase, leading to a higher EDLC. This higher capacitance enables the battery to store more electrical charge, resulting in improved energy storage capacity and power density [181]. Batteries with higher EDLC values exhibit enhanced performance characteristics, such as faster

charging/discharging rates and increased energy efficiency [173]. However, certain factors can hinder EDLC and, consequently, battery performance. For instance, degradation mechanisms that affect the electrode material, structure or electrolyte composition can degrade the EDL, leading to reduced capacitance and diminished battery performance. These changes can be physical resulting in changes in electrode structure.

A.1.3 Charge Transfer

Charge transfer (CT) involves movement of Li+ ions and the accompanied transfer of electrons during the intercalation and de-intercalation processes in the electrodes [174]. The kinetics of CT processes encompasses the solvation of the Li+ in the liquid electrolyte, de-solvation of the solvated Li+ and transport in the preformed SEI [123]. With the EDL formed, a concentration gradient is created between the IHP and the OHP. This concentration difference drives the diffusion of ions from the bulk electrolyte towards the electrode surface [123]. The charge transfer resistance (R_{ct}) is a parameter used to quantify how fast the charges are moving during the charge transfer process. The Butler-Volmer equation, shown in (A.1), provides a framework for describing the faradaic current density (j_n) associated with charge transfer reactions and the relationship between the factors influencing charge transfer [41, 173].

$$j_n = j_0 \left[\exp\left(\frac{\alpha \eta F \eta_{ct}}{RT}\right) - \exp\left(-\frac{(1-\alpha)\eta F \eta_{ct}}{RT}\right)\right] \tag{A.1}$$

In (A.1) j_n is the faradaic current density (A/m²), j_0 is the exchange current density (A/m²) which reflects the rate of charge transfer at equilibrium (i.e. with no applied voltage η_{ct}= 0). A higher j_0 indicates a faster intrinsic charge transfer process for a specific electrode-electrolyte combination. α is the symmetry factor ($0 < \alpha < 1$), indicates how readily the reaction proceeds in the forward (oxidation) or backward (reduction) direction for a given overpotential. F is the Faraday constant (C/mol), η_{ct} is the surface overpotential which represents the additional potential required to drive the reaction away from equilibrium due to limitations in the charge transfer process. R and T are the gas constant (J/mol*K) and temperature (K) respectively. While the Butler-Volmer equation in (A.1), has limitation in describing the entire charge transfer process at high overpotentials or complex electrode surfaces, this equation can be linearized for small overpotentials (η_{ct} < 6 mV) to estimate charge transfer resistance in batteries [41, 173]. The linearised form of (A.1) is expressed in (A.2)

$$R_{ct} = \left[\frac{\partial j_n}{\partial \eta_{ct}}\Big|_{\eta_{ct}=0}\right]^{-1} = \frac{RT}{nFj_0} \tag{A.2}$$

In (A.2) the inverse relationship between R_{ct} and j_0, becomes evident [116]. Efficient charge transfer ensures the successful intercalation of Li^+ into the cathode, maximizing the battery's capacity to store charge. At higher frequencies, the rapid changes in the electric field hinder the mobility of Li^+ ions, limiting their ability to effectively intercalate into the cathode and de-intercalate from the anode [182]. This translates to a decrease in a battery's capacity to store charge and to deliver power during discharge. Consequently, the measured high frequency impedance primarily reflects the increased resistance associated with these limitations at the electrode-electrolyte interface [26]. While bulk charge transfer processes within the electrolyte might still be occurring, their contribution to the impedance may be masked by the dominant effect of the interfacial limitations at these high frequencies [26, 182].

A.1.4 Ohmic Resistance

All components present in the battery structure present some level of resistance to current flow. Ohmic resistance refers to the inherent opposition to current flow present in components such as electrolyte, separator, and electrode materials, each contributing to the overall resistance [13, 183]. This resistance is influenced by factors such as electrolyte composition, concentration, and temperature.

A.1.5 Mass Transport Effects

Mass transport describes the movement of lithium ions (Li^+), solvent molecules, and other species such as lithium salts and reaction byproducts through the electrolyte, separator, and electrodes [184]. Lithium-ion transport typically involves migration and diffusion processes [144]. Migration of Li+ ions occur due to electric fields and can be hindered by solvated molecules and reaction byproducts in the electrolyte while ionic diffusion, is triggered by the presence of a concentration gradient [144, 185, 186]. Majority of the mass transport is due to ionic diffusion through the electrolyte and alterations to its composition and viscosity can limit this movement [144]. Also, separator structure, SEI layer composition and thickness and the electrode geometry can limit the diffusion of ions into the electrodes, ultimately affecting battery dynamics and performance. Fick's Law in (A.3) highlights the dependence of diffusion on the concentration gradient and the material's diffusion coefficient [187].

$$J = -D\left(\frac{\partial c}{\partial x}\right) \tag{A.3}$$

where J is the flux of Li^+ ions (mol/m²s), D is the diffusion coefficient (m²/s), and $(\frac{\partial c}{\partial x})$ is the concentration gradient (mol/m³). The Warburg element, W, is generally used to describe mass transport processes in batteries [21]. It represents the semi-linear diffusion, and its magnitude is inversely proportional to the frequency of measurement shown in (A.4). Z_w is the impedance associated with diffusion process, f is the frequency of measurement (Hz) and σ is the diffusion coefficient, which is typically obtained by parameter fitting of impedance curve.

$$Z_W = \frac{\sigma}{\sqrt{2\pi f i}} \tag{A.4}$$

Equations (A(A.5) and (A.6) are modifications to the Warburg element that consider geometry and nature of boundaries within a system[21, 188]. Equation (A.5) represents the Finite Space Warburg (T element) which is a modification of the Warburg element to account for mass transport in a finite space [21, 122]. Equation (A.6) describes diffusion through thin films or transmission boundaries [21]. Z_T and Z_O are frequency dependent impedances due to finite space and finite length diffusion processes respectively. σ_T and σ_O are the respective diffusion coefficients, also determined by curve fitting. τ_T and τ_O are parameters determined from diffusion coefficients and diffusion distance.

$$Z_T = \frac{\sigma_T}{\sqrt{2\pi f i}} \coth(\tau_T \sqrt{2\pi f i}) \tag{A.5}$$

$$Z_O = \frac{\sigma_O}{\sqrt{2\pi f i}} \tanh\left(\tau_O \sqrt{2\pi f i}\right) \tag{A.6}$$

With the graphite electrodes having finite capacity, (A.5) is useful in describing the insertion process in the graphite electrodes [21, 189]. Equation (A.6) is also applied to describing the diffusion through the SEI layer or diffusion of Li^+ through electrolyte or electrode pores [21, 190].

A.1.6 Ionic Shunt and Skin Effect

The inductance of the metallic electrodes increases with frequency. This contributes to the overall impedance of the electrodes experienced by the ions. Therefore, at high frequency, a small portion of the ions might take an alternate path through the electrolyte, bypassing some of the electrode material. This bypass of ionic flow from the ideal electrochemical pathways, is termed as ionic shunt effect and can lead to distorted high-frequency impedance measurements

[11, 29]. In conductors carrying high-frequency currents, the current distribution becomes non-uniform. This phenomenon, known as the skin effect, arises due to the changing magnetic field of the AC current that induces opposing eddy currents within the conductor [135]. These eddy currents are strongest towards the centre of the conductor and tend to push the main AC current towards the surface. The surface-concentrated current interacts less with the bulk material, effectively reducing the usable conductive area and further amplifying the surface current density [191]. Skin effect can influence battery high frequency impedance by affecting the internal resistance. Also, as current flow becomes limited to the surface of current collectors, it interacts less with the bulk of the electrode material. This reduction in effective area limits the utilization of the entire active electrode area for efficient charge transfer reactions, hindering overall capacity [192]. Further, the concentrated surface current amplifies the influence of phenomena occurring near the electrode surface, such as those within the SEI and the double layer [29, 193]. This has the potential to skew the understanding of the measured impedance, leading to misinterpretations of battery health if solely relying on high-frequency impedance measurements [29].

On the other hand, the increased ionic flow through the electrolyte-electrode interface at high frequencies due to the combined ionic shunt and skin effects might offer a potential benefit. Operating within this interface, where there is significant presence of electrolyte, suggests that electrolyte parameters such as complex dielectric can be reflected in measured high frequency impedance.

A.2 Application of the Telegrapher's Equations and Transmission Line Theory to Characterise Conductors

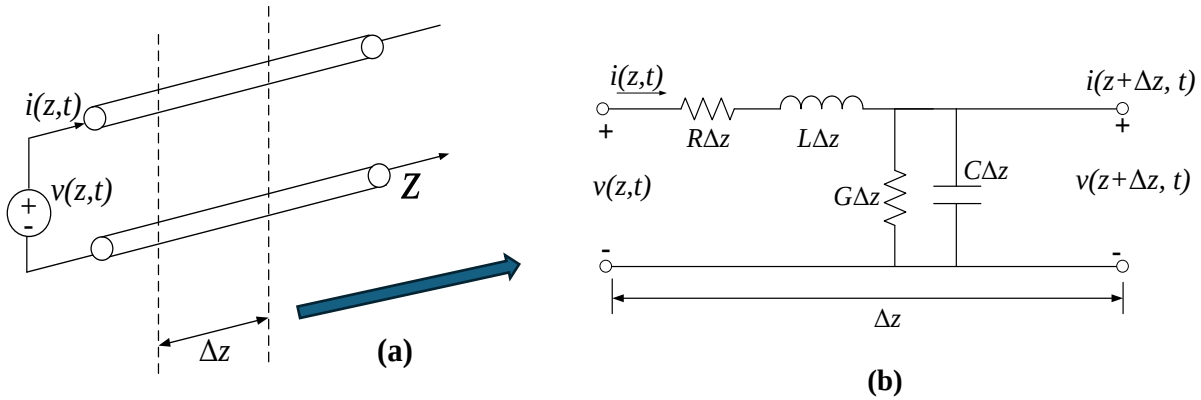

Figure A.4 Voltage and current definitions for a segment of transmission line. (a) A segment of transmission line. (b) Equivalent lumped-element model [135, 136].

When an infinitesimal length of transmission line ($\Delta z \longrightarrow 0$) is considered, transmission line equations (A.7) and (A.8) are obtained in time domain and (A.9) and (A.10) are obtained under sinusoidal steady-state conditions with cosine-based phasors [135, 136].

$$\frac{\partial V(z,t)}{\partial z} = -L\frac{\partial I(z,t)}{\partial t} - RI(z,t) \tag{A.7}$$

$$\frac{\partial I(z,t)}{\partial z} = -C\frac{\partial I(z,t)}{\partial t} - GV(z,t) \tag{A.8}$$

$$\frac{dV(z)}{dz} = -(R + j\omega L)I(z) \tag{A.9}$$

$$\frac{dI(z)}{dz} = -(G + j\omega C)V(z) \tag{A.10}$$

The solutions to (A.9) and (A.10) produces second-order wave equations for voltage and current signals traveling on the transmission line. These second-order wave equations have solutions in the form of (A.11) and (A.12) [135, 137].

$$V(z) = V_0^+ e^{-\gamma z} + V_0^- e^{\gamma z} \tag{A.11}$$

$$I(z) = I_0^+ e^{-\gamma z} + I_0^- e^{\gamma z} \tag{A.12}$$

Where $V(z), V_0^+, V_0^-, I(z), I_0^+, I_0^-$ are phasors. $V_0^+ e^{-\gamma z}$and $I_0^+ e^{-\gamma z}$ represents the forward travelling voltage and current waves in the $+z$ direction respectively and $V_0^- e^{\gamma z}$ and $I_0^- e^{\gamma z}$ respectively for waves traveling backwards in the $-z$ direction [136]. γ is the frequency-dependent propagation constant expressed in (A.13) [135]. α is the attenuation coefficient in $\frac{Np}{m}$ and β is the phase constant in $\frac{rad}{m}$ [135, 136].

$$\gamma = \alpha + j\beta = \sqrt{(R + j\omega L)(G + j\omega C)} \tag{A.13}$$

Appendix B - Decomposition of PLSR Latent variables

Latent variables (LV) in PLSR are determined by performing algorithms such SVD or eigen decomposition iteratively to ensure maximum covariance between predictor matrix X and response matrix Y variables. For the first LV, weight vectors, w and c are determined by (B.1) and (B.2)

$$w = E^T u \tag{B.1}$$

$$c = F^T t \tag{B.2}$$

a is the index of the variable in X being considered. The u vector is initially formed with random values [169]. The scores of the $Xstandardised$ and $Ystandardised$ are estimated by (B.3) and (B.4) respectively such that $t^T t = 1, w^T w = 1, t^T u = max$ [169].

$$t = Ew \tag{B.3}$$

$$u = Tc \tag{B.4}$$

when t converges, the scalar b and vectors p and q are calculated using (B.5) – (B.7) respectively [168, 172].

$$b = t^T u \tag{B.5}$$

$$p = E^T t \tag{B.6}$$

$$q = F^T c \tag{B.7}$$

The effect of the first LV is removed from X and Y by (B.8) and (B.9) respectively, after which the vectors t, u, c, w, p are stored in their respective matrices. The scalar b forms the diagonal element in matrix B, which contains the regression weights used in predicting Y by the expression in (B.10) [112].

$$E = E - tp^T \tag{B.8}$$

$$F = F - btc^T \tag{B.9}$$

$$\hat{Y} = TBC^T \tag{B.10}$$

Where $\hat{Y}$ is the estimated response variable matrix. The process is repeated until X is empty [112, 194].

Appendix C - EIS Impedance Based Equivalent Circuit Models of Cells

As presented in chapter 3, EIS test were performed to study the impedance changes in the cells during cyclic aging. ECM based models were generated to provide insight into the electrochemical processes contributing to the changes in impedance observed. These models are based on variations of Randles circuits. Figures C.1 to C.19 present for each cell the experimental response and the model response in the new and the aged states. Also shown in Table C1 is the model parameters.

In the models, L, is the inductance at high frequency and R1, represents the ESR. R2 and C1 represent the charge transfer resistance and double -layer capacitance processes respectively. The third sub-circuit R3 and Q1 (combination of Qn_1 and Qy_1) represent the resistance and capacitance of the SEI layer. The CPE Q1, is used instead of C3 in Figure C.1, to represent the non-ideal behaviour of the complex processes that deviate from traditional capacitive and resistive behaviour. Diffusion processes are represented by elements, Ws_1 and Ts_1 (combination of Ts_1 and Tt_1). Ws_1 represents a semi-infinite diffusion whereas Ts_1 suggests a finite space diffusion.

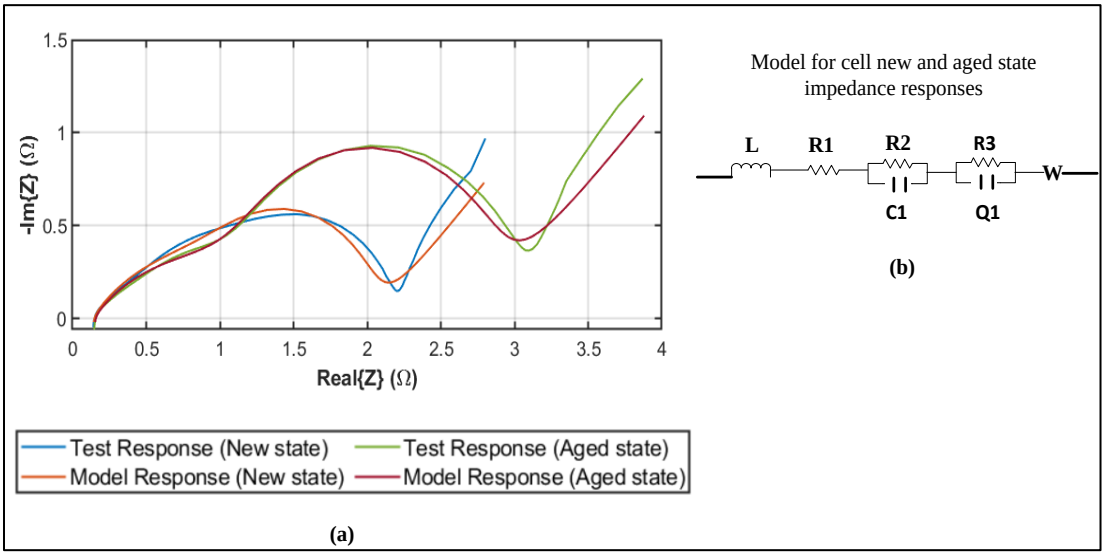

Figure C.1 EIS Impedance based responses and model for Cell 1 (a) EIS test impedance and EIS-based ECM impedance for new and aged state. (b) ECM models for new and aged state.

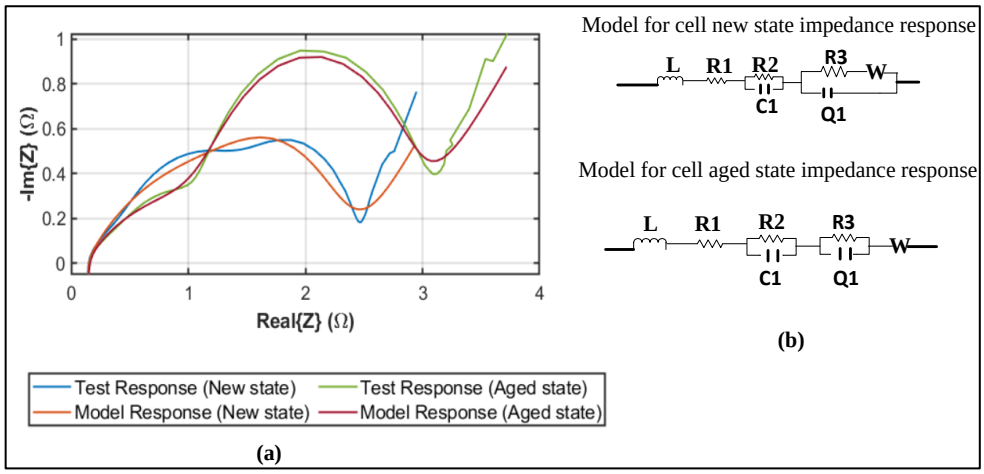

Figure C.2 EIS Impedance based responses and model for Cell 2 (a) EIS test impedance and EIS-based ECM impedance for new and aged state. (b) ECM models for new and aged state.

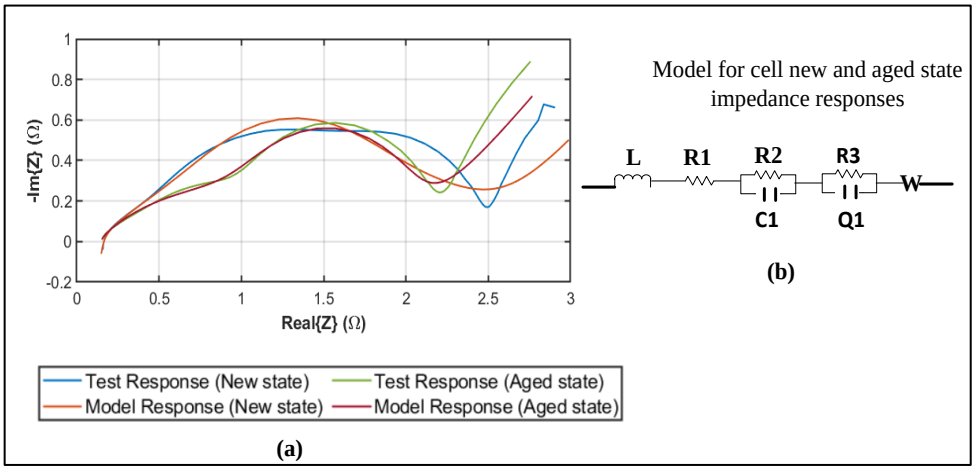

Figure C.3 EIS Impedance based responses and model for cell 3 (a) EIS test impedance and EIS-based ECM impedance for new and aged state. (b) ECM models for new and aged state.

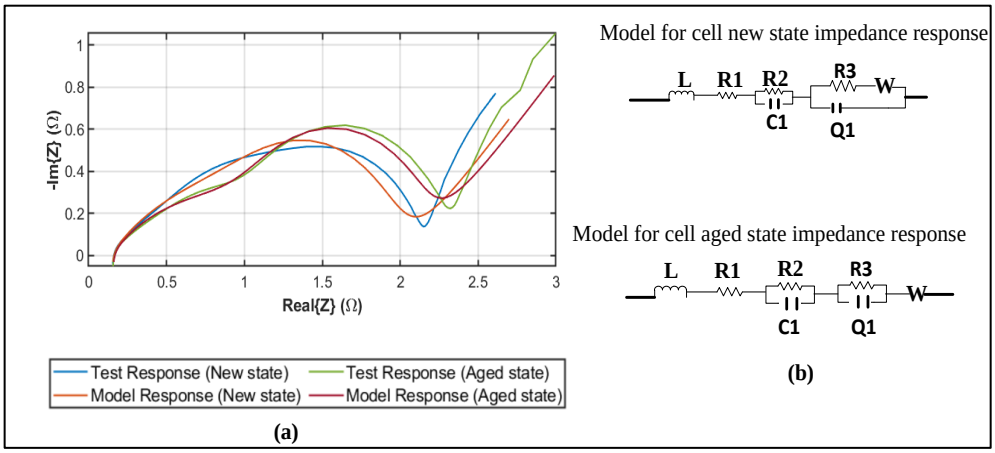

Figure C.4 EIS Impedance based responses and model for cell 4 (a) EIS test impedance and EIS-based ECM impedance for new and aged state. (b) ECM models for new and aged state.

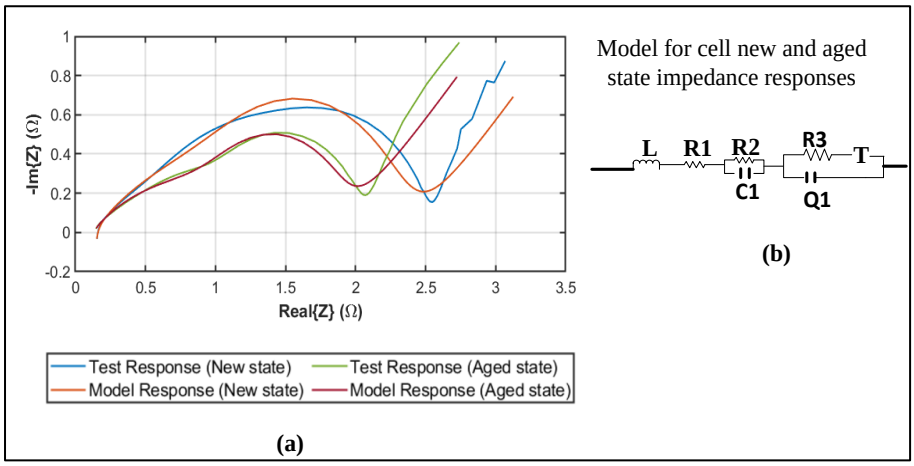

Figure C.5 EIS Impedance based responses and model for cell 5 (a) EIS test impedance and EIS-based ECM impedance for new and aged state. (b) ECM models for new and aged state.

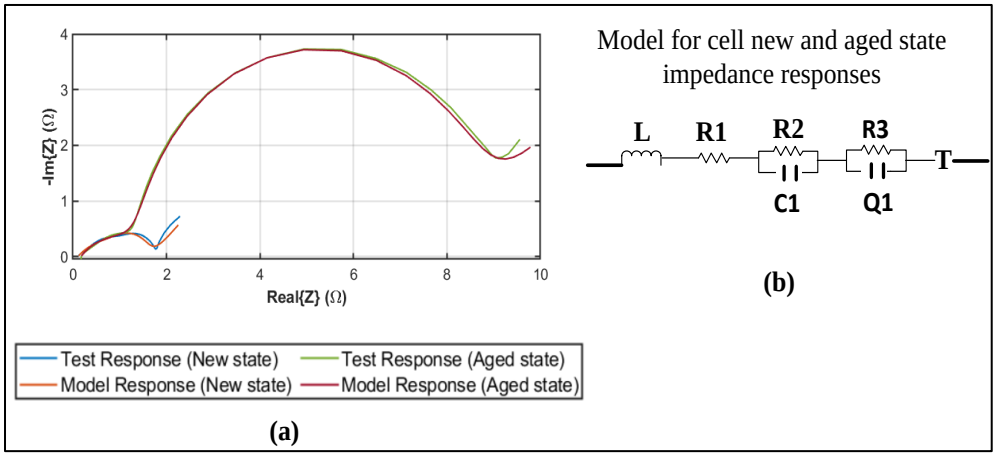

Figure C.6 EIS Impedance based responses and model for cell 6 (a) EIS test impedance and EIS-based ECM impedance for new and aged state. (b) ECM models for new and aged state.

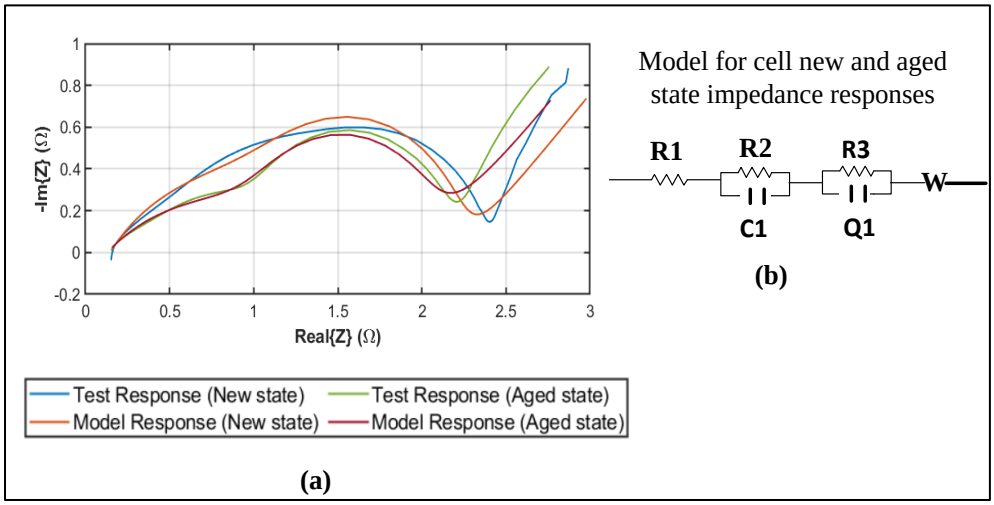

Figure C.7 EIS Impedance based responses and model for cell 7 (a) EIS test impedance and EIS-based ECM impedance for new and aged state. (b) ECM models for new and aged state.

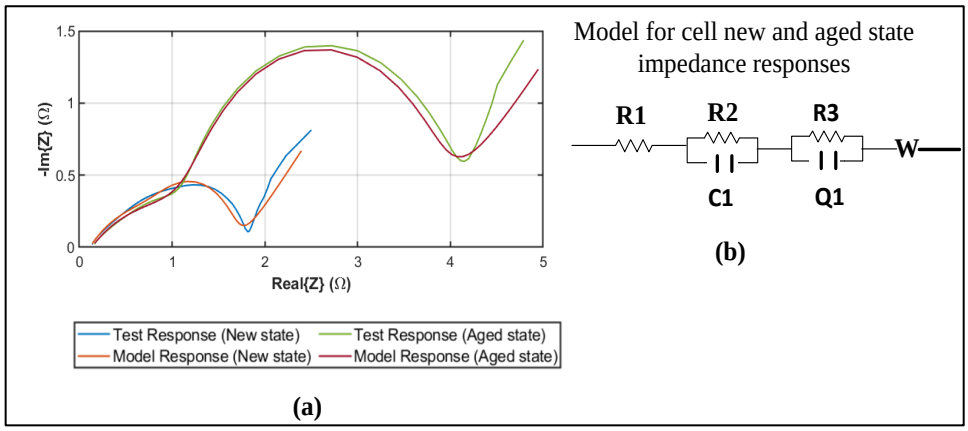

Figure C.8 EIS Impedance based responses and model for cell 8 (a) EIS test impedance and EIS-based ECM impedance for new and aged state. (b) ECM models for new and aged state.

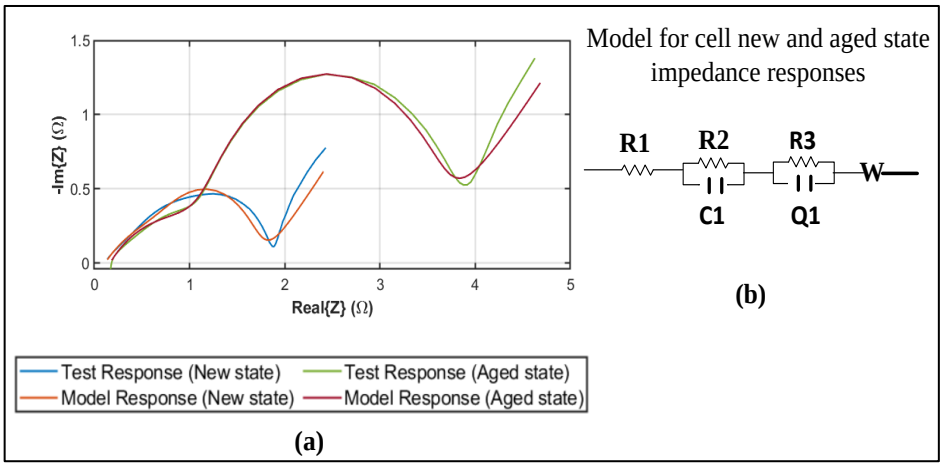

Figure C.9 EIS Impedance based responses and model for cell 9 (a) EIS test impedance and EIS-based ECM impedance for new and aged state. (b) ECM models for new and aged state.

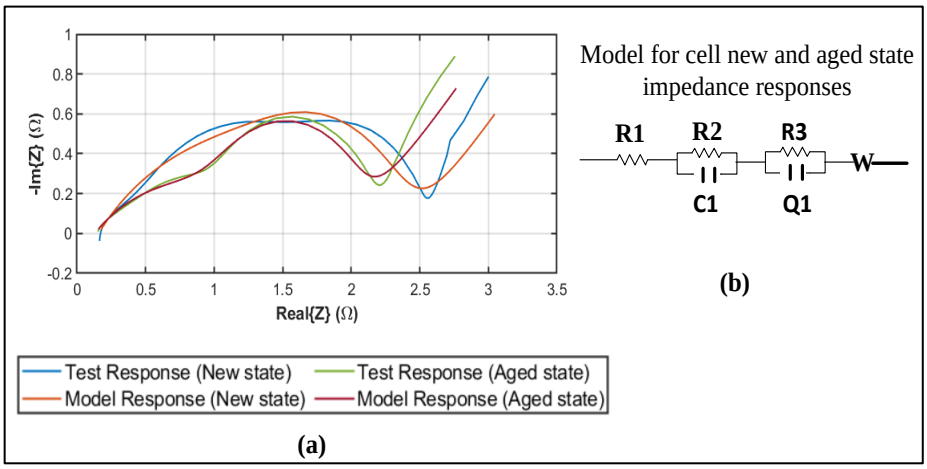

Figure C.10 EIS Impedance based responses and model for cell 10 (a) EIS test impedance and EIS-based ECM impedance for new and aged state. (b) ECM models for new and aged state

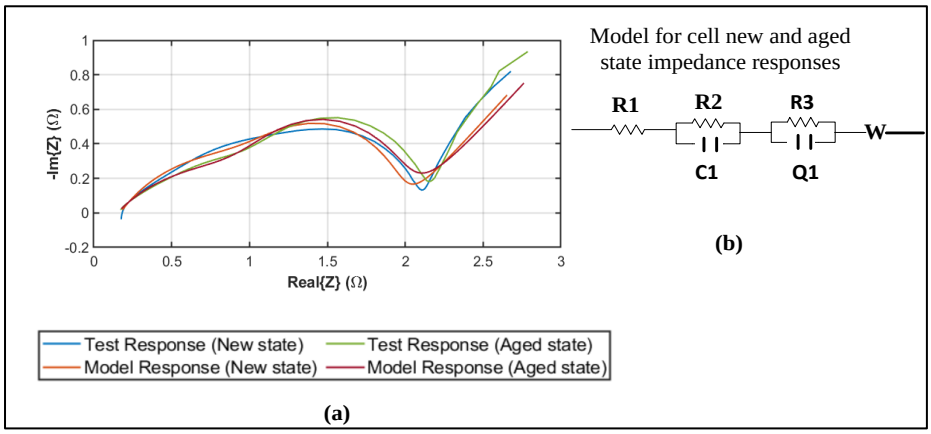

Figure C.11 EIS Impedance based responses and model for cell 11 (a) EIS test impedance and EIS-based ECM impedance for new and aged state. (b) ECM models for new and aged state.

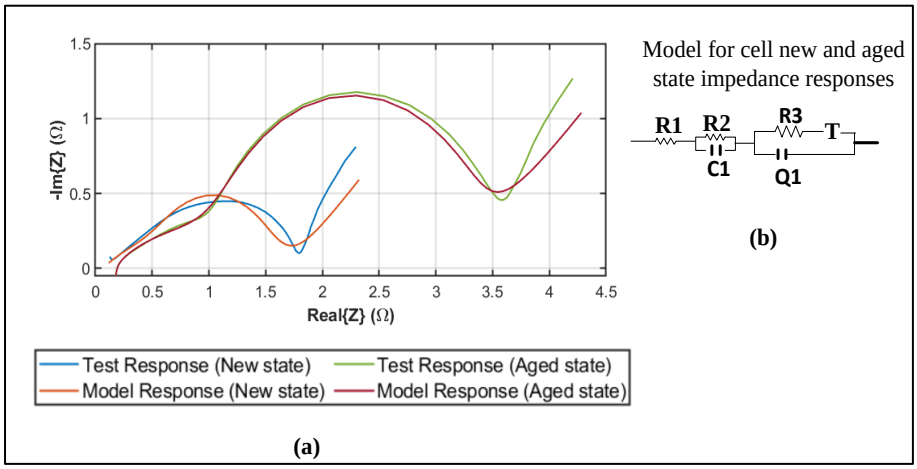

Figure C.12 EIS Impedance based responses and model for cell 12 (a) EIS test impedance and EIS-based ECM impedance for new and aged state. (b) ECM models for new and aged state.

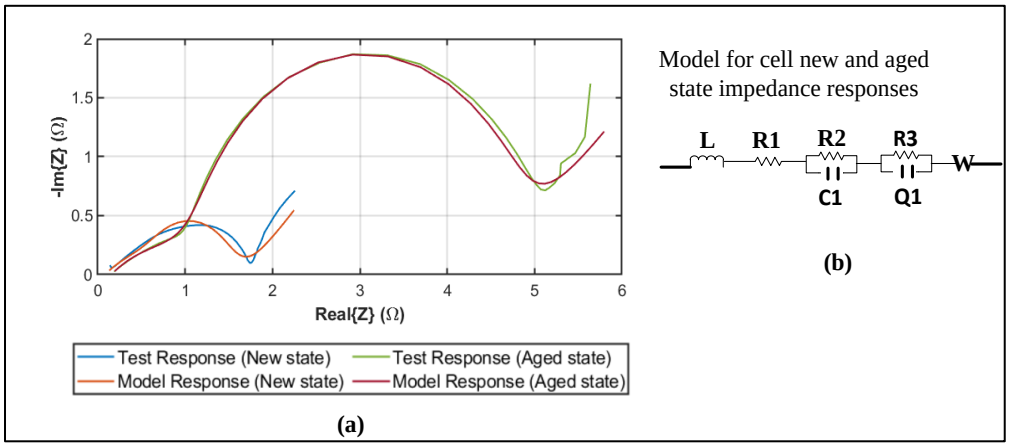

Figure C.13 EIS Impedance based responses and model for cell 13 (a) EIS test impedance and EIS-based ECM impedance for new and aged state. (b) ECM models for new and aged state.

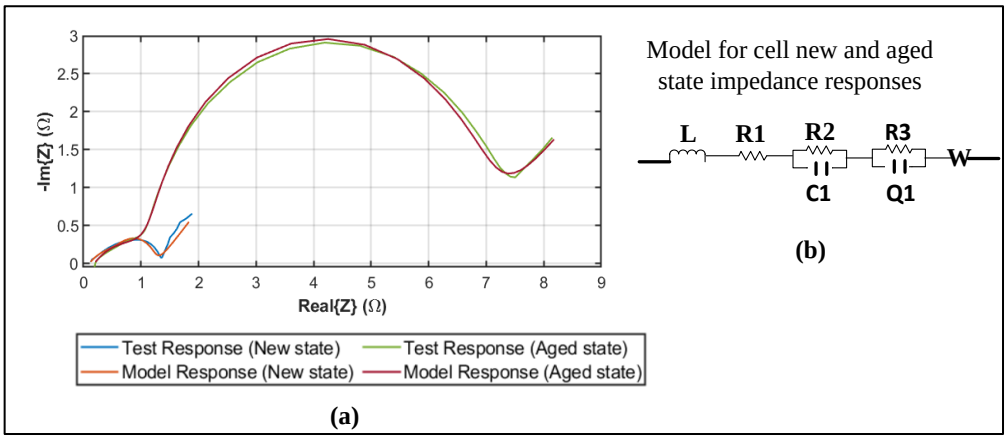

Figure C.14 EIS Impedance based responses and model for cell 14 (a) EIS test impedance and EIS-based ECM impedance for new and aged state. (b) ECM models for new and aged state.

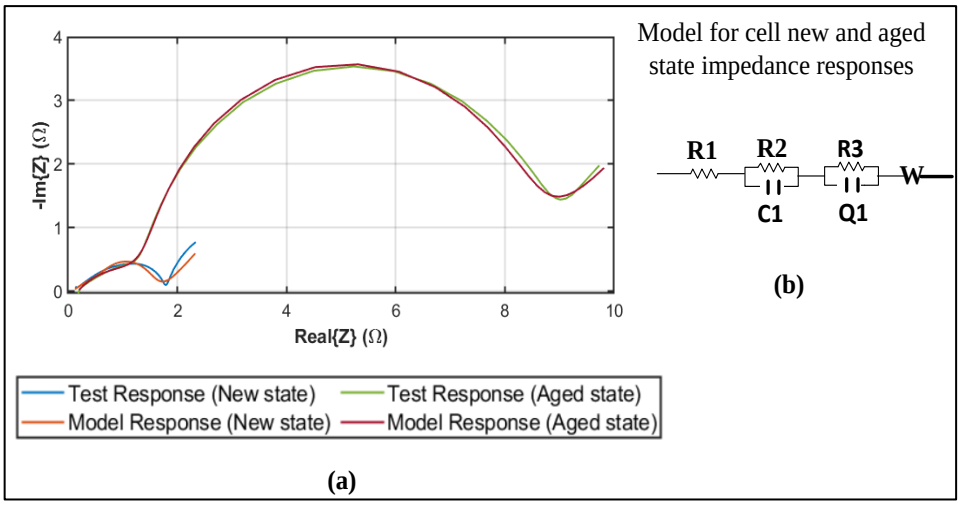

Figure C.15 EIS Impedance based responses and model for cell 15 (a) EIS test impedance and EIS-based ECM impedance for new and aged state. (b) ECM models for new and aged state.

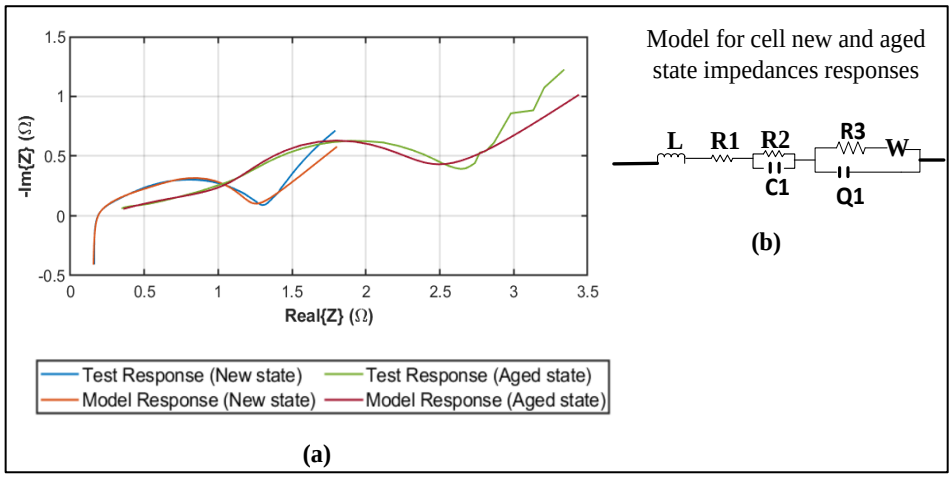

Figure C.16 EIS Impedance based responses and model for cell 16 (a) EIS test impedance and EIS-based ECM impedance for new and aged state. (b) ECM models for new and aged state

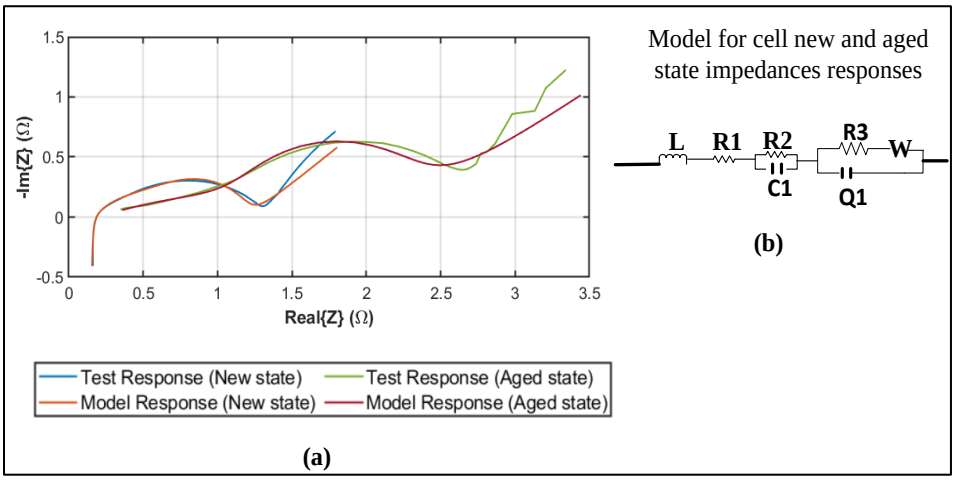

Figure C.17 EIS Impedance based responses and model for cell 16 (a) EIS test impedance and EIS-based ECM impedance for new and aged state. (b) ECM models for new and aged state.

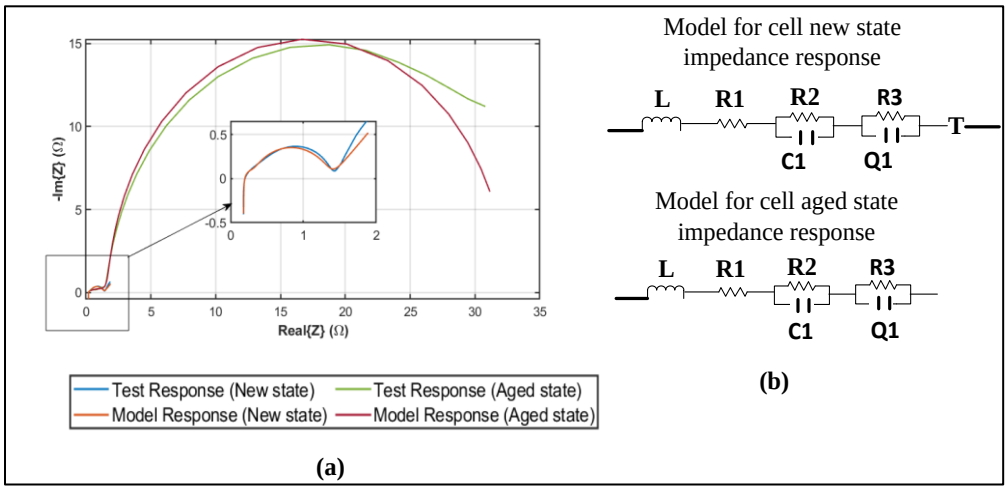

Figure C.18 EIS Impedance based responses and model for cell 18 (a) EIS test impedance and EIS-based ECM impedance for new and aged state. (b) ECM models for new and aged state.

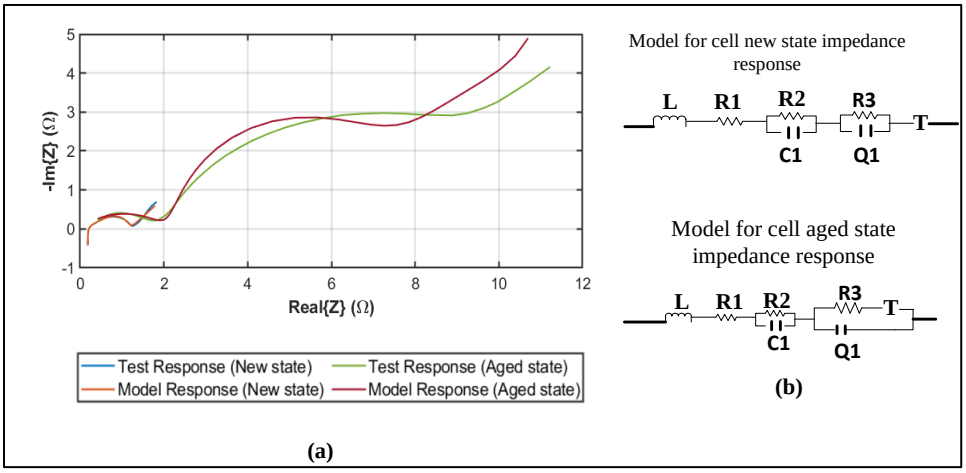

Figure C. 19 EIS Impedance based responses and model for cell 19 (a) EIS test impedance and EIS-based ECM impedance for new and aged state. (b) ECM models for new and aged state.

Table C.1 New state and aged state ECM Model parameters for cells

Cell 1									
New state	L_1	R_1	R_2	C_1	R_3	Qy_1	Qn_1	Ws_1	
	5.40E-08	0.131	0.735	0.024	1.209	0.027	0.561	0.257	
Aged state	L_1	R_1	R_2	C_1	R_3	Qy_1	Qn_1	Ws_1	
	5.40E-08	0.138	1.43	0.055	1.24	0.037	0.530	0.381	
Cell 2									
New state	L_1	R_1	R_2	C_1	R_3	Ws_1	Qy_1	Qn_1	
	9.51E-08	0.120	0.396	0.085	1.980	0.178	0.043	0.493	
Aged state	L_1	R_1	R_2	C_1	R_3	Qy_1	Qn_1	Ws_1	
	1.20E-07	0.117	1.397	0.104	1.398	0.072	0.433	0.297	
Cell 3									
New state	L_1	R_1	R_2	C_1	R_3	Qy_1	Qn_1	Ws_1	
	1.49E-07	0.103	0.557	0.013	1.960	0.079	0.404	0.158	
Aged state	L_1	R_1	R_2	C_1	R_3	Qy_1	Qn_1	Ws_1	
	2.25E-08	0.122	0.740	0.101	1.236	0.071	0.436	0.246	
Cell 4									
New state	L_1	R_1	R_2	C_1	R_3	Ws_1	Qy_1	Qn_1	
	8.15E-08	0.134	0.583	0.023	1.373	0.227	0.033	0.517	
Aged state	L_1	R_1	R_2	C_1	R_3	Qy_1	Qn_1	Ws_1	
	8.15E-08	0.139	0.857	0.052	1.158	0.040	0.501	0.299	
Cell 5									
New state	L_1	R_1	R_2	C_1	R_3	Ts_1	Tt_1	Qy_1	Qn_1
	9.69E-08	0.122	0.790	0.015	1.575	0.242	26888.5	0.033	0.493
Aged state	L_1	R_1	R_2	C_1	R_3	Ts_1	Tt_1	Qy_1	Qn_1
	1.13E-08	0.116	0.621	0.051	1.259	0.282	21344.8	0.049	0.457
Cell 6									
New state	L_1	R_1	R_2	C_1	R_3	Qy_1	Qn_1	Ts_1	Tt_1
	1.48E-22	0.107	0.391	0.063	1.214	0.053	0.501	0.197	5060
Aged state	L_1	R_1	R_2	C_1	R_3	Qy_1	Qn_1	Ts_1	Tt_1
	1.49E-23	0.170	6.650	0.100	1.310	0.040	0.53551	0.595	14886
Cell 7									
New state	R_1	R_2	C_1	R_3	Qy_1	Qn_1	Ws_1		
	0.147027	0.879	0.016	1.222	0.017	0.587	0.25968		
Aged state	R_1	R_2	C_1	R_3	Qy_1	Qn_1	Ws_1		
	0.129763	0.776	0.096	1.168	0.062	0.457	0.25152		
Cell 8									
New state	R_1	R_2	C_1	R_3	Qy_1	Qn_1	Ws_1		
	0.115476	0.532	0.019	1.089	0.029	0.517	0.234		
Aged state	R_1	R_2	C_1	R_3	Qy_1	Qn_1	Ws_1		
	0.132699	2.287	0.062	1.355	0.052	0.455	0.424		

Cell 9									
New state	R_1	R_2	C_1	R_3	Qy_1	Qn_1	Ws_1		
	0.115476	0.532	0.0185	1.089	0.0292	0.517	0.235		
Aged state	R_1	R_2	C_1	R_3	Qy_1	Qn_1	Ws_1		
	0.132699	2.284	0.062	1.35	0.052	0.455	0.424		
Cell 10									
New state	R_1	R_2	C_1	R_3	Qy_1	Qn_1	Ws_1		
	0.157	0.496	0.051	1.828	0.0313	0.537	0.206		
Aged state	R_1	R_2	C_1	R_3	Qy_1	Qn_1	Ws_1		
	0.130	0.776	0.09	1.168	0.062	0.457	0.252		
Cell 11									
New state	R_1	R_2	C_1	R_3	Qy_1	Qn_1	Ws_1		
	0.170607	0.674	0.024	1.135	0.019	0.579	0.240		
Aged state	R_1	R_2	C_1	R_3	Qy_1	Qn_1	Ws_1		
	0.150161	0.729	0.046	1.155	0.044	0.481	0.262		
Cell 12									
New state	R_1	R_2	C_1	R_3	Ts_1	Tt_1	Qy_1	Qn_1	
	0.062494	0.62	0.008	1.118	0.211	9709.6	0.072	0.398	
Aged state	L_1	R_1	R_2	C_1	R_3	Ws_1	Qy_1	Qn_1	
	1.236	0.142	1.884	0.064	1.342	0.371	0.068	0.428	
Cell 13									
New state	R_1	R_2	C_1	R_3	Qy_1	Qn_1	Ws_1		
	0.082164	0.540	0.011	1.116	0.068	0.410	0.188		
Aged state	R_1	R_2	C_1	R_3	Qy_1	Qn_1	Ws_1		
	0.154338	3.258	0.065	1.268	0.078	0.417	0.407		
Cell 14									
New state	R_1	R_2	C_1	R_3	Qy_1	Qn_1	Ws_1		
	0.098778	0.389	0.0162	0.804	0.037	0.498	0.193		
Aged state	R_1	R_2	C_1	R_3	Qy_1	Qn_1	Ws_1		
	0.186974	5.388	0.056	1.087	0.038	0.511	0.541		
Cell 15									
New state	R_1	R_2	C_1	R_3	Ws_1	Qy_1	Qn_1		
	0.075361	0.561	0.010	1.158	0.212	0.064	0.412		
Aged state	R_1	R_2	C_1	R_3	Qy_1	Qn_1	Ts_1	Tt_1	
	0.175187	6.454	0.057	1.426	0.036	0.50	0.630	20.174	
Cell 16									
New state	L_1	R_1	R_2	C_1	R_3	Ws_1	Qy_1	Qn_1	
	6.74E-07	0.143	0.336	0.017	0.759	0.205	0.028	0.560	
Aged state	L_1	R_1	R_2	C_1	R_3	Ws_1	Qy_1	Qn_1	
	6.74E-20	0.5100	0.791	0.121	1.992	0.501	0.209	0.244	

Cell 17									
New state	L_1	R_1	R_2	C_1	R_3	Qy_1	Qn_1	Ts_1	Tt_1
	6.95E-07	0.175	0.451	0.012	0.699	0.028	0.566	0.210	215.41
Aged state	L_1	R_1	R_2	C_1	R_3	Qy_1	Qn_1	Ts_1	Tt_1
	6.95E-10	0.52	2.148	0.158	4.565	0.375	0.140	0.533	43698
Cell 18									
New state	L_1	R_1	R_2	C_1	R_3	Qy_1	Qn_1	Ws_1	
	6.43E-07	0.178	0.093	0.0005	1.099	0.016	0.714	0.184	
Aged state	L_1	R_1	R_2	C_1	R_3	Qy_1	Qn_1		
	2.23E-18	0.5	30.30	0.108	2.342	0.106	0.237		
Cell 19									
New state	L_1	R_1	R_2	C_1	R_3	Qy_1	Qn_1	Ts_1	Tt_1
	6.97E-07	0.167	0.400	0.012	0.626	0.0291	0.571	0.212	43385
Aged state	L_1	R_1	R_2	C_1	R_3	Ts_1	Tt_1	Qy_1	Qn_1
	1.05E-18	0.0024	3.8608	0.1141	2.0585	1.8646	8.92950	0.0039	0.454

Appendix D - Datasets and MATLAB Codes for Multivariate Statistical Analysis

D.1 Dataset used in PCA and MSPC

Table D.1 contains the subset of samples selected for PCA and MSPC implementation. Samples 1 to 57 formed the training set for MSPC and the remaining samples 53-130 formed validation samples 1-73.

Table D.1 Summary of Selected Samples for PCA and MSPC

Sample Number	Cell ID	Cycle in lifetime	SoH*	ESR value	Sample Number	Cell ID	Cycle in lifetime	SoH*	ESR value
1	cell 18	22	40.57	0.3	35	cell 6	2	39.04	0.17
2	cell 18	32	35.77	0.34	36	cell 6	22	40.08	0.18
3	cell 19	12	50.18	0.26	37	cell 10	2	32.49	0.2
4	cell 19	22	48.07	0.23	38	cell 10	22	39.53	0.2
5	cell 19	32	47.13	0.31	39	cell 12	2	44.72	0.2
6	cell 19	42	46.09	0.24	40	cell 15	0	32.05	0.23
7	cell 19	52	46.99	0.23	41	cell 15	2	45.62	0.24
8	cell 19	62	46.69	0.23	42	cell 7	0	33.63	0.22
9	cell 19	82	42.62	0.24	43	cell 7	2	43.9	0.21
10	cell 19	102	38.59	0.31	44	cell 8	0	35.91	0.22
11	cell 19	122	39.43	0.29	45	cell 8	2	44.13	0.21
12	cell 16	22	43.22	0.15	46	cell 1	0	46.12	0.19
13	cell 16	32	42.01	0.19	47	cell 1	2	32.04	0.2
14	cell 16	42	41.63	0.18	48	cell 1	22	46.91	0.19
15	cell 16	52	41.61	0.17	49	cell 3	0	46.13	0.22
16	cell 16	62	41.5	0.2	50	cell 3	2	34.2	0.23
17	cell 16	82	36.89	0.35	51	cell 3	42	32.86	0.22
18	cell 16	102	37.16	0.3	52	cell 2	2	46.02	0.21
19	cell 17	2	50.82	0.22	53	cell 2	22	34.26	0.21
20	cell 17	12	48.73	0.26	54	cell 2	42	32.66	0.21
21	cell 17	22	43.5	0.18	55	cell 2	62	34.77	0.21
22	cell 17	32	42.77	0.21	56	cell 14	0	44.1	0.24
23	cell 17	42	42.45	0.17	57	cell 14	2	43.59	0.25
24	cell 17	52	42.68	0.26	58	cell 18	2	48.45	0.21
25	cell 17	62	42.47	0.17	59	cell 19	0	52.09	0.22
26	cell 4	0	46.22	0.22	60	cell 16	0	49.44	0.2
27	cell 4	2	37	0.21	61	cell 17	0	50.82	0.19
28	cell 13	0	46.21	0.23	62	cell 19	2	50.27	0.21
29	cell 13	2	38.63	0.22	63	cell 16	12	46.87	0.24
30	cell 9	0	46.76	0.21	64	cell 17	82	37.91	0.2
31	cell 9	2	37.61	0.21	65	cell 19	202	36.03	0.22
32	cell 5	0	45.8	0.23	66	cell 18	42	33.26	0.4
33	cell 5	2	35.69	0.22	67	cell 9	42	30.92	0.21
34	cell 11	2	33.09	0.21	68	cell 5	22	29.62	0.22

69	cell 13	22	29.56	0.22	109	cell 8	102	18.32	0.22
70	cell 16	222	31.6	0.27	110	cell 7	62	18.94	0.22
71	cell 13	42	29.49	0.23	111	cell 14	42	17.53	0.26
72	cell 9	22	29.83	0.21	112	cell 10	82	17.9	0.24
73	cell 3	62	29.42	0.22	113	cell 15	22	17.03	0.24
74	cell 3	82	29.4	0.23	114	cell 15	42	16.56	0.23
75	cell 2	102	28.77	0.22	115	cell 10	142	16.31	0.23
76	cell 8	22	27.4	0.21	116	cell 14	62	14.69	0.25
77	cell 2	82	28.58	0.21	117	cell 12	82	15.76	0.23
78	cell 5	42	28.21	0.22	118	cell 7	102	14.75	0.23
79	cell 8	42	25.75	0.21	119	cell 15	82	14.07	0.24
80	cell 1	42	26.78	0.19	120	cell 14	102	13.65	0.24
81	cell 6	82	27.54	0.2	121	cell 12	142	14.76	0.23
82	cell 11	42	25.88	0.21	122	cell 12	202	12.06	0.24
83	cell 5	62	26.11	0.23	123	cell 11	82	10.66	0.24
84	cell 4	22	26.31	0.21	124	cell 18	102	11.18	0.6
85	cell 13	62	26.11	0.24	125	cell 16	442	7.77	0.49
86	cell 4	42	25.44	0.21	126	cell 11	142	7.04	0.24
87	cell 10	42	25.46	0.22	127	cell 17	442	6.22	0.52
88	cell 6	62	25.89	0.21	128	cell 19	362	3.7	1.03
89	cell 9	62	25.19	0.22	129	cell 11	202	3.09	0.24
90	cell 3	102	23.67	0.22	130	cell 18	202	1.08	0.57
91	cell 8	62	22.43	0.22					
92	cell 12	42	24.01	0.21					
93	cell 7	42	23.02	0.21					
94	cell 5	102	22.76	0.22					
95	cell 7	22	22.3	0.21					
96	cell 6	202	23.2	0.23					
97	cell 1	62	22.43	0.19					
98	cell 4	62	22.38	0.22					
99	cell 17	222	24.54	0.26					
100	cell 9	102	21.72	0.22					
101	cell 14	22	20.16	0.25					
102	cell 1	122	21.03	0.2					
103	cell 10	202	21.18	0.24					
104	cell 4	102	20.85	0.22					
105	cell 6	142	20.78	0.2					
106	cell 1	82	19.95	0.2					
107	cell 15	122	19.14	0.25					
108	cell 13	102	19.5	0.24					

* SoH = Remaining Capacity (mAh)

D.2 PCA MATLAB Code

```
% Preprocess data using normalization (zscore)
[PCA_EIS_AllDataNorm22,    PCA_EIS_AllDataMean22,    PCA_EIS_AllDataStd22]    =
zscore(PCA_EIS_AllDataRaw22);
```

```
% Implement pca
[PCA_EIS_AllDataLoadings22,  PCA_EIS_AllDataScore22,  PCA_EIS_AllDatalatent22,
PCA_EIS_AllDataTsquared22,PCA_EIS_AllDataexplained22]                          =
pca(PCA_EIS_AllDataNorm22);

figure("Name",'PCA_EIS_AllData scree')
bar(PCA_EIS_AllDataexplained22(1:20),1,'FaceColor',[0.0196078431372549,0.07450
98039215686,0.670588235294118])
hold on
plot(1:20,
cumsum(PCA_EIS_AllDataexplained22(1:20)),"Marker","*","LineWidth",2)
xlabel('Principal Components (PCs)',"FontWeight","bold")
ylabel('Variance Explained (%)',"FontWeight","bold")
legend ('PC', 'PC Cummulative percentage variance',"FontSize",12)
grid on
ax=gca;
ax.FontSize = 14;

t1 = 1:25;                      % A @70
t2 = 58:64;                     % A @70
t3 = [65 66 70];                % A@ 69-60
t4 = 99;                        % A@59-30
t5 = [124 125 127 128 130];     % A@30
t6=26:57;                        % B@70
t7=[67:69 71:78];               % B@69-60
t8=[79:98 100:121];                 % B@59-30
t9 = [122 123 126 129];             % B@30

figure("Name”, ‘score plot')
p1                      =                       plot(PCA_EIS_AllDataScore22(t1,1),
PCA_EIS_AllDataScore22(t1,2),"LineStyle","none","LineWidth",2,"Marker","+","Co
lor",'#00FF00');
hold on
plot(PCA_EIS_AllDataScore22(t2,1),
PCA_EIS_AllDataScore22(t2,2),"LineStyle","none","LineWidth",2,"Marker","+","Co
lor",'#00FF00')
p2                      =                       plot(PCA_EIS_AllDataScore22(t3,1),
PCA_EIS_AllDataScore22(t3,2),"LineStyle","none","LineWidth",2,"Marker","+","Co
lor",'#FF00FF');
p3                      =                       plot(PCA_EIS_AllDataScore22(t4,1),
PCA_EIS_AllDataScore22(t4,2),"LineStyle","none","LineWidth",2,"Marker","+","Co
lor",'#FF0000') ;
p4                                             =plot(PCA_EIS_AllDataScore22(t5,1),
PCA_EIS_AllDataScore22(t5,2),"LineStyle","none","LineWidth",2,"Marker","+","Co
lor",'#000000');

% Batch B
plot(PCA_EIS_AllDataScore22(t6,1),
PCA_EIS_AllDataScore22(t6,2),"LineStyle","none","LineWidth",2,"Marker","o","Co
lor",'#00FF00')
plot(PCA_EIS_AllDataScore22(t7,1),
PCA_EIS_AllDataScore22(t7,2),"LineStyle","none","LineWidth",2,"Marker","o","Co
lor",'#FF00FF')
plot(PCA_EIS_AllDataScore22(t8,1),
PCA_EIS_AllDataScore22(t8,2),"LineStyle","none","LineWidth",2,"Marker","o","Co
lor",'#FF0000')
```

```
plot(PCA_EIS_AllDataScore22(t9,1),
PCA_EIS_AllDataScore22(t9,2),"LineStyle","none","LineWidth",2,"Marker","o","Co
lor",'#000000')
grid on;

    ylabel('PC2',"FontSize",12,"FontWeight","bold")
    xlabel('PC1',"FontSize",12,"FontWeight","bold")
    legend([p1 p2 p3 p4],{"cell at 70% and above capacity","cell at 69%-60%
capacity","cell    at    59%-30%    capacity","cell    at    less    than    30%
capacity"},"FontSize",14)
ax = gca;    ax.FontSize = 14;


figure("Name",'Individual PC Loadings and scores')
subplot(3,2,1)
    stem(1:142, PCA_EIS_AllDataLoadings22(:,1))
subplot(3,2,3)
    stem(1:142, PCA_EIS_AllDataLoadings22(:,2))
subplot(3,2,5)
    stem(1:142, PCA_EIS_AllDataLoadings22(:,3))


subplot(3,2,2)
hold on
% Batch A
plot(t1,PCA_EIS_AllDataScore22(t1,1),"LineStyle","none","LineWidth",2,"Marker"
,"+","Color",'#00FF00')
plot(t2,PCA_EIS_AllDataScore22(t2,1),"LineStyle","none","LineWidth",2,"Marker"
,"+","Color",'#00FF00')
plot(t3,PCA_EIS_AllDataScore22(t3,1),"LineStyle","none","LineWidth",2,"Marker"
,"+","Color",'#FF00FF')
plot(t4,PCA_EIS_AllDataScore22(t4,1),"LineStyle","none","LineWidth",2,"Marker"
,"+","Color",'#FF0000')
plot(t5,PCA_EIS_AllDataScore22(t5,1),"LineStyle","none","LineWidth",2,"Marker"
,"+","Color",'#000000')
 % Batch B

plot(t6,PCA_EIS_AllDataScore22(t6,1),"LineStyle","none","LineWidth",2,"Marker"
,"o","Color",'#00FF00')

    plot(t7,
PCA_EIS_AllDataScore22(t7,1),"LineStyle","none","LineWidth",2,"Marker","o","Co
lor",'#FF00FF')
plot(t8,PCA_EIS_AllDataScore22(t8,1),"LineStyle","none","LineWidth",2,"Marker"
,"o","Color",'#FF0000')
plot(t9,PCA_EIS_AllDataScore22(t9,1),"LineStyle","none","LineWidth",2,"Marker"
,"o","Color",'#000000')
    grid on;
    ylabel('Score',"FontSize",12,"FontWeight","bold")
    xlabel('PC1',"FontSize",12,"FontWeight","bold")

subplot(3,2,4)
hold on
% Batch A
plot(t1,PCA_EIS_AllDataScore22(t1,2),"LineStyle","none","LineWidth",2,"Marker"
,"+","Color",'#00FF00')
```

```
plot(t2,PCA_EIS_AllDataScore22(t2,2),"LineStyle","none","LineWidth",2,"Marker"
,"+","Color",'#00FF00')
plot(t3,PCA_EIS_AllDataScore22(t3,2),"LineStyle","none","LineWidth",2,"Marker"
,"+","Color",'#FF00FF')
plot(t4,PCA_EIS_AllDataScore22(t4,2),"LineStyle","none","LineWidth",2,"Marker"
,"+","Color",'#FF0000')
plot(t5,PCA_EIS_AllDataScore22(t5,2),"LineStyle","none","LineWidth",2,"Marker"
,"+","Color",'#000000')
% Batch B
plot(t6,PCA_EIS_AllDataScore22(t6,2),"LineStyle","none","LineWidth",2,"Marker"
,"o","Color",'#00FF00')
plot(t7,PCA_EIS_AllDataScore22(t7,2),"LineStyle","none","LineWidth",2,"Marker"
,"o","Color",'#FF00FF')
plot(t8,PCA_EIS_AllDataScore22(t8,2),"LineStyle","none","LineWidth",2,"Marker"
,"o","Color",'#FF0000')
plot(t9,PCA_EIS_AllDataScore22(t9,2),"LineStyle","none","LineWidth",2,"Marker"
,"o","Color",'#000000')
 grid on;
 ylabel('Score',"FontSize",12,"FontWeight","bold")
 xlabel('PC2',"FontSize",12,"FontWeight","bold")

subplot(3,2,6)
hold on
% Batch A
plot(t1,PCA_EIS_AllDataScore22(t1,3),"LineStyle","none","LineWidth",2,"Marker"
,"+","Color",'#00FF00')
plot(t2,PCA_EIS_AllDataScore22(t2,3),"LineStyle","none","LineWidth",2,"Marker"
,"+","Color",'#00FF00')
plot(t3,PCA_EIS_AllDataScore22(t3,3),"LineStyle","none","LineWidth",2,"Marker"
,"+","Color",'#FF00FF')
plot(t4,PCA_EIS_AllDataScore22(t4,3),"LineStyle","none","LineWidth",2,"Marker"
,"+","Color",'#FF0000')
plot(t5,PCA_EIS_AllDataScore22(t5,3),"LineStyle","none","LineWidth",2,"Marker"
,"+","Color",'#000000')
% Batch B
plot(t6,PCA_EIS_AllDataScore22(t6,3),"LineStyle","none","LineWidth",2,"Marker"
,"o","Color",'#00FF00')
plot(t7,PCA_EIS_AllDataScore22(t7,3),"LineStyle","none","LineWidth",2,"Marker"
,"o","Color",'#FF00FF')
plot(t8,PCA_EIS_AllDataScore22(t8,3),"LineStyle","none","LineWidth",2,"Marker"
,"o","Color",'#FF0000')
plot(t9,PCA_EIS_AllDataScore22(t9,3),"LineStyle","none","LineWidth",2,"Marker"
,"o","Color",'#000000')
    grid on;
    ylabel('Score',"FontSize",12,"FontWeight","bold")
    xlabel('PC3',"FontSize",12,"FontWeight","bold")
```

D.3 MSPC MATLAB Code

```
% Preprocess data using normalization (zscore)

[MSPC_EIS_TrainDataNorm,   MSPC_EIS_TrainDataMean,   MSPC_EIS_TrainDataStd]   =
zscore(MSPC_EIS_TrainDataRaw);
```

```
% Implement pca
[MSPC_EIS_TrainDataLoadings, MSPC_EIS_TrainDataScore, MSPC_EIS_TrainDatalatent,
MSPC_EIS_TrainDataTsquared,MSPC_EIS_TrainDataexplained]                    =
pca(MSPC_EIS_TrainDataNorm);

figure("Name",'PCA_EIS_AllData scree')
bar(MSPC_EIS_TrainDataexplained(1:20),1,'FaceColor',[0.0196078431372549,0.0745
098039215686,0.670588235294118])
hold on
plot(1:20,
cumsum(MSPC_EIS_TrainDataexplained(1:20)),"Marker","*","LineWidth",2)
xlabel('Principal Components (PCs)',"FontWeight","bold")
ylabel('Variance Explained (%)',"FontWeight","bold")
legend ('PC', 'PC Cummulative percentage variance',"FontSize",12)
grid on
ax=gca;
ax.FontSize = 14;


% Assign number to PCs to a
MSPC_EIS_Train_PCsel = 2;
a1 = MSPC_EIS_Train_PCsel;

% Find Tsqurared in pca space thus mahalanobis distance
MSPC_EIS_TrainData_Mahal                                                   =
mahal(MSPC_EIS_TrainDataScore(:,1:MSPC_EIS_Train_PCsel),MSPC_EIS_TrainDataScor
e(:,1:MSPC_EIS_Train_PCsel));

N = 57;                 % number of rows in faulty matrix
alpha = 0.05;           % 0.05 significance level used in ttest

% Fvalue = 3.16;        % read from F-distribution table F(0.05,2,58)
Fvalue = 2.77;        % read from F-distribution table F(0.05,3,57)
MSPC_EIS_TrainData_Tlimit   =   (((((N^2)-1)*MSPC_EIS_Train_PCsel)   /   (N*(N-
MSPC_EIS_Train_PCsel))))*Fvalue


% Find residuals of PCA using the number of selected PCs
MSPC_EIS_TrainData_Residual          =          pcares(MSPC_EIS_TrainDataNorm,
MSPC_EIS_Train_PCsel);

% Find SPE as sum of squares of residuals using SPE = sum of columns(res^2)
% equation format 2 using matrices and finding sum(x-(xhat))^2

MSPC_EIS_TrainData_SPE = sum(((MSPC_EIS_TrainDataNorm -MSPC_EIS_TrainDataNorm *
MSPC_EIS_TrainDataLoadings(:,1:a1)*MSPC_EIS_TrainDataLoadings(:,1:a1)')').^2);

MSPC_EIS_TrainData_SPEcon= ((MSPC_EIS_TrainDataNorm -MSPC_EIS_TrainDataNorm *
MSPC_EIS_TrainDataLoadings(:,1:a1)*MSPC_EIS_TrainDataLoadings(:,1:a1)')').^2;

% calpha = 1.96;                                    % standard normal deviate
~1.96 for alpha = 0.05
calpha = 1.645;

MSPC_EIS_TrainData_theta1 = sum(MSPC_EIS_TrainDatalatent(a1+1:56));
MSPC_EIS_TrainData_theta2 = sum(MSPC_EIS_TrainDatalatent(a1+1:56).^2);
MSPC_EIS_TrainData_theta3 = sum(MSPC_EIS_TrainDatalatent(a1+1:56).^3);
```

```
% finding ho
t3 = 2*MSPC_EIS_TrainData_theta1*MSPC_EIS_TrainData_theta3;
t4 = 3*(MSPC_EIS_TrainData_theta2^2);
ho = 1-(t3/t4);

% Find the Q limit
t5 = (ho*calpha*(sqrt(2*MSPC_EIS_TrainData_theta2)))/MSPC_EIS_TrainData_theta1;
t6 = (MSPC_EIS_TrainData_theta2*ho*(ho-1)) / ((MSPC_EIS_TrainData_theta1)^2);
MSPC_EIS_TrainDatalatent_Qlimit = MSPC_EIS_TrainData_theta1*((t5 + 1 +
t6)^(1/ho))

% Fault Matrix
MSPC_EIS_ValDataRaw;

% normalise fault data
MSPC_EIS_ValDataNorm = zeros(73,142);                          % new EIS data
normalised to capTrain dataset

for i = 1:142
    MSPC_EIS_ValDataNorm(:,i)       =       (MSPC_EIS_ValDataRaw(:,i)       -
    MSPC_EIS_TrainDataMean(i))./ MSPC_EIS_TrainDataStd(i);
end

tt7 = MSPC_EIS_ValDataNorm;                 % normalised raw data matrix
t8 = MSPC_EIS_TrainDataLoadings(:,1:a1);                    % [pc coeffs]
t9 = diag(MSPC_EIS_TrainDatalatent(1:a1));                % forming a diagonal
matrix so inverse can be found
t10 = inv(t9);                                          % (lambda pc)^-1

% [z] * [PCvector]* inv[eigenValues]*transpose[PCvector]*transpose[z]
MSPC_EIS_ValDataTSorted2 = (tt7*t8(:,1)).^2/MSPC_EIS_TrainDatalatent(1);
MSPC_EIS_ValDataTSorted2         =         MSPC_EIS_ValDataTSorted2         +
(tt7*t8(:,2)).^2/MSPC_EIS_TrainDatalatent(2);


%   Faulty SPE                                  ((x-x*p*p')')^2

MSPC_EIS_ValDataQSorted2 = sum(((MSPC_EIS_ValDataNorm - MSPC_EIS_ValDataNorm *
MSPC_EIS_TrainDataLoadings(:,1:a1)*MSPC_EIS_TrainDataLoadings(:,1:a1)')').^2);

% SPE contributions
MSPC_EIS_ValDataQconSorted2 = ((MSPC_EIS_ValDataNorm - MSPC_EIS_ValDataNorm *
MSPC_EIS_TrainDataLoadings(:,1:a1)*MSPC_EIS_TrainDataLoadings(:,1:a1)')').^2;


figure("Name", 'eis stats colours')
m1 = 1:7;          % 70% and above
m2 = [8 9 13];     %  60% and above
m3 = 42;           % 59% and below
m4 =[67 68 70 71 73];     % 30% and below
m5 = [10:12 14:21];
m6 = [22:41 43:64];
m7 = [65 66 69 72];


figure("Name", 'sorted pp stats colours')
```

```
subplot (2,1,1)

semilogy(1:25,MSPC_EIS_TrainData_Mahal(1:25),'LineWidth',2,'Marker','+','Color
','b')
hold on
semilogy(26:57,     MSPC_EIS_TrainData_Mahal(26:57),'LineWidth',2,'Marker','o',
'Color','b')
yline(MSPC_EIS_TrainData_Tlimit,'--','LineWidth',3,"Color",'r')

 % batch A

semilogy(m1,MSPC_EIS_ValDataTSorted2(m1),'LineWidth',2,"Color",'g','Marker','+
')
%                       70%                       and                       above
semilogy(m2,MSPC_EIS_ValDataTSorted2(m2),'LineWidth',2,"Color",'m','Marker','+
')
 %60% and above
semilogy(m3,MSPC_EIS_ValDataTSorted2(m3),'LineWidth',2,"Color",'r','Marker','+
')
%59% and below
semilogy(m4,MSPC_EIS_ValDataTSorted2(m4),'LineWidth',2,"Color",'k','Marker','+
')
% 30% and below    % batch B


semilogy(m5,MSPC_EIS_ValDataTSorted2(m5),'LineWidth',2,"Color",'m','Marker','o
')                              %                   60%         and         above
semilogy(m6,MSPC_EIS_ValDataTSorted2(m6),'LineWidth',2,"Color",'r','Marker','o
')                                  %           59%           and           below
semilogy(m7,MSPC_EIS_ValDataTSorted2(m7),'LineWidth',2,"Color",'k','Marker','o
')   % 30% and below
    grid on
    ylabel('T^2 Statistic', "FontSize",14,"FontWeight","bold")
    xlabel({'Sample Number';'(a)'}, "FontSize",14,"FontWeight","bold")
    ax = gca;
    legend('Training   Dataset','T^2   threshold',   'Cells   at   Above   70%
Capacity','Cells at 69%-60% Capacity','Cells at 59%-30% Capacity','Cells at
below 30% Capacity')
    ax.FontSize = 14;


subplot (2,1,2)
hold on
semilogy(1:25,
MSPC_EIS_TrainData_SPE(1:25),'LineWidth',2,'Marker','+','Color','b')
 semilogy(26:57,      MSPC_EIS_TrainData_SPE(26:57),'LineWidth',2,'Marker','o',
'Color','b')
yline(MSPC_EIS_TrainDatalatent_Qlimit,'--','LineWidth',3,"Color",'r')


% batch A
plot(m1,MSPC_EIS_ValDataQSorted2(m1),'LineWidth',2,"Color",'g','Marker','+')
% 70% and above

plot(m2,MSPC_EIS_ValDataQSorted2(m2),'LineWidth',2,"Color",'m','Marker','+')
% 60% and above
```

```
plot(m3,MSPC_EIS_ValDataQSorted2(m3),'LineWidth',2,"Color",'r','Marker','+')
% 59% and below

plot(m4,MSPC_EIS_ValDataQSorted2(m4),'LineWidth',2,"Color",'k','Marker','+')
% 30% and below
% batch B
plot(m5,MSPC_EIS_ValDataQSorted2(m5),'LineWidth',2,"Color",'m','Marker','o')
% 60% and above
plot(m6,MSPC_EIS_ValDataQSorted2(m6),'LineWidth',2,"Color",'r','Marker','o')
% 59% and below
 plot(m7,MSPC_EIS_ValDataQSorted2(m7),'LineWidth',2,"Color",'k','Marker','o')
% 30% and below
    grid on
    ylabel('SPE', "FontSize",12,"FontWeight","bold")
    xlabel({'Sample Number';'(b)'}, "FontSize",12,"FontWeight","bold")
    ax = gca;
ax.FontSize = 14;
set(gca,'YScale','log')
```

D.4 Results for MSPC Implemented using all S-parameters

Figures D.1 to D.4 show the results for MSPC done when considering the entire S parameters. The training matrix was 57×1608 and the validation matrix was 73×1608. Figure D.1 shows the scree plot and D.2 shows the score plot of the training data. Figures D.3 and D.4 show the T^2 and SPE control charts for the FDR Data.

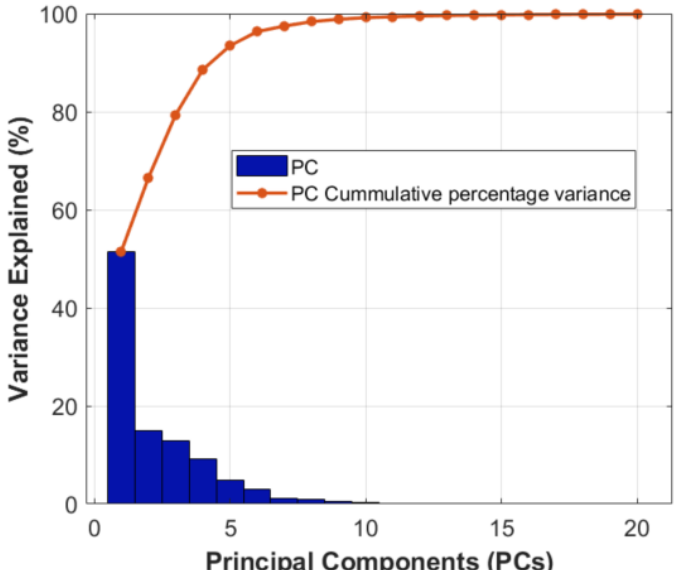

Figure D.1 Scree plot for PCA-based MSPC based on using all FDR S-parameters

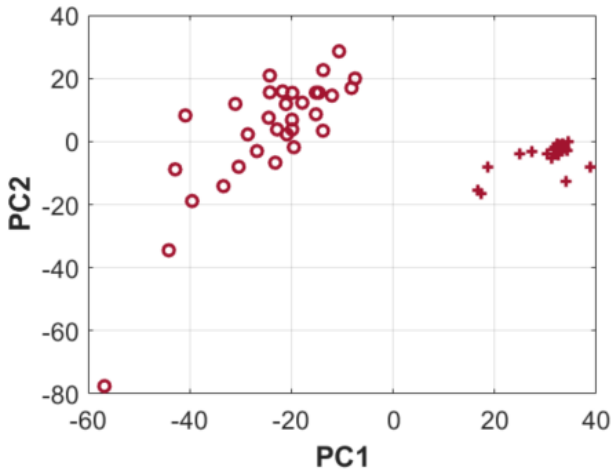

Figure D.2 Score projection for PCA-based MSPC on using all FDR S-parameters.

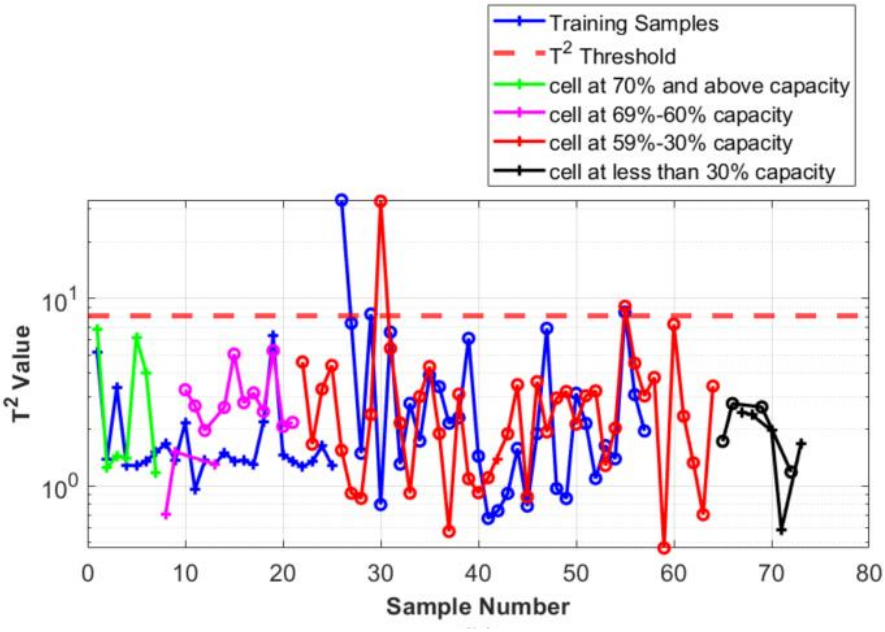

Figure D.3 T^2 Control Chart based on using all FDR S-parameters.

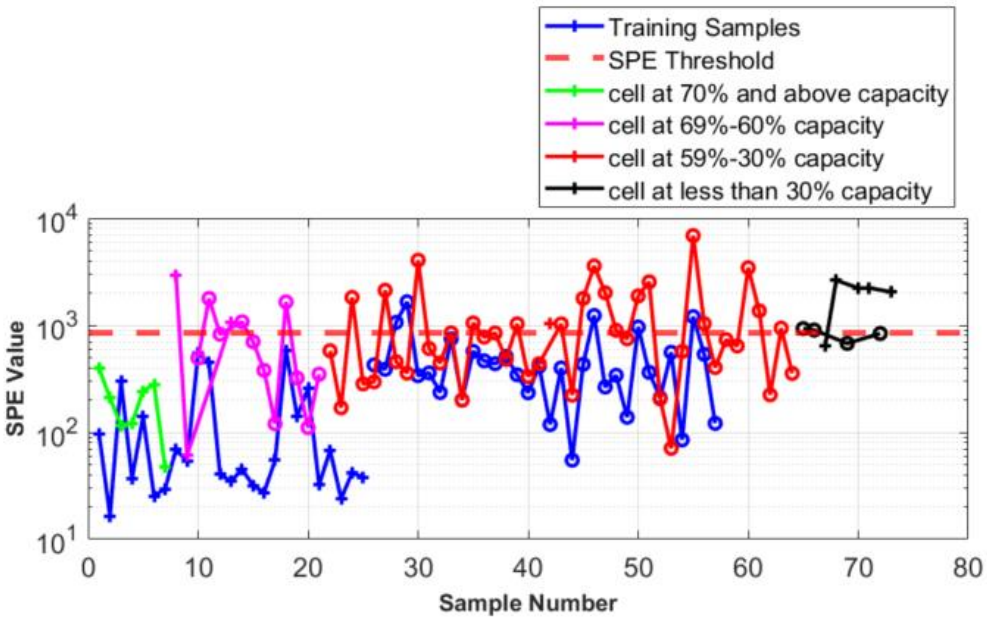

Figure D.4 SPE Control Chart based on using all FDR S-parameters.

D.5 Dataset used for PLSR

Tables D.2 and D.3 presents details of samples used in PLSR. All cycles of the sample cells were used in the PLSR implementation.

Table D.2 Details of samples used in PLSR training dataset.

Sample Number	Cell ID	Cycle in lifetime	SoH*	ESR value	Sample Number	Cell ID	Cycle in lifetime	SoH*	ESR value
1	Cell 18	2	48.45	0.21	36	Cell 16	2	49.44	0.2
2		12	46.66	0.22	37		12	46.87	0.24
3		22	40.57	0.3	38		22	43.22	0.15
4		32	35.77	0.34	39		32	42.01	0.19
5		42	33.26	0.4	40		42	41.63	0.18
6		52	34.03	0.44	41		52	41.61	0.17
7		62	32.53	0.35	42		62	41.5	0.2
8		82	18.43	0.39	43		82	36.9	0.35
9		102	11.18	0.6	44		102	37.16	0.3
10		122	5.54	0.51	45		122	34.8	0.24
11		142	2.19	0.51	46		142	33.84	0.24
12		162	1.99	0.55	47		162	33.04	0.24
13		182	1.05	0.51	48		182	32.68	0.24
14		202	1.08	0.57	49		202	32.83	0.25
15	Cell 19	2	52.09	0.21	50		222	31.6	0.27
16		12	50.18	0.26	51		262	32.75	0.25
17		22	48.07	0.23	52		282	31.11	0.26
18		32	47.13	0.31	53		302	26.35	0.26
19		42	46.09	0.24	54		322	24.71	0.28
20		52	46.99	0.23	55		342	21.83	0.31
21		62	46.69	0.23	56		362	19.78	0.32
22		82	38.32	0.24	57		382	15.9	0.33
23		102	38.59	0.31	58		402	14.09	0.38
24		122	36.23	0.29	59		422	12.64	0.46
25		142	35.91	0.21	60		442	8.71	0.49
26		162	35.95	0.21	61	Cell 4	2	46.22	0.22
27		182	35.26	0.21	62		22	26.31	0.21
28		202	36.03	0.22	63		42	25.44	0.21
29		222	34.67	0.22	64		62	22.38	0.22
30		262	33.89	0.22	65		82	22.9	0.22
31		282	31.52	0.23	66		102	20.85	0.22
32		302	25.66	0.23	67	Cell 13	2	46.21	0.23
33		322	9.8	0.59	68		22	29.56	0.22
34		342	3.96	0.88	69		42	29.49	0.23
35		362	3.84	1.03	70		62	26.31	0.24
					71		82	24.32	0.24
					72		102	19.5	0.24

73	Cell 9	2	46.76	0.21	105	Cell 15	2	44.72	0.23
74		22	30.6	0.21	106		22	17.03	0.24
75		42	30.92	0.21	107		42	16.56	0.23
76		62	25.19	0.22	108		62	15.31	0.25
77		82	21.5	0.22	109		82	14.07	0.24
78		102	21.72	0.22	110		102	14.58	0.23
79	Cell 11	22	27.28	0.22	111	Cell 7	2	45.62	0.22
80		42	25.88	0.21	112		22	22.3	0.21
81		62	11.17	0.24	113		42	23.02	0.21
82		82	10.66	0.24	114		62	18.94	0.22
83		102	9.15	0.23	115		82	15.87	0.23
84		122	10.31	0.24	116		102	14.75	0.23
85		142	7.04	0.24	117	Cell 1	2	46.12	0.19
86		162	6.85	0.24	118		22	29.78	0.2
87		182	6.72	0.25	119		42	26.78	0.19
88		202	3.09	0.24	120		62	22.43	0.19
89	Cell 6	22	39.04	0.18	121		82	19.95	0.2
90		42	39.2	0.18	122		102	21.03	0.19
91		62	25.89	0.21	123	Cell 3	2	46.13	0.22
92		82	27.54	0.2	124		22	34.22	0.23
93		102	27.98	0.21	125		42	30.06	0.22
94		122	25.58	0.2	126		62	29.42	0.22
95		142	20.78	0.2	127		82	29.4	0.23
96		162	24.25	0.21	128		102	23.67	0.22
97		182	27.53	0.21	129	Cell 2	2	46.02	0.21
98		202	23.2	0.23	130		22	34.95	0.21
99	Cell 10	22	32.49	0.2	131		42	32.66	0.21
100		42	25.46	0.2	132		62	34.77	0.21
101		62	19.67	0.22	133		82	28.58	0.21
102		82	17.9	0.24	134		102	28.77	0.22
103		102	17.43	0.22					
101		62	19.67	0.22					
102		82	17.9	0.24					
103		102	17.43	0.22					
104		122	12.33	0.23					

* SoH = Remaining Capacity (mAh)

Table D.3 Details of samples used in PLSR validation dataset.

Sample Number	Cell ID	Cycle in lifetime	SoH*	ESR value	Sample Number	Cell ID	Cycle in lifetime	SoH*	ESR value
1	Cell 17	2	50.82	0.22	36		102	14.63	0.23
2		12	48.73	0.26	37		122	15.69	0.24
3		22	44.1	0.18	38		142	14.76	0.23
4		32	42.77	0.21	39		162	13.89	0.23
5		42	42.45	0.17	40		182	16.19	0.25
6		52	42.68	0.26	41		202	12.06	0.24
7		62	42.47	0.17	42	Cell 8	2	43.9	0.22
8		82	34.65	0.2	43		22	27.4	0.21
9		102	31.05	0.26	44		42	25.75	0.21
10		122	30.26	0.23	45		62	22.43	0.22
11		142	28.46	0.23	46		82	21.83	0.23
12		162	28.51	0.23	47		102	18.32	0.22
13		182	27.81	0.24	48	Cell 14	2	43.59	0.24
14		202	26.53	0.24	49		22	20.32	0.25
15		222	25.76	0.26	50		42	17.53	0.26
16		262	24.54	0.27	51		62	14.69	0.25
17		282	22.88	0.29	52		82	13.74	0.25
18		302	23.52	0.31	53		102	13.65	0.24
19		322	18.1	0.37					
20		342	17.2	0.39					
21		362	15.03	0.39					
22		382	12.56	0.42					
23		402	6.65	0.48					
24		422	5.03	0.54					
26	Cell 5	2	45.8	0.23					
27		22	29.62	0.22					
28		42	28.21	0.22					
29		62	26.11	0.23					
30		82	20.86	0.23					
31		102	22.76	0.22					
32	Cell 12	22	30.13	0.2					
33		42	25.3	0.21					
34		62	17.99	0.23					
35		82	15.76	0.23					

* SoH = Remaining Capacity (mAh)

D.6 PLSR code implemented in MATLAB

```
% standardised training set
[PLS_pp_TrainPredS21_Scaled,                    PLS_pp_TrainPredS21_ScaleMean,
PLS_pp_TrainPredS21_ScaledSTD] = zscore(PLS_pp_TrainPredS21_Raw);
[PLS_pp_TrainResS21_Scaled,                     PLS_pp_TrainResS21_ScaleMean,
PLS_pp_TrainResS21_ScaledSTD] = zscore(PLS_pp_TrainResS21_Raw);
```

```
% implement PLSregress
[PLS_pp_TrainPredS21_load,PLS_pp_TrainResS21_Load,PLS_pp_TrainPredS21_Score,PL
S_pp_TrainResS21_Score,PLS_pp_TrainS21_beta,PLS_pp_TrainS21_PCTVAR]          =
plsregress(...
    PLS_pp_TrainPredS21_Scaled,PLS_pp_TrainResS21_Scaled,20);


% Plot the percent of variance explained in the response variable as a function
of the number of components.
figure("Name",'Response Matrix Variability Explained by Components')
bar((PLS_pp_TrainS21_PCTVAR(2,:)*100),'DisplayName','Latent Variables')
hold on
plot(1:20,cumsum(100*PLS_pp_TrainS21_PCTVAR(2,:)),'-
bo','DisplayName','Cummulative                                    Explained
Variance',"LineWidth",1.5,"Color",[0.8500 0.3250 0.0980]);
xlabel('Latent Variables',"FontWeight","bold");
ylabel({"Percentage      of      variance      in";      "response      matrix
captured"},"FontWeight","bold");
grid on;
ax = gca;
ax.FontSize = 14;
% title('Response Matrix Variance explained by Principal Components EIS')
legend("show")

% rng(123);
clear rng
n = 30;
[PLS_pp_TrainPredS21_load,PLS_pp_TrainResS21_Load,PLS_pp_TrainPredS21_Score,PL
S_pp_TrainResS21_Score,PLS_pp_TrainS21_beta,PLS_pp_TrainS21_PCTVAR,PLS_pp_Trai
n_MSEP,PLS_pp_Train_stats]                                                    =
plsregress(PLS_pp_TrainPredS21_Scaled,PLS_pp_TrainResS21_Scaled,n,'cv',n);

figure("Name",'Estimated Mean Squared Prediction Error-EIS')
plot(0:n,PLS_pp_Train_MSEP(2,:),"LineWidth",2);
xlabel('Number of Latent variables',"FontWeight","bold");
ylabel({"Estimated Mean Squared"; "Prediction Error"},"FontWeight","bold");
% legend({'PLSR'},'location','NE');
grid on


m=10;
[PLS_pp_TrainPredS21_load2,PLS_pp_TrainResS21_Load2,PLS_pp_TrainPredS21_Score2
,PLS_pp_TrainResS21_Score2,PLS_pp_TrainS21_beta2,PLS_pp_TrainS21_PCTVAR2,PLS_p
p_TrainS21_MSEP2,PLS_pp_TrainS21_stats2]  = plsregress( ...
  PLS_pp_TrainPredS21_Scaled,PLS_pp_TrainResS21_Scaled,m);

% Plot the percent of variance explained in the response variable as a function
of the number of components.
figure("Name",'Response Matrix Variability Explained by selected Components')
bar((PLS_pp_TrainS21_PCTVAR2(2,:)*100),'DisplayName','Principal Components')
hold on
plot(1:m,cumsum(100*PLS_pp_TrainS21_PCTVAR2(2,:)),'-
bo','DisplayName','Cummulative                                    Explained
Variance',"LineWidth",1.5,"Color",[0.8500 0.3250 0.0980]);
```

```
xlabel('PLS Components'); ylabel('Percent Variance Explained in y'); grid on;
title('Response Matrix Variance explained by Principal Components')
legend("show")


%fitting training set
X = PLS_pp_TrainPredS21_Scaled;
XRows = size(X,1);
PLS_pp_TrainS21_Fit = [ones(XRows,1) X]*PLS_pp_TrainS21_beta2;


%      standardised version             <===>    unstandardised version
% [Z,gpamean,gpastdev] = zscore(gpa);   <===>  gpa2 =Z * gpastdev + gpamean;
PLS_pp_TrainS21_Unscaled  =  PLS_pp_TrainS21_Fit*PLS_pp_TrainResS21_ScaledSTD  +
PLS_pp_TrainResS21_ScaleMean;


% Tss  = total sum of squares
TSS = sum((PLS_pp_TrainResS21_Raw-mean(PLS_pp_TrainResS21_Raw)).^2);
RSS_PLS = sum((PLS_pp_TrainResS21_Raw-PLS_pp_TrainS21_Unscaled).^2);
rsquaredPLS = 1 - RSS_PLS/TSS
PLS_pp_ValPredS21_Scaled = zeros(53,402);
for i = 1:402
  PLS_pp_ValPredS21_Scaled(:,i)      =      (PLS_pp_ValPredS21_Raw(:,i)      -
PLS_pp_TrainPredS21_ScaleMean(i))./ PLS_pp_TrainPredS21_ScaledSTD(i);
end

X = PLS_pp_ValPredS21_Scaled;
XRows = size(X,1);
PLS_pp_ValS21_Fit = [ones(XRows,1) X]*PLS_pp_TrainS21_beta2;
%------- unscaling -------
%      standardised version             <===>    unstandardised version
% [Z,gpamean,gpastdev] = zscore(gpa);   <===>  gpa2 =Z * gpastdev + gpamean;
PLS_pp_ValS21_FitUnscaled  =  PLS_pp_ValS21_Fit*PLS_pp_TrainResS21_ScaledSTD  +
PLS_pp_TrainResS21_ScaleMean;


figure("Name", 'Val Data')
plot(PLS_pp_ValS21_FitUnscaled(:),'DisplayName',"PLS                    fitted
Response","LineWidth",1, "Color",'red')
hold on
plot(PLS_pp_ValRes_Raw(:),   'DisplayName',"   Scaled   Response","LineWidth",1,
"Color",'k',"LineStyle","--")
grid on
legend('show')
xlabel('cell cycles')
ylabel('Standardised mAH')
title('training set')

% Tss  = total sum of squares
TSS = sum((PLS_pp_ValRes_Raw-mean(PLS_pp_ValRes_Raw)).^2);
RSS_PLS = sum((PLS_pp_ValRes_Raw-PLS_pp_ValS21_FitUnscaled).^2);
rsquaredPLS = 1 - RSS_PLS/TSS
```

```
figure("Name", 'Val Data')
subplot(3,2,1)
plot([2 22 42 62 82 102], PLS_pp_ValS21_FitUnscaled(26:31),'DisplayName',"PLS
fitted Response","LineWidth",1.5, "Color",'red')
hold on
plot([2 22 42 62 82 102],PLS_pp_ValRes_Raw(26:31), 'DisplayName'," Scaled
Response","LineWidth",1.5, "Color",'k',"LineStyle","--")
grid on
legend('show')
xlabel({"Cell cycles"; "(a)"},"FontWeight","bold")
ylabel('Capacity (mAh)',"FontWeight","bold")
title('Cell 5',"FontWeight","bold")


subplot(3,2,2)
plot([2 22 42 62 82 102],PLS_pp_ValS21_FitUnscaled(42:47),'DisplayName',"PLS
fitted Response","LineWidth",1.5, "Color",'red')
hold on
plot([2 22 42 62 82 102], PLS_pp_ValRes_Raw(42:47), 'DisplayName'," Scaled
Response","LineWidth",1.5, "Color",'k',"LineStyle","--")
grid on
legend('show')
xlabel({"Cell cycles"; "(b)"},"FontWeight","bold")
ylabel('Capacity (mAh)',"FontWeight","bold")
title('Cell 8',"FontWeight","bold")

subplot(3,2,3)
plot([22     42     62     82     102     122     142     162     182     202],
PLS_pp_ValS21_FitUnscaled(32:41),'DisplayName',"PLS                    fitted
Response","LineWidth",1.5, "Color",'red')
hold on
plot([22  42  62  82  102  122  142  162  182  202],PLS_pp_ValRes_Raw(32:41),
'DisplayName'," Scaled Response","LineWidth",1.5, "Color",'k',"LineStyle","--")
grid on
legend('show')
xlabel({"Cell cycles"; "(c)"},"FontWeight","bold")
ylabel('Capacity (mAh)',"FontWeight","bold")
title('Cell 12',"FontWeight","bold")


subplot(3,2,4)
plot([2 22 42 62 82 102], PLS_pp_ValS21_FitUnscaled(48:53),'DisplayName',"PLS
fitted Response","LineWidth",1.5, "Color",'red')
hold on
plot([2 22 42 62 82 102], PLS_pp_ValRes_Raw(48:53), 'DisplayName'," Scaled
Response","LineWidth",1.5, "Color",'k',"LineStyle","--")
grid on
legend('show')
xlabel({"Cell cycles"; "(d)"},"FontWeight","bold")
ylabel('Capacity (mAh)',"FontWeight","bold")
title('Cell 14',"FontWeight","bold")

subplot(3,2,5)
```

```
plot([2 12 22 32 42 52 62 82 102 122 142 162 182 202 222 262 282 302 322 342
362 382 402 422 442],...
    PLS_pp_ValS21_FitUnscaled(1:25),'DisplayName',"PLS                    fitted
Response","LineWidth",1.5, "Color",'red')
hold on
plot([2 12 22 32 42 52 62 82 102 122 142 162 182 202 222 262 282 302 322 342
362 382 402 422 442],...
    PLS_pp_ValRes_Raw(1:25), 'DisplayName'," Scaled Response","LineWidth",1.5,
"Color",'k',"LineStyle","--")
grid on
legend('show')
xlabel({"Cell cycles"; "(e)"},"FontWeight","bold")
ylabel('Capacity (mAh)',"FontWeight","bold")
title('Cell 17',"FontWeight","bold")
```

D.7 Model Coefficients for PLSR models using EIS and FDR Data

Table D.4 Model Coefficients for PLSR models using EIS and FDR Data

Variable Index	EIS Model Coefficients	FDR Model Coefficients
1	6.05E-16	2.91E-15
2	-0.077963335	-0.042146833
3	-0.081219051	-0.022084809
4	-0.082132701	-0.017596934
5	-0.080125893	-0.01736649
6	-0.068932377	-0.007803147
7	-0.061529722	0.000734576
8	-0.051347655	0.00480787
9	-0.036876027	0.008540157
10	-0.017137039	0.013131165
11	0.002339022	0.015659438
12	0.020513339	0.013309586
13	0.036542147	0.025737782
14	0.049467068	0.023141832
15	0.059217043	0.020303386
16	0.065413824	0.023528276
17	0.067919756	0.023284016
18	0.067408855	0.015815765
19	0.063066134	0.014422681
20	0.054944382	0.019809888
21	0.044737647	0.038461509
22	0.03148718	0.058565291
23	0.014901841	0.04172084
24	-0.004828857	0.057360627
25	-0.026455248	0.063325447
26	-0.050374248	0.064082992
27	-0.074348233	0.02884167
28	-0.096799953	0.005975925

29	-0.115969555	0.013027942
30	-0.126300533	0.014709952
31	-0.130684783	0.005709771
32	-0.127414507	0.002908234
33	-0.106651184	0.01438476
34	-0.073113624	0.027236222
35	-0.024287288	0.018523726
36	0.033663163	0.014914028
37	0.096885516	0.01268542
38	0.160154229	0.010791288
39	0.191207969	0.012585721
40	0.20325012	0.009396265
41	0.176230252	0.006213754
42	0.122895522	0.003050706
43	0.060328803	0.000896029
44	-0.019158896	-0.001200536
45	-0.082215026	-0.004989916
46	-0.118109188	-0.000942969
47	-0.108154244	0.014797288
48	-0.074771917	0.002249405
49	-0.033962304	0.029215745
50	-0.005816188	0.027502637
51	0.009104617	0.052403536
52	0.003295033	0.02246123
53	-0.00700805	0.020955117
54	-0.014599507	0.008773621
55	-0.01927569	-0.001380847
56	-0.013499389	-0.012810869
57	-0.012227921	0.001337152
58	-0.013965461	0.012825198
59	-0.016762528	0.017100292
60	-0.025476851	0.008972256
61	-0.03097285	0.006865481
62	-0.032729519	0.009982244
63	-0.031400507	0.008657771
64	-0.028263346	0.003952491
65	-0.012031456	-0.004706318
66	-0.020813921	-0.009019741
67	-0.016444929	-0.0122737
68	-0.031714221	-0.010151722
69	2.71E-05	-0.018701127
70	0.020121995	-0.018961396
71	0.013997852	-0.011687043
72	0.023467162	0.000660084
73	-0.152700168	0.004358326
74	-0.14548598	0.006472282
75	-0.131831297	0.010016554

76	-0.109311232	0.012804107
77	-0.073967686	0.014616205
78	-0.036549026	0.012559908
79	0.010051771	0.013952325
80	0.056333173	0.007146817
81	0.098146497	0.003642332
82	0.128572399	-0.002599165
83	0.151279743	-0.001363068
84	0.148754329	0.00165268
85	0.134326749	0.009257043
86	0.105316757	0.008225463
87	0.065644862	0.010764048
88	0.018568027	0.010411723
89	-0.030757762	0.014184791
90	-0.081594772	0.015211684
91	-0.128747488	0.017995735
92	-0.169538598	0.024306379
93	-0.19398638	0.027141514
94	-0.209008507	0.033252805
95	-0.213098434	0.03339075
96	-0.202836577	0.037293838
97	-0.180527265	0.019456831
98	-0.145463751	0.01339073
99	-0.103617601	0.013090051
100	-0.049068134	0.014233259
101	0.010810782	0.013105603
102	0.069814566	0.012280449
103	0.126100621	0.012204664
104	0.17846363	0.010706914
105	0.221130844	0.007633545
106	0.250202846	0.007772569
107	0.260121032	0.005681829
108	0.243936516	0.004495903
109	0.201729536	6.83E-05
110	0.115326921	0.000333234
111	0.01226699	-0.002741159
112	-0.096345882	-0.004850037
113	-0.180141568	-0.006479463
114	-0.214317373	-0.006286707
115	-0.198200709	-0.004428363
116	-0.142473925	-0.004667428
117	-0.069456486	-0.004832915
118	-0.002648429	-0.005098821
119	0.035756938	-0.006743384
120	0.042057798	-0.006818357
121	0.024015832	-0.009484039
122	0.001919572	-0.010187808

123	-0.020399797	-0.008264516
124	-0.026896855	-0.007547951
125	-0.024451606	-0.005543766
126	-0.01832874	-0.004737985
127	-0.015569089	-0.003247465
128	-0.015483407	-0.001984995
129	-0.018972862	-0.001065184
130	-0.021453981	-0.00101555
131	-0.02058419	-0.000759614
132	-0.015282601	-0.00013291
133	-0.006105363	-0.00081394
134	0.002351472	2.52E-05
135	0.00965374	0.001371122
136	0.014473766	0.002903999
137	-0.03718633	0.006224572
138	0.041891604	0.003934476
139	0.026656417	0.002550718
140	-0.030618065	0.000259214
141	-0.039771722	-0.002270765
142	-0.034904937	-0.005565216
143	-0.037080199	-0.00685381
144		-0.006451876
145		-0.005915224
146		-0.003737786
147		-0.001076459
148		0.000694174
149		0.002006187
150		0.002745895
151		0.00471727
152		0.004609039
153		0.004733686
154		0.0047934
155		0.004640826
156		0.005533363
157		0.006659896
158		0.006934175
159		0.007352257
160		0.007334051
161		0.007072942
162		0.006819221
163		0.006065248
164		0.00508206
165		0.004577149
166		0.004284235
167		0.004075956
168		0.003380936
169		0.00370388

170		0.002527482
171		0.002199469
172		0.000616414
173		0.000374304
174		0.003216818
175		0.006740904
176		0.009162247
177		0.009987205
178		0.002441872
179		-0.001738726
180		-0.004894951
181		-0.008338164
182		-0.013231346
183		-0.01555366
184		-0.02000573
185		-0.031447514
186		-0.047708266
187		-0.054953015
188		-0.041579596
189		-0.025277443
190		-0.013462962
191		-0.002558186
192		0.005141561
193		0.012643422
194		0.018427776
195		0.022914163
196		0.029641063
197		0.034913655
198		0.041104486
199		0.04557434
200		0.049414376
201		0.04974132
202		0.04573369
203		0.247038563
204		0.064678208
205		0.026686084
206		0.012841147
207		0.00443385
208		-0.002128638
209		-0.005962453
210		-0.007424463
211		-0.009804169
212		-0.010824871
213		-0.010270546
214		-0.010594102
215		-0.011916926
216		-0.012426544

217		-0.013839478
218		-0.014525405
219		-0.012591838
220		-0.013304571
221		-0.00962324
222		-0.009526408
223		-0.005624927
224		-7.88E-05
225		-0.001281811
226		-0.001744193
227		-0.004851982
228		-0.007445636
229		-0.001988558
230		0.002376867
231		0.00251472
232		0.004556651
233		0.010581764
234		0.018863625
235		0.006278577
236		-0.002514332
237		-0.001966341
238		-0.008380299
239		-0.008927315
240		-0.014890361
241		-0.018559104
242		-0.015405142
243		-0.011521189
244		-0.007522432
245		-0.003606843
246		0.001199861
247		0.006570828
248		0.008951046
249		-0.01731906
250		0.0227083
251		0.00547976
252		-0.005397052
253		-0.009746718
254		-0.009010042
255		-0.006521268
256		-0.001296023
257		0.010813379
258		0.015669935
259		0.011377545
260		0.006115715
261		0.004809867
262		0.008412485
263		0.00588544

264		0.00238561
265		0.002282037
266		0.003738428
267		0.006998848
268		0.011509903
269		0.013029245
270		0.013798898
271		0.020177936
272		0.023729801
273		0.023689501
274		0.022048196
275		0.022492406
276		0.022082353
277		0.019702373
278		0.018106521
279		0.016101467
280		0.013271551
281		0.012972329
282		0.013635068
283		0.013996792
284		0.012362479
285		0.012826379
286		0.011722117
287		0.010050589
288		0.009175564
289		0.007973343
290		0.009383437
291		0.008647461
292		0.006094441
293		0.005982303
294		0.002893699
295		-0.005063813
296		-0.020746015
297		-0.030062812
298		-0.014251873
299		-0.006798389
300		-0.003479188
301		-0.001112244
302		-0.000490843
303		0.0023573
304		0.004092031
305		0.004416546
306		0.006124452
307		0.007144212
308		0.00783974
309		0.008177607
310		0.008165289

311		0.008256915
312		0.008761629
313		0.009093767
314		0.009715841
315		0.009230198
316		0.008410413
317		0.007315125
318		0.008044847
319		0.007444213
320		0.008655983
321		0.008384991
322		0.007920912
323		0.006877968
324		0.006970685
325		0.00609916
326		0.005045117
327		0.005164976
328		0.004240113
329		0.003268414
330		0.002280764
331		0.001189742
332		0.000325951
333		-0.000584266
334		-0.001707875
335		-0.003908706
336		-0.008255197
337		-0.012272536
338		-0.014042486
339		-0.012268247
340		-0.008896401
341		-0.005745091
342		-0.003038272
343		0.00129169
344		0.00452993
345		0.006690469
346		0.009678961
347		0.009718022
348		0.008897283
349		0.005914257
350		0.00371913
351		-0.000478336
352		-0.004981248
353		-0.008600994
354		-0.011136913
355		-0.012830782
356		-0.012158283
357		-0.010458895

358		-0.009194185
359		-0.010190176
360		-0.010602665
361		-0.009598693
362		-0.008866324
363		-0.007637728
364		-0.008124042
365		-0.012360873
366		-0.009125002
367		-0.001591367
368		-0.000187569
369		-0.000344383
370		-0.000769522
371		0.000307553
372		0.003827393
373		0.014780922
374		0.02558272
375		0.030612372
376		0.026830377
377		0.020935024
378		0.016742765
379		0.014638242
380		0.011679224
381		0.007632749
382		0.003797377
383		0.00041205
384		-0.001282212
385		-0.002466949
386		-0.002584006
387		0.000196238
388		0.002067162
389		0.005210597
390		0.013274641
391		0.027880157
392		0.030178359
393		0.026564785
394		0.01604646
395		0.009631788
396		0.005503259
397		0.001294813
398		-0.003797358
399		-0.008224114
400		-0.011407429
401		-0.016145871
402		-0.021665406
403		-0.023913094

Appendix E

E.1 Antiresonance Effects in Parallel Capacitors

Typically, capacitors have self-resonance frequencies that is dictated by their inherent equivalent series inductances (ESLs) arising from the capacitor leads [165]. The impedance of capacitors decreases with frequency until the resonance point, after which the impedance increases with frequency. This behaviour after the resonance point suggest the ESL is dominant within this region of operation . When two capacitors with different self-resonance frequencies are connected in parallel, the capacitor with the lowest resonance frequency (f_{res1}) will resonate first. This is usually the capacitor with the largest capacitance of the two [165]. This resonance is determined by its capacitance (C_1) and its inherent parasitic inductance ESL (ESL_1) which can be express as (E.1).Where f_{res}, L, C are the resonance frequency, inductance and capacitance of a given element or circuit.

$$f_{res} = \frac{1}{2\pi\sqrt{\mathrm{L} \times \mathrm{C}}} \tag{E.1}$$

The second capacitor has its own resonant frequency (f_{res2}) that is also determined by its (C_2) and its inherent parasitic inductance ESL (ESL_2). After the initial resonance f_{res1}, the ESL_1 dominates and forms a parallel circuit with C_2, instead of two parallel connected capacitors the circuit becomes a capacitor in parallel with an inductor [165]. This parallel connection results in a parallel resonance occurring in between the two individual self-resonance of each of the capacitors .

E.1.1 Application to FDR Setup

The connector PCB has inherent parasitic inductances and capacitances, leading to its own resonance frequency at 855 MHz shown in Figure E.1. Assuming the PCB behaves like a basic parallel plate capacitor, due to it double nature, (E.2) is used to estimate the PCB capacitance (C_{PCB}) to be ≈ 75 pF. Where ε_r = 4 is the dielectric constant for FR4 material used in PCB, $\varepsilon_o = 8.85 \times 10^{-12} F/m$ is the permittivity of free space, A is the surface area of the PCB plates (80 mm by 40 mm) = 3200mm^2 and d = 1.5mm is the FR4 thickness or separation between the PCB layers.

$$C_{PCB} = \frac{\varepsilon_r \varepsilon_o A}{\mathrm{d}} \tag{E.2}$$

Taking the instance of the 91 pF capacitor, $C_{PCB} \approx 75$ pF is less than the inserted 91pF. When this is connected in parallel with a PCB that resonates at 855 MHz, the interactions the two

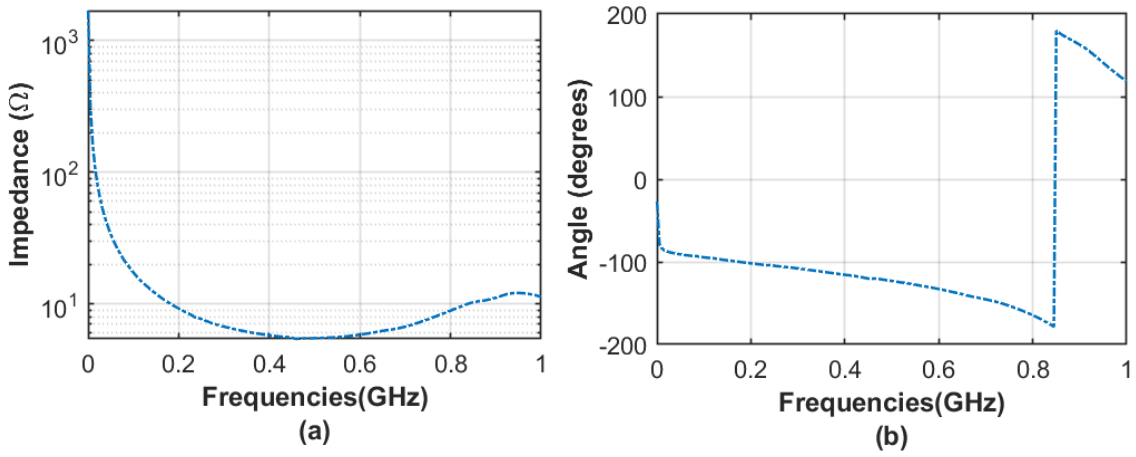

Figure E.1 Impedance of connector PCB used in FDR measurement. (a) Magnitude of PCB impedance. (b) Phase of PCB impedance.

capacitors result in additional resonances observed at 130 MHz and 185 MHz. Firstly, for the same PCB, this effect is absent when inductors and resistors are connected (Figure 4.5c) and 4.5e respectively), and also absent after OSLC compensation (Figure 4.6). These confirm that the effect is due to the interactions between capacitor and PCB.

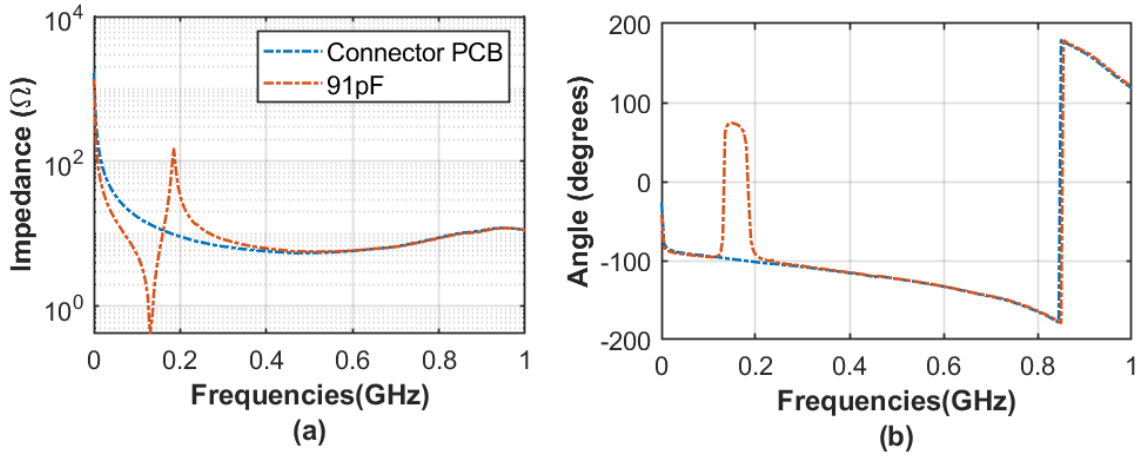

Figure E.2 Impedance of 91pF capacitor and the connector PCB. (a) Magnitude of impedance of connector PCB and 91 pF capacitor. (b) Phase of connector PCB and 91 pF capacitor.

As observed [165, 195] in, the first resonance is the series resonance mostly likely due to the larger valued capacitor 91pF and the second resonance due to the parallel circuit formed by

ESL of the 91 pF capacitor (ESL_{91pF}) and the lower valued capacitor, C_{PCB}.The third resonance is due to the PCB's inherent ESL and remains at 855MHz, irrespective of which element is connected. These suggests that the antiresoance behaviour observed at 130 MHz and 185 MHz is mainly due to the parallel coupling between the inserted capacitor and the PCB.

E.2 FDR Impedance of Passive Elements within the Region of Confidence

Within the region of confidence, VNA frequency of measurement were from 300 kHz to 100 MHz, with 5 MHz incremental intervals. Aside from the boundary frequencies (300 kHz and 100 MHz), a 10 MHz interval was used to sample the frequencies within the RoC. Figures E.3 and E.4 present the pre - and post-OSLC impedance values for the passive elements. The estimated reactance at these frequencies are also summarised in Tables E.1 and E.2 using (E.3) and (E.4) respectively. Table E.1 summarises capacitor values and inductors are summarised in Table E.2. Resistors were assumed not be frequency dependent.

$$X_C = \frac{1}{2\pi f C} \tag{E.3}$$

$$X_L = 2\pi \mathrm{fL} \tag{E.4}$$

Where X_C and X_L are the capacitive and inductive reactance respectively. f is the frequency of measurement, L is the stated inductance value and C is the stated capacitance.

Table E.1 Estimated Capacitive Reactance within RoC

Stated Value	Estimated Capacitive Reactance at RoC frequencies									
	300 kHz	15 MHz	25 MHz	35 MHz	45 MHz	55 MHz	65 MHz	75 MHz	85 MHz	100 MHz
91pF	2132.09	99.40	60.27	43.31	33.87	27.79	23.60	20.49	18.22	15.58
200pF	1386.70	54.60	32.69	23.04	17.55	13.89	11.25	9.18	7.46	5.18
470pF	1553.81	34.41	20.04	13.51	9.59	6.78	4.55	2.56	0.61	2.73
560pF	856.14	18.67	10.34	6.27	3.60	1.54	0.92	2.70	4.93	9.52
680pF	776.66	14.47	7.46	3.89	1.40	0.75	2.82	5.12	7.91	14.23
750pF	641.62	12.26	6.10	2.89	0.58	1.46	3.48	5.75	8.55	14.99
820pF	586.26	10.53	5.00	2.04	0.18	2.13	4.14	6.45	9.34	16.11
1nF	575.84	9.78	4.60	1.81	0.28	2.13	4.02	6.17	8.81	14.82
10nF	404.98	8.37	3.82	1.34	0.79	2.47	4.29	6.41	9.02	15.09
22nF	57.74	0.36	1.88	3.24	4.69	6.35	8.36	11.00	14.60	24.22
47nF	25.31	1.12	2.43	3.74	5.20	6.91	9.04	11.88	15.82	26.81
57nF	12.45	1.30	2.46	3.66	5.02	6.61	8.58	11.20	14.76	24.39
100nF	9.52	1.41	2.59	3.82	5.22	6.88	8.94	11.68	15.45	25.88

Table E.2 Estimated Inductive Reactance within RoC

Stated Value	Estimated Inductive Reactance at RoC frequencies									
	300 kHz (pH)	**15 MHz** (nH)	**25 MHz** (nH)	**35 MHz** (nH)	**45 MHz** (nH)	**55 MHz** (nH)	**65 MHz** (nH)	**75 MHz** (nH)	**85 MHz** (nH)	**100 MHz** (nH)
0.1nH	0.188	0.00961	0.0159	0.0222	0.0285	0.0347	0.041	0.0473	0.0536	0.063
47nH	1.88	0.0961	0.159	0.222	0.285	0.347	0.41	0.473	0.536	0.63
100nH	88.6	4.52	7.47	10.4	13.4	16.3	19.3	22.2	25.2	29.6
220nH	188	9.61	15.9	22.2	28.5	34.7	41	47.3	53.6	63
400nH	415	21.1	35	48.8	62.6	76.4	90.2	104	118	139
820nH	754	38.4	63.6	88.7	114	139	164	189	214	252
2.2uH	1550	78.8	130	182	233	285	336	388	439	517
11uH	1880	96.1	159	222	285	347	410	473	536	630
33uH	4150	211	350	488	626	764	902	1040	1180	1390
47uH	20700	1060	1750	2440	3130	3820	4510	5200	5890	6930

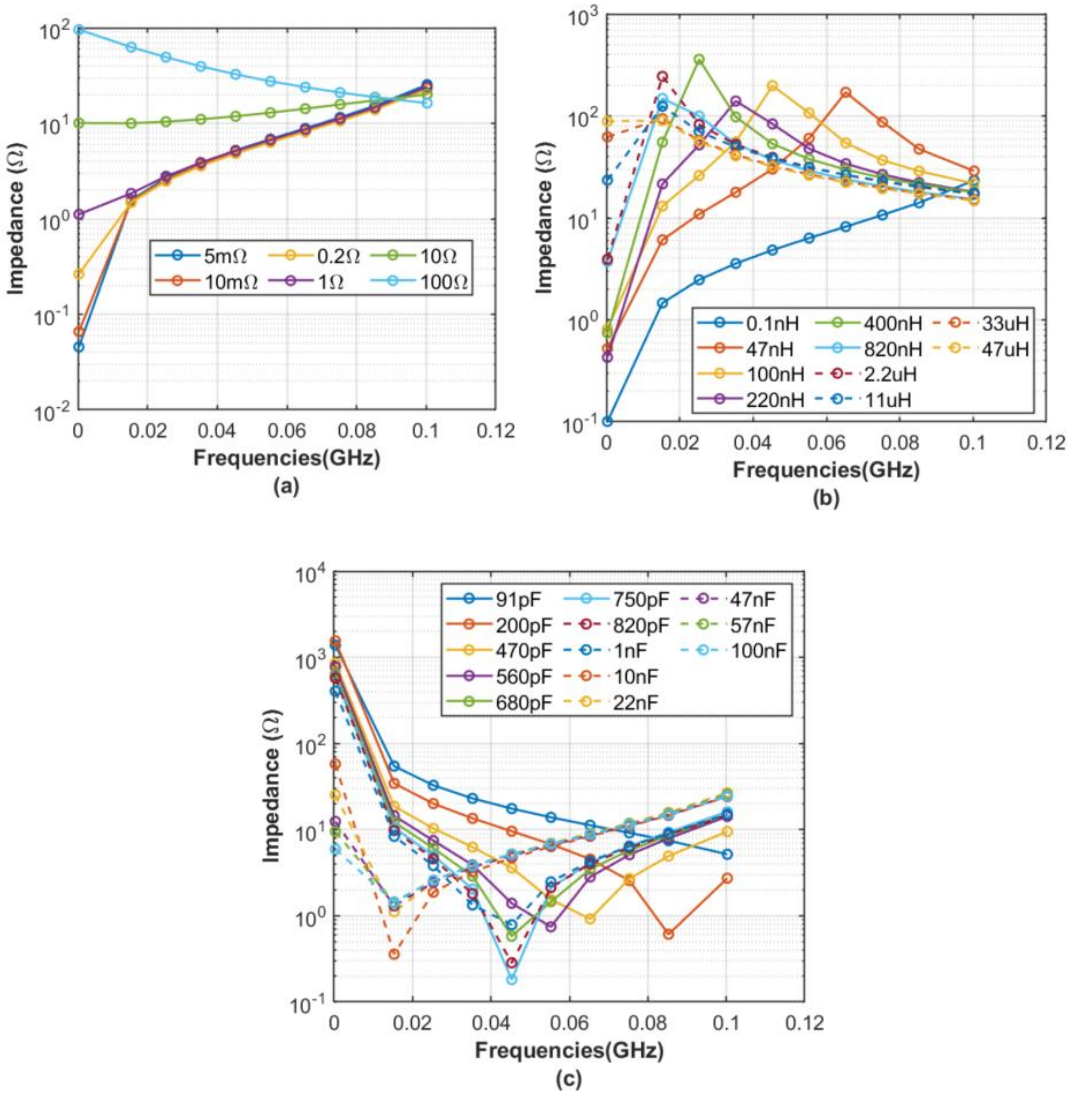

Figure E.3 Pre-OSLC impedance of Passive Elements within the RoC. (a) Pret-OSLC resistance. (b) Pre-OSLC inductive reactance. (c) Pre-OSLC capacitive reactance.

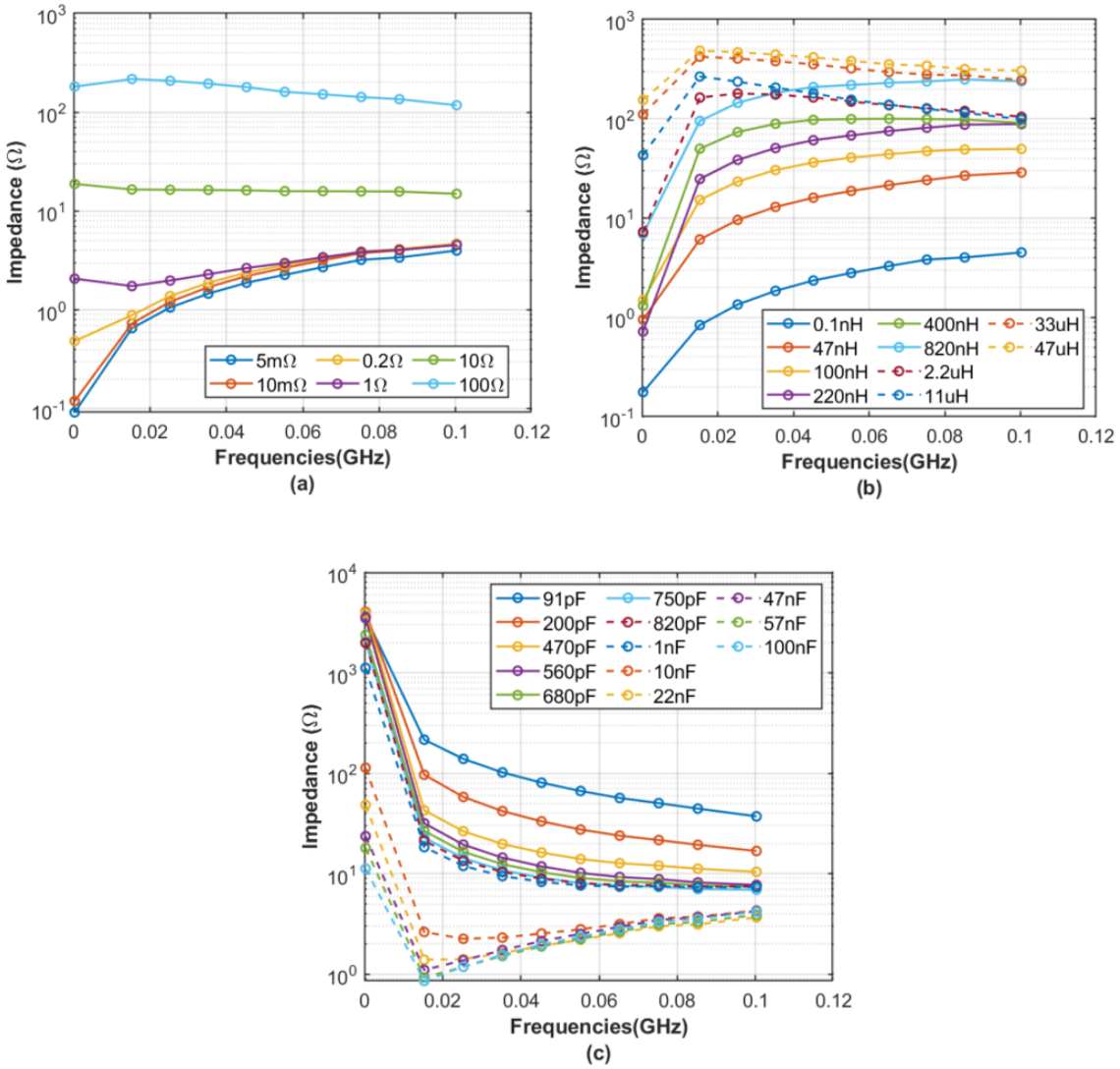

Figure E.4 Post-OSLC impedance of Passive Elements within the RoC. (a) Post-OSLC resistance. (b) Post-OSLC inductive reactance. (c) Post-OSLC capacitive reactance.

Appendix F - FDR Impedance Responses for Li-ion Cells

F.1 Full Spectrum FDR Responses for Samples cells

Figures F.1 – F.19 show the full spectrum FDR impedance responses of the 19 samples cells at different cycles during their aging. In each figure, both pre-OSLC and post- OSLC impedances are shown.

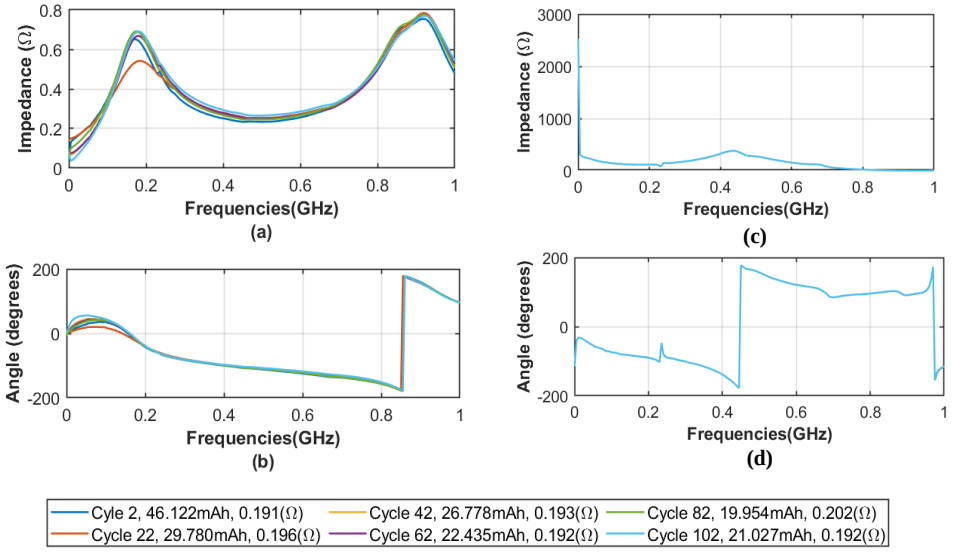

Figure F.1 Cell 1 FDR Impedance. (a)-(b) Magnitude and Phase of Pre-OSLC impedance. (c) - (d) Magnitude and Phase of Post-OSLC impedance.

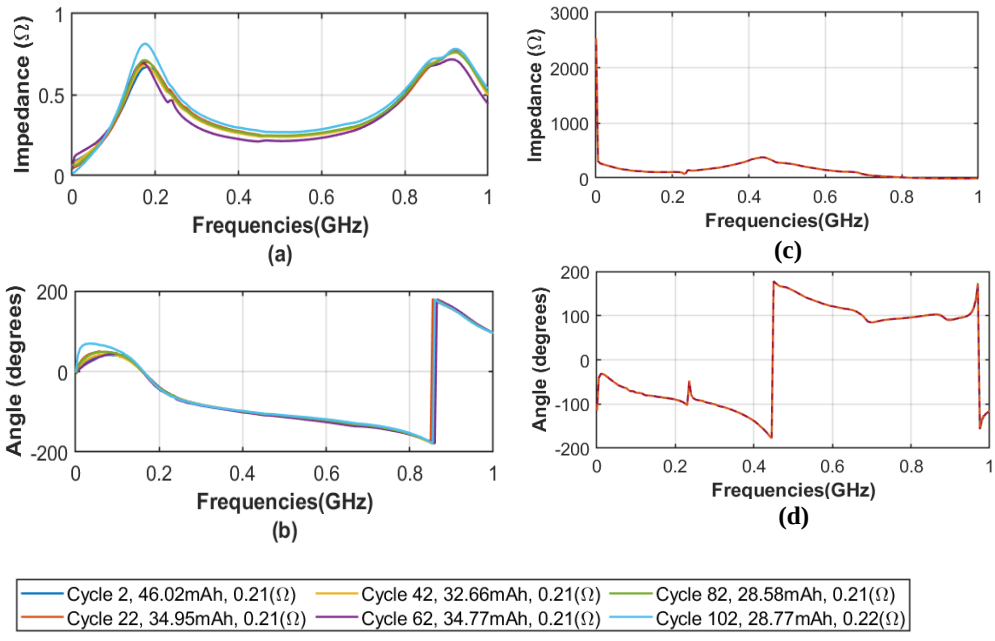

Figure F.2 Cell 2 FDR Impedance. (a)-(b) Magnitude and Phase of Pre-OSLC impedance. (c) - (d) Magnitude and Phase of Post-OSLC impedance.

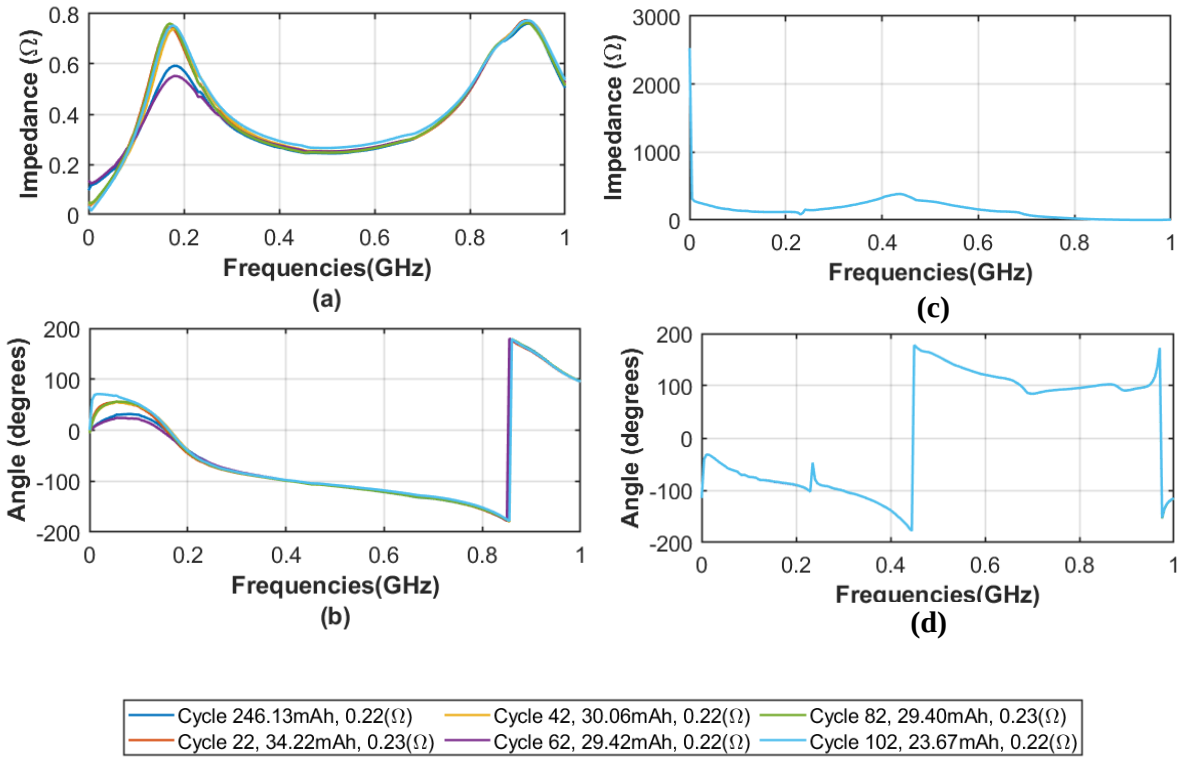

Figure F.3 Cell 3 FDR Impedance. (a)-(b) Magnitude and Phase of Pre-OSLC impedance. (c) - (d) Magnitude and Phase of Post-OSLC impedance.

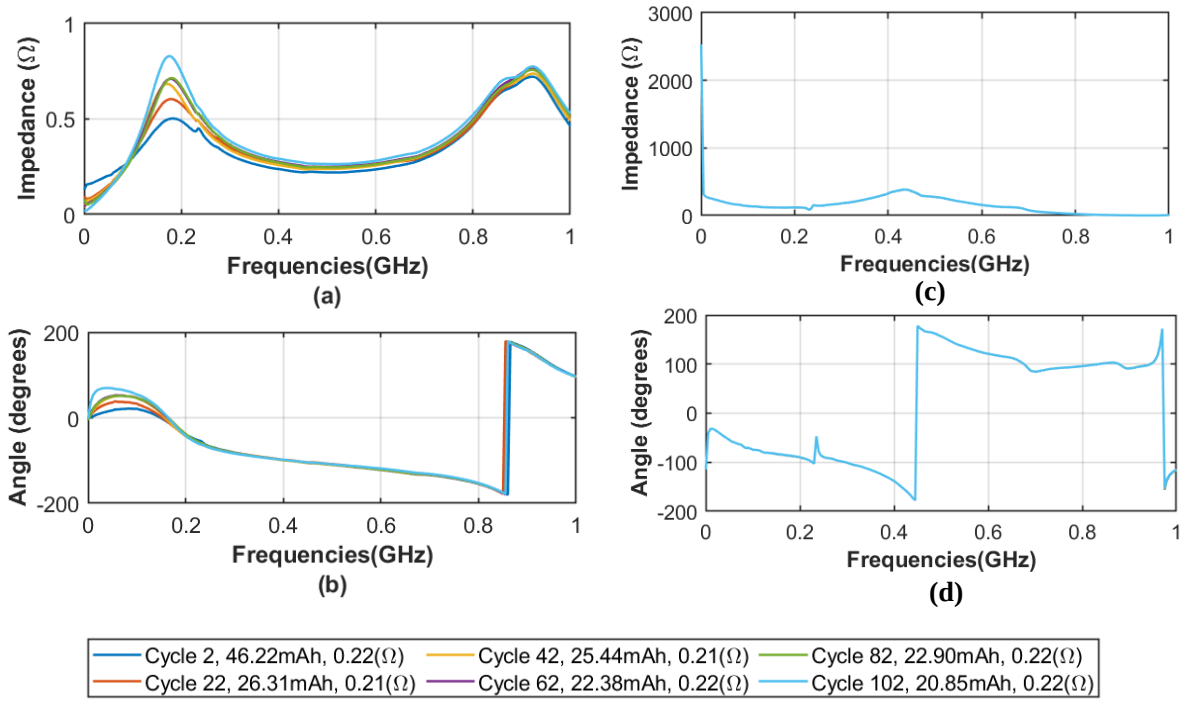

Figure F.4 Cell 4 FDR Impedance. (a)-(b) Magnitude and Phase of Pre-OSLC impedance. (c) - (d) Magnitude and Phase of Post-OSLC impedance.

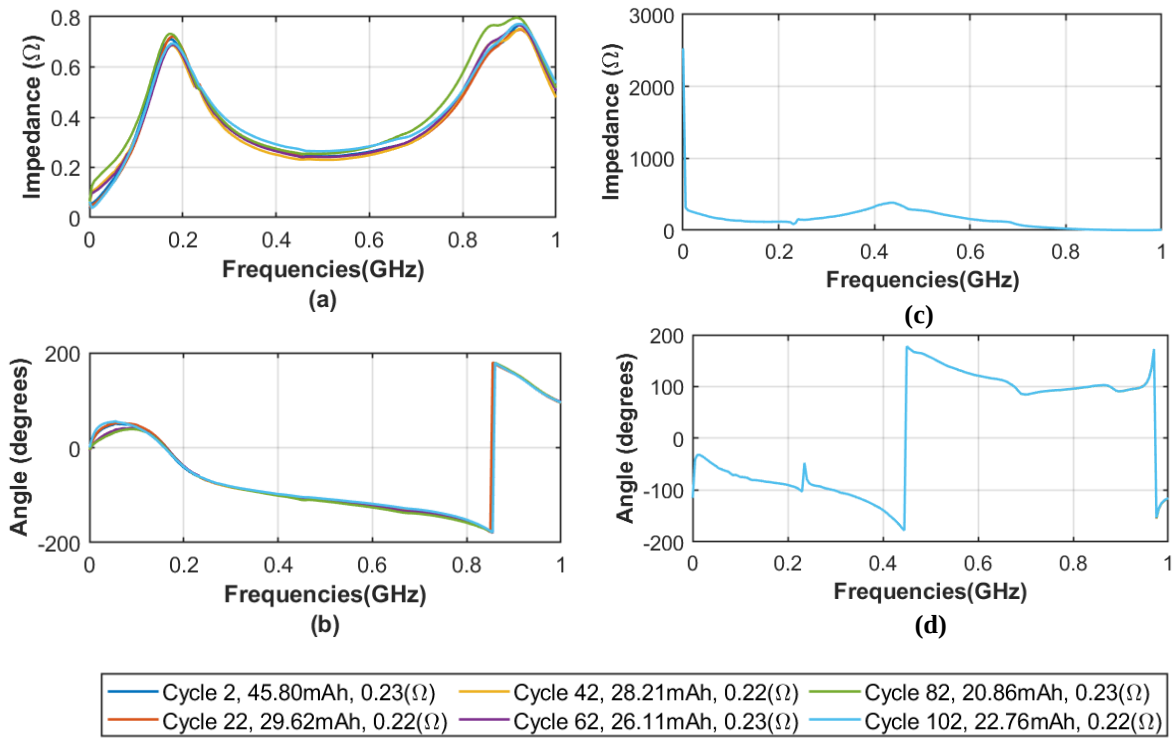

Figure F.5 Cell 5 FDR Impedance. (a)-(b) Magnitude and Phase of Pre-OSLC impedance. (c) - (d) Magnitude and Phase of Post-OSLC impedance.

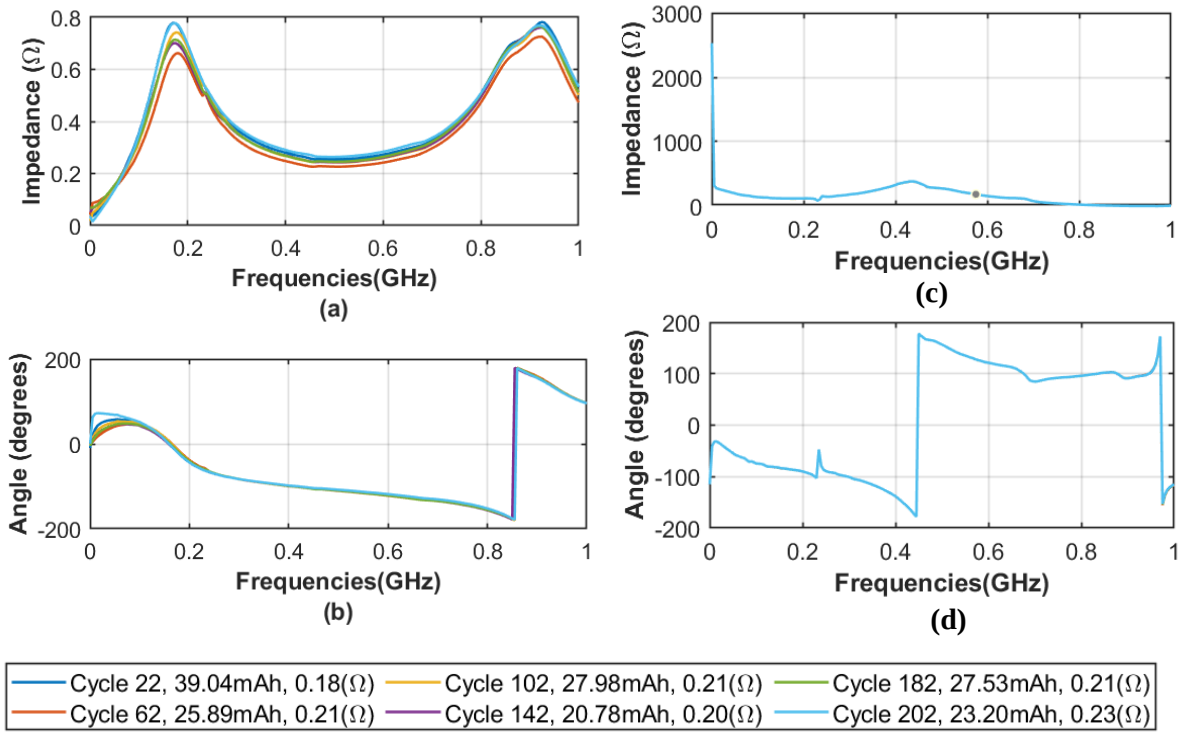

Figure F.6 Cell 6 FDR Impedance. (a)-(b) Magnitude and Phase of Pre-OSLC impedance. (c) - (d) Magnitude and Phase of Post-OSLC impedance.

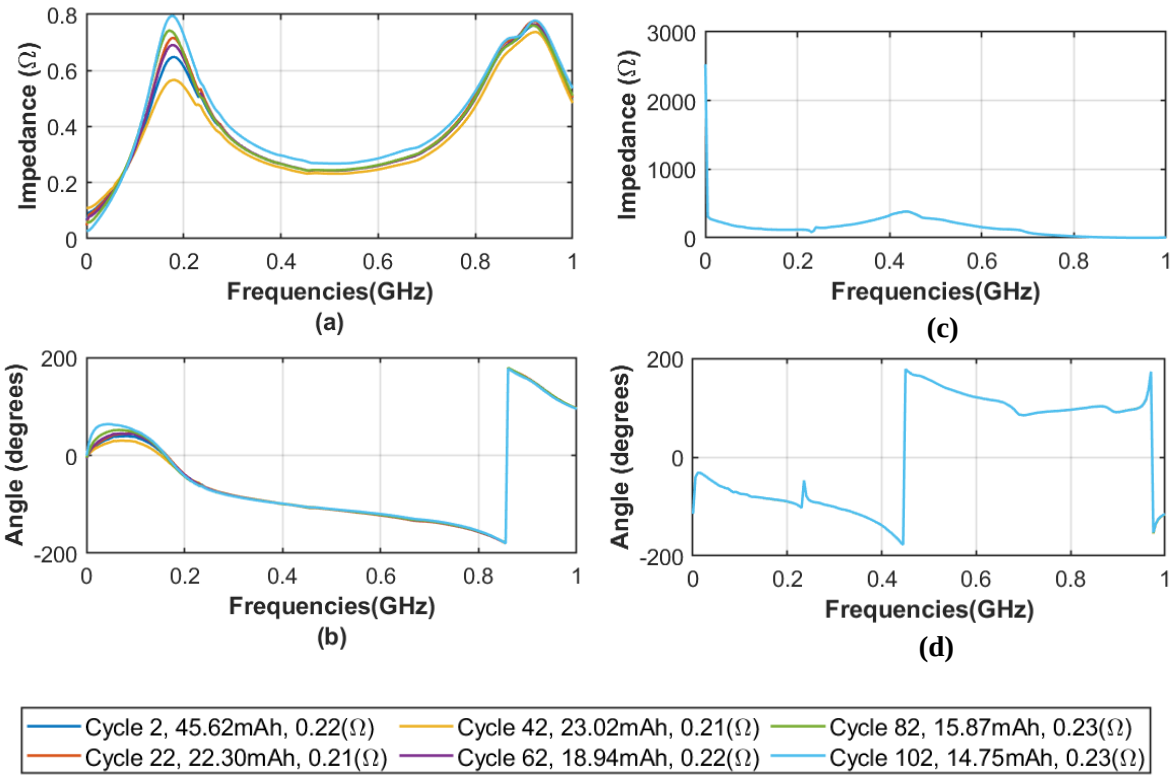

Figure F.7 Cell7 FDR Impedance. (a)-(b) Magnitude and Phase of Pre-OSLC impedance. (c) - (d) Magnitude and Phase of Post-OSLC impedance.

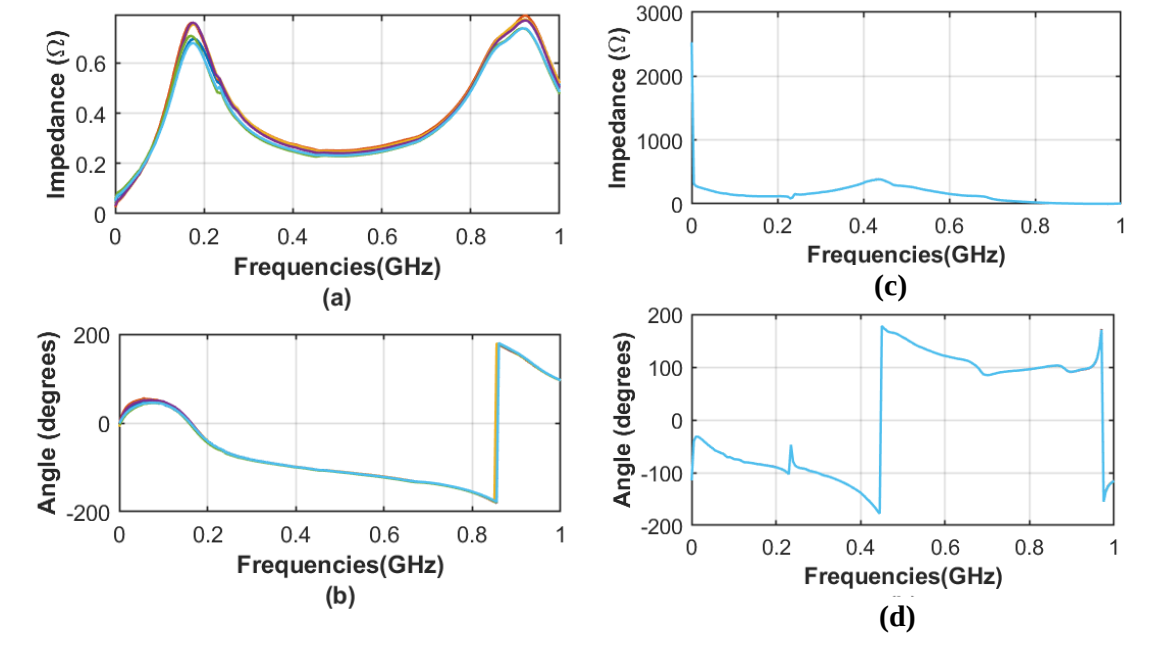

Figure F.8 Cell 8 FDR Impedance. (a)-(b) Magnitude and Phase of Pre-OSLC impedance. (c) - (d) Magnitude and Phase of Post-OSLC impedance.

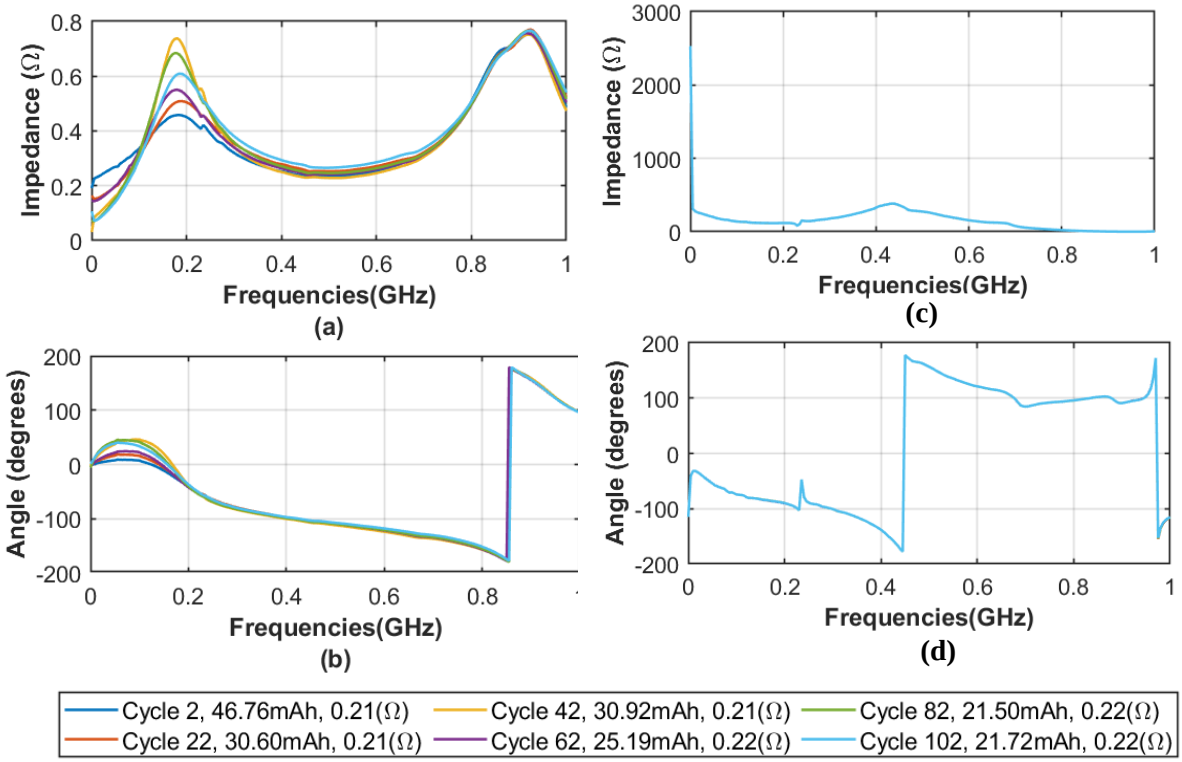

Figure F.9 Cell 9 FDR Impedance. (a)-(b) Magnitude and Phase of Pre-OSLC impedance. (c) - (d) Magnitude and Phase of Post-OSLC impedance.

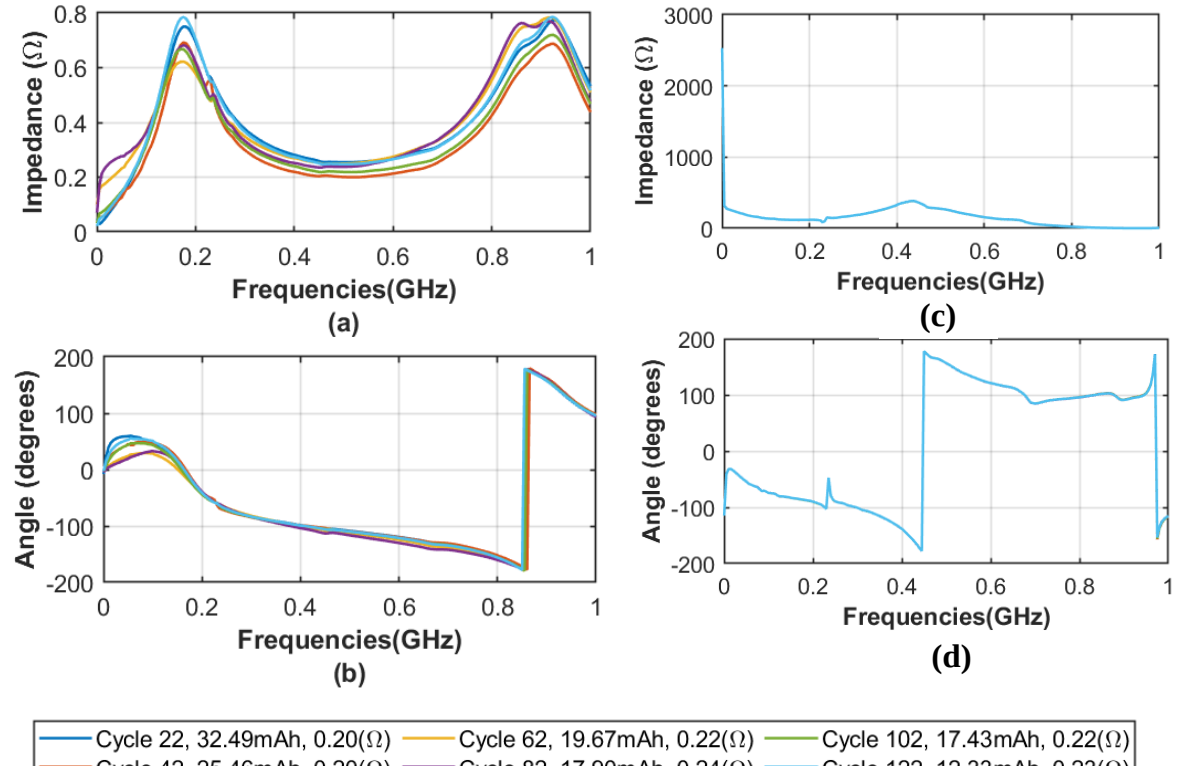

Figure F.10 Cell 10 FDR Impedance. (a)-(b) Magnitude and Phase of Pre-OSLC impedance. (c) - (d) Magnitude and Phase of Post-OSLC impedance.

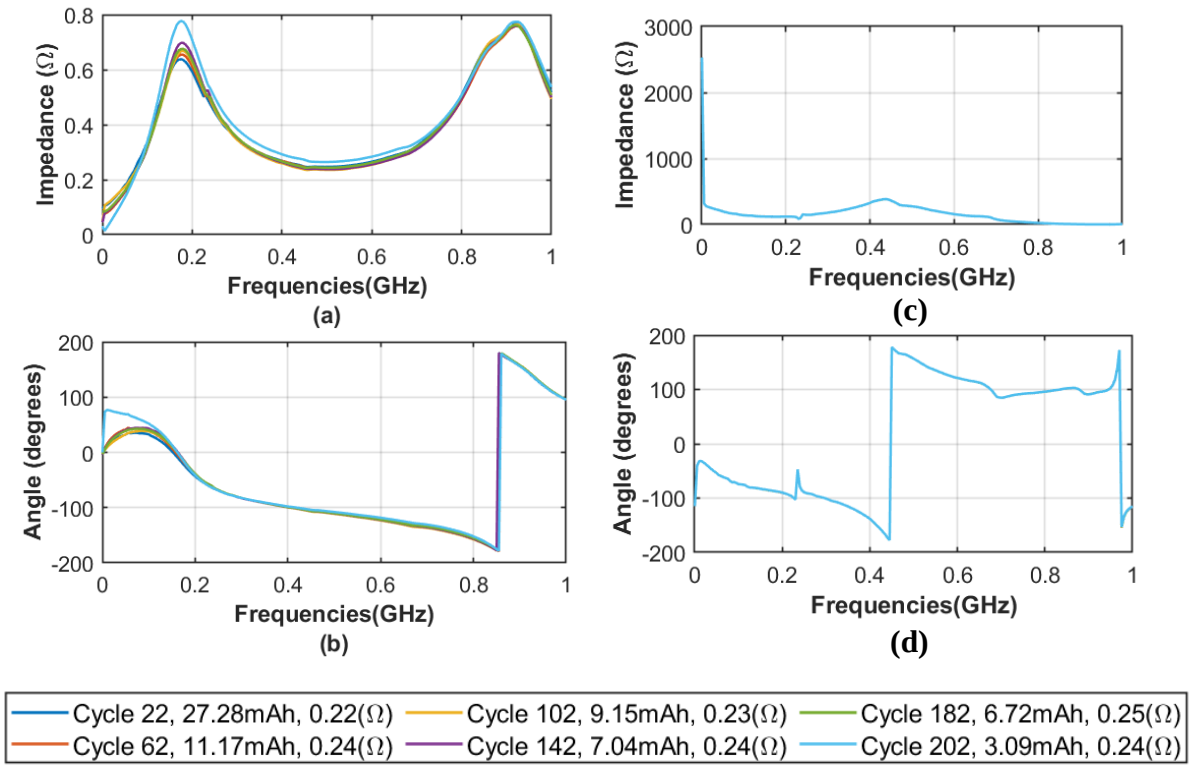

Figure F.11 Cell 11 FDR Impedance. (a)-(b) Magnitude and Phase of Pre-OSLC impedance. (c) - (d) Magnitude and Phase of Post-OSLC impedance

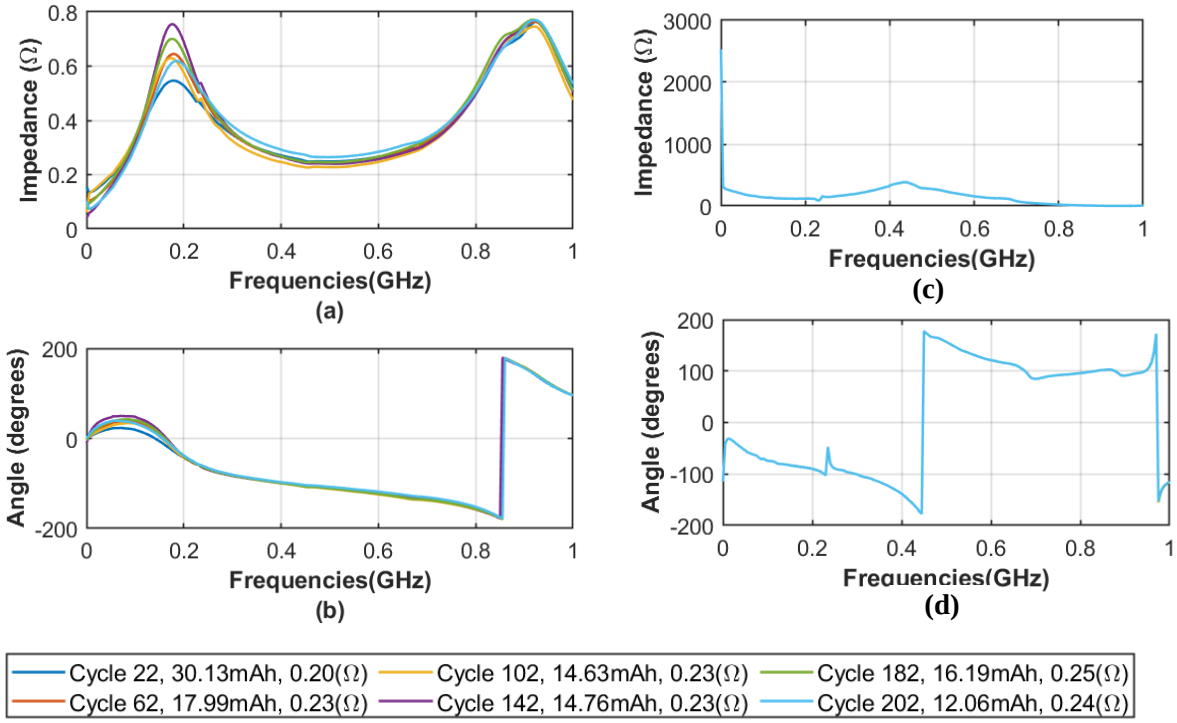

Figure F.12 Cell 1 FDR Impedance. (a)-(b) Magnitude and Phase of Pre-OSLC impedance. (c) - (d) Magnitude and Phase of Post-OSLC impedance.

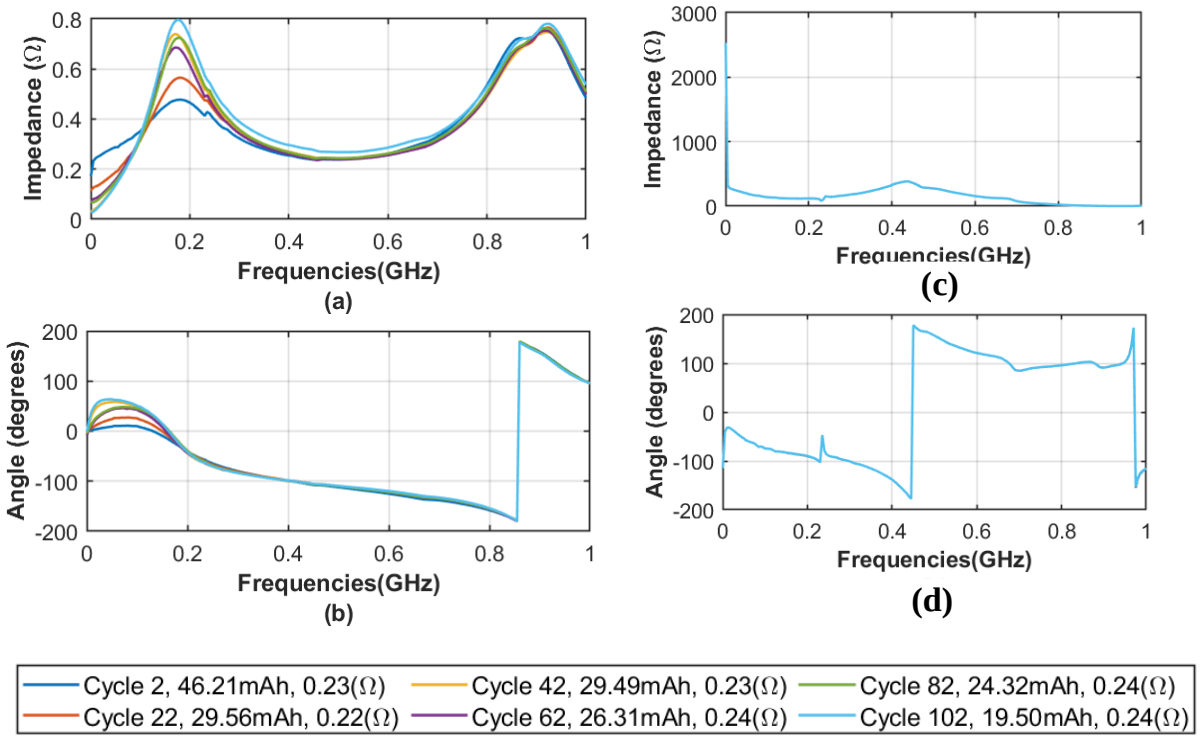

Figure F.13 Cell 13 FDR Impedance. (a)-(b) Magnitude and Phase of Pre-OSLC impedance. (c) - (d) Magnitude and Phase of Post-OSLC impedance.

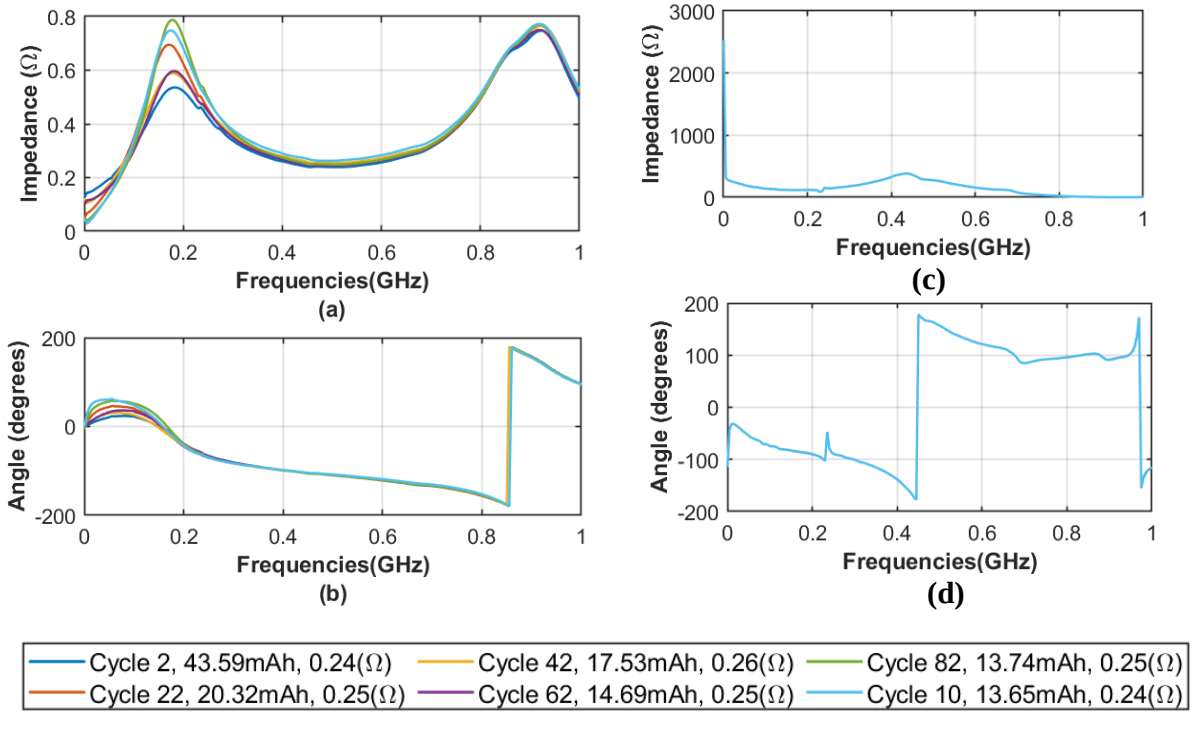

Figure F.14 Cell 14 FDR Impedance. (a)-(b) Magnitude and Phase of Pre-OSLC impedance. (c) - (d) Magnitude and Phase of Post-OSLC impedance.

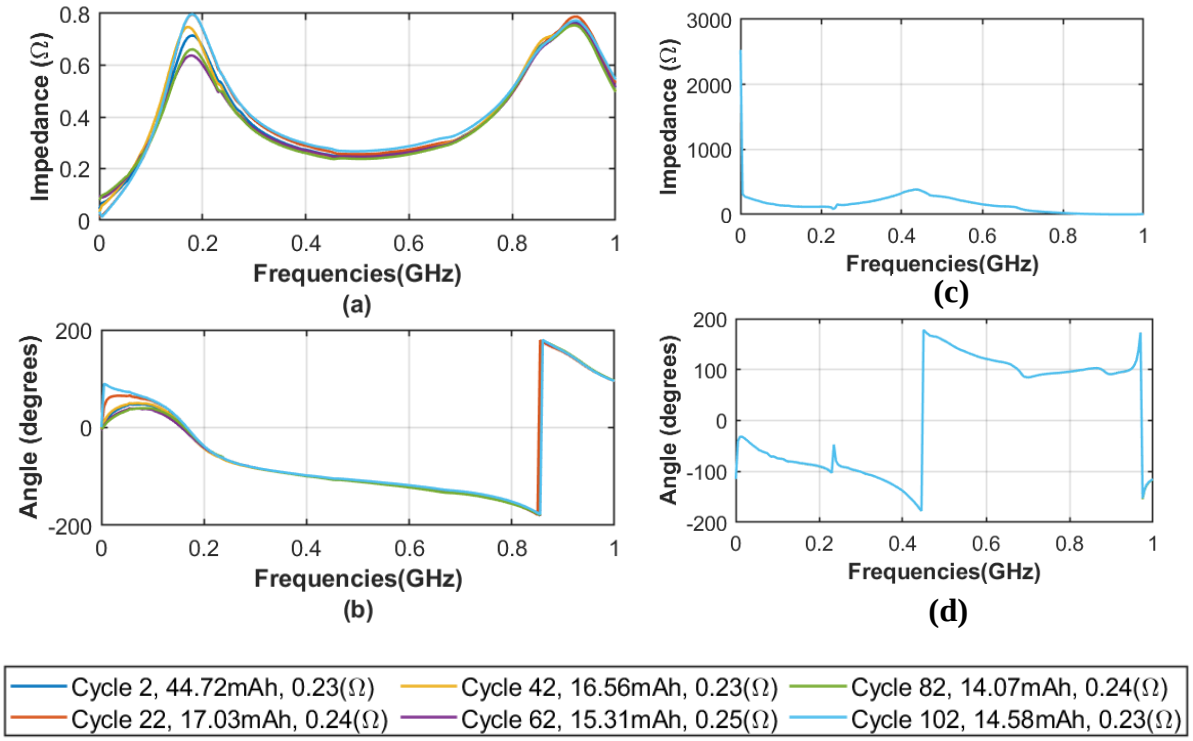

Figure F.15 Cell 15 FDR Impedance. (a)-(b) Magnitude and Phase of Pre-OSLC impedance. (c) - (d) Magnitude and Phase of Post-OSLC impedance.

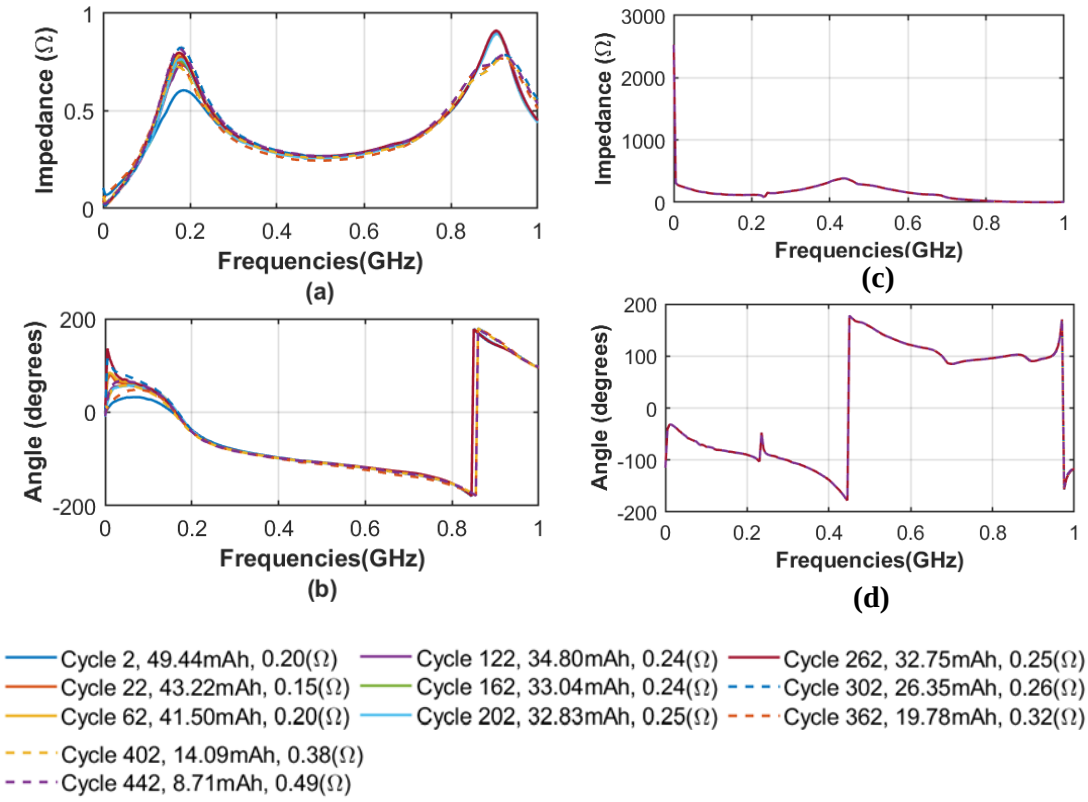

Figure F.16 Cell 16 FDR Impedance. (a)-(b) Magnitude and Phase of Pre-OSLC impedance. (c) - (d) Magnitude and Phase of Post-OSLC impedance.

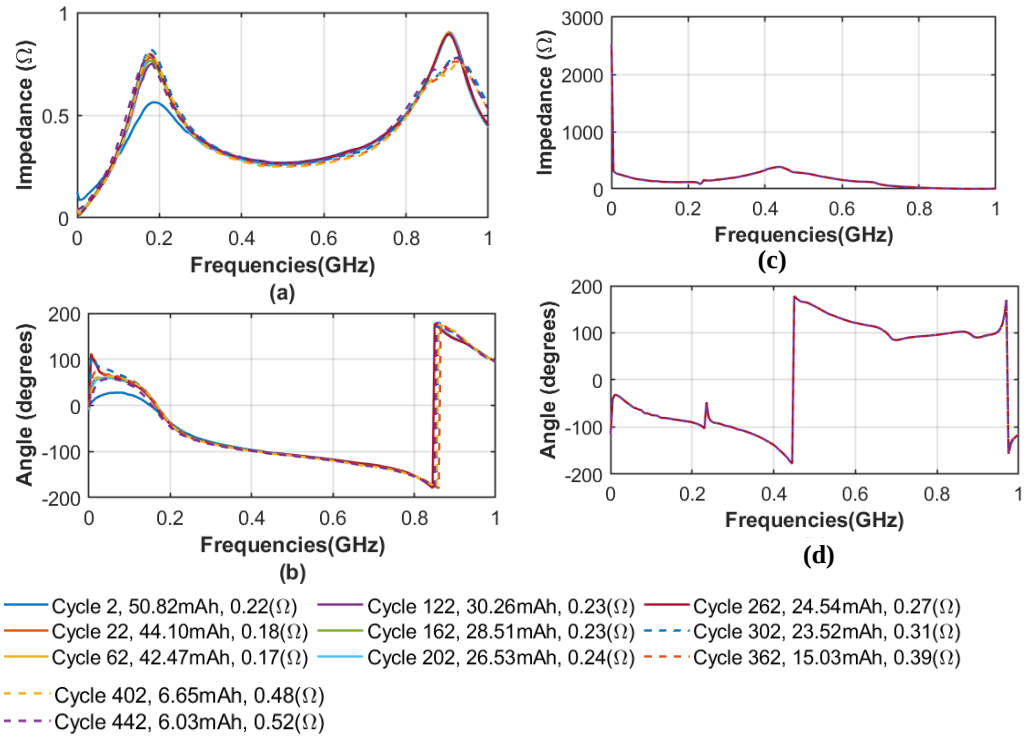

Figure F.17 Cell 17 FDR Impedance. (a)-(b) Magnitude and Phase of Pre-OSLC impedance. (c) - (d) Magnitude and Phase of Post-OSLC impedance.

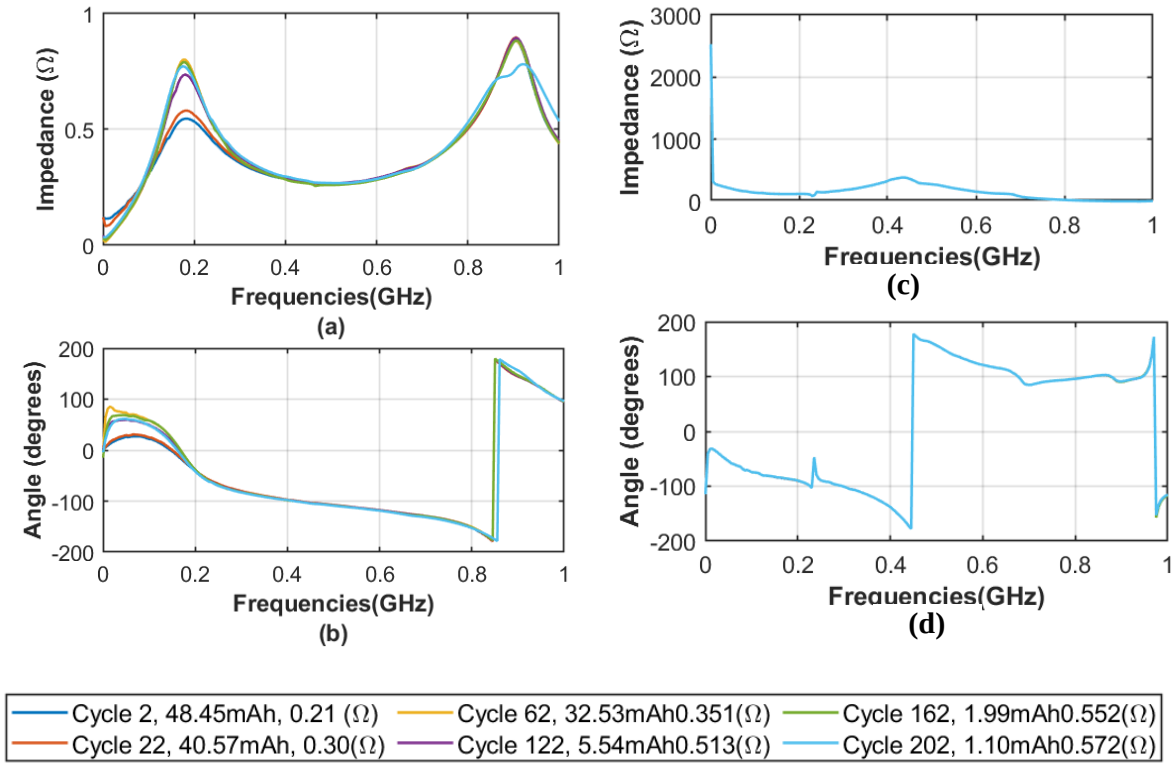

Figure F.18 Cell 18 FDR Impedance. (a)-(b) Magnitude and Phase of Pre-OSLC impedance. (c) - (d) Magnitude and Phase of Post-OSLC impedance.

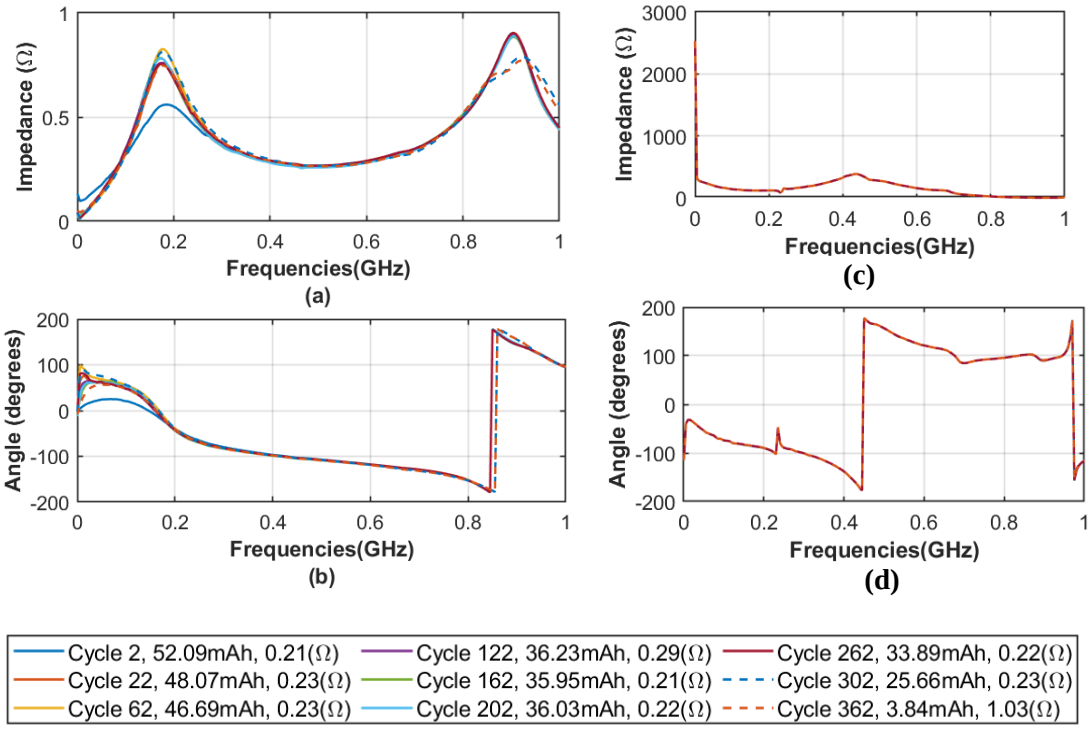

Figure F.19 Cell 19 FDR Impedance. (a)-(b) Magnitude and Phase of Pre-OSLC impedance. (c) - (d) Magnitude and Phase of Post-OSLC impedance.

F.2 FDR Impedance at 300 kHz, for a sample cell from Batch B

Figure F.20, illustrates the limited number of data points using a cell from Batch B. This shows how the small number of samples does not establish an identifiable trend.

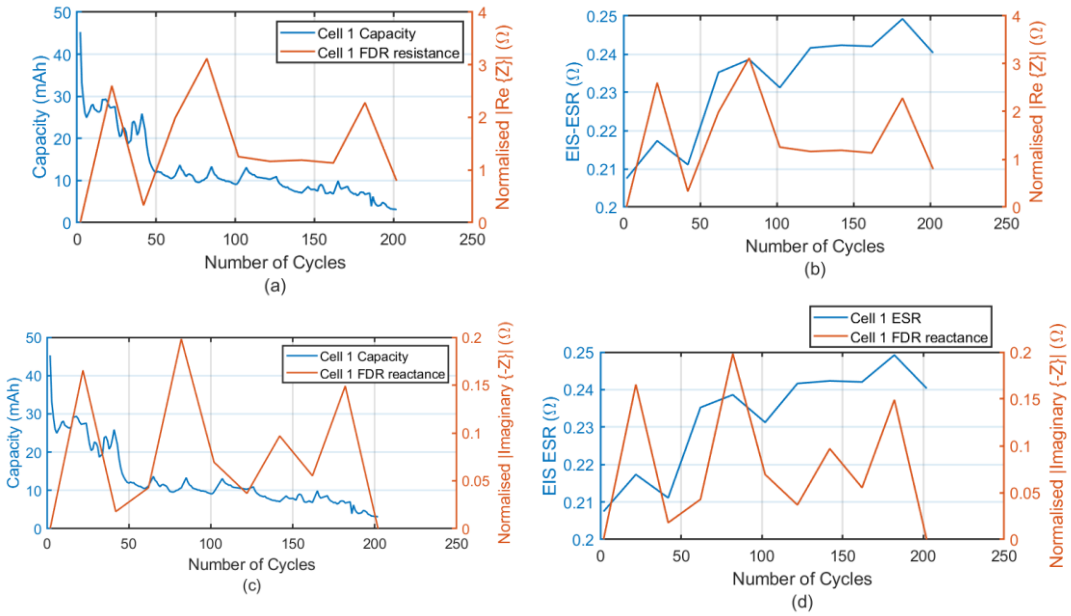

Figure F.20 Variations in FDR measured resistance of Cell 20 at 300 kHz compared with variations in health indicators. (a) Comparison of FDR measured resistance and cell capacity. (b) Comparison of FDR measured resistance and cell ESR.

F.3 FDR Impedance of sample cells at their respective last cycles

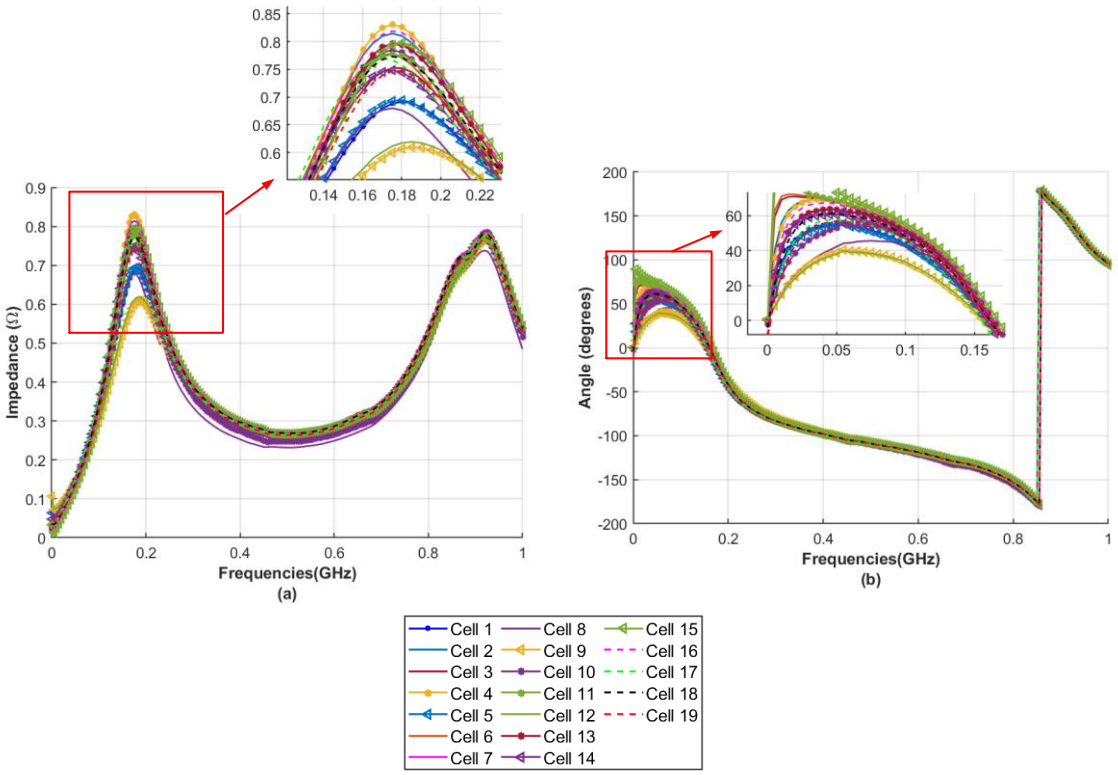

Figure F.21 Full spectrum pre-OSLC impedance of all 19 cells. (a) Magnitude of pre-OSLC impedance. (b) Phase of pre-OSLC impedance.

F.4 Comparison of FDR measured resistance and EIS-measured ESR

Figure F.22 and F.23 show how the FDR-measured resistance and reactance respectively, changes with cycles in cell 19 and how each compare to EIS-measured ESR changes. It is observed that though a similar trend occurs in both tests, FDR resistances are relatively higher than the EIS values. This is likely due to the influence of PCB parasitics.

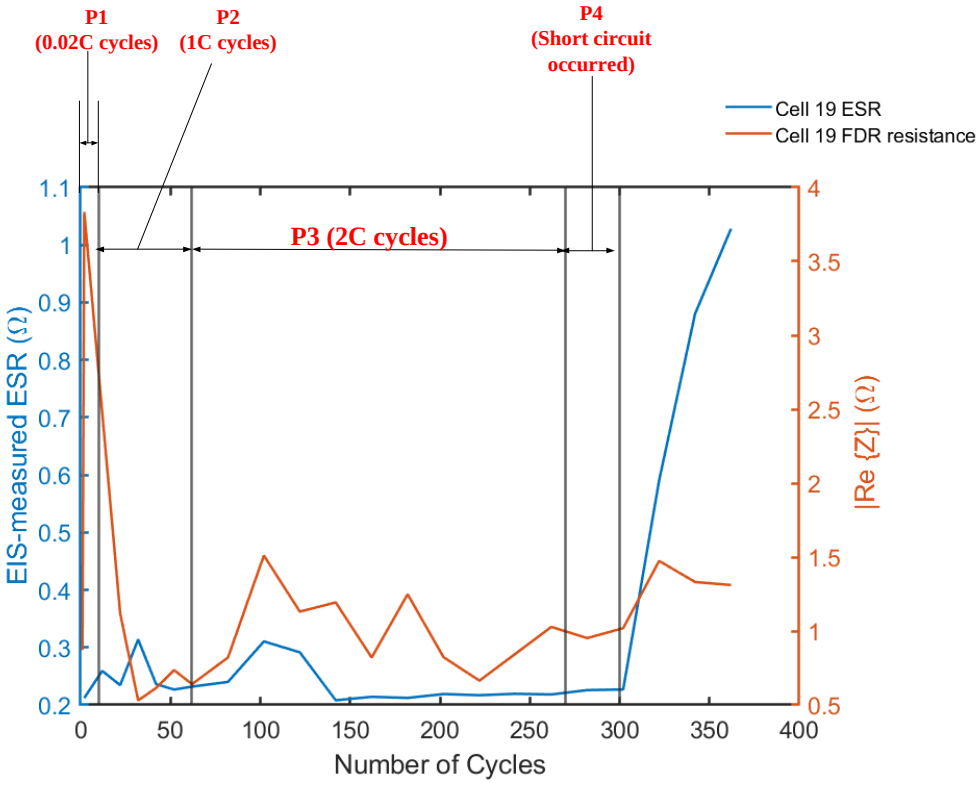

Figure F.22 Comparison of FDR measured resistance and cell ESR over cycling.

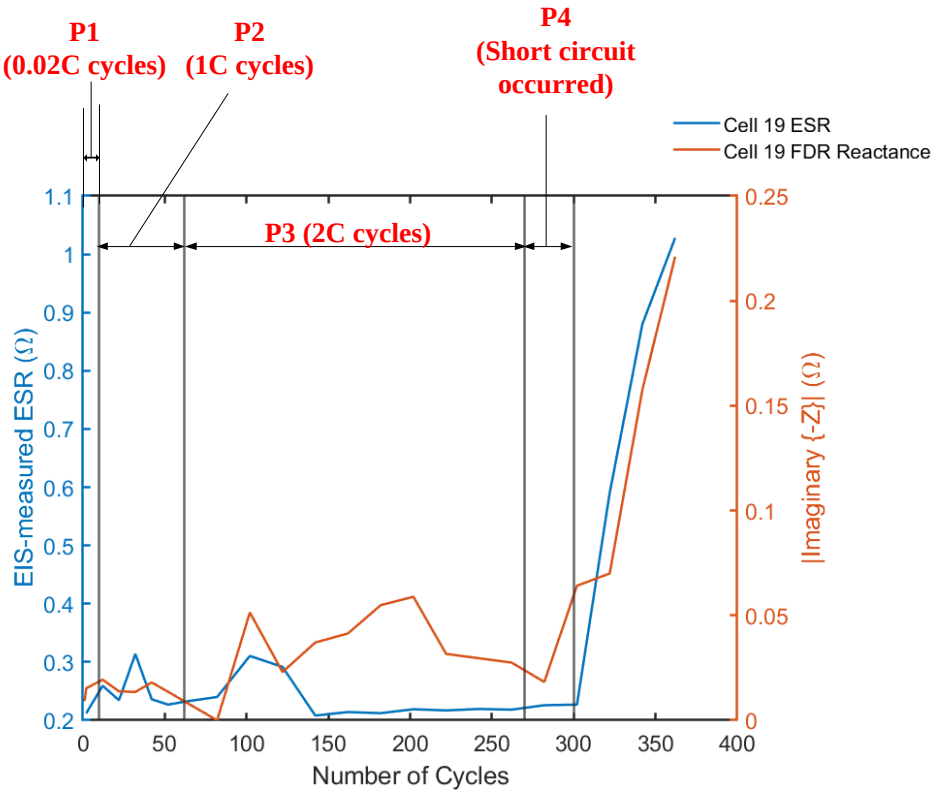

Figure F.23 Comparison of FDR measured reactance and cell ESR over cycling.

F.5 FDR PCB Design

Figure F.24 shows the design of the PCB and the layout highlighting the positions of the components.

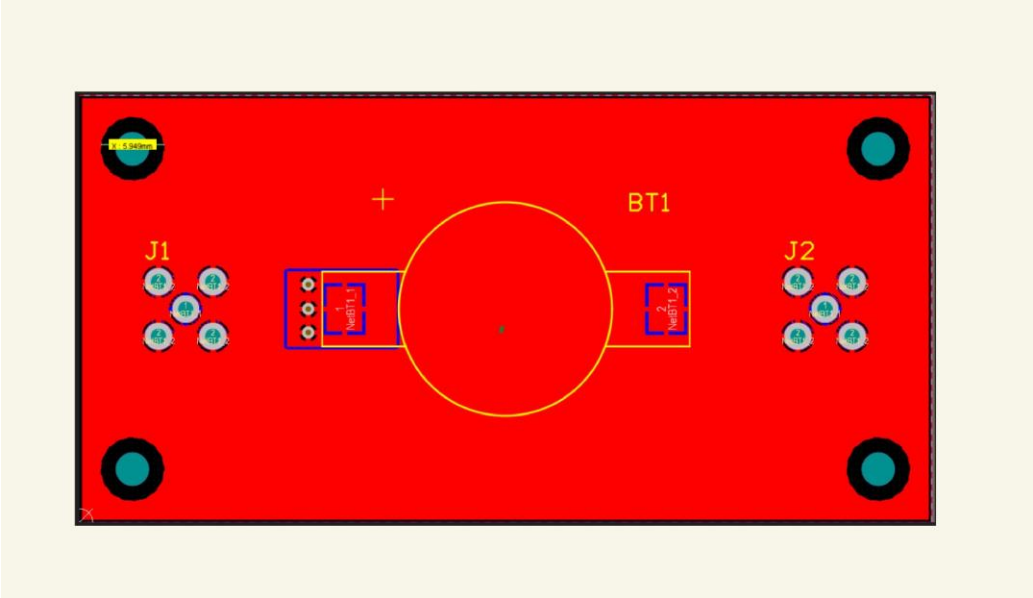

Figure F.24 Gerber file design of PCB used for FDR tests.

APPENDIX G – De-Embedding Response For FDR Setup

Figure G.1 shows the Responses for open, short, load standards used for de-embedding the FDR setup. Also included is a response of a sample cell for comparison. The region of confidence (RoC) is also highlighted. This was later modified after tests on passive elements.

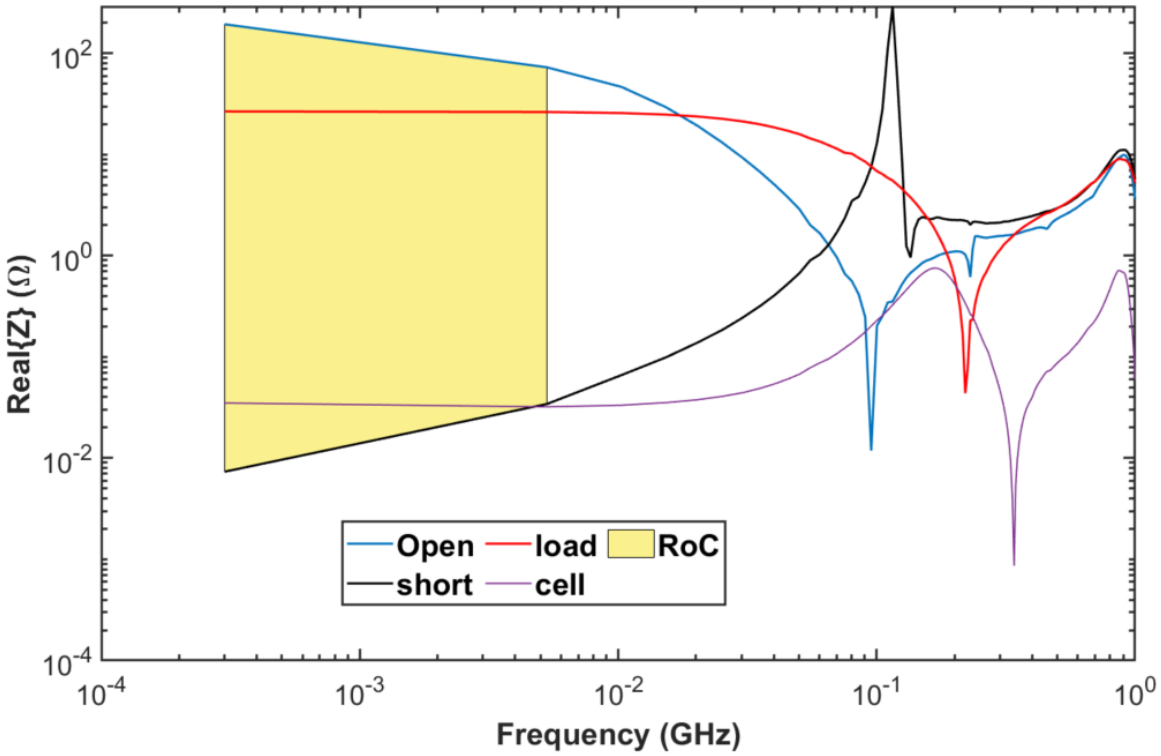

Figure G.1 Responses for open, short, load standards used for de-embedding the FDR setup and the response of a sample cell.

References

1 Internation Energy Agency: ‘Batteries and Secure Energy Transitions – Analysis - IEA’ (2023)

2 Birkl, C.R., Roberts, M.R., McTurk, E., Bruce, P.G., Howey, D.A.: ‘Degradation diagnostics for lithium ion cells’*J Power Sources*, 2017, 341, pp. 373–386.

3 Edge, J.S., O’Kane, S., Prosser, R., *et al.*: ‘Lithium ion battery degradation: what you need to know’*Physical Chemistry Chemical Physics*, 2021, 23, (14), pp. 8200–8221.

4 Furse, C.M.: ‘Frequency Domain Reflectometry System For Testing Wires and Cables Utilizing in-situ Connectors, Passive Connectivity, Cable Fray Detection and Live Wire Testing’. US 6,868,357 B2, 2005

5 Furse, C., Chung, Y., Lo, C., Pendayala, P.: ‘A critical comparison of reflectometry methods for location of wiring faults’*Smart Struct Syst*, 2006, 2.

6 Furse, C., Chung, Y.C., Dangol, R., Nielsen, M., Mabey, G., Woodward, R.: ‘Frequency-domain reflectometry for on-board testing of aging aircraft wiring’*IEEE Trans Electromagn Compat*, 2003, 45, (2), pp. 306–315.

7 Furse, C.M., Kafal, M., Razzaghi, R., Shin, Y.-J.: ‘Fault Diagnosis for Electrical Systems and Power Networks: A Review’*IEEE Sens J*, 2021, 21, (2), pp. 888–906.

8 Hanif, A., Das, S., Khan, F.: ‘Active power cycling and condition monitoring of IGBT power modules using reflectometry’*Conference Proceedings - IEEE Applied Power Electronics Conference and Exposition - APEC*, 2018, 2018-March, pp. 2827–2833.

9 Skierucha, W., Wilczek, A.: ‘A FDR Sensor for Measuring Complex Soil Dielectric Permittivity in the 10–500 MHz Frequency Range’*Sensors*, 2010, 10, (4), pp. 3314–3329.

10 Umenyiora, C.A., Druce, R.L., Curry, R.D., *et al.*: ‘Dielectric Constant of Sand Using TDR and FDR Measurements and Prediction Models’*IEEE Transactions on Plasma Science*, 2012, 40, (10), pp. 2408–2415.

11 Korth Pereira Ferraz, P., Schmidt, R., Kober, D., Kowal, J.: ‘A high frequency model for predicting the behavior of lithium-ion batteries connected to fast switching power electronics’*J Energy Storage*, 2018, 18, pp. 40–49.

12 Landinger, T.F., Schwarzberger, G., Jossen, A.: ‘High frequency impedance characteristics of cylindrical lithium-ion cells: Physical-based modeling of cell state and cell design dependencies’*J Power Sources*, 2021, 488, p. 229463.

13 Meddings, N., Heinrich, M., Overney, F., *et al.*: 'Application of electrochemical impedance spectroscopy to commercial Li-ion cells: A review'*J Power Sources*, 2020, 480, p. 228742.

14 Noura, N., Boulon, L., Jemeï, S.: 'A review of battery state of health estimation methods: Hybrid electric vehicle challenges'*World Electric Vehicle Journal*, 2020, 11, (4), pp. 1–20.

15 Kafadarova, N.M., Stoyanova-Petrova, S. V., Sotirov, S.I., Stoyanova, D. V., Vakrilov, N. V.: 'A Review of State of Health Battery Diagnostics Methods: Current Status and Future Challenges'*2022 31st International Scientific Conference Electronics, ET 2022 - Proceedings*, 2022.

16 Fly, A., Wimarshana, B., Bin-Mat-Arishad, I., Sarmiento-Carnevali, M.: 'Temperature dependency of diagnostic methods in lithium-ion batteries'*J Energy Storage*, 2022, 52, p. 104721.

17 Berecibar, M., Gandiaga, I., Villarreal, I., Omar, N., Van Mierlo, J., Van den Bossche, P.: 'Critical review of state of health estimation methods of Li-ion batteries for real applications'*Renewable and Sustainable Energy Reviews*, 2016, 56, pp. 572–587.

18 Zhang, Y., Tang, Q., Zhang, Y., Wang, J., Stimming, U., Lee, A.A.: 'Identifying degradation patterns of lithium ion batteries from impedance spectroscopy using machine learning'*Nat Commun*, 2020, 11, (1), p. 1706.

19 Zhang, Q., Wang, D., Schaltz, E., Stroe, D.-I., Gismero, A., Yang, B.: 'Degradation mechanism analysis and State-of-Health estimation for lithium-ion batteries based on distribution of relaxation times'*J Energy Storage*, 2022, 55.

20 Ng, K.S., Moo, C.-S., Chen, Y.-P., Hsieh, Y.-C.: 'Enhanced coulomb counting method for estimating state-of-charge and state-of-health of lithium-ion batteries'*Appl Energy*, 2009, 86, (9), pp. 1506–1511.

21 Perry, D., Mamlouk, M.: 'Probing mass transport processes in Li-ion batteries using electrochemical impedance spectroscopy'*J Power Sources*, 2021, 514, p. 230577.

22 Saha, P., Mohanta, T.R., Kumar, A.: 'Chapter 6 - SEI layer and impact on Si-anodes for Li-ion batteries', in Kumta, P.N., Hepp, A.F., Datta, M.K., Velikokhatnyi, O.I. (Eds.): 'Silicon Anode Systems for Lithium-Ion Batteries' (Elsevier, 2022), pp. 183–263

23 Masrakin, K., Abdul Malek, S., Zuraidah Ibrahim, S., Rahim, H.A., Dewani, A.A.: 'Dielectric Properties Characterization of Material Under Test using Microstrip Ring Resonator'2021, p. 12017.

24 Talie, A.P., Pribyl, W.A., Hofer, G.: ‘Electric Vehicle Battery Management System Using Power Line Communication Technique’, in ‘2018 14th Conference on Ph.D. Research in Microelectronics and Electronics (PRIME)’ (2018), pp. 225–228

25 Bolsinger, C., Brix, J., Dragan, M., Birke, K.P.: ‘Investigating and modeling the transmission channel of a prismatic lithium-ion cell and module for powerline communication’*J Energy Storage*, 2017, 10, pp. 11–19.

26 Doersam, T., Schoerle, S., Hoene, E., Lang, K.D., Spieker, C., Waldmann, T.: ‘High frequency impedance of Li-ion batteries’*2015 IEEE International Symposium on Electromagnetic Compatibility (EMC)*, 2015, 2015-Septmber, pp. 714–719.

27 Landinger, T.F., Schwarzberger, G., Jossen, A.: ‘A Novel Method for High Frequency Battery Impedance Measurements’, in ‘2019 IEEE International Symposium on Electromagnetic Compatibility, Signal & Power Integrity (EMC+SIPI)’ (2019), pp. 106–110

28 KeysightTechnologies: ‘Keysight Technologies Ultra-Low Impedance Measurements Using 2-Port Measurements’ (2014)

29 Landinger, T.F., Schwarzberger, G., Jossen, A.: ‘A Physical-Based High-Frequency Model of Cylindrical Lithium-Ion Batteries for Time Domain Simulation’*IEEE Trans Electromagn Compat*, 2020, 62, (4), pp. 1524–1533.

30 Roy, S., Khan, F.: ‘Detection of Degraded/Aged Cell in a Li-ion Battery Pack using Spread Spectrum Time Domain Reflectometry (SSTDR)’, in (2020), pp. 1483–1488

31 Zhao, J., Feng, X., Tran, M.-K., Fowler, M., Ouyang, M., Burke, A.F.: ‘Battery safety: Fault diagnosis from laboratory to real world’*J Power Sources*, 2024, 598, (January), p. 234111.

32 Middlemiss, L.A., Rennie, A.J.R., Sayers, R., West, A.R.: ‘Characterisation of batteries by electrochemical impedance spectroscopy’*Energy Reports*, 2020, 6, pp. 232–241.

33 Rufino Júnior, C.A., Sanseverino, E.R., Gallo, P., *et al.*: ‘Unraveling the Degradation Mechanisms of Lithium-Ion Batteries’*Energies 2024, Vol. 17, Page 3372*, 2024, 17, (14), p. 3372.

34 Xiong, R., Li, L., Tian, J.: ‘Towards a smarter battery management system: A critical review on battery state of health monitoring methods’*J Power Sources*, 2018, 405, pp. 18–29.

35 Tang, A., Hu, G., Liu, M.: ‘Mechanical degradation of electrode materials within single particle model in Li-ion batteries for electric vehicles’*J Math Chem*, 2017, 55, (10), pp. 1903–1915.

36 Wu, Q., McDowell, M.T., Qi, Y.: 'Effect of the Electric Double Layer (EDL) in Multicomponent Electrolyte Reduction and Solid Electrolyte Interphase (SEI) Formation in Lithium Batteries'*J Am Chem Soc*, 2023, 145, (4), pp. 2473–2484.

37 Rahman, T., Alharbi, T.: 'Exploring Lithium-Ion Battery Degradation: A Concise Review of Critical Factors, Impacts, Data-Driven Degradation Estimation Techniques, and Sustainable Directions for Energy Storage Systems'*Batteries 2024, Vol. 10, Page 220*, 2024, 10, (7), p. 220.

38 Lou, T., Zhang, W., Guo, H., Wang, J.: 'The internal resistance characteristics of lithium-ion battery based on HPPC method'*Adv Mat Res*, 2012, 455–456, pp. 246–251.

39 Zhang, G., Wei, X., Wang, X., *et al.*: 'Lithium-ion battery sudden death: Safety degradation and failure mechanism'*eTransportation*, 2024, 20, p. 100333.

40 Hu, W., Peng, Y., Wei, Y., Yang, Y.: 'Application of Electrochemical Impedance Spectroscopy to Degradation and Aging Research of Lithium-Ion Batteries'*Journal of Physical Chemistry C*, 2023, 127, (9), pp. 4465–4495.

41 Vennam, G., Sahoo, A., Ahmed, S.: 'A survey on lithium-ion battery internal and external degradation modeling and state of health estimation'*J Energy Storage*, 2022, 52, p. 104720.

42 Han, B., Zou, Y., Xu, G., *et al.*: 'Additive stabilization of SEI on graphite observed using cryo-electron microscopy'*Energy Environ Sci*, 2021, 14, (9), pp. 4882–4889.

43 Gaye, S., Catuche, J., Kabir, M., Xu, J.: 'Design and Development of an Automated Lithium-Ion Battery Temperature and Internal Pressure Monitoring Device'*InterSociety Conference on Thermal and Thermomechanical Phenomena in Electronic Systems, ITHERM*, 2022, 2022-May.

44 Essl, C., Seifert, L., Rabe, M., Fuchs, A.: 'Early detection of failing automotive batteries using gas sensors'*Batteries*, 2021, 7, (2).

45 Metzger, M., Gasteiger, H.A., Metzger, M., Gasteiger, A.: 'Diagnosing Battery Degradation via Gas Analysis'*Energy & Environmental Materials*, 2022, 5, (3), pp. 688–692.

46 Ju, L., Li, X., Geng, G., Jiang, Q.: 'Degradation diagnosis of lithium-ion batteries considering internal gas evolution'*J Energy Storage*, 2023, 71, p. 108084.

47 Montoya-Bedoya, S., Bernal, M., Sabogal-Moncada, L.A., Martinez-Tejada, H. V., Garcia-Tamayo, E.: 'Noninvasive ultrasound for Lithium-ion batteries state estimation'*LAUS 2021 - 2021 IEEE UFFC Latin America Ultrasonics Symposium, Proceedings*, 2021.

48 Wu, Y., Wang, Y., Yung, W.K.C., Pecht, M.: 'Ultrasonic Health Monitoring of Lithium-Ion Batteries'*Electronics 2019, Vol. 8, Page 751*, 2019, 8, (7), p. 751.

49 Mousavi, M., Taskhiri, M.S., Holloway, D., Olivier, J.C., Turner, P.: 'Feature extraction of wood-hole defects using empirical mode decomposition of ultrasonic signals'*NDT & E International*, 2020, 114, p. 102282.

50 Lipu, M.S.H., Hannan, M.A., Hussain, A., *et al.*: 'A review of state of health and remaining useful life estimation methods for lithium-ion battery in electric vehicles: Challenges and recommendations'*J Clean Prod*, 2018, 205, pp. 115–133.

51 Pradhan, S.K., Chakraborty, B.: 'Battery management strategies: An essential review for battery state of health monitoring techniques'*J Energy Storage*, 2022, 51, p. 104427.

52 Blidberg, A.: 'Correlation between different impedance measurement methods for battery cells'no date.

53 Zhang, H., Mu, H.W., Zhang, Y., Han, J.: 'Calculation and Characteristics Analysis of Lithium Ion Batteries' Internal Resistance Using HPPC Test'*Adv Mat Res*, 2014, 926–930, pp. 915–918.

54 Jin An, S., Li, J., Daniel, C., *et al.*: 'Optimum Model-Based Design of Diagnostics Experiments (DOE) with Hybrid Pulse Power Characterization (HPPC) for Lithium-Ion Batteries'*J Electrochem Soc*, 2024, 171, (7), p. 070544.

55 Weng, C., Cui, Y., Sun, J., Peng, H.: 'On-board state of health monitoring of lithium-ion batteries using incremental capacity analysis with support vector regression'*J Power Sources*, 2013, 235, pp. 36–44.

56 Safari, M., Delacourt, C.: 'Aging of a Commercial Graphite/LiFePO4 Cell'*J Electrochem Soc*, 2011, 158, (10), p. A1123.

57 Mingant, R., Bernard, J., Sauvant Moynot, V., *et al.*: 'EIS Measurements for Determining the SoC and SoH of Li-Ion Batteries'*ECS Trans*, 2011, 33, (39), pp. 41–53.

58 Zhang, K., Yin, J., He, Y.: 'Acoustic Emission Detection and Analysis Method for Health Status of Lithium Ion Batteries'*Sensors 2021, Vol. 21, Page 712*, 2021, 21, (3), p. 712.

59 Locorotondo, E., Cultrera, V., Pugi, L., Berzi, L., Pierini, M., Lutzemberger, G.: 'Development of a battery real-time state of health diagnosis based on fast impedance measurements'*J Energy Storage*, 2021, 38, p. 102566.

60 Ma, R., He, J., Deng, Y.: 'Investigation and comparison of the electrochemical impedance spectroscopy and internal resistance indicators for early-stage internal short circuit detection through battery aging'*J Energy Storage*, 2022, 54, p. 105346.

61 Allam, A., Onori, S.: ‘Online Capacity Estimation for Lithium-Ion Battery Cells via an Electrochemical Model-Based Adaptive Interconnected Observer’*IEEE Transactions on Control Systems Technology*, 2020, 29, (4), pp. 1636–1651.

62 Zhang, Q., Li, X., Du, Z., Liao, Q.: ‘Aging performance characterization and state-of-health assessment of retired lithium-ion battery modules’*J Energy Storage*, 2021, 40, p. 102743.

63 Iurilli, P., Brivio, C., Wood, V.: ‘On the use of electrochemical impedance spectroscopy to characterize and model the aging phenomena of lithium-ion batteries: a critical review’*J Power Sources*, 2021, 505, p. 229860.

64 Hu, X., Liu, W., Lin, X., Xie, Y.: ‘A Comparative Study of Control-Oriented Thermal Models for Cylindrical Li-Ion Batteries’*IEEE Transactions on Transportation Electrification*, 2019, 5, (4), pp. 1237–1253.

65 Li, D., Yang, D., Li, L., Wang, L., Wang, K.: ‘Electrochemical Impedance Spectroscopy Based on the State of Health Estimation for Lithium-Ion Batteries’*Energies 2022, Vol. 15, Page 6665*, 2022, 15, (18), p. 6665.

66 Plett, G.L.: ‘Extended Kalman filtering for battery management systems of LiPB-based HEV battery packs: Part 3. State and parameter estimation’*J Power Sources*, 2004, 134, (2), pp. 277–292.

67 Remmlinger, J., Buchholz, M., Soczka-Guth, T., Dietmayer, K.: ‘On-board state-of-health monitoring of lithium-ion batteries using linear parameter-varying models’*J Power Sources*, 2013, 239, pp. 689–695.

68 Zhang, F., Liu, G., Fang, L.: ‘Battery state estimation using unscented kalman filter’*Proc IEEE Int Conf Robot Autom*, 2009, pp. 1863–1868.

69 Doyle, M., Fuller, T.F., Newman, J.: ‘Modeling of Galvanostatic Charge and Discharge of the Lithium/Polymer/Insertion Cell’*J Electrochem Soc*, 1993, 140, (6), pp. 1526–1533.

70 Fuller, T.F., Doyle, M., Newman, J.: ‘Simulation and Optimization of the Dual Lithium Ion Insertion Cell’*J Electrochem Soc*, 1994, 141, (1), pp. 1–10.

71 Lotfi, N., Li, J., Landers, R.G., Park, J.: ‘Li-ion Battery State of Health Estimation based on an improved Single Particle model’*Proceedings of the American Control Conference*, 2017, pp. 86–91.

72 Zheng, L., Zhang, L., Zhu, J., Wang, G., Jiang, J.: ‘Co-estimation of state-of-charge, capacity and resistance for lithium-ion batteries based on a high-fidelity electrochemical model’*Appl Energy*, 2016, 180, pp. 424–434.

73 Bartlett, A., Marcicki, J., Onori, S., Rizzoni, G., Yang, X.G., Miller, T.: 'Model-based state of charge estimation and observability analysis of a composite electrode lithium-ion battery'*Proceedings of the IEEE Conference on Decision and Control*, 2013, pp. 7791–7796.

74 Zou, C., Manzie, C., Nešić, D., Kallapur, A.G.: 'Multi-time-scale observer design for state-of-charge and state-of-health of a lithium-ion battery'*J Power Sources*, 2016, 335, pp. 121–130.

75 Li, J., Adewuyi, K., Lotfi, N., Landers, R.G., Park, J.: 'A single particle model with chemical/mechanical degradation physics for lithium ion battery State of Health (SOH) estimation'*Appl Energy*, 2018, 212, pp. 1178–1190.

76 Deshpande, R., Verbrugge, M., Cheng, Y.-T., Wang, J., Liu, P.: 'Battery Cycle Life Prediction with Coupled Chemical Degradation and Fatigue Mechanics'*J Electrochem Soc*, 2012, 159, (10), pp. A1730–A1738.

77 Chen, S., Zhang, Q., Wang, F., Wang, D., He, Z.: 'An electrochemical-thermal-aging effects coupled model for lithium-ion batteries performance simulation and state of health estimation'*Appl Therm Eng*, 2024, 239, p. 122128.

78 Tian, J., Xiong, R., Shen, W.: 'State-of-Health Estimation Based on Differential Temperature for Lithium Ion Batteries'*IEEE Trans Power Electron*, 2020, 35, (10), pp. 10363–10373.

79 Jiang, T., Ma, M., Hu, Q., Song, Q.: 'Improved PSO-BPNN Multi-Parameter Identification Method and Its Application in Battery Thermal Network Model'*PEAS 2023 - 2023 IEEE 2nd International Power Electronics and Application Symposium, Conference Proceedings*, 2023, pp. 1907–1911.

80 Tran, M.K., Dacosta, A., Mevawalla, A., Panchal, S., Fowler, M.: 'Comparative Study of Equivalent Circuit Models Performance in Four Common Lithium-Ion Batteries: LFP, NMC, LMO, NCA'*Batteries 2021, Vol. 7, Page 51*, 2021, 7, (3), p. 51.

81 Bairwa, B., Pareek, K., Manohar, K.A., Nanditha Varshini, E.: 'Electrical Equivalent Circuit Modeling of Lithium-Ion Battery'*Proceedings of the 3rd International Conference on Smart Technologies in Computing, Electrical and Electronics, ICSTCEE 2022*, 2022.

82 Santhanagopalan, S., Zhang, Q., Kumaresan, K., White, R.E.: 'Parameter Estimation and Life Modeling of Lithium-Ion Cells'*J Electrochem Soc*, 2008, 155, (4), p. A345.

83 Raszmann, E., Baker, K., Shi, Y., Christensen, D.: 'Modeling stationary lithium-ion batteries for optimization and predictive control'*2017 IEEE Power and Energy Conference at Illinois, PECI 2017*, 2017.

84 Illig, J.: 'Physically based Impedance Modelling of Lithium-Ion Cells'*Physically based Impedance Modelling of Lithium-Ion Cells*, 2014, pp. 1–202.

85 Plett, G.L.: 'Battery Management Systems Volume I Battery Modeling' (Artech House, 2015)

86 Wang, Z., Feng, G., Zhen, D., Gu, F., Ball, A.: 'A review on online state of charge and state of health estimation for lithium-ion batteries in electric vehicles'*Energy Reports*, 2021, 7, pp. 5141–5161.

87 Simic, M., Stavrakis, A.K., Kojic, T., Jeoti, V., Stojanovic, G.M.: 'Parameter Estimation of the Randles Equivalent Electrical Circuit Using Only Real Part of the Impedance'*IEEE Sens J*, 2023, 23, (5), pp. 4922–4929.

88 Simić, M., Stavrakis, A.K., Stojanović, G.M.: 'A Low-Complexity Method for Parameter Estimation of the Simplified Randles Circuit With Experimental Verification'*IEEE Sens J*, 2021, 21, (21), pp. 24209–24217.

89 Afshari, H.H., Attari, M., Ahmed, R., Delbari, A., Habibi, S., Shoa, T.: 'Reliable state of charge and state of health estimation using the smooth variable structure filter'*Control Eng Pract*, 2018, 77, pp. 1–14.

90 Shu, X., Li, G., Shen, J., Lei, Z., Chen, Z., Liu, Y.: 'An adaptive multi-state estimation algorithm for lithium-ion batteries incorporating temperature compensation'*Energy*, 2020, 207, p. 118262.

91 Saha, B., Goebel, K., Poll, S., Christophersen, J.: 'Prognostics methods for battery health monitoring using a Bayesian framework'*IEEE Trans Instrum Meas*, 2009, 58, (2), pp. 291–296.

92 Zhang, J., Wang, P., Gong, Q., Cheng, Z.: 'SOH estimation of lithium-ion batteries based on least squares support vector machine error compensation model'*Journal of Power Electronics*, 2021, 21, (11), pp. 1712–1723.

93 Jaworski, R.K.: 'Statistical parameters model for predicting time to failure of telecommunications batteries'*INTELEC, International Telecommunications Energy Conference (Proceedings)*, 1999, pp. 24–23.

94 Schweiger, H.G., Obeidi, O., Komesker, O., *et al.*: 'Comparison of Several Methods for Determining the Internal Resistance of Lithium Ion Cells'*Sensors (Basel)*, 2010, 10, (6), p. 5604.

95 Tang, A., Jiang, Y., Yu, Q., Zhang, Z.: 'A hybrid neural network model with attention mechanism for state of health estimation of lithium-ion batteries'*J Energy Storage*, 2023, 68, p. 107734.

96 Lee, P.Y., Kwon, S., Kang, D., Cho, I., Kim, J.: 'Principle component analysis-based optimized feature extraction merged with nonlinear regression model for improved state-of-health prediction'*J Energy Storage*, 2022, 48, p. 104026.

97 Schmid, M., Kneidinger, H.-G., Endisch, C.: 'Data-Driven Fault Diagnosis in Battery Systems Through Cross-Cell Monitoring'*IEEE Sens J*, 2021, 21, (2), pp. 1829–1837.

98 Zenati, A., Desprez, P., Razik, H., Rael, S.: 'Impedance measurements combined with the fuzzy logic methodology to assess the SOC and SOH of lithium-ion cells'*2010 IEEE Vehicle Power and Propulsion Conference, VPPC 2010*, 2010.

99 Tinnemeyer, J.: 'Fuzzy logic method and apparatus for battery state of health determination'. US 7,072,871 B1, 2001

100 Yang, F., Wang, D., Zhao, Y., Tsui, K.L., Bae, S.J.: 'A study of the relationship between coulombic efficiency and capacity degradation of commercial lithium-ion batteries'*Energy*, 2018, 145, pp. 486–495.

101 Naha, A., Han, S., Agarwal, S., *et al.*: 'An Incremental Voltage Difference Based Technique for Online State of Health Estimation of Li-ion Batteries'*Scientific Reports 2020 10:1*, 2020, 10, (1), pp. 1–11.

102 Abdillah, A.A., Zhang, C., Sun, Z., Li, J., Xu, H., Zhou, Q.: 'Data-driven Modelling for EV Battery State of Health Estimation using SFS-PCA Learning'*2023 7th CAA International Conference on Vehicular Control and Intelligence (CVCI)*, 2023.

103 Wu, M., Zhong, Y., Wu, J., Wang, Y., Wang, L.: 'State of health estimation of the lithium-ion power battery based on the principal component analysis-particle swarm optimization-back propagation neural network'*Energy*, 2023, 283, p. 129061.

104 Vasta, E., Scimone, T., Nobile, G., *et al.*: 'Models for Battery Health Assessment: A Comparative Evaluation'*Energies (Basel)*, 2023, 16, (2).

105 Zaman, M.H.M., Mustafa, M.M., Hussain, A.: 'Critical equivalent series resistance estimation for voltage regulator stability using hybrid system identification and neural network'*Int J Adv Sci Eng Inf Technol*, 2017, 7, (4), pp. 1381–1388.

106 Sun, S., Lin, Q., Li, H., Zhan, Y., Dai, Y.: 'Simultaneous Estimation of SOH and SOC of Batteries Based on SVM'*2022 4th International Conference on Smart Power and Internet Energy Systems, SPIES 2022*, 2022, pp. 1934–1938.

107 Luo, W., Syed, A.U., Nicholls, J.R., Gray, S.: 'An SVM-Based Health Classifier for Offline Li-Ion Batteries by Using EIS Technology'*J Electrochem Soc*, 2023, 170, (3), p. 030532.

108 Light Yuwei Lu, S., Zhang, J., Yin, L., *et al.*: 'State of health estimation for lithium-ion battery based on improved support vector regression'*J Phys Conf Ser*, 2023, 2483, (1), p. 012024.

109 Wang, G., Lyu, Z., Li, X.: 'An Optimized Random Forest Regression Model for Li-Ion Battery Prognostics and Health Management'*Batteries 2023, Vol. 9, Page 332*, 2023, 9, (6), p. 332.

110 Tian, J., Zhang, J., Huangy, C., Chowz, M.Y., Luo, H.: 'Random Forest Regression for Battery State-of-Health Estimation Based on Unsupervised Transfer Component Analysis Domain Adaptation'*Proceedings of the IEEE International Conference on Industrial Technology*, 2022, 2022-August.

111 Fuentes-García, M., Maciá-Fernández, G., Camacho, J.: 'Evaluation of diagnosis methods in PCA-based Multivariate Statistical Process Control'*Chemometrics and Intelligent Laboratory Systems*, 2018, 172, (March 2017), pp. 194–210.

112 Chen, A., Zhou, H., An, Y., Sun, W.: 'PCA and PLS monitoring approaches for fault detection of wastewater treatment process', in '2016 IEEE 25th International Symposium on Industrial Electronics (ISIE)' (2016), pp. 1022–1027

113 Prasad, G.K., Rahn, C.D.: 'Model based identification of aging parameters in lithium ion batteries'*J Power Sources*, 2013, 232, pp. 79–85.

114 Eddahech, A., Briat, O., Vinassa, J.M.: 'Real-time SOC and SOH estimation for EV Li-ion cell using online parameters identification'*2012 IEEE Energy Conversion Congress and Exposition, ECCE 2012*, 2012, pp. 4501–4505.

115 Barai, A., Uddin, K., Dubarry, M., *et al.*: 'A comparison of methodologies for the non-invasive characterisation of commercial Li-ion cells'*Prog Energy Combust Sci*, 2019, 72, pp. 1–31.

116 Landinger, T.F.: 'Electrochemical Impedance Spectroscopy and Power Line Communications for Automotive Battery Management Systems'. 2021

117 Gamry Instruments: 'Measuring Batteries using the Right Setup: Dual-cell CR2032 and 18650 Battery Holder' (2015)

118 Lazanas, A.C., Prodromidis, M.I.: 'Electrochemical Impedance Spectroscopy─A Tutorial'*ACS Measurement Science Au*, 2023, 3, (3), pp. 162–193.

119 Waremra, R.S., Betaubun, P.: ‘Analysis of Electrical Properties Using the four point Probe Method’*E3S Web of Conferences*, 2018, 73, p. 13019.

120 Zhang, Y., Jiang, M., Zhou, Y., Zhao, S., Yuan, Y.: ‘Towards High-Safety Lithium-Ion Battery Diagnosis Methods’*Batteries 2023, Vol. 9, Page 63*, 2023, 9, (1), p. 63.

121 Vivier, V., Orazem, M.E.: ‘Impedance Analysis of Electrochemical Systems’*Chem Rev*, 2022, 122, (12), pp. 11131–11168.

122 Bonanos, N., Steele, B.C.H., Butler, E.P., *et al.*: ‘Applications of Impedance Spectroscopy’, in ‘Impedance Spectroscopy’ (John Wiley & Sons, Ltd, 2018), pp. 175–478

123 Bao, Y., Gong, Y.: ‘Li-ion battery charge transfer stability studies with direct current impedance spectroscopy’*Energy Reports*, 2023, 9, pp. 34–41.

124 Suarez-Hernandez, R., Ramos-Sánchez, G., Santos-Mendoza, I.O., Guzmán-González, G., González, I.: ‘A Graphical Approach for Identifying the Limiting Processes in Lithium-Ion Battery Cathode Using Electrochemical Impedance Spectroscopy’*J Electrochem Soc*, 2020, 167, (10), p. 100529.

125 ‘Potentiostat Calibration with Dummy Cell Gamry Instruments’, https://www.gamry.com/support-2/technical-support/troubleshooting/troubleshooting-walkthrough/potentiostat-calibration/, accessed April 2025

126 Hewlette Packard: ‘Effective Impedance Measurement Using OPEN/SHORT/LOAD Correction’ (1998), p. 12

127 Torrents, J.M., Pallàs-Areny, R.: ‘Error analysis in two-terminal impedance measurements with residual correction’*IEEE Trans Instrum Meas*, 2005, 54, (5), pp. 2113–2116.

128 Hackl, H., Ibel, M., Landinger, T.F., Pommerenke, D.J., Auinger, B.: ‘Li-Ion Cell Impedance Measurement Using Open/Short/Load Compensation for De-Embedding’*2021 Joint IEEE International Symposium on Electromagnetic Compatibility Signal and Power Integrity, and EMC Europe, EMC/SI/PI/EMC Europe 2021*, 2021, pp. 190–195.

129 Kaistha, N., Upadhyaya], B.R.: ‘Incipient Fault Detection and Isolation of Field Devices in Nuclear Power Systems Using Principal Component Analysis’*Nucl Technol*, 2001, 136, (2), pp. 221–230.

130 Glass, S.W., Fifield, L.S., Jones, A.M., Hartman, T.S.: ‘Frequency Domain Reflectometry Modeling and Measurement for Nondestructive Evaluation of Nuclear Power Plant Cables’, in Jackson, J.H., Paraventi, D., Wright, M. (Eds.): ‘Proceedings of

the 18th International Conference on Environmental Degradation of Materials in Nuclear Power Systems -- Water Reactors' (Springer International Publishing, 2019), pp. 1267–1280

131 Cataldo, A., De Benedetto, E.: 'Broadband Reflectometry for Diagnostics and Monitoring Applications'*IEEE Sens J*, 2011, 11, (2), pp. 451–459.

132 Llamazares, A., Garcia-Gracia, M., Martin-Arroyo, S.: 'Characterization of Parasitic Impedance in PCB Using a Flexible Test Probe Based on a Curve-Fitting Method'*IEEE Access*, 2021, 9, pp. 40695–40705.

133 Xu, J., Ma, X., Logsdon, S.D., Horton, R.: 'Frequency measurement of FDR based on soil dielectric spectrum in LF-UHF'*Nongye Jixie Xuebao/Transactions of the Chinese Society for Agricultural Machinery*, 2013, 44, (7), pp. 67–72.

134 Teran-Bahena, E.Y., Sejas-Garcia, S.C., Torres-Torres, R.: 'Characterization of transmission lines on PCB from s-parameters by determining the dielectric and conductor losses at the crossover frequency'*IEEE Trans Compon Packaging Manuf Technol*, 2018, 8, (5), pp. 867–874.

135 Pozar, D.: 'Microwave Engineering' (John Wiley & Sons Inc, 2012, 4th edn.)

136 Steer, M.: 'Microwave and RF Design, Volume 2: Transmission Lines' (University of North Carolina Press, 2019)

137 Steer, M.: 'Fundamentals of Microwave and RF Design' (North Carolina State University Libraries, 2019)

138 KeysightTechnologies: 'Understanding the Fundamental Principles of Vector Network Analysis | Keysight' (2000)

139 UserManual: 'PicoVNA 6 and 8.5 GHz Vector Network Analyzers' (2020)

140 'Agilent De-embedding and Embedding S-Parameter Networks Using a Vector Network Analyzer 2'no date.

141 KeysightTechnologies: 'Impedance Measurements of EMC Components with DC Bias Current | Keysight', https://www.keysight.com/us/en/assets/7018-01969/application-notes/5989-9887.pdf, accessed May 2023

142 Pake Talei, A., Pribyl, W.A., Hofer, G.: 'Considerations for a power line communication system for traction batteries'*Elektrotechnik und Informationstechnik*, 2021, 138, (1), pp. 3–14.

143 Ruddle, A.R., Chen, J., Teo, Y.X.: 'Measurement of RF impedance for automotive 18650 cylindrical lithium ion cells', in '2017 International Symposium on Electromagnetic Compatibility - EMC EUROPE' (2017), pp. 1–6

144 Jossen, A.: ‘Fundamentals of battery dynamics’*J Power Sources*, 2006, 154, (2), pp. 530–538.

145 Kawaura, H., Harada, M., Kondo, Y., *et al.*: ‘Operando Measurement of Solid Electrolyte Interphase Formation at Working Electrode of Li-Ion Battery by Time-Slicing Neutron Reflectometry’*ACS Appl Mater Interfaces*, 2016, 8, (15), pp. 9540–9544.

146 Owejan, J.E., Owejan, J.P., Decaluwe, S.C., Dura, J.A.: ‘Solid electrolyte interphase in Li-ion batteries: Evolving structures measured in situ by neutron reflectometry’*Chemistry of Materials*, 2012, 24, (11), pp. 2133–2140.

147 Kruse, L.E., Schill, J., Landsiedel, O., Pachnicke, S.: ‘Optical Monitoring of Second-Life Batteries Enhanced by Machine Learning’*2022 IEEE 13th International Symposium on Power Electronics for Distributed Generation Systems, PEDG 2022*, 2022.

148 Saleh, M.U., Deline, C., Kingston, S., *et al.*: ‘Detection and Localization of Disconnections in PV Strings Using Spread-Spectrum Time-Domain Reflectometry’*IEEE J Photovolt*, 2020, 10, (1), pp. 236–242.

149 Reuter, M., Friedl, T., Tenbohlen, S., Kohler, W.: ‘Emulation of conducted emissions of an automotive inverter for filter development in HV networks’*IEEE International Symposium on Electromagnetic Compatibility*, 2013, pp. 236–241.

150 Laman, F.C., Matsen, M.W., Stiles, J.A.R.: ‘Inductive Impedance of a Spirally Wound Li / MoS2 Cell’*J Electrochem Soc*, 1986, 133, (12), p. 2441.

151 Schindler, S., Danzer, M.A.: ‘Influence of cell design on impedance characteristics of cylindrical lithium-ion cells: A model-based assessment from electrode to cell level’*J Energy Storage*, 2017, 12, pp. 157–166.

152 Taiwan NEXCell battery Company: ‘Material Safety Data Sheet Induex-25 MATERIAL SAFETY DATA SHEET’ (2021)

153 Woehrle, T.: ‘Lithium-ion cell’, in Korthauer, R. (Ed.): ‘Lithium-Ion Batteries: Basics and Applications’ (Springer Berlin Heidelberg, 2018), pp. 101–111

154 RS Components Ltd: ‘RS Pro Lithium-ion button battery Datasheet’ (2022)

155 Luc, P.M., Bauer, S., Kowal, J.: ‘Reproducible Production of Lithium-Ion Coin Cells’*Energies 2022, Vol. 15, Page 7949*, 2022, 15, (21), p. 7949.

156 Lall, P., Soni, V., Sethi, G., Yiang, K.: ‘Estimation of SOH Degradation of Coin Cells Subjected to Accelerated Life Cycling with Randomized Cycling Depths and C-Rates’*IEEE International Reliability Physics Symposium Proceedings*, 2023, 2023-March.

157 Maity, J., Dutta, S., Khanra, M.: ‘Constant Voltage Charging Curve Based Features and State of Health Estimation of Li-ion Batteries: A Comprehensive Study’*2022 International Conference on Smart Generation Computing, Communication and Networking, SMART GENCON 2022*, 2022.

158 Kucinskis, G., Bozorgchenani, M., Feinauer, M., Kasper, M., Wohlfahrt-Mehrens, M., Waldmann, T.: ‘Arrhenius plots for Li-ion battery ageing as a function of temperature, C-rate, and ageing state – An experimental study’*J Power Sources*, 2022, 549, p. 232129.

159 ‘PEIS or GEIS or GEIS-AA? That is the question. - BioLogic Learning Center’, https://www.biologic.net/topics/peis-or-geis-that-is-the-question/, accessed April 2025

160 Murer, N., Diard, J.P., Petrescu, B.: ‘The effects of time-variance on impedance measurements: Examples of a corroding electrode and a battery cell’*Journal of Electrochemical Science and Engineering*, 2020, 10, (2), pp. 127–140.

161 Usman Tahir, M., Sangwongwanich, A., Stroe, D.I., Blaabjerg, F.: ‘Overview of multi-stage charging strategies for Li-ion batteries’*Journal of Energy Chemistry*, 2023, 84, pp. 228–241.

162 Ishigaki, M., Ishikawa, K., Usuki, T., Kondo, H., Komagata, S., Sasaki, T.: ‘Operando Li metal plating diagnostics via MHz band electromagnetics’*Nature Communications 2023 14:1*, 2023, 14, (1), pp. 1–9.

163 KeysightTechnologies: ‘Performing Impedance Analysis with the E5061B ENA Vector Network Analyzer’ (2018)

164 Sharawi, M.S.: ‘Practical Issues in high speed PCB design’*IEEE Potentials*, 2004, 23, (2), pp. 24–27.

165 Davis, A.K.: ‘Effect of magnetic coupling between the mounting loops of two parallel capacitors on antiresonance’*IET Science, Measurement and Technology*, 2016, 10, (8), pp. 889–899.

166 Fujita, Y., Kono, A., Suzuki, Y., Urushibata, H., Naoe, N., Hanaoka, R.: ‘Analysis of Current, Polarization and Lithium Concentration in the Porous Electrode of a Lithium-ion Battery during High-frequency, High-current (10,000C) Flow’*2023 32nd International Scientific Conference Electronics, ET 2023 - Proceedings*, 2023.

167 Ishikawa, K., Komagata, S., Morimoto, R., Ishigaki, M., Kondo, H., Sasaki, T.: ‘High-Frequency Electrochemical Impedance Spectroscopy for Detecting Li Deposition Toward Assessing Thermal Stability in LiBs’*ECS Meeting Abstracts*, 2024, MA2024-01, (1), p. 169.

168 Brunton, S., Kutz, N.J.: ‘Data Driven Science & Engineering Machine Learning, Dynamical Systems, and Control’ (2017)

169 Jolliffe, I.T.: ‘Principal Component Analysis’ (Springer, 2002, Second Edi)

170 Ding, S.X.: ‘Data-driven Design of Fault Diagnosis and Fault-tolerant Control Systems’ (2014)

171 He, Y., Zhang, Z., Wang, L., Li, W., He, J., Jun, Z.: ‘An interesting phenomenon in the C-V measurements of nanocrystal based MOS capacitor’*Proceeding of 2007 International Workshop on Electron Devices and Semiconductor Technology, IEDST 2007*, 2007, pp. 129–132.

172 Härdle, W.K., Simar, L.: ‘Applied multivariate statistical analysis, fourth edition’ (2015)

173 Lück, J., Latz, A.: ‘The electrochemical double layer and its impedance behavior in lithium-ion batteries’*Physical Chemistry Chemical Physics*, 2019, 21, (27), pp. 14753–14765.

174 Jow, T.R., Delp, S.A., Allen, J.L., Jones, J.-P., Smart, M.C.: ‘Factors Limiting Li+ Charge Transfer Kinetics in Li-Ion Batteries’*J Electrochem Soc*, 2018, 165, (2), p. A361.

175 Luo, G., Zhang, Y., Tang, A.: ‘Capacity Degradation and Aging Mechanisms Evolution of Lithium-Ion Batteries under Different Operation Conditions’*Energies (Basel)*, 2023, 16, (10), p. 4232.

176 Brand, M.J., Utz, H., München, V.·: ‘Lithium-ion battery cells and systems under dynamic electric loads’no date.

177 Sungjemmenla, Vineeth, S.K., Soni, C.B., Kumar, V., Seh, Z.W.: ‘Understanding the Cathode–Electrolyte Interphase in Lithium-Ion Batteries’*Energy Technology*, 2022, 10, (9), p. 2200421.

178 Andjelkovic, M., Krstic, M., Kraemer, R., Veeravalli, V.S., Steininger, A.: ‘A critical charge model for estimating the SET and SEU sensitivity: A Muller C-element case study’*Proceedings of the Asian Test Symposium*, 2018, pp. 78–83.

179 Chen, S., Gao, Z., Sun, T.: ‘Safety challenges and safety measures of Li-ion batteries’*Energy Sci Eng*, 2021, 9, (9), pp. 1647–1672.

180 Zhang, W., Lu, Y., Wan, L., *et al.*: ‘Engineering a passivating electric double layer for high performance lithium metal batteries’*Nature Communications 2022 13:1*, 2022, 13, (1), pp. 1–12.

181 Sui, X., He, S., Vilsen, S.B., Meng, J., Teodorescu, R., Stroe, D.I.: ‘A review of non-probabilistic machine learning-based state of health estimation techniques for Lithium-ion battery’*Appl Energy*, 2021, 300, p. 117346.

182 Zhou, X., Huang, J., Pan, Z., Ouyang, M.: ‘Impedance characterization of lithium-ion batteries aging under high-temperature cycling: Importance of electrolyte-phase diffusion’*J Power Sources*, 2019, 426, pp. 216–222.

183 Sheraz, M., Choi, W.: ‘A Novel Technique for Fast Ohmic Resistance Measurement to Evaluate the Aging of Lithium-Ion xEVs Batteries’*Energies 2023, Vol. 16, Page 1416*, 2023, 16, (3), p. 1416.

184 Katzenmeier, L., Gößwein, M., Carstensen, L., *et al.*: ‘Mass transport and charge transfer through an electrified interface between metallic lithium and solid-state electrolytes’*Communications Chemistry 2023 6:1*, 2023, 6, (1), pp. 1–8.

185 Hassini, M., Redondo-Iglesias, E., Venet, P.: ‘Lithium–Ion Battery Data: From Production to Prediction’*Batteries 2023, Vol. 9, Page 385*, 2023, 9, (7), p. 385.

186 Bard, A.J., Faulkner, L.R.: ‘Polarography and Pulse Voltammetry’*Electrochemical Methods: Fundamentals and Applications*, 2001, pp. 261–304.

187 Newman, J.S., Balsara, N.P.: ‘Infinitely Dilute Solutions’*Electrochemical systems*, 2020, 0, pp. 229–249.

188 Macdonald, J.R., Johnson, W.B.: ‘Fundamentals of Impedance Spectroscopy’*Impedance Spectroscopy*, 2018, pp. 1–20.

189 Schönleber, M., Uhlmann, C., Braun, P., Weber, A., Ivers-Tiffée, E.: ‘A Consistent Derivation of the Impedance of a Lithium-Ion Battery Electrode and its Dependency on the State-of-Charge’*Electrochim Acta*, 2017, 243, pp. 250–259.

190 Aurbach, D., Talyosef, Y., Markovsky, B., *et al.*: ‘Design of electrolyte solutions for Li and Li-ion batteries: A review’*Electrochim Acta*, 2004, 50, (2-3 SPEC. ISS.), pp. 247–254.

191 Vornacheva, I. V., Pankov, D.N., Malikov, V.N., *et al.*: ‘On the use of the skin effect for eddy-current control of cylindrical metal products’*J Phys Conf Ser*, 2022, 2388, (1), p. 012054.

192 Elmahallawy, M., Elfouly, T., Alouani, A., Massoud, A.M.: ‘A Comprehensive Review of Lithium-Ion Batteries Modeling, and State of Health and Remaining Useful Lifetime Prediction’*IEEE Access*, 2022, 10, pp. 119040–119070.

193 Badot, J.C., Lestriez, B., Dubrunfaut, O.: ‘Interest in broadband dielectric spectroscopy to study the electronic transport in materials for lithium batteries’*Materials Science and Engineering: B*, 2016, 213, pp. 190–198.

194 Jolliffe, I.T.: ‘Principal Component Analysis’ (Springer, 2002, Second Edi)

195 Paul, C.R.: ‘Effectiveness of multiple decoupling capacitors’*IEEE Trans Electromagn Compat*, 1992, 34, (2), pp. 130–133.